STUDIES ON TRIBOLOGICAL CHARACTERISTICS OF DUAL PHASE STEELS

A THESIS

Submitted in fulfilment of the requirements for the award of the degree of

DOCTOR OF PHILOSOPHY

in

METALLURGICAL AND MATERIALS ENGINEERING

By

RAJNESH TYAGI

DEPARTMENT OF METALLURGICAL AND MATERIALS ENGINEERING
UNIVERSITY OF ROORKEE
ROORKEE-247 667 (INDIA)

FEBRUARY, 2001

UNIVERSITY OF ROORKEE
ROORKEE

CANDIDATE'S DECLARATION

I hereby certify that the work which is being presented in the thesis, entitled **"STUDIES ON TRIBOLOGICAL CHARACTERISTICS OF DUAL PHASE STEELS"** in fulfillment of the requirements for the award of the degree of Doctor of Philosophy and submitted in the Department of Metallurgical and Materials Engineering of the University, is an authentic record of my own work carried out during a period from July, 1997 to February, 2001 under the supervision of Dr. S. K. Nath and Dr. S. Ray.

The matter embodied in this thesis has not been submitted by me for the award of any other degree of this or any other University.

Rajnesh Tyagi

(RAJNESH TYAGI)
Signature of the Candidate

This is to certify that the above statement made by the candidate is correct to the best of our knowledge.

Date: 8th February, 2001

(Dr. SUBRATA RAY)
Professor and Head

(Dr. S. K. NATH)
Assoc. Professor

Department of Metallurgical and Materials Engineering
University of Roorkee,
Roorkee – 247667, India

The Ph.D. Viva-Voice examination of **Rajnesh Tyagi,** Research Scholar, has been held on 29 NOVEMBER, 2001.

Signature of Supervisor(s) Signature of H.O.D Signature of External Examiner

Prof. and Head
Deptt. of Metallurgical and Materials Engg.
Indian Institute of Technology, Roorkee
ROORKEE - 247667 (Uttaranchal)

ABSTRACT

The physical and chemical nature of the interaction between the mating surfaces in relative motion needs a thorough understanding for the development of wear resistant materials. Strength, toughness and ductility are undoubtedly the most important properties of the materials but the major difficulty in optimising these properties arises from the fact that strength is usually inversely related to toughness and ductility. The two phase materials are the best means for optimising these mutually exclusive properties. The underlying principle is to utilise the beneficial effects of the second phase and at the same time mitigating the less desirable features by the presence of the other constituent phase. The size, distribution, shape and volume fraction of the second phase critically controls the mechanical properties of the two phase systems. It is a well established fact that the friction and wear behaviour of the materials is affected by their mechanical properties which in turn are the function of the microstructure of the materials. Hence, a study of the morphology of the second phase in a microstructure and its influence on the friction and wear behaviour is critically important in two-phase wear resistant materials.

Metals and alloys are the most common materials employed in engineering for wear resistant applications. Thus, despite growing interest in ceramics and polymeric composites as engineering tribo-materials, much of the wear research being conducted is directed towards metallic materials. Although, aluminium and magnesium alloys and composites based on these matrix materials containing particles or fibers, are being used or developed for wear resistant applications but the steels have retained their place intact in wide ranging wear resistant applications. The steels offer a unique advantage of tailoring their properties by development of a variety of microstructure and properties by simple heat treatment

techniques. In the quest for developing new wear resistant materials, the dual phase steels are the most promising among the two phase metallic materials because they possess some unique mechanical properties viz., continuous yielding, high tensile strength, high rate of work hardening and a high uniform and total elongation. In addition, the microstructure has relatively softer ferrite matrix containing islands of hard martensite phase. Hence, the present investigation is aimed to analyse the friction and wear behaviour of the dual phase steels under dry sliding conditions using a pin-on-disc wear testing machine in the specific context of the role of microstructure.

In the present study, the plain carbon steel containing 0.42 wt pct carbon have been intercritically annealed in the (α+γ) region of Fe-C phase diagram at a constant temperature of 740^0C for different holding times followed by water quenching to develop dual phase structures having four different martensite content. Normalised steel having the same carbon content has been used as a reference material. Armco iron and hardened 0.42 wt pct carbon steel with fully martensitic structure have been used to simulate the properties of the constituent phases of the dual phase steel. The plain carbon steel containing 0.14 wt pct carbon has also been intercritically annealed for five minutes followed by water quenching to develop the dual phase structure. The microstructures and the mechanical properties of all the different materials used in the present investigation have been characterised. The friction and wear behaviour under dry sliding condition has been determined for all these materials having different microstructures. The present study also focuses on the synergy between the matrix of ferrite and hard martensite islands during dry sliding of dual phase steels and its effect on the observed friction and wear behaviour which may enrich our understanding of the material aspects of friction and wear.

Chapter-1 contains the introductory remarks highlighting the technological importance of the problem under investigation.

Chapter-2 begins with a critical review of the existing literature on the techniques of production and mechanical properties of dual phase steels. It is followed by an exhaustive survey on the various aspects of the friction and wear behaviour of the metallic materials in general, and of steels in particular. The different types of mechanisms giving rise to wear have been outlined. The existing models for different types of wear mechanisms are presented in the literature. The effects of microstructure, mechanical properties, normal load, sliding velocity, surface roughness and environments on the friction and wear behaviour of the steels have also been reviewed. The limited knowledge on the role of microstructure and the normal load on the friction and wear characteristics of dual phase steels has been given a special attention as the role of these two variables has been particularly investigated in the present study. In the end the formulation of problem is presented.

Chapter-3 outlines the experimental procedures followed in the present investigation. The method used to determine the chemical composition is given. The details of the vertical tube furnace used for intercritical annealing heat treatment for the development of both the dual phase and the fully martensitic structure have been described along with the parameters used for the heat treatment schedule. The procedures followed for the study of microstructure, hardness and uniaxial tensile tests have also been described in this chapter. Fracture surfaces of the specimens have been examined under scanning electron microscope. The friction and dry sliding wear in the Armco iron, normalised steels both low (LCN) and medium carbon (N), dual phase (DP) steels and fully martensitic steel (FMS) have been determined by tests carried out on pin-on-disc machine against a counterface of En-32 steel hardened to HRC 62 to 65, following procedures outlined in this section. Pin weight losses have been measured at different intervals of time. Five normal loads viz., 14.7, 19.6, 24.5, 29.4 and 34.3 N have been used for Armco iron and 0.42 wt. pct carbon steels whereas, the low carbon normalised and dual phase steel containing 0.14 wt pct carbon have been tested under the normal loads of

14.7, 24.5 and 34.3 N in the present investigation. For all the friction and wear tests the sliding speed has been maintained at a constant value of 1.15 m/s. The wear debris generated during sliding has been observed under stereo-optical microscope. The X-ray diffraction analysis of the wear debris collected during sliding has been carried out to identify the phase constituents following the method described in this chapter. The wear surfaces as well as the subsurface of the pin after sliding have been examined under scanning electron microscope (SEM). The method of determining the rise in temperature of the pin surface has been presented. The method to examine the microstructure of the deformed subsurface of the pin after the sliding also forms a part of this chapter.

Chapter-4 describes a model developed to predict the oxidative wear rate of two phase materials like the dual phase steels. It has been assumed that oxidation of both the phases take place with the same kinetics but the hardness of the underlying phases are different. The oxide layer builds up over successive contacts and the oxide under the contact breaks up into wear debris once the oxide builds upto a critical level of thickness. The calculated results for wear rate assuming parabolic law of oxide growth have been compared with those observed experimentally under different loads. It is observed that this model has consistently overestimated the wear rate. However, if the critical thickness of the oxide is taken a little higher or the oxidation rate constant is taken a little lower than those assumed on the basis of reported values, the calculated wear rate may match the observed ones. In another model, where the critical thickness of the oxide layers, for their removal as debris particle have been estimated separately from the experimental results of the fully ferritic Armco iron and fully martensitic steel, the calculated wear rates for dual phase steels have given an underestimation of results.

Chapter-5 describes the results on microstructure and mechanical properties characterising Armco iron, low and medium carbon normalised steels, dual phase steels and

fully martensitic steel (FMS). The martensite content in dual phase steels and the microstructure of all the materials have been characterised by optical microscopy. The increasing time of holding during intercritical annealing followed by water quenching results in increasing volume fraction of martensite in medium carbon dual phase steels (DP1, DP2, DP3 and DP4). The distribution of martensite in dual phase steels has generally been homogeneous. The Brinell hardness measurements point towards an increasing hardness with martensite volume fraction. The dual phase steels show a continuous yielding behaviour under tension confirmed by the absence of yield point in the load-extension curve while a clear yield point phenomenon is visible in the load-extension curve of normalised steel. The Armco iron simulating ferrite phase in DP steel shows typically ductile mode of fracture whereas the fully martensitic steel shows a typically brittle fracture. The dual phase steels show the mixed mode (ductile + brittle) of fracture with an increasing dominance of brittle mode with the martensite content. The UTS has the highest value for fully martensitic steel and the lowest for Armco iron with those for normalised and dual phase steels falling in between. The UTS in DP steels increases with martensite content. The percentage elongation decreases with increasing volume fraction of martensite in the dual phase steels. The strain hardening coeficient decreases linearly with increasing martensite content.

Chapter-6 contains the results and discussion pertaining to the friction and wear characteristics of the Armco iron, medium carbon normalised (N) and dual phase steels (DP1, DP2, DP3 and DP4) and fully martensitic steel (FMS). The variation of wear volume at a given load and sliding velocity is generally found to be linear and the wear rate at that normal load has been determined from the linear least square fit of the variation of wear volume with sliding distance. If the variation of the wear rate with normal load is linear, it implies that Archard's law is being obeyed. The wear coefficient, K_A, has been determined using Archard's equation as given below.

$$K_A = \frac{V H}{L S} \qquad (1)$$

Where, V is the cumulative volume loss under a normal load of L after a sliding distance of S. H is the initial hardness of the softer one (pin) of two mating materials sliding against each other. The wear coefficient has been estimated from the slope of the linear variation of wear rate with load, V/SL, by multiplying it with the initial hardness of the corresponding pin material. The variation of cumulative wear volume has been analysed using two separate stages (run-in and steady state) of wear behaviour. Two linear segments will also allow remaining within the framework of Archard's law. The change in slope has been observed after the first six experimental points (first stage-run-in), fitted by one line, and the latter six points (steady state) have been fitted with another line with the sixth point common between them. Both the lines have been determined by the linear least square fit and their slopes give the corresponding wear rate. The variation of the cumulative wear volume with sliding distance has been found to be linear in both the segments i.e., run-in and steady state, and the cumulative volume loss increases with load. All the materials having different microstructures, used in the present investigation have followed this common trend. The cumulative wear volume is found to be the highest for Armco iron and the lowest for fully martensitic steel with those for the N steel and the dual phase steels lying in-between. Thus, at a given load, the cumulative volume loss decreases with increasing martensite volume fraction.

The wear rate for the Armco iron is observed to be the highest whereas it is found to be the lowest for fully martensitic steel in both the run-in and the steady state stages of wear. The wear rates for the normalised steel and all the dual phase steels are considerably lower than those for Armco iron but higher as compared to those of fully martensitic steel

corresponding to both the stages of wear. The wear rate has been found to increase linearly with the normal load corresponding to both the linear segments for Armco iron, dual phase steels and fully martensitic steels. In case of the normalised steel it is found that the wear rate varies linearly with the load corresponding to the first linear segment but in the second linear segment, the variation of the wear rate is nonlinear. The wear rate is less in second segment (steady state) as compared to that in the first segment (run-in) for all the materials investigated in the present study. At the loads used in the present investigation, the mechanism of wear is primarily oxidative although subsurface cracking and delamination wear could also be observed in a few places. The second linear segment could result from a dynamic steady state of the transfer layer of compacted oxide wear debris on the sliding surfaces. The oxidative nature of the wear has been confirmed by X-ray diffraction analysis of the wear debris corresponding to both the segments. It has revealed the presence of α-Fe_2O_3 alone in the wear debris. The wear rate has been found to decrease with the increasing martensite volume fraction in dual phase steels. A higher martensite volume fraction imparts higher hardness to the steel and consequently, results in a lower real area of contact. Hence, the decrease of wear rate with hardness as observed, is anticipated.

The variation of coefficient of friction with sliding distance for different loads has shown a fluctuating trend, characteristic of pin-on disc experiment for all the materials used in the current study. It is noted that friction coefficient in the run-in stage fluctuates around a mean level, then lessens and stabilizes after a certain period. The Armco iron has shown a consistently higher value of the average coefficient of friction as compared to those observed for the fully martensitic steel (FMS). The average coefficients of friction for medium carbon normalised (N) steel and dual phase steels have been found to lie in-between those for Armco iron and fully martensitic steel. For the dual phase steels the average coefficient of friction has been observed to decrease with increasing martensite volume fraction. The average coefficient of friction is found to decrease more or less linearly with increasing load for all the

materials used in the study that may be explained on the basis of the extent of cover provided by the highly compacted transfer layer of oxide at these loads. X-ray diffraction analysis indicates that the transfer layer contains both amorphous and crystalline oxides, which will have lower adhesion with the counterface and will give rise to junctions of lower shear strength and thus, the coefficient of friction may decrease. Contrary to the folklore that the friction is directly proportional to the real area of contact (load/ initial hardness of the material), the average coefficient of friction is found to decrease linearly with increasing real area of contact and normal load for a given material.

The wear rates calculated on the basis of (i) estimated load sharing between the constituent phases and (ii) the observed wear coefficients of Armco iron and FMS are relatively higher than the observed wear rates in dual phase steels in both the run-in and the steady state of wear. The calculated wear rates are comparable to the observed wear rates at lower loads but have increasingly larger difference with increasing loads. However, when the volume fraction of martensite increases, the difference between the estimated and the observed wear rates decreases even at higher loads. This difference between the estimated and the observed wear rates is relatively lower in the steady state compared to that in the run-in stage of wear. The difference in the calculated and the observed wear rates may be attributed to the flow of the softer phase of ferrite over the hard martensite islands resulting in easily oxidised junctions of low shear strength while maintaining the same real area of contact. The higher oxidative wear of this ferrite over that of martensite may lead to higher observed wear rates. As the martensite volume fraction increases, the flow of ferrite gets restrained and thereby a better matching between the experimental and the calculated results, is observed because the sliding surface has both ferrite and martensite in amounts as presumed in the calculation.

The wear rates have also been estimated using the oxidative wear model proposed in Chapter-4, where it is assumed that the critical thickness of oxide and the probability of its removal are the same in both the phases of ferrite and martensite in DP steels. The estimated wear rates are consistently higher than those observed experimentally at all the loads in both the run-in and the steady state of wear. It may be attributed to the assumed values of the critical thickness of oxide and the oxidation rate constant. The estimated wear rates could match the observed wear rates if one takes either a higher value of the critical thickness of oxide or a lower value of oxidation rate constant.

The wear rates have been estimated on the basis of different oxidation behaviour of the constituent phases of ferrite and martensite where the critical thickness of oxide layer and the probability of its removal are presumed different for both the phases in DP steels. The critical thickness of oxides and the probability of their removal for ferrite and martensite have been determined from the oxidative wear behaviour of fully ferritic Armco iron and martensitic FMS respectively. The calculated wear rates are comparable to the observed wear rates at lower loads but are increasingly higher at higher loads in both the run-in and the steady state of wear. However, when volume fraction of martensite increases the difference between the estimated and observed values of wear rate decreases even at higher loads. The difference in the estimated and the observed wear rates may be attributed to the flow of the softer ferrite over the hard martensite islands as described earlier. A good matching at the lower loads may be attributed to the insignificant flow of ferrite and the sliding surface has relative area fractions of ferrite and martensite as presumed. The increasing difference in the estimated and the observed wear rates at higher loads may be due to a higher area fraction of ferrite which flows over the hard martensite islands, resulting in a higher rate of oxidative wear. A better matching between the estimated and the observed wear rates obtained at higher martensite volume fractions may be attributed to the restricted flow of ferrite over martensite islands.

The coefficients of friction in the steady state have been estimated on the basis of the rule of mixture and the observed friction coefficients of Armco iron and FMS. The calculated coefficients are found to be a little higher than those observed experimentally in DP steels. The coefficients of friction in the steady state, calculated on the basis of (i) estimated load sharing between the constituent phases and (ii) the observed friction coefficients of Armco iron and FMS, are relatively lower than those observed experimentally in dual phase steels. The lower values of the estimated friction coefficients may be attributed to the flow of the softer phase of easily oxidised ferrite over the hard martensite islands in the dual phase steels, which results in the formation of the lower shear strength junction and subsequently, a lower coefficient of friction.

The wear coefficient which may be interpreted as wear rate per unit real area of contact, does not change significantly between the Armco iron and the dual phase steels (DP1 and DP2 containing 42 and 51 pct martensite respectively) in the run in stage of wear. But the wear coefficient decreases sharply as one moves from DP2 (51 pct martensite) to DP4 (72 pct martensite) indicating decreasing wear rate dominating over the decrease in real area of contact due to increasing hardness. In the steady state, the wear coefficient decreases linearly with increasing volume fraction of martensite. The decrease in wear coefficient may be attributed to decreasing wear rate dominating over decreasing real area of contact due to increasing hardness. For wear coefficient, because of its definition, decrease in real area of contact becomes a disadvantage. Hence, Wear coefficient as a sensitive discriminating wear parameter may not, therefore, be adequate in materials of similar property and structure and the wear rates may be a better indicator.

Chapter-7 describes the results and discussion pertaining to the friction and wear characteristics of the low carbon normalised (LCN) steel and dual phase (DP) steel. The

variation of wear volume at a given load and sliding velocity is found to be linear, obeying Archard's law and wear rate at that normal load has been determined from the linear least square fit of the variation of wear volume with sliding distance. The cumulative volume loss is found to be higher for LCN steel compared to that in DP steel. The wear rate increases linearly with increasing load in both the run-in and the steady state of wear for DP steel. However, for LCN steel, the variation is linear in the run-in stage but in steady state, the wear rate increases rapidly at higher load. The DP steel has shown a lower wear rate compared to the LCN steel in both the run-in and the steady state of wear. At the loads used in the present investigation, the mechanism of wear is primarily oxidative although subsurface cracking and delamination wear could also be observed in a few places. The oxidative nature of wear has been confirmed by X-ray diffraction analyses of the wear debris corresponding to both the segments. It has revealed the presence of α-Fe_2O_3 alone in the wear debris. The wear rate has been found to decrease with the increasing martensite volume fraction in dual phase steels irrespective of the carbon content of the steel. The average friction coefficient decreases nonlinearly with increasing load for both LCN and DP steels but LCN steel has a slightly higher value of friction consistently at all the loads than those in DP steel.

Chapter-8 presents the major conclusions of the current study on microstructure, mechanical properties and tribological behaviour of low and medium carbon dual phase steels in the context of friction and wear behaviour of its constituents simulated by Armco iron and fully martensitic steel. The friction and wear behaviour of low and medium carbon normalised steels are used as reference material for the study of friction and wear behaviour of dual phase steels.

ACKNOWLEDGEMENTS

The author is pleased to express his immense sense of gratitude to Dr. S. K. Nath, Associate Professor and Dr. S. Ray, Professor and Head, Department of Metallurgical and Materials Engineering, University of Roorkee, Roorkee for their invaluable guidance, constructive criticism, thought provoking discussions and painstaking efforts throughout the course of this work. Their invaluable and prompt remarks at the time of preparation of the manuscript are especially appreciated.

The author acknowledges his deep sense of gratitude to the Head, Met. & Mat. Engg., Deptt., Head, Mech. & Ind. Engg. Deptt. and Director, University Science and Instrumentation Centre for providing him the facilities during the course of experimental work.

The author is highly obliged and wishes to express his sincere thanks to the technical staff of the Metallurgical & Materials Engineering Department, especially to Mr. S.C. Kaushik, Mr. Ajmer singh, Mr. Shakti Gupta, Mr. M. Pandey, Mr. J. P. Sharma, Dr. A.P. Nautiyal, Mr. S. N. Kaushik, Mr. Madhu Singh, Mr. N. K. Seth, Mr. Rajendra Sharma, Mr. Balesh Sharma, Mr. S. P. Sharma, Mr. Dharam Pal, Mr. Vidya Prakash, Mr. Shamsher Singh, Mr. R. K. Sharma, Mr. Ahuja and Mr. Giri, Mr. Ram Kishan, Mr. N. K. Sharma, Mr. Dhan Prakash and Mr. A. Kush, who have helped him in all possible ways during the experimental work. Thanks are also due to Mr. Sunil Sharma, the Librarian of Met. and Mat. Engg. Deptt. for providing help at crucial times. The author also acknowledges his sincere thanks to Mrs. Rekha Sharma and Mr. S. K Saini of the University service and Instrumentation Centre, University of Roorkee. Thanks are also due to Mr. Jagpal Singh of Welding Research Laboratory, MIED, UOR for his cooperation during the experimental work of the thesis. Thanks are also due to Mr. Puran Sharma and Mr. Kameshvar Saini for preparing high quality micrographs and drawings.

The author wishes to register his sincere thanks to Dr. S. Bhattacharyya whose critical and timely suggestions proved to be helpful at the time of preparation of this thesis.

The author wishes to acknowledge with deep sense of gratitude the help and moral support rendered by Dr. (Mrs.) Vijaya Agarwala and Prof. M. L. Kapoor during the crucial phase of the work.

The facilities provided by U. P Steels, Muzaffarnagar, B.H.E.L., Ranipur for carrying out chemical and quantitative analysis are also sincerely acknowledged. The author is also indebted to Deptt. of Hydrology for providing some useful data on relative humidity.

The financial support provided by Council of Scientist and Industrial research, New Delhi is highly acknowledged.

When hurdles appeared insurmountable and targets unachievable, the encouragement and camaraderie of friends helped keep things in perspective. Author wishes to thank to many friends and colleagues who helped lighten the burden, especially to Mr. Sunil Sharma, Mr. Narendra, Mr. Shantanu, Mr. Rajnish Garg, Dr. Ramalingaiah, Dr. Jawdat, Dr. Satyabir Singh and Mr. S.P Singh.

The author would like to express his reverence and great admiration for his grand mother and parents, to whom he owes everything. They have been a guiding force all his life and the author has tried to measure up to their expectations. The author humbly dedicates this work to them. The author wishes to express his sincere thanks to his brothers, sisters and other family members who have shown patience during the entire duration of this work. Thanks are also due to all nears and dears who have helped the authors in various ways during the course of this work.

At last thanks to the almighty god who has given the author spiritual support and courage to carry out this work.

(Rajnesh Tyagi)

CONTENTS

LIST OF FIGURES

LIST OF TABLES

NOMENCLATURE

σ	True stress
ε	True strain
τ	Shear strength of the junction
μ	Coefficient of friction
κ	Constant of proportionality
η	Standard deviation of asperity heights
β	Oxidation rate constant
λ	Spacing between asperity contacts
ρ_0	Density of oxide
β_0	Arrhenius constant
ν_1, ν_2	Poisson's ratios
μ_a	Adhesive coefficient of friction
ξ_c	Critical thickness of oxide
$\xi_{c,f}$	Critical thickness of oxide for ferrite
$\xi_{c,m}$	Critical thickness of oxide for martensite
μ_d	Coefficient of friction due to deformation
μ_{DP}	Coefficient of friction in DP steel
ΔL	Contact length
Δm	Mass of oxygen taken up by oxide per unit area
σ_T	Tensile strength of composite
$\sigma_{T,\alpha}$	Tensile strength of ferrite phase
$\sigma_{T,m}$	Tensile strength of martensite phase
ε_u	True uniform strain
$(V/S)_{DP}$	Wear rate of DP steel
σ_y	Yield strength of composite
$\sigma_{y,\alpha}$	Yield strength of ferrite phase
$\sigma_{y,m}$	Yield strength of martensite phase
a	Asperity radius
A_a	Apparent area of contact
A_p	Volume of the plastically deformed zone
A_r	Real area of contact
B	Burger's vector
$d\sigma/d\varepsilon$	Rate of work hardening
e	Engineering strain
E'	Effective young's modulus
E_1 , E_2	Young's modulus
F	Frictional force
f	Mass fraction of oxygen in oxide
F_a	Deformation component of the friction force

F_d	Adhesive component of the friction force
F_f	Friction force shared by martensite
F_m	Friction force shared by ferrite
G	Shear modulus
H	Initial hardness of the material
K_{1f}	Probability of removal of oxide layer in ferrite.
K_{1m}	Probability of removal of oxide layer in martensite
K_A	Wear coefficient
k_m	Thermal conductivity
L	Normal load
l_c	Crack spacing
L_f	Load shared by ferrite phase
L_m	Load shared by martensite phase
N	Strain hardening index
N	Total number of asperity contacts
Nc	Number of cracks
N_w	Number of cracking sheets
P	Yield pressure
r	Radius of the sphere
R_a	Centre line average value
R_s	Root mean square value
S	Engineering stress
S	Sliding distance
t	Time
T_0	Temperature of oxidation at contacts (^{0}C)
T_c	Contact temperature at asperity tips (^{0}C)
T_S	General surface temperature or bulk temperature (^{0}C)
v	Sliding velocity
V	Wear volume
V_f	Volume fraction of ferrite
V_m	Volume fraction of martensite
W	Wear rate

LIST OF PUBLICATIONS

1. Tyagi, R., Nath, S.K. and Ray, S., (to be published in Feb., 2001), "Dry Sliding Friction and Wear in Plain Carbon Dual Phase Steels", *Metallurgical and Materials Transaction,* Pennsylvania, USA.

2. Tyagi, R., Nath, S.K. and Ray, S., (1999), "Friction and Wear Behaviour of Dual Phase Steel Under Dry Sliding", Annual Technical Meeting of the *Indian Institute of Metals* held at IIT Kanpur, India during Nov. 13-16, 1999, *Transactions of Indian Institute of Metals*, Vol. 52.

Chapter 1

INTRODUCTION

The important prerequisites of any engineering system are its reliability, efficiency and long life. Relative sliding movement between the two components in an engineering system causes a loss of the material from the surfaces of both the components and this loss, termed as "*wear*", may affect its reliability, efficiency and long life. In most of the situations, the failure of the machines is due to the wear and not due to the breakage of component. Wear is not an intrinsic property of a material but a characteristic of an engineering system. Wear is rarely catastrophic, but it reduces the operating efficiency and increases power losses, oil consumption, and component replacement rates. It, therefore, becomes necessary that the parts having sliding motion relative to each other may be designed to minimise wear. During rubbing some fundamental changes occur in the surface of the contacting materials and these changes determine the nature of the wear process and friction force. The study of the complex phenomena occurring during rubbing and the need to minimise both energy and material losses in mechanical systems has led to an enlarged interest in the field of "Tribology", the science of friction, wear and lubrication.

Wear leads to an unwanted and inevitable loss of material, which can only be minimised but can not altogether be completely mitigated. Wear encountered in the industry has been classified as the following types and their estimated relative occurrences are: Abrasive 50%; Adhesive 15%; Erosive 8%; Fretting 8% and Chemical 5% (Eyre, 1978). In 1983, it was estimated that a total loss of 38.71 billion DM (£ 13 billion) is incurred through tribological causes in FRG. Unlubricated systems accounted for a loss of 17.78 billion DM (≈ £ 6 billion). In Steel and other Metallurgical Industries in Germany, the loss due to

unlubricated wear was estimated as 53% of the total loss. Economic loss in the United States due to wear and friction has been put at about 2.5 % of GNP while in Germany it has been put at 4.5 % of GNP (Ramesh *et al*, 1991). As a consequence, it is vital to become aware of different aspects of wear and take preventive steps to avoid the huge economic loss due to wear. It is believed that a proper attention given to tribology, especially in education, research and application, could lead to economic savings between 1.3% to 1.6% of the GNP (Jost, 1990). Hence, in view of the quantum of the loss due to wear it becomes imperative for an engineer to develop better defence against wear by exploring newer wear resistant and cost effective materials for the tribological applications.

The necessity to minimise wear has given impetus to the development of the new wear resistant materials and has attracted the attention of the materials scientists worldwide. A lot of research work is going on in the direction of the development and the tribological characterisation of lightweight composites based on aluminium or magnesium alloys for the last thirty-five years. The industries manufacturing the transport systems, be it land, air or space, are continuing their quest to reduce weight and have a high strength/weight ratio of the components in order to increase the life and efficiency of engineering systems. The aim of the composite development is to attain a spectrum of properties, which can not otherwise be obtained in any of the constituent materials. A wide variety of composites containing the fibres, whiskers and ceramic particles have been developed for wear resistant applications. However, despite the growing interest in polymers, ceramics or composites, metals and alloys, are still the most widely used materials in tribology. The steels have retained their place in the wide ranging applications e.g., bearings, shafts, journals, gears etc. The importance of steels lies in the fact that the properties could be tailored to match a particular requirement through the development of different microstructures following heat treatment procedures.

Wear and friction behaviour of materials depends on the mechanical properties of the constituent phases like hardness and shear strength. Many of the tribological applications like bearing, there is contradictory requirement. The material should be soft in order to follow clearly the contour of the shaft so that conditions for elastohydrodynamic lubrication could be established. At the same time, the material has to be hard enough to bear the load under a given condition. It is not possible to meet these properties in single phase materials limiting their use in wear resistant applications. Two phase alloys and other materials may, however, be designed to serve as better alternatives for tribological applications. Some of the two phase materials like Cu-Sn, Cu-Ti alloys, Fe-TiC composites, aluminium based alloys, magnesium based alloys etc. have been widely employed in bearing and other wear resistant applications. The underlying principle here is to utilise the mutual advantages of both the phases when the less desirable features of these phases are mitigated by the presence of the second phase. The morphology i.e., size, shape, distribution and volume fraction of the second phase critically controls the mechanical properties of the two phase system which in turn influence its tribological behaviour.

In the composites, the incorporation of both the soft and the hard particles has been found to lower friction and improve wear resistance (Rohatgi *et al*, 1992). The loss of the hardness and strength by the incorporation of the softer phase is presumably compensated by the addition of the hard phase. Further, the addition of soft phase is expected to give an increased real area of contact during sliding which in turn will give higher wear inspite of the fact that a softer phase will result in the junctions of lower shear strength and subsequent lowering of the coefficient of friction. The incorporation of hard phase will reduce the real area of contact, thereby reducing the wear loss.

Dual phase (DP) steels are two phase materials, which have the potential to be used as wear resistant materials. It has unique structure consisting of hard martensite islands in the

ductile matrix of ferrite. These steels possess some special properties viz., absence of yield point phenomena, large ratio of tensile strength to yield strength, high rates of work hardening, high total and uniform elongation, excellent forming characteristics and high fracture toughness. The mechanical properties of the dual phase steels can be tailored by changing the amount of martensite in the structure, by carrying out intercritical annealing heat treatment for different holding times followed by water quenching. Due to superior properties and relatively simple processing, the dual phase steels show a great promise for a wide range of applications. These steels have been employed in several automotive components such as bumpers, wheel discs and rims, steering columns, chassis components, doors, pulleys, spring supports, car bodies etc. The use of these steels in automobiles has led to a weight reduction of upto 30% with a notable increase in the life of the components (Abdalla *et al*, 1999). In the field of mineral processing, mining and pipeline transportation of slurry, dual phase steel has already been employed as wear resistant material (Sui *et al*, 1992) but still there is a need to understand the tribological behaviour of dual phase steels in order to explore its full potential as tribological material.

The microstructure plays a crucial role in dictating the tribological behaviour of the two phase materials. It is not only the amount and the morphology of the second phase but also the coherency of the dispersed phase with the matrix, which has a significant effect on the wear behaviour. In the steels with spheroidised carbides, the interface between the carbides and the ferrite is, in general, incoherent which causes dislocation pile-up during straining leading to the nucleation of voids and fracture. In dual phase steels the coherency between the martensite and the ferrite phase allows the penetration of the dislocation from the ferrite phase into the martensite and so, large strain concentrations do not result in the boundary and the fracture occurs at relatively higher strains.

In dual phase steel, the relatively softer phase of ferrite provides the junctions of the lower shear strength thus, lowering the friction and the hard martensite phase imparts hardness to the steel resulting in decrease in the real area of contact and consequently, the lower wear loss. Thus, the dual phase steel may prove to be an interesting material from tribological point of view and the aim of the present study is, therefore, an understanding of the friction and behaviour of the dual phase steel. The presence of the second phase markedly influences the wear behaviour of the materials but the effect has not been systematically investigated so far. In the present study, it will also be aimed to develop a theoretical model for oxidative wear and study the effect of the second phase on the wear behaviour of these steels.

In summary, the present study has been carried out in order to correlate the microstructure evolved after the intercritical annealing with the observed mechanical properties and tribological behaviour of the dual phase steels. The knowledge base generated through this study is expected to provide a better understanding of this unique class of steels and help utilise its potential as a future material for tribological application.

Chapter 2

REVIEW OF LITERATURE

Sliding wear is the most complex form of wear as pointed out by Blau (1997) in a recent review. It involves not only the cutting and plowing as in abrasion but also adhesion between the asperities, third body (wear debris) interaction, subsurface crack initiation and propagation, the transfer of material to and from the mating surface, changes in the surface roughness during run-in, tribochemical film formation and other processes. Hence, despite the continued research for the five decades or so, the knowledge of the wear of materials is still imperfect and the controversies still exist (Rigney, 1997). For example there is no unanimity on whether the surface layer is harder or softer than the substrate. A generalised equation for the prediction of wear rate for a given combination of materials, environment, geometry, load and sliding speed is still elusive and only a simple linear wear equation given by Archard is being used widely. Wang *et al* (1999) have indicated that there is no simple relationship between hardness and wear resistance. The effect of microstructure and the dramatic changes in the microstructure as a result of tribochemical processes during sliding are still ill defined. The microstructure have been shown not to affect the wear rate in eutectoid steels by Wang *et al* (1996, 1999) while Sawa and Rigney (1987) have found a striking difference in the wear rates of the dual phase steels having different microstructure. Similarly, most of the work carried out in the oxidative wear done till date has revolved around formation and changes in the composition of the oxide with the change in contact temperature but the role of the second phase particles on the oxidative wear of two phase or multiphase structures has not been explored specifically. The model given by Quinn (1967) for the oxidative wear also does not include the effect of the second phase particle on the oxidative wear. Hence, there is a need to

focus investigations towards understanding and predicting the sliding wear of two phase materials.

This chapter contains a critical review of the existing literature on the techniques of attaining the microstructure and the mechanical properties in dual phase steels. A comprehensive review of the surface characteristics and the effect of surface interactions on the friction and wear processes are also included in this chapter. It is followed by an exhaustive survey on the various aspects of friction and wear behaviour of the metals, in general, and of steels in particular. The different types of mechanisms giving rise to wear and the existing models for different types of wear mechanisms are presented in the literature. The effects of microstructure, mechanical properties, normal load, sliding velocity, surface roughness and environments on the friction and wear behaviour of steels have also been reviewed. In the end the formulation of the problem is presented.

2.1 DUAL PHASE STEELS AND THEIR PROPERTIES

Dual phase steels are characterised by microstructure consisting of islands of martensite embedded in a ductile matrix of ferrite. The term dual phase essentially refers to the presence of two phases - ferrite and martensite, in the microstructure although small amounts of retained austenite, bainite and /or pearlite may also be present.

2.1.1 Types of Dual Phase Steels

Dual phase steels are produced by heating low / medium carbon steel into two phase ferrite-austenite ($\alpha+\gamma$) region of Fe-C phase diagram, followed by rapid cooling to transform

austenite (γ) into martensite, resulting in a structure of ferrite and martensite. Dual phase steels are of two types,

(i) Plain Carbon Dual Phase Steels

These steels are low or medium carbon steels having no alloying elements (Bailey, 1979). Typical compositions of plain carbon dual phase steels are shown in Table 2.1. Due to the absence of alloying elements, these steels have poor hardenability.

(ii) Alloyed Dual Phase Steels

Typical compositions of alloyed dual phase steels are also shown in Table 2.1. The chief alloying elements are manganese and silicon. Manganese is roughly around 1.5 pct and silicon is in the range of 1 pct. Other alloying elements like chromium, vanadium and molybdenum are in small amounts. Due to higher hardenability of these steels, dual-phase structure can be obtained by simple air cooling from intercritical region (Rashid 1976; Hayami and Furukawa, 1976; Spiech and Miller, 1979) in relatively thicker sections.

2.2.2 Development of Dual Phase Microstructure

There are two methods mainly used for developing dual phase microstructure in steels, namely, (a) intercritical annealing and (b) direct hot rolling technique.

(a) Intercritical Annealing

Dual phase microstructure in steels may be developed by heat treatment of either continuous intercritical annealing (Matsuoka and Yamoori, 1975; Furukawa *et al*, 1979; Tanaka *et al*, 1979) or

Table 2.1

Typical composition of dual phase steel, Weight Percent. (Coldren *et al.*, 1980)

Production Technique	C	Mn	Si	Cr	Mo	V	Al	N	S	P	Others
A. Plain carbon dual phase steels											
Continuous annealing followed by water quenching	0.05	0.33	0.02	-	-	-	0.051	0.006	0.017	0.012	-
-do-	0.10	0.41	0.11	-	-	-	0.051	0.0063	0.007	0.011	-
-do-	0.03	0.28	0.49	-	-	-	0.049	0.0058	0.006	0.017	-
-do	0.04	0.39	-	-	-	-	-	0.0031	0.008	0.118	-
B. Low alloy dual phase steels											
Continuous annealing	0.12	1.55	0.61	-	-	0.06	0.05	0.007	0.006	0.015	Rare earths
Hot-rolled gages	0.11	1.43	0.58	0.12	0.08	-	0.04	0.007	0.012	0.015	-
Continuous annealing Hot-rolled gages	0.11	1.20	0.40	-	-	-	0.04	-	0.005	0.015	-
Box-annealing	0.13	2.20	1.50	1.0	-	-	0.08	-	0.020	0.02	Rare earths
As-rolled	0.06	0.90	1.35	0.50	0.35	-	0.03	0.007	0.010	0.010	Rare earths

box-annealing (Matsuka and Yamoori, 1975; Mould and Skena, 1979). The continuous annealing technique is mostly used because of higher production rates and better uniformity in properties. The possibility of use of either low carbon steel strips or low alloy steel is also an added advantage of this technique. However, box-annealing has also been used where continuous annealing facilities are not available.

In the continuous annealing technique, the steel strip is heated for a short time (1-2 minutes) in intercritical temperature range as shown in Fig. 2.1, to form ferrite-austenite mixtures. This is followed by rapid cooling so as to allow the transformation of austenite into martensite. The actual cooling rate depends on the sheet thickness and quenching conditions on a given production line. Hence, the steel compositions need to be adjusted to obtain the hardenability needed for the sheet thickness at the given cooling rate. Typical chemical compositions of dual phase steels are given in Table 2.1 (Coldren *et al*, 1980).

In the box-annealing technique, similar heat treatment is carried out but the duration of annealing is relatively much longer (~ 3 hours) and the cooling rates are slower (20^0C/ hr). Due to this slow cooling rate, there is a need to have much higher level of alloying in steels to achieve the desired hardneability. For this annealing technique, 2.5 pct manganese steels containing appreciable amounts of silicon and chromium have been proposed (Matsuoka and Yamoori, 1975; Mould and Skena, 1979).

(b) Direct Hot Rolling Technique

In addition to the use of intercritical annealing heat treatment, dual phase steels have also been produced by direct hot rolling method or in the as-rolled conditions by carefully controlling the continuous-cooling transformation characteristics of the steels (Coldren and Tither, 1978; Eldis and Coldren, 1980). This essentially requires the addition of substantial amounts of silicon,

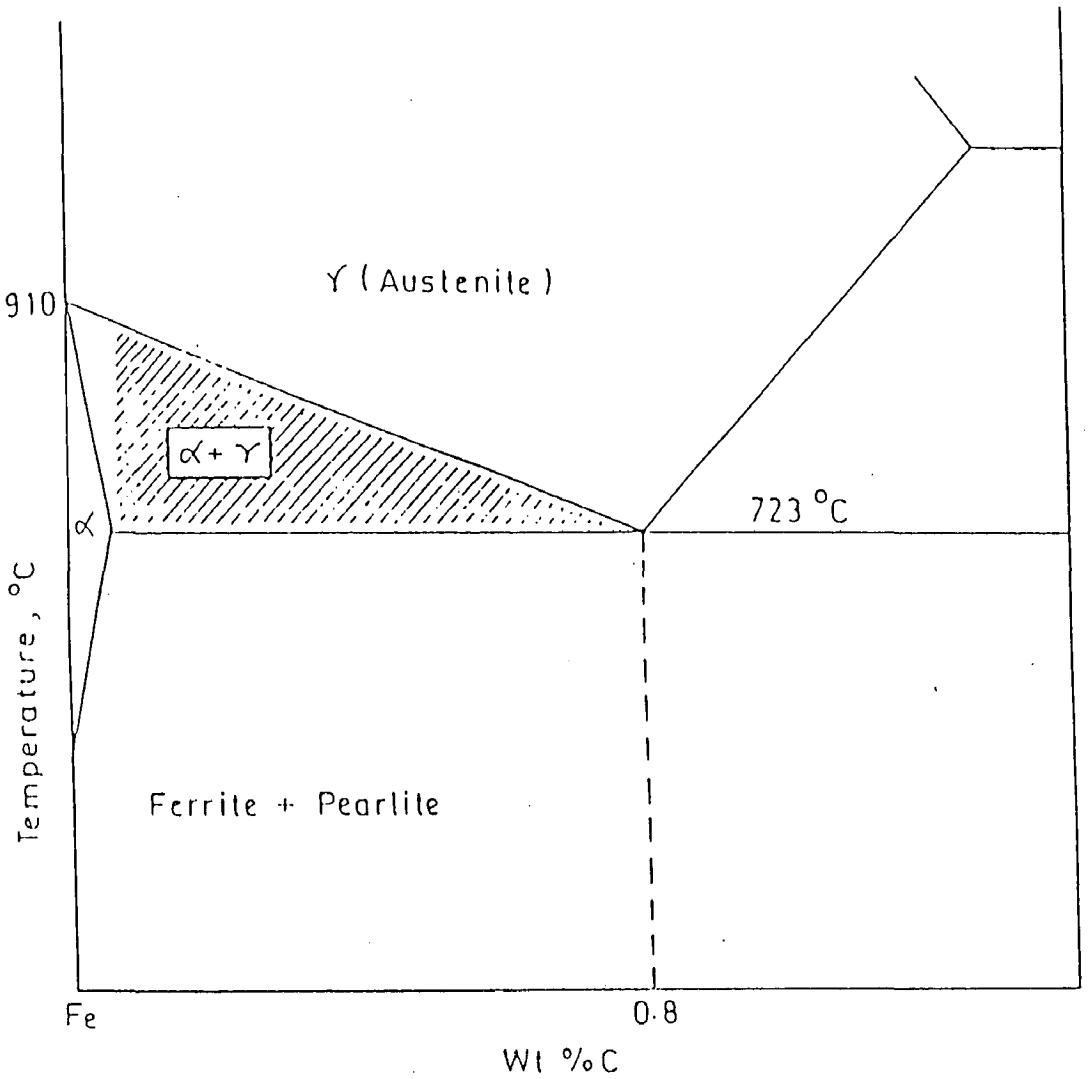

Fig. 2.1 Schematic diagram of Fe-rich portion of Fe-C phase diagram; shaded area indicates the region in which the hypoeutectoid steels are intercritically annealed.

chromium and molybdenum in addition to about 1.0 wt pct manganese as given in Table 2.1. In this method, the strip is allowed to cool rapidly on the run out table for about 10 seconds, after the last roll pass on a hot strip mill. At this stage, a large amount of polygonal ferrite (about 80 pct) forms but the formation of pearlite is suppressed and the remaining islands of carbon enriched austenite transform to martensite during the cooling of the strip in air. A desired type of continuous cooling transformations diagram is shown in Fig. 2.2 (Repas, 1979).

Production of dual phase steels by direct hot rolling has the advantage of saving energy costs by eliminating a heat treatment step. Also, dual phase steels can be produced when continuous-annealing facilities are not available. However, balanced against these advantages are the disadvantages of higher alloy cost and more variability in the properties in the production route of direct hot rolling. Seen against this background, the continuous annealing followed by rapid quenching seems to be the best bet for producing dual phase steels. However, there are certain limitations, which put restrictions on the size of the sheets to be used. The main problem for the application of dual phase plain carbon steel, is its material dimension limited by insufficient hardenability.

2.1.3 Mechanical Properties of Dual Phase Steels

Dual phase steels exhibit some unique properties, which are as follows:

(i) continuous yielding behaviour i.e. absence of yield point phenomenon.

(ii) a low 0.2% offset yield strength (~340 MPa) and a high tensile strength (~ 690 MPa).

(iii) a high rate of work hardening.

(iv) high uniform and total elongation (ductility).

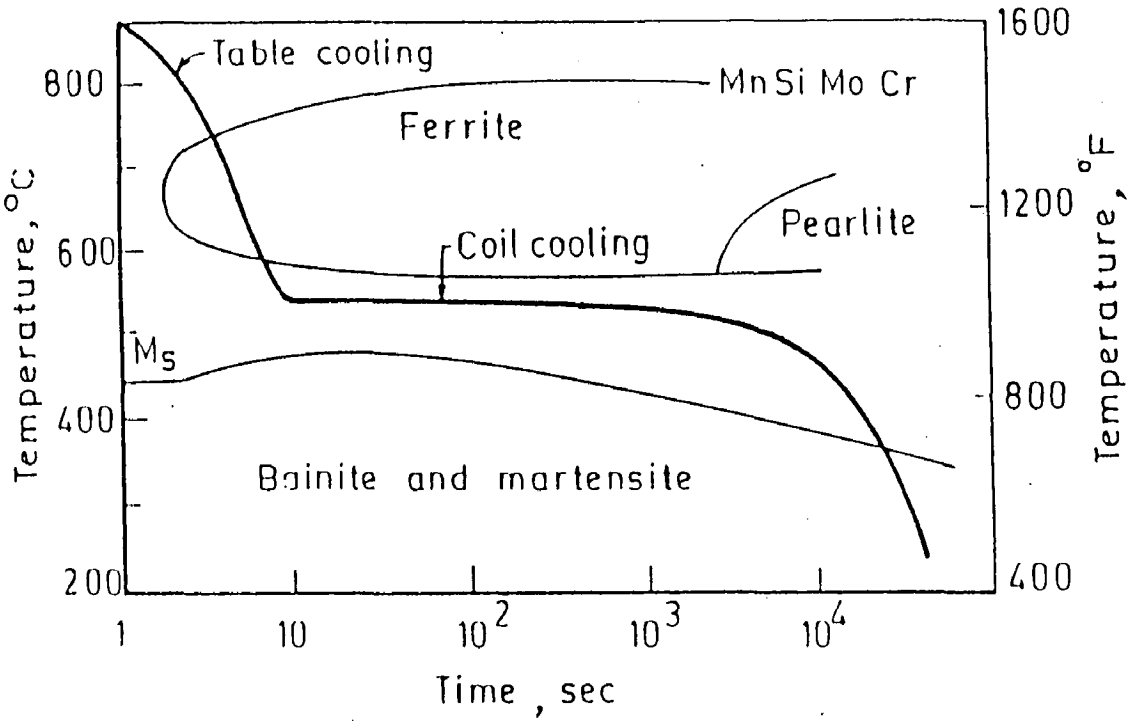

Fig. 2.2 Continuous –cooling transformation behaviour in Mn-Si-Mo-Cr steel resulting in dual phase microstructure in as-rolled product. (Repas, 1979)

(i) Continuous Yielding of Dual Phase Steel

Ferrite-martensite dual phase steels, in general, do not show yield point phenomenon as shown in Fig. 2.3 (Rashid, 1976; Dabkowski and Speich, 1977; Ramos *et al*, 1979). This is because of the combination of high residual stresses and high mobile dislocation density generated in ferrite phase immediately surrounding the martensite islands, as a result of stress generated during transformation of austenite to martensite, which is accompanied by volume expansion of 2-4 pct. The ferrite phase deforms plastically to accommodate this volume expansion. When this dual phase steel is deformed, plastic flow begins simultaneously at many sites throughout the specimen, thereby suppressing the discontinuous yielding or yield point phenomenon. Also, the absence of yield point in these steels eliminates Luder band formations and assures a good surface finish after forming operation.

(ii) Yield Strength and Tensile Strength

Based on the simple composite strengthening theory, it is expected that the strength of dual phase steel should increase when either the volume fraction or the strength of martensite phase is increased (Leslie *et al*, 1967; Speich, and Miller, 1979; Koo *et al*, 1980; Nath *et al*, 1993). If equal strains are assumed in both phases (which is far from reality in actual practice as strain should be more in softer ferrite phase), the variation of yield strength, σ_y, and tensile strength, σ_T, of ferrite-martensite mixtures when volume fraction of martensite is V_m, can be deduced from the " Law of Mixtures", as,

$$\sigma_y = \sigma_{y,\alpha}\,(1 - V_m) + \sigma_{y,m}\,V_m \qquad (2.1)$$

and

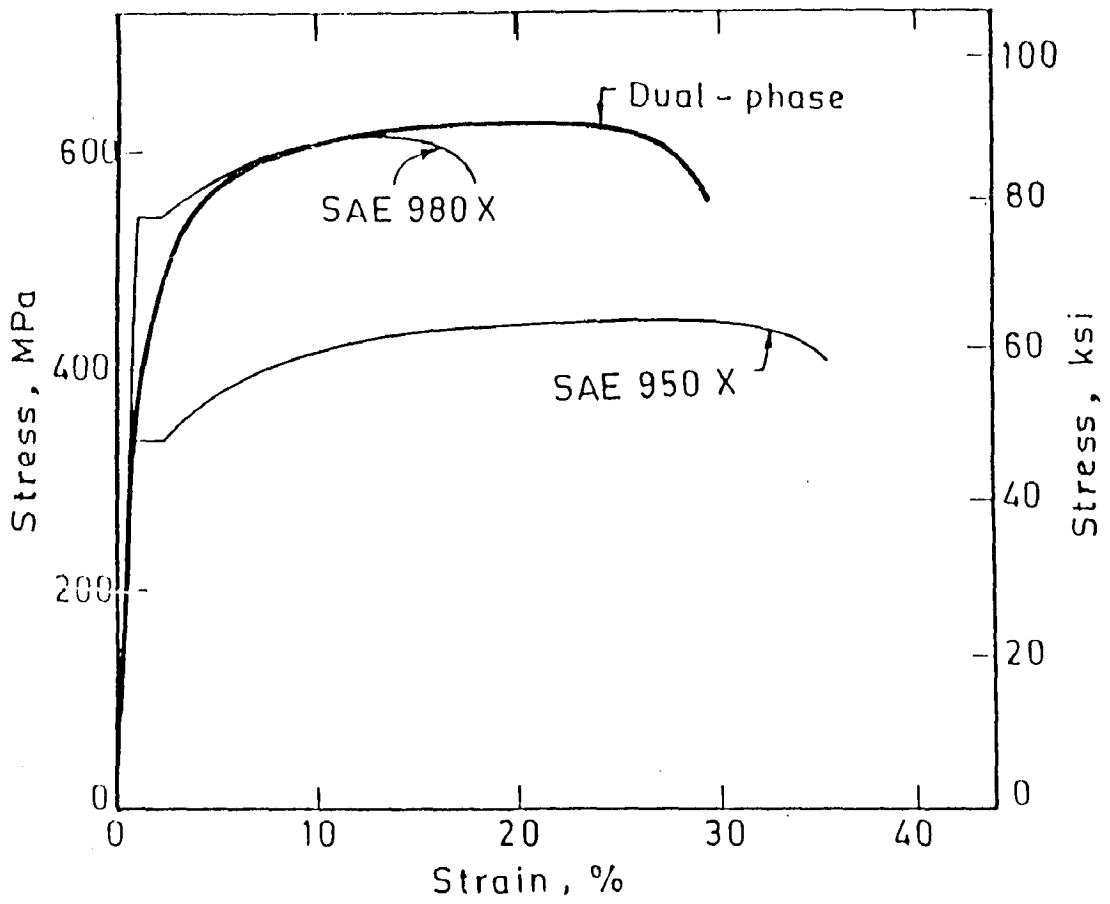

Fig. 2.3 Stress-strain curves for HSLA and dual phase steels. (Rashid, 1976)

$$\sigma_T = \sigma_{T,\alpha}\,(1-V_m) + \sigma_{T,m}\,V_m \qquad (2.2)$$

Where, $\sigma_{y,\alpha}$ and $\sigma_{y,m}$ are the yield strengths and $\sigma_{T,\alpha}$ and $\sigma_{T,m}$ are the tensile strength, respectively of ferrite and martensite phases. V_m and $(1-V_m)$ are respectively the volume fractions of martensite and ferrite phases. Davies, (1978) in his studies on dual phase steels having 1.5 wt pct manganese has shown that these two equations are obeyed over the entire range of volume fraction as shown in Fig. 2.4. But Spiech and Miller (1979), while studying the effect of volume fraction and carbon content of martensite on the yield and tensile strength, reported a linear relationship between strength and volume fraction of martensite only over a limited range of martensite volume fraction (50 pct) as shown in Fig. 2.5. Beyond this value the variation is non-linear.

Nath *et al* (1993) developed a single-particle model based on shear lag analysis to determine the theoretical tensile strength of the dual phase steels while taking into account the shape of the embedded second phase particles and the work hardening term. They assumed the martensite islands to be of cylindrical shape (radius r and half length l) with the hemispherical ends and arrived at the following expression for the ultimate tensile strength of the dual phase steels,

$$\sigma_{u,c} = \sigma_{u,m}\left[1-\frac{r}{l}\right]V_m + \sigma_{u,f}\left[1-\left\{\frac{2}{3}\frac{r}{l}-1\right\}V_m\right] + K\,G\sqrt{\frac{\bar{b}\,V_m\,\varepsilon}{0.41\,\bar{D}_m}} \qquad (2.3)$$

Where, $\sigma_{u,c}$, $\sigma_{u,m}$ and $\sigma_{u,f}$ are the ultimately tensile strengths of the dual phase steel, martensite phase and matrix (ferrite), respectively, $\bar{b}$ is the burgers vector of the matrix dislocations, V_m is the volume fraction of second phase particles, D_m is average particle size of

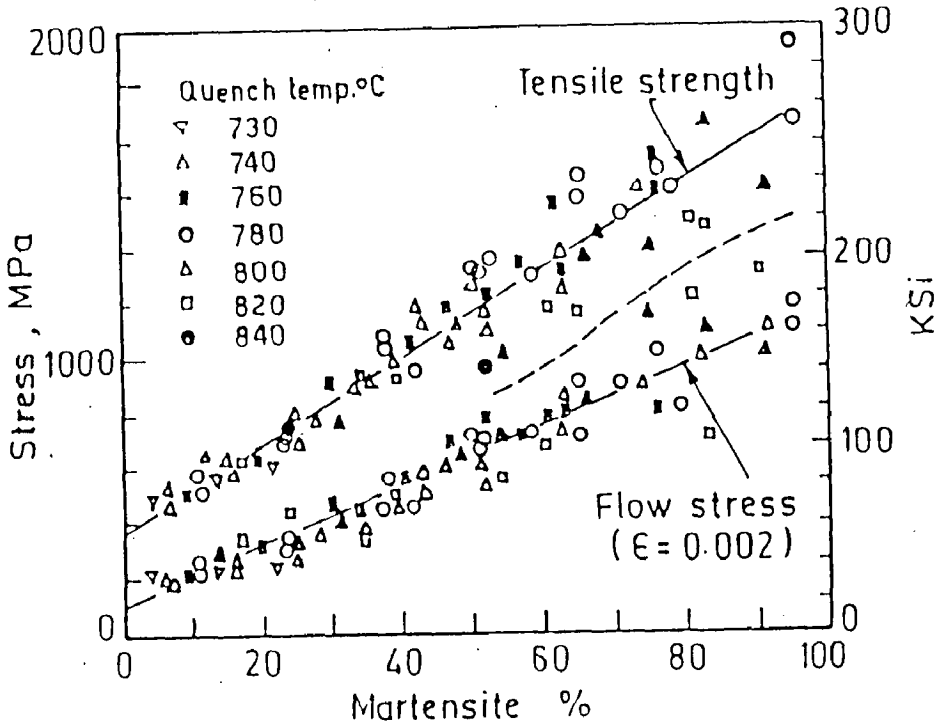

Fig. 2.4 The 0.2 pct flow stress and tensile strength as a function of percent martensite for Fe-Mn-C alloys. (Davies, 1978)

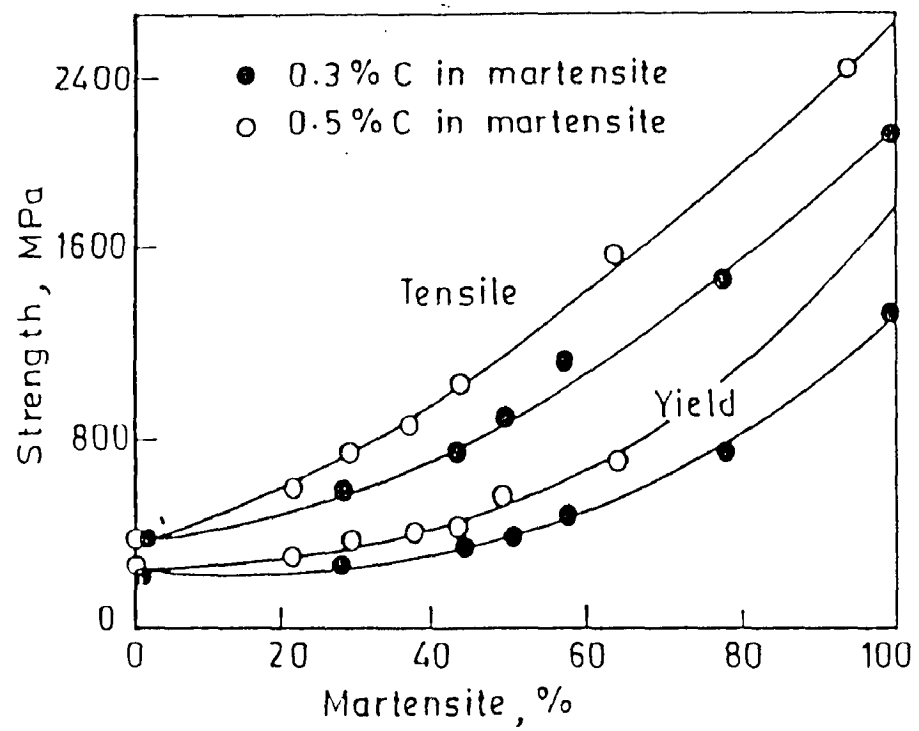

Fig. 2.5 Yield and tensile strength of ferrite-martensite mixtures in 1.5 Mn steels. (Speich and Miller, 1979)

martensite, ε is the true strain and K is a constant of order unity. Using this relation, they have shown theoretical UTS of the dual phase steel is in good agreement with the experimental measured strength, but when the shape of the martensite particle is assumed spherical, then the theoretical strength predicted by the shear-lag analysis do not conform with experimental values of strength observed in dual phase steels.

The three factors contributing to strengthening of dual phase steels are: (1) strain hardening of ferrite due to strain from martensitic transformation (2) the constraint on plastic deformation of ferrite by adjacent martensite during deformation and (3) load transfer by ferrite to martensite enabling the latter to carry load as in composite materials.

(iii) High Rates of Work Hardening

Balinger and Gladman (1981) have indicated that the work hardening rates are directly associated with the amount of martensite and size of martensite particles or islands. After carrying out TEM examinations of deformed dual phase structures it has been shown by them that martensite remains undeformed, even at relatively high strains and polygonal ferrite flows extensively around the martensite.

Ashby (1966) has proposed a theory of work hardening where the second phase particles act as the barrier in the movement of dislocations and has shown that the rate of work-hardening $d\sigma / d\varepsilon$ is given by,

$$\frac{d\sigma}{d\varepsilon} = 0.78\, K\, G \frac{b^{-1/2}}{\varepsilon^{-1/2}} \sqrt{\frac{V_m}{D_m}} \qquad (2.4)$$

Where, σ is the true stress, G is the shear modulus of the matrix and b is the burgers vector of the matrix dislocations. V_m is the volume fraction of second phase particles, D_m is average particle diameter and K is a constant of order unity.

This expression indicates that at a given strain, the work hardening rate is directly proportional to the square root of the volume fraction of hard particles and inversely proportional to the square root of mean particle diameter. Therefore, the work hardening rate increases with increasing volume fraction of martensite and with decreasing martensite particle size. In terms of relative importance, the volume fraction of martensite is more important in controlling the level of strength, while the martensite island size is more important in determining the work hardening rate and, therefore, the uniform elongation at a given strength level.

(iv) High Uniform and Total Elongation (Ductility)

The capability of withstanding plastic deformation is an important property of engineering materials. In fact, it reflects the ability of a material to avoid localised failure during loading. This property commonly referred as the "ductility" of the material, is indicated by the percentage strain at fracture. Thus, higher percentage elongation means higher ductility. Dual phase steels have high total and uniform elongation, hence these steels have high ductility. The various factors influencing the ductility of dual phase steels are:

(i) volume fraction of martensite

(ii) size of martensite island

(iii) alloy content of ferrite

(iv) carbon content of ferrite

(v) amount of epitaxial ferrite and retained austenite.

Davies (1978) has studied the effect of martensite volume fraction on uniform elongation and interpreted the results on the basis of the theory of Milieko (1969). From, Considere (1985) conditions, at the point of instability (maximum load) and assuming that a power law relation between stress and strain is obeyed, it could be shown that,

$$\varepsilon_u = n \tag{2.5}$$

Where, ε_u, is the true uniform elongation and n is the strain hardening coefficient, given by the exponent of strain in the stress-strain power law relation.

Assuming that in a mixture of ferrite and martensite phases in dual phase structure, the strains are equal in each phase, Milieko (1969) has evaluated uniform strain, ε_u for a composite from the values of K and n for each of the phases. Davies (1978) has also used this theory to interpret his results and concluded that there is a good agreement between the experimental values and the values calculated by the Milieko's theory. However, Speich and Miller (1979) and Rashid (1979) have shown that power law relationship between stress and strain is not followed for dual phase steels because the strains in the two phases of ferrite and martensite, are widely different.

2.2 SURFACE INTERACTIONS AND WEAR

Whenever two solid surfaces touch each other so that the forces of action and reaction are brought into play, the solids are said to undergo surface interaction. Surface interaction phenomena are important in various engineering situations. For example, the ways the heat

and electricity are transmitted across contacting solids are concerns of disciplines of heat transfer and electric contact theory.

2.2.1 Characteristics of Surfaces

All engineering surfaces are rough. This is their first important characteristic, which is tribologically significant. The other properties which govern the surface interaction behaviour are volume properties which relate to the contacting bodies as a whole and the surface properties which determine the nature of contacting interface between these bodies.

Surface roughness is defined as the departure of the surface shape from some ideal or prescribed contour. A perfectly flat surface cannot be achieved by the usual methods of surface preparations hence the surfaces have asperities, that is undulations in the form of peaks and valleys. The surfaces may have same peak to valley height ratio but still can have different roughness. In actual engineering surfaces, depending on the method of production, the heights of the peaks may vary between 0.05 μm to 50 μm while the spacing between them range from 0.5 μm to 5 mm.

The surface roughness is measured by the stylus profilometer. Roughness of the surfaces has been described in the following way:

(i) The maximum peak to valley height.

(ii) The centre line average, cla and the root mean square, rms.

A lot of work has been done to characterise the surface finish or surface topography mathematically (Whitehouse, 1980). However, the relationships between the surface

topography and functional requirement for friction are yet to be understood. Based on the available information, it appears that the original surface finish does not affect the steady-state friction and wear behaviour significantly in low-speed dry sliding applications. However, it is important when lubricants are used. In dry sliding, the surface geometry is altered drastically. The initial surface finish does affect the initial wear rate of the materials under dry sliding conditions. When the harder surface slides over the softer surface, the softer asperities either fracture or deform. The rate at which these asperities are removed by sliding process initially and the mechanism of their removal depend on the initial surface roughness, the applied load and the mechanical properties of asperities.

Abrahamson *et al* (1975) have shown that the initial wear rate of AISI 1018 steel is higher for rougher surfaces than for smoother surfaces when the applied load is high, but the opposite is true for the lighter loads, as shown in Fig. 2.6. In the asperity deformation process the high asperities are deformed first and the lower ones are not affected. As the deformation proceeds the lower asperities also deform and consequently, form a layered structure of deformed asperities. Some of the asperities fracture without undergoing any deformation, whereas rest of the asperities eventually fracture after significant deformation upon repeated loading. Once the steady-state condition is reached, the wear process will generate new asperities, and therefore the initial surface finish has little effect. However, under certain special conditions the initial surface finish can have lasting impact on friction and wear if the initial wear particles generated by fracture of the original asperities gets entrapped between the sliding surfaces and affect the number of steady-state wear particles (Suh, 1981).

The chemical and physical properties of the metallic surfaces are different from the bulk. The most important physical properties from the point of view of tribology are the flow strength and the hardness of the material near the surface. The flow strength of the surface determines the shear strength of the junctions formed during sliding contact whereas the

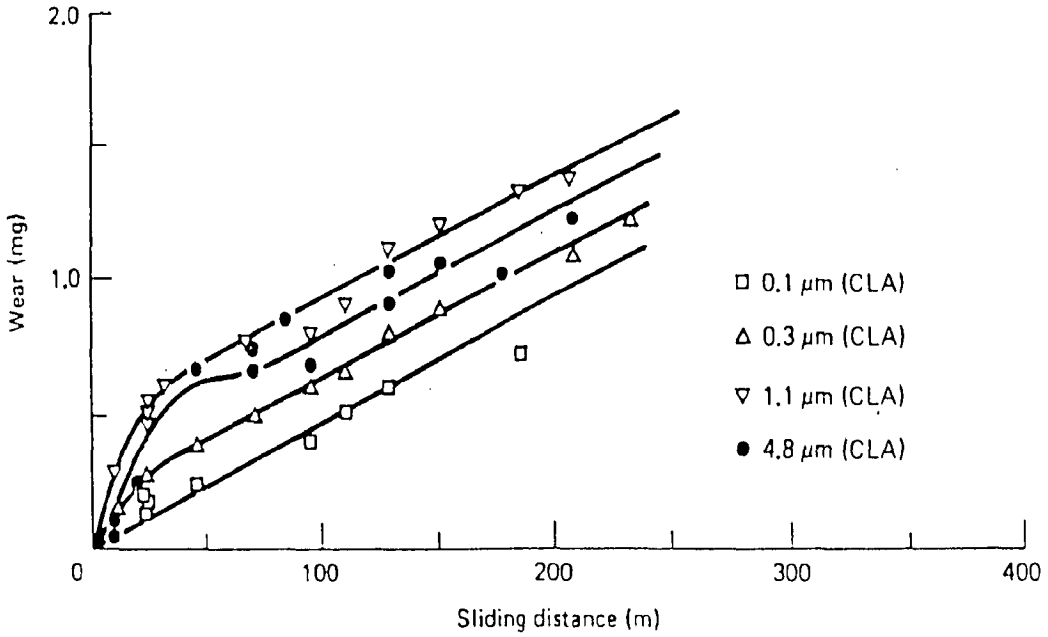

Fig. 2.6 Effect of surface roughness on weight loss under dry sliding in argon atmosphere under a normal load of 300 g. (Abrahamson *et al*, 1975)

hardness affects the real area of contact, which in turn, affects the friction and wear behaviour of materials. The harder the material the lower will be the real area of contact and therefore, a lower volume loss would occur due to wear. The lower the shear strength of the junction, lower will be the friction.

The surface properties, which are significant, are the chemical reactivity and the tendency of the surface to adsorb molecules from the environment. The tendency of the surface to acquire a surface film of different chemical composition than that of the substrate is known as the chemical reactivity. All but some metals form surface oxide films in air while in other environments, other films like nitrides, sulfides and chlorides may form. Quinn (1983) has suggested that in dry unlubricated wear of metals, oxide films can be developed on the sliding surface due to the chemical interaction with the environment which markedly influence the friction and wear behaviour of materials by inhibiting direct metal-metal contact. For steels, the thickness of these reaction films of oxides has been shown to reach a critical value in the range 1-5 μm depending on their load bearing capacity (Quinn *et al,* 1983 and Sullivan *et al*, 1988). Oxide film formation due to tribochemical reaction has a beneficial character and a reduction in the wear rates by an order of two magnitudes has been attributed to oxide formation (ASM hand book, Vol. 18). Besides the chemical corrosion product films which are formed on the metal surface in reactive environments, there are other films called adsorbed films that are wholly derived from the environment. The presence of such films drastically changes the nature of surface interaction between the contacting materials by not allowing the adhesion or direct metal-metal contact to take place. Lancaster (1990) has also pointed out that the water vapour adsorbed on the sliding surface plays a significant role in forming and compacting the debris.

2.2.2 Surface Contacts

When two nominally flat surfaces are brought in contact by applying a normal load, they touch each other at the tips of asperities only. Hence the real area of contact is much less compared to the apparent area of contact (Archard, 1980). The small regions where the contacting surfaces are close together, are referred to as "junctions" and sum of the areas of all the junctions constitute the real area of contact, A_r. The total interfacial area, consisting both of real area of contact, A_r, and those regions which appear as if contact might have been made there (but was not) is taken as the apparent area of contact, A_a. The numbers, size and distance of separation of junctions play a dominant role in influencing the friction and wear behaviour of materials in sliding contact.

According to Rabinowicz (1965), when the deformation of the asperity is plastic in a single asperity contact, the real area of contact is directly proportional to the normal load and is given by the equation,

$$A_r = \frac{L}{H} \tag{2.6}$$

Where, L is the normal load and H is the initial hardness of the softer of the two materials in contact.

Holm (1958) and Bowden and Tabor (1954) have also shown that the limiting value of the pressure at the contacting interface is set by the hardness of the softer of the two materials and the real area of contact is given by the above equation. Further, it has been concluded by them that the real area of contact is independent of the surface topography and the apparent area of contact.

(a) Single Asperity Contact

The deformation of asperity can be of two types - elastic deformation and plastic deformation. Hertz (1881) has described the single asperity deformation by taking a simple model of an elastic sphere pressed against a plane under a normal load. If the applied normal load is L, then the contact between the two occurs over a circular area of radius a, given by,

$$a = \left(\frac{3 L r}{4 E} \right)^{1/3} \tag{2.7}$$

Where, r is the radius of the sphere and E is the elastic modulus which depends on Young's moduli, E_1 and E_2 and the poisson's ratios, ν_1 and ν_2, for the materials of the sphere and the plane according to the following relation,

$$\frac{1}{E} = \frac{\left(1-\nu_1^2\right)}{E_1} + \frac{\left(1-\nu_2^2\right)}{E_2} \tag{2.8}$$

The area of contact πa^2, between the sphere and plane thus comes out to be,

$$A_r = \pi a^2 = 0.83 \pi \left(\frac{L r}{E} \right)^{2/3} \tag{2.9}$$

It is clear from the above relation that the area is proportional to $L^{2/3}$. The mean pressure over the contact area is $L/\pi a^2$, and it varies as $L^{1/3}$. The stress is not uniform over the contact area, but is maximum at the centre and zero at the edges as shown in Fig. 2.7.

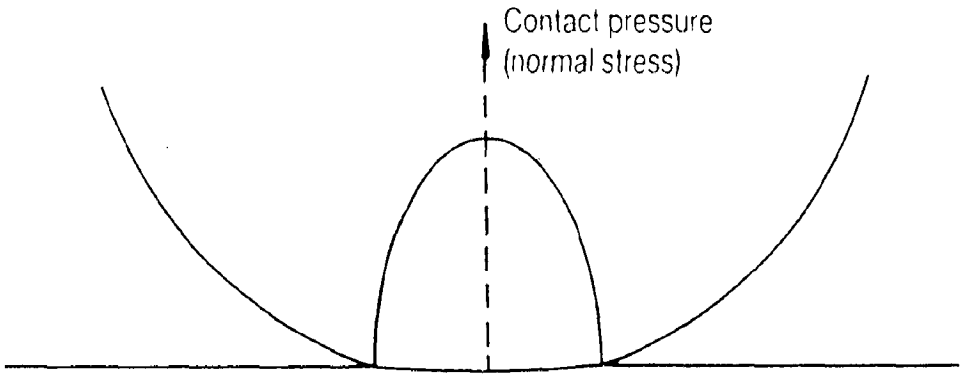

Fig. 2.7 The distribution of normal stress under a sphere loaded elastically against a plane.

As the load is increased the deformation becomes plastic. Hertz (1881) has shown that the maximum shear stress beneath the indenter occurs at a depth of about $0.47a$ (where a is radius of the contact circle) and the plastic flow starts from this point when the yield criterion is satisfied. The real area of contact in the plastic deformation is proportional to the load L.

(b) Multiple Asperity Contact

The single asperity deformation theory has been extended for the multiple asperity contact, which generally takes place when the two engineering surfaces rub together under a normal load. The total real area of contact in a multiple contact condition, is the sum of the areas of contact of individual asperity. This area is proportional to the load, L, if the deformation is plastic and is proportional to $L^{2/3}$ if the deformation is elastic.

In real surfaces, the radii and the heights of the asperities are statistically distributed. When the load on the surface is increased there are two types of changes occurring simultaneously: (i) the area of contact of individual asperity increases and (ii) more asperities now come in contact and start taking load. If the average area of contact for each asperity remains constant and the increase in load is borne by the increased number of asperities, then even for purely elastic condition, the real area of contact will be proportional to the load.

Archard (1980) has finally reported that the real area of contact is proportional to the normal load because of the complexities of the surface topography irrespective of the mechanism of asperity deformation. Hence, despite the serious reservations by many researchers about the elastic/plastic controversy in the single asperity deformation it is now well established that the real area of contact is independent of the apparent area of contact and is proportional to the normal load regardless of the deformation being elastic or plastic.

2.3 FRICTION BEHAVIOUR OF MATERIALS

Friction is defined as the resistance encountered by one body when it moves or tries to move over the other body. The frictional force arises due to the interactions between the opposing asperities of the two mating surfaces. Each asperity interaction contributes to the friction force thus, the total friction force at any time is the sum of the forces at the individual asperity contacts. Bowden and Tabor (1964) and Dowson (1978) have reported the basic laws of friction enunciated by Amonton (1699) which are given below:

(i) The friction force is proportional to normal load.

(ii) The friction force is independent of the apparent area of contact.

(iii) The friction is independent of the sliding velocity.

The first and second quantitative laws of friction proposed by Amonton (1699) are generally well followed but the third law has exceptions and is not obeyed in general. A drop in coefficient of friction is observed as the sliding velocity increases, which may be due to the thermal softening at the interface (Rabinowicz, 1965).

2.3.1 Theories of Friction

Bowden and Tabor (1950) proposed the adhesion theory of friction which states that, when a relative motion is imparted to the interface by applying a tangential force, each pair of contacting asperities weld together and shear to accommodate the relative motion. The friction arises from two sources: an adhesion force developed at the real area of contact

between the surfaces (asperity junctions) and a delamination force needed to plough the asperities of the harder surface through the softer ones.

According to this theory, major force of friction is the force required to shear the junctions formed between the two bodies at the real area of contact. This force of friction is given by,

$$F = \tau A_r \tag{2.10}$$

Where, τ is the shear strength of these junctions, which is a function of the materials of the bodies (and, of any intervening surface film). The coefficient of friction μ, is then given by the following equation.

$$\mu = \frac{F}{L} = \frac{\tau A_r}{H A_r} = \frac{\tau}{H} \tag{2.11}$$

Thus friction coefficient can be taken as the ratio of two quantities τ and H, representing respectively, the resistance to plastic flow of the weaker of the contacting materials in shear and in compression. The above theory has been criticised by various workers as it assumes only a simple model of asperity deformation.

Suh and Sin (1981) have established that there are three basic mechanisms responsible for the origin of friction. These are (i) asperity deformation, (ii) plowing and (iii) adhesion. The asperity deformation determines static coefficient of friction and also, affects the dynamic coefficient of friction. Since new asperities are generated only with the formation of delaminated wear particles, which requires a large number of cyclic loading by the asperities of the counterface, the contribution of the asperity deformation to the dynamic friction

coefficient is not large relative to those by plowing and adhesion. The plowing component of the frictional force can be due to the penetration of hard asperities or due to the penetration of wear particles into the softer material. When both the mating surfaces are of equal hardness, the particle can penetrate both the surfaces. If one of the surfaces is very hard and smooth, the wear particle will simply slide along the hard surface and no plowing would occur. However, when the hard surface is very rough wear particles may anchor in the hard surface and plow the soft surface (Sin *et al*, 1979).

Liu *et al*, (1992) have indicated that friction force arises due to the interaction between the asperities as (a) adhesion at the contacting points and (b) deformation either elastic or plastic of the asperities by load. The force required to overcome friction will consist of the force required to shear the adhesion bond F_a and the force required to deform elastically or plastically, F_d the obstructing asperities of the relatively softer material in the path of the asperities of the relatively harder material. The coefficient of friction μ is, therefore, expressed as,

$$\mu = \frac{F_a + F_d}{L} = \mu_a + \mu_d \qquad (2.12)$$

Where, L is the applied normal load on the contacting surface, μ_a and μ_d are the friction coefficients due to adhesion and deformation, respectively.

2.3.2 Factors Affecting the Friction Behaviour of Steels

The coefficient of friction, i.e., the ratio of the tangential force to the normal load, is not a given material property but it also depends on the mechanical properties of the opposing surfaces and the environmental conditions. The frictional behaviour is affected by the

following factors such as sliding velocity, applied load, sliding distance, environmental conditions, surface topography and mechanical properties of the two mating materials.

Friction between two rubbing bodies is not independent of the velocity as suggested by Coulomb (1781). Rabinowicz (1965) and many other researchers have shown that friction is a function of sliding velocity and not dependent on the load alone. Rabinowicz (1965) has indicated that a drop in friction is universally observed as sliding speeds are raised to high values due to the thermal softening of the interface, resulting in lower shear strength of the interfacial layer while maintaining the substrate at almost the same level of hardness. Li *et al* (1991) have also observed a decrease in the coefficient of friction with increasing sliding velocity in eutectoid steels and have attributed this decrease to the thermal softening of the outermost layer and simultaneous hardening of the subsurface layers. The friction has also been shown to decrease with increasing normal load. Bowden and Tabor (1964) have shown that in carbon steels the coefficient of friction decreases with increasing load as shown in Fig. 2.8. It has been suggested that this is the result of the presence of the oxides on the surface of steel (Hutchings, 1992). Li *et al* (1991) have also observed similar results for the dry sliding friction of the eutectoid steels and have attributed it to the thermal softening of the surface layers due to frictional heating.

The frictional behaviour of steels is dependent on the history of sliding. The frictional force undergoes significant changes during early stages of sliding before reaching a steady-state frictional behaviour. Suh and Sin (1981) and Blau (1981) have reported that during sliding the friction may evolve in three distinct stages: (i) an initial stage which depends on the surface finish and the nature and breakdown of the oxide films, (ii) a second stage consisting of plastic deformation and work hardening of the near surface layers and (iii) a third stage which may involve constant microstructure or equilibrium of sliding processes, resulting from temperature stability and equilibrium of oxide formation and breakdown.

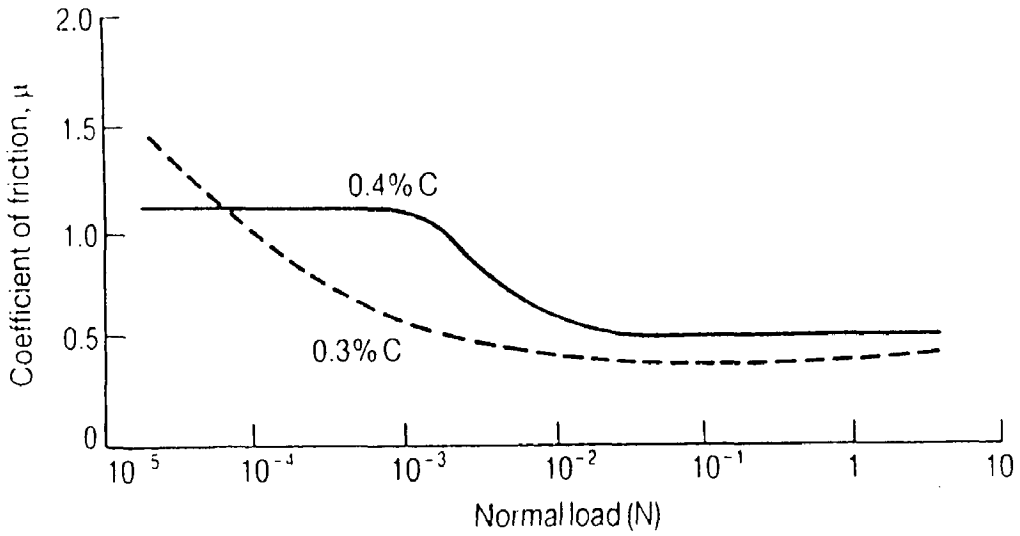

Fig. 2.8 The variation of coefficient of friction for steels under dry sliding in air against themselves. (Bowden and Tabor, 1964)

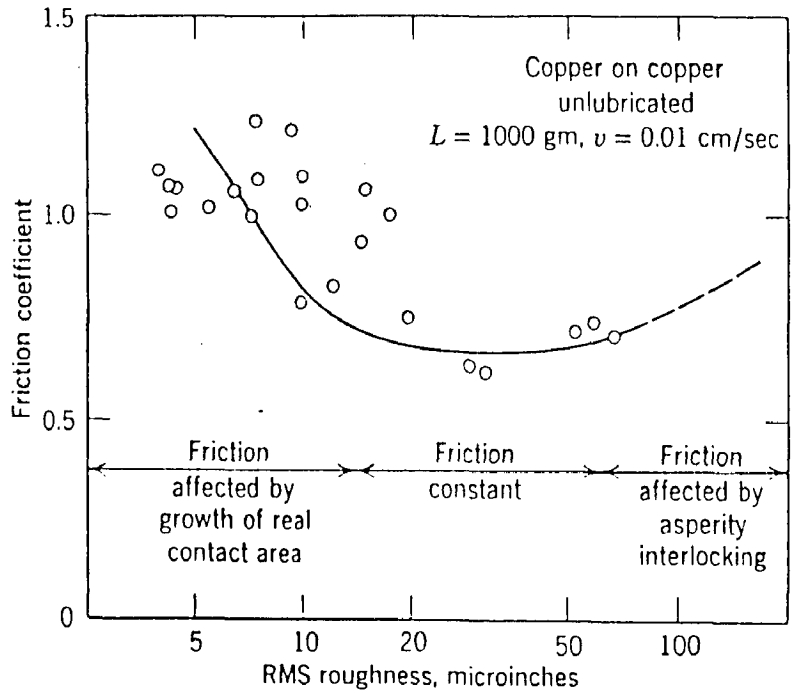

Fig. 2.9 The variation of coefficient of friction with surface roughness. (Rabinowicz, 1965)

Madakson (1983) has reported that the friction at the initial stage rises and then settles to an almost steady value. He has further indicated that for a given condition of load and sliding velocity, the friction coefficient is heavily influenced by the oxidation characteristics of the materials in rubbing contact. According to Rigney and Hirth (1979), the steady state friction is due to the attainment of a steady state microstructure. Vingsbo *et al* (1981) and Lim *et al* (1989) have also reported that the coefficient of friction depends on the microstructure of steels but no reasonable explanation has been forwarded by them.

Friction has also been shown to depend on the surface roughness. Rabinowicz (1965) has given a plot of friction coefficient as a function of surface roughness (RMS) which is shown in Fig. 2.9. He has suggested that for very smooth surfaces, the friction tends to be high because of larger real area of contact, whereas with very rough surfaces the friction is high because of the need to lift one surface over the asperities on the other. But in the intermediate range of surface roughness normally used in the engineering surfaces, the friction is almost constant and independent of the roughness of the surface.

2.4 TYPES OF WEAR

The progressive loss of substance from the operating surface of a body occurring as a consequence of the interfacial rubbing process is called *wear* (Ramesh *et al*, 1991). Wear may be classified on the basis of appearance of the worn parts or mechanisms and conditions, which prevail during material removal. The types of wear classified according to the wear mechanisms and conditions are: (i) adhesive wear (ii) abrasive wear (iii) erosive wear (iv) impact wear (v) fatigue wear and (vi) corrosive wear.

Adhesive wear is associated with low sliding velocity, small load and smooth surfaces. This is a universal type of wear that can occur in every machine and is hard to be

eliminated but can only be reduced. Adhesion processes involve the interaction of asperities on two opposing surfaces in relative motion. When the asperities come in close contact, they may weld together, forming a bond at the junction, which has rupture strength greater than the yield strength of one of the contacting solids. In such a case fracture may take place in one of the asperities resulting in transfer of material from one contacting body to other. **Abrasive wear** occurs when two surfaces, one of which is harder and rougher than the other, are in sliding contact. Abrasive wear is the removal or the displacement of material from one surface by the harder asperities of another surface or by harder, loose particles. This type of wear is dangerous because it can occur suddenly with introduction of a contaminant and may lead to high wear rates and extensive damage to the surfaces. **Erosive wear** is a combined process of repeated deformation and cutting. When a solid surface is gradually worn away by the action of fluids and particles, it is called erosion. Erosion of materials can take place under four different conditions: (1) impingement of solid particles against a solid surface, (2) impingement of liquid droplets against a solid surface, (3) flow of hot gases over a solid surface and (4) cavitation at a solid surface in liquid media. The most important form of erosion is that caused by solid particle impingement. **Impact wear** arises from repetitive impact of two surfaces, which differs from impact of solid particles on a surface causing erosive wear. **Fatigue wear** refers to the cyclically repeated imposition of a stress state on the surface of a component, inducing a small degree of mechanical damage in the surface and subsurface regions with each stress pulse. Ultimately, the damage accumulation leads to failure by deformation and/or fracture at the surface. **Corrosive wear** is the synergistic effect of chemical reaction at a surface with any of the mechanical wear mechanisms. In a corrosive environment sliding surface experience corrosive wear. However, in some cases the reaction layer may protect the surface or even act as a lubricant.

2.5 DRY SLIDING WEAR OF STEELS

Wear of metals in air at room temperature in the absence of any lubricant is termed as *dry sliding wear*. Dry sliding wear of steels has long been the object of research. Intensive investigations have been conducted by various investigators to explore different aspects of dry sliding wear behaviour of steels under different conditions. Research has mainly been centered around investigating the effects of sliding conditions like load, sliding velocity, initial surface roughness, microstructure, mechanical properties, environment etc., and at the same time to detect the mechanisms of wear operating under these conditions.

2.5.1 Microstructure and Dry Sliding Wear

A lot of work has been carried out to correlate the microstructure with the observed behaviour of metals, in general, and of steels, in particular, but only a few studies have been reported on dual phase steels. Wang *et al* (1999) have studied the wear behaviour of 52100 and 1080 steels with different microstructures under dry sliding. It has been reported that in the region of mild wear, there is no change in the wear volumes of different microstructures. However, considerable differences in the wear volumes are observed in the regime of severe wear. It has also been indicated that the difference in the wear resistance of various microstructures is closely related to thermal stability, resistance to plastic deformation and resistance to nucleation and propagation of microcracks for a given microstructure. Wang and Lie (1996) have also reported similar findings for the wear behaviour of 1080 steel under dry sliding. Aksoy *et al* (1996) have investigated the dry sliding wear of low carbon dual phase steels containing different amounts of martensite and ferrite, using a cylinder-on-cylinder configuration. It has been indicated that the wear resistance of the dual phase steel decreases with martensite proportions and increases with increasing martensite hardness and elongation

of steel. Saka (1978) has indicated that the friction and wear are not reversible processes and the initial microstructure is altered substantially during sliding. The steady state microstructure attained near the surface after sliding, is completely different from the initial microstructure. The steady state microstructure is a function of not only the initial microstructure but also the friction and wear behaviour of the material in the transition period. Hence, one has to follow the microstructural changes from time to time during sliding upto the attainment of the steady state. Since friction and wear are essentially surface phenomena, large gradients in the microstructure may develop and affect some basic properties during sliding which, in turn, influences the friction and wear behaviour of materials.

Saka (1978) has shown that the wear rate of metals and alloys is a function of subsurface deformation, crack propagation and crack nucleation, which are dependent on the microstructure of the materials. Similar findings have also been reported by Argon (1978), who concluded that the microstructure of a material has a bearing on its wear behaviour. He also examined the effect of the second phase particles on the wear rate of a two phase alloys and stated that it is not only the hardness but mean free path as well, which controls the wear rate. The wear rate also depends on the particle size and coherency because these parameters affect the crack nucleation rate. When the particles are large (>100 $\mathring{A}$) and the coherency is lost, the wear rate of two phase materials increases even though the hardness may increase due to decreasing mean free path between the particles. Abrahamson and Suh (1975) have also reported similar effects of coherency and particle size in spherodized steels.

Suh (1986) has indicated that the hardness and the toughness are the two most important properties in the context of wear of materials and these properties are affected by the microstructure. Hence, a change in microstructure changes these properties, consequently changing the wear behaviour of a material. It has been further reported that the toughness of a material is closely related to the crack propagation rate, which also affects the wear.

Wayne and Rice (1983) have studied the role of microstructure on the wear of AISI 1045 and 2.25 Cr–Mo steels. Two types microstructure (A and B) - dual phase and spherodized, have been developed in these steels through heat treatment. Duplex structure of type A has consisted of continuous ferrite matrix surrounding islands of martensite and the type B has a continuous martensite network surrounding the ferrite. It has been concluded that the dual phase microstructure offers a much higher wear resistance than that observed in a steel with spheroidal carbides and the wear resistance of dual phase steel depends on the volume fraction of martensite in it.

Sawa and Rigney (1987) have also investigated the dependence of wear on the microstructure of dual phase steels. The same A and B types of duplex microstructures as investigated by Wayne and Rice (1983) have been developed in a plain carbon steel containing 0.15-0.20 wt pct carbon. The sliding wear tests have been carried out on pin-on-disc machine in air and vacuum respectively. It has been found that the wear behavior of dual phase steel also depends strongly on the morphology, i.e., shape, size and distribution, of martensite. They observed that the results of wear for type A and type B microstructure were similar in case of sliding under vacuum. However, in air, the two materials behave differently and the sliding wear rate of A on A is about one by hundredth of that for B on B. The segmented nature of martensite in type B structure as against the blocky martensite in type A structure has been considered responsible for these results. Martensite in type A structure is in a better position to constrain the deformation in the base material.

Bhattacharyya (1980) has also shown that the interlamellar spacing below a particular value in pearlite, influences the wear rate markedly. The wear rate is observed to be lower for a fine pearlite as compared to that for coarse pearlite. It has been attributed to a much higher load for the mild-to-severe transition in wear in case of fine pearlite. On the other hand, the volume fraction of carbide in spheroidized steels is not found to affect the transition load.

Horn Bogen (1981) and Zum Ghar (1987) have shown that the wear resistance of lamellar pearlitic structure is better than that of spheroidized structure (ferrite plus spheroidized cementite). Kalousek *et al* (1985) have reported that the wear resistance of lamellar pearlitic structure is even better than that of tempered martensite. Wang *et al* (1991) have also examined the wear behaviour of 0.79 wt pct carbon steels having lamellar pearlitic and spheroidized structures, which have shown a sudden change in wear volume at critical interlamellar spacing and particle diameter respectively. Bhattacharyya (1980) has also made similar observations for interlamellar spacing in pearlitic structure. It has been claimed that the effect of the particle diameter of cementite on wear volume is much stronger than that of interlamellar spacing.

In order to evolve a correlation between the wear behaviour and basic material properties, Clayton (1980) has investigated different types of pearlitic steels having 0.30 to 0.79 wt pct carbon and a pearlite volume fraction ranging from 40 to 100 pct. It has been concluded that the wear rate is influenced by the microstructure of the steels and that the wear resistance improves as the volume fraction of pearlite increases.

Clayton (1980) has emphasised that the alloying contents influence the microstructure of the steels and consequently the wear resistance of the pearlitic steels. Carbon is the most influential alloying element because it controls the amount of the cementite and therefore to a large extent the volume fraction of pearlite. Gladman (1970) has observed two distinct effects of manganese addition on the morphology of pearlite. Firstly, it reduces the eutectoid reaction temperature to give a fine pearlite with reduced interlamellar spacing. Secondly, it lowers the carbon level required to achieve the fully pearlitic steel and thus, increasing the volume fraction of pearlite in a hypoeutectoid steel for a given carbon content. These changes taking place due to manganese addition influence the microstructure and result in properties, which are found to provide a better wear resistance.

The wear behaviour of the bainitic steels has also been investigated thoroughly by a number of researchers. It has been shown that the bainitic steels are less wear resistant than the pearlitic steels, demonstrating again the effect of microstructure on wear behaviour. Kalousek *et al* (1985) have pointed out that the wear resistance of the pearlitic steels is better than that of bainitic steels and similar conclusions have also been drawn by Clayton and Devnathan (1992). Clayton *et al* (1987) have also investigated the wear behaviour of bainitic steels with different morphologies of bainite and have compared it with the previous work on pearlitic steels under the same conditions of dry sliding. It has been reported that keeping the best pearlitic steel apart, the best bainitic steel tested is better than some of the fully pearlitic steels.

2.5.2 Oxidative and Metallic Wear

(i) Oxidative Wear

Oxidative wear is a mechanism of mild wear in which protective oxide films are formed at the real areas of contact during sliding. It is also termed as "mild wear". Mild wear results due to reactions between the surface and the oxygen in the atmosphere (Quinn, 1983). When two surfaces come in sliding contact, the initial stage is that of severe wear, in which the mating surfaces attain a measure of conformity. After this initial stage, the large areas of both surfaces come into contact during sliding. At any given instant, one of these areas bears most of the load. This area then expands thermally in the direction perpendicular to the plain of contact between the specimen in a similar fashion proposed by Barber (1969), so that there will be a plateau of contact. This plateau will tend to remain in contact until it is removed by wear. If the load and sliding speed are such that there is sufficient frictional heating, the contacting plateau will oxidise preferentially in comparison to the other plateaux and the remainder of the surface. This oxidation mainly occurs during contact between opposing surfaces at a temperature, T_c, at the real area of contact, well in excess of the general surface

temperature, T_s, outside the contact area. Suh (1977) and Quinn (1969) have observed the existence of these plateaux and have indicated that they are extremely smooth with fine wear tracks parallel to the direction of sliding. The surface cracks are seen perpendicular to the direction of sliding at these plateaux. The surfaces surrounding each plateaux are rough and packed with wear debris and wear tracks are not seen. It would seem that these wear debris are fragments of the previously existing contact plateau which, upon reaching its critical height, became unstable, cracked and detached from the bulk material in form of wear debris.

In oxidative wear, the contacting plateau is the site of all asperity / asperity interaction between two opposing surfaces. These asperities are the sites of oxidation at the temperature T_c and oxidation occurs by diffusion of oxygen ions inwards and (sometimes) by metal ions outwards. The area of these plateaux (A) has been found by assuming that the entire load is borne by only one of these plateaux at a time and is given by,

$$A = \frac{L}{H} \tag{2.13}$$

Where, L is the normal load and H is the hardness of the bulk metal of the softer of the two contacting surfaces.

The plateau / plateau interaction does not take place along the entire surface area of a plateau but there are several sub – areas of contact on each plateau and these are the regions of actual contact at which oxidation occurs. The oxide film builds up until it reaches a critical thickness, ξ_c, when it is assumed that the film becomes unstable and is removed. When all the sub-areas of contact get removed from the plateau, then other plateau elsewhere on the surface becomes operative. The virgin surface beneath the original plateau now becomes out of contact and can only get oxidised at the general surface temperature (T_s). Without external

heating, the amount of oxidation at a typical value of T_s (say, 80^0C), is very less compared to that taking place at a typical value of T_c around 400^0C. Hence, the original plateau or its subsurface region when goes out of contact, will not oxidise significantly until it becomes the dominant area of contact once again.

The formation of oxides on the sliding surfaces has a beneficial effect in reducing wear during sliding of metals and alloys. The oxide film prevents direct metal-metal contact between the two mating surfaces and thus mitigates the severe adhesive wear. When surfaces are oxidised, the wear debris is finely divided oxide. The rubbing surfaces remain smooth and the rate of material loss is low (Arnell *et al*, 1991). Stott and Woods (1978) and Stott (1998) have also reported that the formation of oxide on the sliding surfaces is instrumental in reducing the wear rates in metal and alloys. Stott (1998) has also indicated that in dry sliding, the oxides are formed by oxidation of metal asperities while in contact and the extent of oxidation depends on the temperature developed at the asperity contacts, the duration of contacts and the oxidation characteristics of metal. These oxides may be removed completely during subsequent sliding, exposing fresh metallic surface for further oxidation. The resulting wear debris may be swept aside or may be compacted between the sliding surfaces to give a transfer layer of oxide (sometimes termed as 'glaze'), which also provides protection against wear. Stott (1998) has further reported that during sliding, oxide may also form by oxidation of metallic debris. The metallic particles may get oxidised spontaneously and completely due to the heat of oxidation and the resulting oxide debris may develop into a wear protective transfer layer. In steels, the formation of the compacted layer of oxide, which helps in reducing the wear rate, has also been reported by Iwabuchi *et al* (1988).

Archard and Hirst (1959) were the first to recognize a close relationship between the oxide films and wear of steels. Since then, a number of investigations have been carried out to establish the role of oxide films on the wear of steels. Many theories of oxidative wear have

been proposed and the notable ones are those given by Quinn (1967) and Wilson *et al* (1980). Quinn's studies are dedicated to mild wear at high sliding speeds where the contact temperatures are several hundred-degree Celsius. Quinn (1967) contends that at the start the oxide films found on the unworn surface are destroyed and an initial period of severe wear commences. Then, by some unknown processes, the surface recovers and a state of mild wear is reached. The thick oxide layers are established and the wear rate decreases drastically from the initial high rate. The oxide layer builds up gradually up to a critical level, at which it becomes unstable and detaches from the surface in the form of fine oxide wear debris. In contrast to the study carried out by Quinn (1967), Wilson *et al* (1980) have investigated oxidative wear under the condition of low sliding speeds of a few millimeters per second. It has been advocated that at the start of the wear, the oxide films found on the unworn surfaces are progressively destroyed and a period of severe wear ensues. Then the metallic and oxide wear debris accumulates to form thick layers, which enables mild wear to be attained.

Welsh (1965) has done a pioneering work on the dry sliding wear of different steels with carbon contents ranging from 0.026 to 0.98 wt pct carbon, tested under a wide range of loads from 10 g to 10 kg and sliding speeds from 1.7 to 266 cm/s. It has been concluded that at equilibrium, wear process is either of a severe type producing coarse metallic debris or of a mild type producing fine oxidised wear debris. It has been further observed that there are three transitions where the nature of wear changes from one type to the other. The three transitions are (i) T_1, a change from mild to severe wear at light loads, (ii) T_2, a change from severe back to mild at higher loads and (iii) T_3, a minor change in the mild wear rate at loads above T_2. He reported that mild wear takes place in both the transitions after an initial short period of severe wear. However, hardening by surface transformation and surface oxidation takes place progressively with time and the mild wear has been attributed to the presence of the thick oxide layers adhering to the wear surface. It has further been demonstrated that both hardening and oxidation are essential for protection of the surfaces.

Sullivan and Hodgson (1988) have studied the dry sliding wear of AISI 52100 steel in the range of load from 5 to 50 N below the Welsh T_1 transition with varying sliding speeds ranging from 10^{-3} to 1 m/s. It has been found that the wear rate decreases with increasing speed. They have concluded that in the load range below the T_1 transition, the wear of the steel is mild oxidative governed by the formation of oxide on the surface and generating agglomerated wear debris composed of rhombohedral oxide α-Fe_2O_3, with varying proportion of metallic debris.

Quinn *et al* (1980) have applied the oxidational theory to the wear of low alloy EN-8 steel while sliding against itself at a sliding velocity of 2 m/s under loads ranging from 4 to 40 N. It has been reported that the three transitions in the wear are concurrent with the change of the nature of the oxide formed during sliding. The nature of oxide has been shown by them to change from α-Fe_2O_3 to Fe_3O_4 and from Fe_3O_4 to FeO as the temperature during sliding increases. Sullivan *et al* (1980) have also reported similar findings and have shown that α-Fe_2O_3 forms below a temperature of 450^0C whereas the formation of FeO takes place above 600^0C. The other oxide, Fe_3O_4, is shown to form between 450 - 600^0C.

Venkatesan and Rigney (1992) have conducted dry sliding wear tests on AISI 1045 steel in air near the Welsh T_1 transition with sliding speed ranging from 0.05 to 0.25 m/s, on a cylinder-on-cylinder wear testing machine having crossed cylinder configuration. They have reported that under conditions of mild wear, a smooth coating of oxide layer forms on the surface and wear takes place by the removal of this layer during sliding. The presence of both α-Fe_2O_3 and Fe_3O_4 has been detected in the wear debris for the mild wear conditions.

By citing several references including their own work, Lim and Ashby (1987) have indicated that the wear of steels above a sliding speed of 1 m/s, occurs by the oxidation of surface as the flash temperature at this sliding velocity is sufficient to cause oxidation of the

surface. After a short initial period of severe (metallic) wear, the wear rate is found to drop and the nature of wear debris changes to oxide. Also, there could be martensite formation after quenching from the flash temperature. It has been reported that there are two regimes of oxidative wear - (i) mild oxidative, which occurs at a sliding velocity around 1 m/s when local flash temperature is enough to cause local oxidation and the oxide for most of the time is thin, patchy, cold and brittle and (ii) severe oxidational wear, which occurs at higher sliding velocities of 10 m/s, when the oxide film is thicker, more continuous, relatively hotter and more plastic and the characteristics of the wear process change. Interestingly, severe oxidative wear leads to a lower wear rate as the volume loss is relatively less.

Bhattarcharyya (1980) has also concluded that under the mild wear conditions, the caked oxide layer forms over the surface of steels and the wear is governed by the rate at which this oxide layer is broken up exposing the fresh metallic surface for further interaction. Czicos and Habig (1986) have shown that the change from the initial severe wear to the mild wear in carbon steels is due to the formation of the reaction layers on the surface through tribo-oxidative process and these layers reduce the wear rate. They have also confirmed the fact that the hardness and the state of oxidation of the rubbing surfaces are the principal factors controlling the wear rate pattern and its variation in the carbon steels as it was noted originally by Welsh (1965).

(ii) Metallic Wear

The metallic wear takes place when there is metal to metal contact between the two sliding surfaces under relative motion. This can happen under two conditions: (i) at low load and speed when frictional heating is negligible and the oxide film does not form over the surface, thereby, allowing direct metal-metal contact and (ii) at high loads and low sliding velocities when the contact pressure is enough to penetrate through the thin layer of oxide and

direct metal-metal contact takes place (Lim and Ashby, 1987). The plastic shear strain accumulated in the subsurface layer increases sharply due to resultant frictional traction, resulting in nucleation and growth of cracks parallel to the surface, which eventually break out to give larger flakes of metallic debris of size 10-100 μm. Even at high sliding velocities, when a thick but brittle oxide layer forms over the surface by local heating at the asperity on the softer surface, if the load is high enough to penetrate this oxide, metal to metal contact may result. This causes deep tearing of the surface giving rise to severe metallic wear.

Archard and Hirst (1956) have shown that at low sliding velocities below 0.1 m/s surface heating is negligible and the effect of frictional force is primarily to deform the metal surface, shearing it in the direction of sliding. The shearing causes the removal of slivers of metal from one or both the surfaces by plastic failure. When one surface is softer than the other metal may be transferred from the softer to the harder surface. If both the surfaces are equally hard, flakes or particles of metallic debris form due to wear. It has also been reported by them that in severe wear the subsurface is heavily deformed and the crystal structure becomes highly distorted.

Welsh (1965) has reported that there is a critical load at each sliding speed, at which the wear changes from mild (oxidative) to severe (metallic) type. It has been shown by him that for the steels, an abrupt transition from oxidative to metallic wear occurs at a critical load and this transition has been labeled as T_1. The wear rates in severe wear are around 100 times higher than those observed in the case of mild oxidative wear. Above T_1, the wear debris consists of large metallic particles visible to unaided eye and the surfaces are severely torn and damaged.

Saka *et al* (1977) have investigated the dry sliding wear of AISI 1020 and AISI 304 stainless steel using a pin-on-ring wear testing rig at a constant load of 49 N and sliding

speeds ranging from 0.5 to 10 m/s. The wear at these speeds is found to occur through the processes of subsurface deformation, crack nucleation and growth leading to delamination and the wear debris is metallic in nature consisting of large particles of metal, indicating a severe or metallic wear. Clayton (1980) has also studied the severe metallic wear of pearlitic steels in the load range between 75 and 200 kgf using a pin on ring wear testing apparatus. In the entire load range, the wear is found to be metallic and the wear debris is composed of large metallic flakes.

Bhattacharyya (1980) has evaluated the mild and severe regimes of wear in pearlitic and spheroidized steels. AISI 1018 and AISI 1040, AISI 1095 steels have been given different heat treatments to develop different structures - fine pearlite, coarse pearlite and spheroidized carbides. These steels have been tested in the load range from 1.11 to 267 N at a constant sliding speed of 41.9 m/min (0.698 m/s) using a pin on cylinder wear testing machine. A sharp transition from the mild to severe wear has been observed indicating that in the severe wear regime, a dynamic condition between work hardening and transformation hardening on one hand and attrition due to oxidation, adhesion, rupture and thermal softening on the other, controls the nature of wear.

Smith (1988) has investigated the wear under sliding against itself, of the high strength martensitic stainless steel on a pin-on-flat arrangement in the load range between 11 to 88 N in air. It has been observed that the wear rate is quite high at the room temperature in air under this load range and the debris is essentially metallic suggesting a metallic mode of wear.

2.6 MODELS FOR WEAR MECHANISMS

Over the years different models have been proposed and developed for the operating wear mechanisms for the dry wear of steels. The following broad classes of wear mechanisms and models based on these mechanisms are of primary importance in understanding wear.

(a) Archard's model of wear

(b) Model for plasticity dominated wear

(c) Model for oxidative wear

(d) Model for seizure wear

(e) Model for melt wear

(a) Archard's Model of Wear

When two surfaces in contact, slide over each other, one or both of the surfaces will suffer material loss. Archard (1953) has given a simple theoretical analysis of this type of wear. This analysis, although simple, highlights the main variables, which influence sliding wear. It also yields a method of describing the severity of wear by means of the *wear coefficient*, K_A, which is widely used as a parameter characterising wear in a material.

The basic assumption of the model proposed by Archard, is that the contact between the two surfaces will occur where the asperities touch and the real area of contact will be the sum of the individual asperity contact areas. This real area of contact is proportional to the normal load and it may be assumed that under most conditions, at least for metals, the local deformation of the asperities will be plastic.

The schematic view of the single asperity contact and its evolution with sliding as outlined by Archard is shown in Fig. 2.10. It is assumed that the contact is circular with radius a. In Fig. 2.10 (c), the contact has reached the maximum size and the normal load supported by it, δL, is given by,

$$\delta L = P \pi a^2 \tag{2.14}$$

Where, P is the yield pressure for the plastically deforming asperity, which is approximately equal to the indentation hardness H of the softer of the two bodies in contact.

As the sliding proceeds, the two surfaces become displaced as shown in Fig. 2.10 (d) and (e), and the load originally borne by the asperity is transferred progressively to other asperity junctions, which are in the process of forming at the other points on the surface. The formation and destruction of junctions take place as the sliding continues. Wear is associated with the detachment of fragments of material due to cracking through relatively weaker materials at the asperity tip contacts when the junction is destroyed during sliding. The volume of each wear fragment is dependent on the size of the asperity junction from which it originates. For the sake of simplicity it is assumed in the model that the wear particles are hemispherical in shape. If the radius of the hemisphere is a, then the volume of material removed by wear, δV, is given by,

$$\delta V = \frac{2}{3} \pi a^3 \tag{2.15}$$

But all the asperity contacts do not give rise to wear particles. When the contact at the junction is strong, the two materials may disengage at the original parting surface during sliding without forming wear particles. If one assumes that only a proportion κ of the

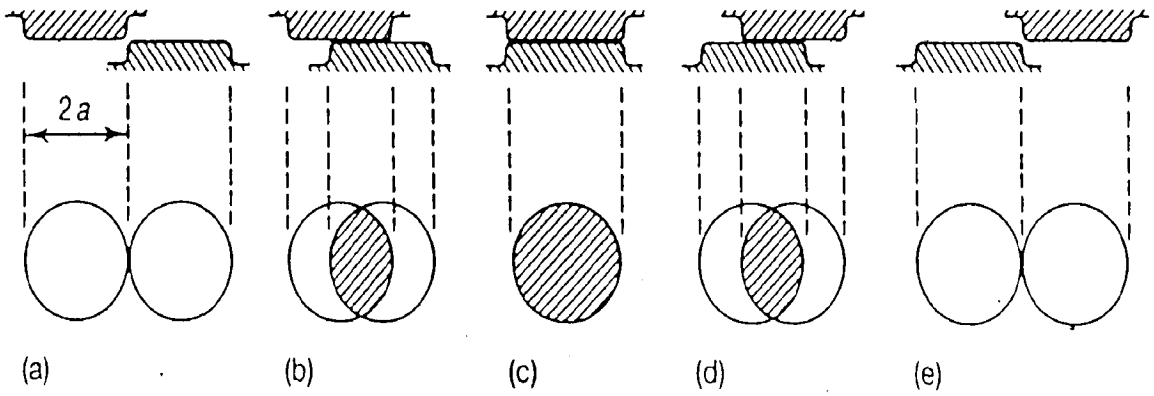

Fig. 2.10 Schematic diagram showing evolution of a single contact as two asperities move over each other. (Archard, 1953)

junctions results in wear particles or fragments, the average volume of the material, δW, worn away per unit sliding distance due to sliding of one pair of asperities through a distance $2a$ is, therefore, given by,

$$\delta W = \kappa \frac{\delta V}{2a} = \kappa \frac{\pi a^2}{3} \tag{2.16}$$

and the overall wear rate, W, arising from all the asperity contacts is the sum of the contributions over the entire real area of contact and it is given by,

$$W = \sum \delta W = \frac{\kappa}{3} \sum \pi a^2 \tag{2.17}$$

The total normal load is given by,

$$L = \sum \delta L = P \sum \pi a^2 \tag{2.18}$$

and hence,

$$W = \kappa \frac{L}{3P} \tag{2.19}$$

The factor 1/3 may be combined into the constant of proportionality, by putting $K_A = \kappa/3$. Assuming that $P = H$, the indentation hardness, one may rewrite the Eq. (2.19) in following form.

$$W = K_A \frac{L}{H} \tag{2.20}$$

If V is the total volume of the material worn after sliding through a distance S, then the wear rate, W, is defined as,

$$W = \frac{V}{S} \tag{2.21}$$

Combining Eqs. (2.20) and (2.21) one gets,

$$V = \frac{K_A L S}{H} \tag{2.22}$$

This equation is often called the *Archard wear equation*, which relates the wear volume, V, to the macroscopic quantities L, the normal load, S, the sliding distance and H, the initial hardness of the softer surface. The constant K_A is a dimensionless parameter known as the *wear coefficient*. Archard has stated that the *wear coefficient*, K_A, represents the proportion of all the asperity contacts, which result in the production of wear particles. Its value is always less than unity and is of the order of 10^{-5} to 10^{-3}.

Shaw (1977) has defined the physical significance of the *wear coefficient*, K_A, in some other way. From Eq. (2.22), the *wear coefficient*, K_A, may be written as,

$$K_A = \frac{V\,H}{L\,S} \tag{2.23}$$

Here, L/H is the real area of contact. Since the cross–sectional area of plastically deformed subsurface zone under the asperity contact, A_p, is of the order of the real area of contact, A_r, Shaw (1977) showed that Eq. (2.23) may be rewritten as,

$$K_A = \frac{V\,H}{L\,S} = \frac{V}{A_p\,S} = \frac{Worn\ volume}{Volume\ of\ the\ plastically\ deformed\ zone} \tag{2.24}$$

Therefore, *wear coefficient*, K_A, for sliding wear may be interpreted as a dimensionless quantity that represents the ratio of the worn volume to the volume of the plastically deformed zone. Since the value of K_A is of the order of 10^{-5} to 10^{-3}, the volume of material removed by wear is a very small fraction of the material undergoing plastic deformation below asperity contact.

(b) Model for Plasticity-Dominated Wear

It has already been highlighted in the previous sections that at the low sliding velocities, surface heating is negligible and wear occurs by the plastic deformation and shearing of the metal surface. The slivers of metals are removed due to the shearing. In the models for the plasticity-dominated wear, the thrust is given to the identification and analysis of the processes of crack nucleation and growth. The models for adhesion owe their origin to the Archard's (1953) wear law, where asperities engaged against each other at an instant during sliding weld together and form junctions. Subsequent sliding shears or plucks off the

tip of the softer asperity, which may remain adhering to the harder surface and later detaches to form wear fragment.

Delamination model proposed by Suh and coworkers (1973, 1977), describe the microstructural observations during severe plasticity dominated wear. Here the basic idea is that the voids are nucleated in the subsurface by unidirectional sliding. These voids then extend and link together to form a crack beneath and parallel to the surface. When this crack is large enough it breaks a fragment from the surface forming a wear particle. Suh and Sin (1981) have developed a wear equation based on the delamination theory. A crack lying below the surface and the movement of an asperity from one to another direction (say left to right) have been considered as shown in Fig. 2.11. For this mechanism of wear, the wear rate is dictated by the crack propagation at both ends i.e., left and right. The crack extension for the i th cycle, ΔC_i, for a given crack may be expressed as,

$$\Delta C_i = f\ (\mu, x, C, material\ properties) \tag{2.25}$$

for both ends. Where, μ is the friction coefficient, x is the distance below the surface at which the crack is located and C is the length of the crack existing before the i th cycle. If N is the total number of asperity passes the volume V_i of wear generated by this crack in the form of sheet of width, w, and thickness, x, equal to the depth at which the crack is extending is, obtained as,

$$V_i = w\, x \sum_{i}^{N} (\Delta C_{L\,i} + \Delta C_{R\,i}) \tag{2.26}$$

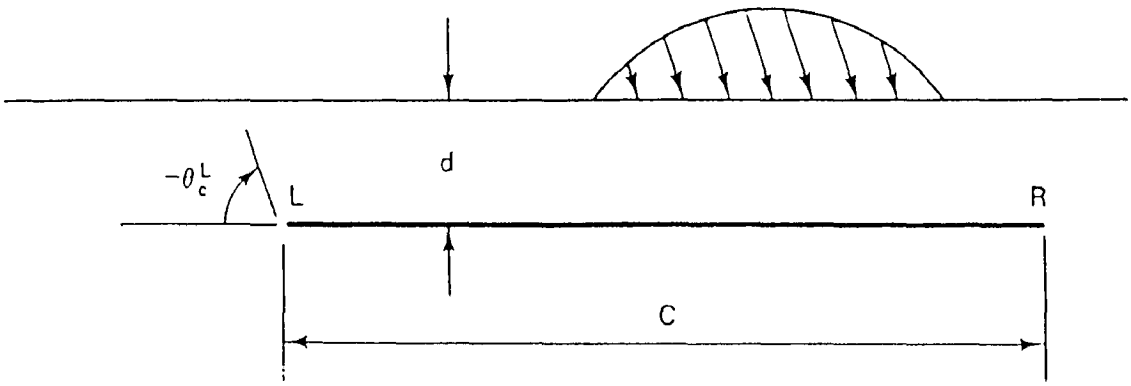

Fig. 2.11 Subsurface crack under a moving asperity. (Suh, 1986)

Therefore, the total volume V of wear for N_c, number of cracks opening in a layer may be given by,

$$V = N_c \, N_w \, w \, x \sum_{i}^{N} (\Delta C_{L\,i} + \Delta C_{R\,i}) \tag{2.27}$$

Where, N_w is the number of cracking sheets in the direction of contact width. Assuming that $N_w \, w$ of the order of the contact width L_w, the volume comes out to be,

$$V = N_c \, L_w \, x \sum_{i}^{N} (\Delta C_{L\,i} + \Delta C_{R\,i}) \tag{2.28}$$

It has been shown that if ΔL is the contact length, l_c is the crack spacing, D is the diameter of a specimen and λ is the spacing between asperity contacts, it may be assumed that L_w is equal to ΔL. The number N_c and N are then given by,

$$N = \frac{S}{\pi D} \frac{\Delta L}{\lambda} \quad and \quad N_c = \frac{\pi D}{l_c} \tag{2.29}$$

Where S is the sliding distance required for the removal of one layer. By substituting the Eq. (2.29) in Eq. (2.28) the wear rate is obtained as,

$$\frac{V}{S} = \frac{\Delta L^2 \, x \, (\Delta \overline{C}_L + \Delta \overline{C}_R)}{\lambda \, l_c} \tag{2.30}$$

Where $\Delta \overline{C}_L$ and $\Delta \overline{C}_R$ are the average lengths of crack propagation during N cycles.

The wear coefficient K_A is obtained by substituting Eq. (2.30) in Archard's equation (2.23), as

$$K_A = \frac{3\,H\,\Delta L^2\,x\,(\Delta\overline{C}_L + \Delta\overline{C}_R)}{L\,\lambda\,l_c} \tag{2.31}$$

Where, H is the hardness of the material and L is the applied load. It can be seen from the Eq. (2.31) that the wear coefficient, K_A, is inversely proportional to the asperity contact spacing and the crack spacing. The crack depth x can be determined by the crack nucleation condition. For a two phase material, the location of the hard particles and the plastic deformation field in the matrix under a given surface traction, controls the exact crack nucleation site. In the most unidirectional situations, the crack propagation rate is the largest for the crack nearest to the surface, since the shear strain at the crack tip increases with increase in the crack depth from the surface. Although many cracks propagate, only the cracks nearest to the surface propagates the fastest and thus controls the wear rate. The crack propagation rate is affected by the material properties such as strain hardening characteristics, cyclic hardening, cyclic softening and the Bauschinger effect. But the effect of all these factors have not been explicitly incorporated in the model.

(c) Models for Oxidative Wear

Over the three decades now, the mild oxidative wear mechanism has been the subject of intensive study. A simple model based on the mechanism of oxidative wear has been given by Uhlig (1954). The implicit assumption in the model is that the weakest point is at the interface between the metal and the oxide and that, as a result of sliding engagement, the oxide layer flakes off at the interface. It is assumed that the real area of contact is an array of

circular junctions and if the wear rate of the *i th* junction is W_i, then the total wear rate, W, is given by,

$$W = n W_i = n \frac{\pi a^2 y}{2a} = \frac{\pi n a y}{2} \tag{2.32}$$

Where, $2a$ is the diameter of the circular junction, n is the number of junctions and y is the thickness of the oxide layer.

By assuming a logarithmic relationship for the initial growth of an oxide film, the thickness of oxide film, y, on the clean metal surface given by,

$$y = \beta \ln\left(\frac{t}{\tau} + 1\right) \tag{2.33}$$

Where, t is time and β and τ are the parameters associated with the kinetics of the oxidation process. β is a constant dependent on both the material and the temperature of oxidation while τ is a constant dependent on the material. β is related to temperature by an Arrhenius type of equation given by,

$$\beta = \beta_0 e^{-Q/RT} \tag{2.34}$$

where β_0 is the Arrhenius constant for the reaction, Q is the activation energy associated with the formation of oxide, R is the gas constant and T is the temperature of the surface. On the basis of a simple model, for the asperity temperature, T, may be estimated as,

$$T = T_0 + \frac{\mu L v}{4 J (k_1 + k_2) a} \tag{2.35}$$

Where, T_0 is the ambient temperature and k_1 and k_2 are the thermal conductivity of the two bodies under sliding contact, L is the applied normal load, v is the velocity and J is the Joule's constant.

It has been reported that for many sliding situations, t/τ is less than unity and for the case of iron, τ is in the range of seconds. Hence the relationship given by Eq. (2.33) can be simplified as,

$$y \approx \frac{\beta t}{\tau} \tag{2.36}$$

Assuming that each time a junction is formed the oxide layer is removed, the equation for the wear rate has been obtained as,

$$W = \left(\frac{\beta}{2 \tau v}\right)\left(\frac{\pi A_a L}{H}\right)^{1/2} \tag{2.37}$$

Where, t is the average time taken by a junction to reform, A_a is the apparent area of contact and H is the hardness of the material. This simple model for oxidative wear indicates the various factors or parameters of a wearing system that can influence this mechanism.

This model has been further developed subsequently by Quinn and coworkers (1980, 1984) and an iterative technique was developed to determine the values of the

parameters which appear in it, from the experimental wear rates (Quinn *et al*, 1984). In their model it has been assumed that there is a thin layer of oxide on the surface all the time. Since the growth rate on the clean surfaces and the oxidised surfaces tends to be different, a parabolic relationship of growth of oxide with time has been assumed following observations of Kubaschewski and Hopkins (1962). The model developed by Quinn *et al* uses the following parabolic relationship.

$$y^2 = (\Delta m)^2 = \beta t \tag{2.38}$$

Where, Δm is the mass of oxygen taken up by a unit area in time t and β is given by the same Arrhenius type Eq. (2.34). In this model it is assumed that a critical oxide thickness ξ_c is required for the detachment of oxide and multiple encounters are required for the formation of wear particle. The model has resulted in the following equation of wear rate.

$$W = \frac{L \beta d}{v H f^2 \xi_c^2 \rho_0^2} e^{\frac{-Q}{RT}} \tag{2.39}$$

Where, f is the fraction of oxygen in the oxide, ρ_0 is the density of the oxide and d is the diameter of the junction.

(d) Model for Seizure Wear

It is an established fact that the real area of contact, A_r, between two sliding surfaces in relative motion is very small and the contact occurs only at the asperities. The large pressures developing at these real areas of contact, may forge metallic junctions and the welded area grows by the shearing of these junctions. It has been shown by Tabor (1959) that under the

of contact and the surfaces seize. An equation for seizure has been proposed under static condition where the mean pressure (L/A_r) on the asperity is equal to the local hardness (H_0) of the material. In addition to normal pressure L/A_r, each asperity is subjected to a shear stress $\tau = \mu L/A_r$ during sliding because of friction and the junctions grow until,

$$\left(\frac{L}{A_r}\right)^2 + \alpha_t \tau^2 = H_0^2 \tag{2.40}$$

This is Tabor's equation for seizure. α_t used in this equation, is a constant and its value can be obtained by fitting the experimental data. Substituting the value of $\tau = \mu L/A_r$ a modified equation can be obtained which now includes the effect of frictional shear as,

$$\frac{L}{A_r} = \frac{H_0}{\left(1 + \alpha_t \mu^2\right)^{1/2}} \tag{2.41}$$

Lim and Ashby (1987) have modified Eq. (2.41) in terms of the normalised variables as

$$\tilde{L} = \frac{1}{\left(1 + \alpha_t \mu^2\right)^{1/2}} \frac{H_0}{H} \tag{2.42}$$

Where , $\tilde{L}$ is the normalised force given by,

$$\tilde{L} = \frac{L}{A_a H} \tag{2.43}$$

and the coefficient of friction μ for steels is given by,

$$\mu = 0.78 - 0.13 \log_{10} (\tilde{v}) \tag{2.44}$$

Where, v is the normalised velocity given as,

$$\tilde{v} = \frac{v\, r_0}{a_0} \tag{2.45}$$

Where, r_0 is the radius of the circular apparent area of contact and a_0 is the thermal diffusivity of the metal and v is the sliding velocity. It has been further pointed out by Lim and Ashby (1987) that the local hardness depends not only on the temperature but also on the strain rate. The bulk temperature, T_b, increases with increasing sliding velocity causing a drop in hardness. At the same time, the strain rate is also high due to higher velocity resulting in increasing hardness. In case of steels, it has been shown that the two effects roughly cancel each other. A simple equation has been derived by Lim and Ashby (1987) to include the effect of temperature and strain rate, which is given below.

$$\tilde{L} = \frac{1}{\left(1 + \alpha_t\, \mu^2\right)^{1/2}} \left[1 - \frac{T_b - T_0}{20\, T_m} \ln \left(\frac{10^6}{\phi\, \tilde{v}} \right) \right] \tag{2.46}$$

Where, T_m is the melting point of the metal and ϕ is a constant equal to l_b/r_0. l_b is the equivalent diffusion distance and r_0 is the radius of the circular apparent area of contact.

(e) Model for Melt Wear

At high sliding velocities of 10 to 100 m/s, localised melting occurs between sliding surfaces. The coefficient of friction drops to a low value because of the formation of the film

of liquid metal giving melt lubrication. The liquid layer supports the normal load by usual hydrodynamic mechanism and the heat generated by the viscous work in the layer continues to melt more solid. Therefore, the wear rate is still high even if the coefficient of friction is low. The metal removed from the surfaces, is ejected as sparks or hot incandescent particles or squirted out in a molten stream. Lim and Ashby (1987) have given a model for the normalised wear rate by considering the heat flow equations in terms of the normalized force, the normalised velocity and the temperature for the pin-on-disc geometry. Out of the total frictional heat, q, generated, only a fraction of αq is assumed to go to the pin. A part of αq is conducted away and a part is absorbed as latent heat L_l (J/m^3) in melting a volume V_1 (m^3) per second of metal at the interface. Thus heat flow equation is,

$$\alpha q = -k_m \nabla T + L_1 \frac{V_1}{A_a} \tag{2.47}$$

Where, αq is the rate of frictional heat input to the pin, the first term in rhs is the rate of heat conduction into the pin and the second term is the rate of heat absorption by the melting of material. But $q = \mu L V_l / A_a$, hence substituting this value in Eq. (2.47), one gets,

$$\alpha \mu \frac{L v}{A_a} = k_m \frac{(T_m - T_0)}{T_b} + L_1 \frac{V_1}{A_a} \tag{2.48}$$

If all the metal, which melts, is ejected, the normalised wear rate may be written as,

$$\tilde{W} = \frac{V_1}{v A_a} \tag{2.49}$$

Using Eq. (2.48) in (2.49), one may write,

$$\tilde{W} = \left(\frac{T_m - T_0}{T^*}\right) \frac{H}{L_1} \frac{1}{\phi \tilde{v}} \left[\alpha \mu \tilde{L} \tilde{v} \frac{T^* \phi}{(T_m - T_0)} - 1\right] \qquad (2.50)$$

Where, T^* is an equivalent temperature for the metal, which is defined as

$$T^* = \frac{a H}{k_m} \qquad (2.51)$$

2.7 FORMULATION OF PROBLEM

From the above review of the available literature, it is obvious that most of the studies conducted in the past have been restricted to the correlation between the microstructure and the mechanical properties of the dual phase steels. The potential of dual phase steel for wear resistant applications has led to limited analysis of the friction and wear characteristics of the dual phase steels. Most of these studies have been carried out with fixed annealing times, at which the austenite volume fraction reaches almost an equilibrium value. Some kinetic studies have also been carried out on the effect of intercritical annealing time to elucidate the mechanism of austenite formation but little effort has been made to study the effect of intercritical annealing time on the mechanical properties of the dual phase steel, which, in turn, affect its tribological behaviour. During iso-thermal annealing, the austenite phase after consuming pearlite areas, grows into the ferrite areas. If quenching is done before equilibrium is attained at the intercritical temperature, the martensite volume fraction progressively increases with increasing intercritical annealing time. This change in the martensite volume fraction influences the mechanical properties of the dual phase steels and it has marked influence on the friction and wear of dual phase steels.

Extensive investigations have been reported in the literature on the friction and wear behaviour of fine pearlite, coarse pearlite, martensite, bainitic and stainless steels but there are only a few investigations carried out to understand the tribological behaviour of the dual phase steels. Though dual phase steels have been extensively studied in order to achieve an optimum combination of mechanical properties required for structural applications but the wear behaviour of plain carbon dual phase steel has hardly drawn any attention. Nonetheless, there are several interesting features in dual phase steels, which may help in enhancing the wear resistance of this steel. The wear studies carried out till date, have emphasised the effect of microstructure on the friction and wear of steels but these studies mainly revolve around the pearlitic or bainitic structures and only a few studies have been reported on the ferrite-martensite dual phase structure.

The present study is motivated by a need to unravel the friction and wear behaviour of plain carbon dual phase steels having varying amounts of the martensite in the microstructure. The martensite content in the microstructure may be varied by changing the time of intercritical annealing at a fixed temperature in order to understand its effect on the friction and the oxidative wear behaviour of dual phase steels.

In the past, different wear models have been developed for the prediction of the wear rates for a single phase material but no attempt has been made to develop a model for the multiphase materials where each phase has its distinct friction and wear characteristics. The model for oxidative wear developed by Quinn (1967) could be extended for two phase materials in order to apply it to dual phase steels. An expression for estimating the wear rate of the dual phase steel may be developed on the basis of the estimated real area of contact in the two phases and the critical thicknesses of the oxides of martensite and ferrite. This will incorporate the effect of the second phase i.e., martensite on the wear of the dual phase steel.

In order to determine the friction and wear behaviour of dual phase steel under sliding condition, pin shaped specimens of plain carbon steel containing 0.14 and 0.42 wt pct carbon have been selected for the present investigation because of hardenability consideration. The following plan for the present work could be followed in order to fill-up the gap in the existing knowledge.

The steel specimens received could be homogenised to attain uniform initial structure throughout the material. The effect of the intercritical annealing time on the evolution of microstructure of the dual phase steels including morphology i.e., size, shape and distribution of martensite, could be investigated. This study is expected to provide an understanding of the effect of the martensite morphology on the mechanical properties of these steels.

The variation of mechanical properties of dual phase steels with increasing volume fraction of martensite could be determined. This will help in explaining the friction and wear characteristics of these steels as it strongly depends on the mechanical properties, especially the hardness of the material. The change in fracture behaviour of the dual phase steels with increasing volume fraction of martensite could be determined by examining the fractured surfaces of tensile specimens under Scanning Electron Microscope (SEM) and the change in the nature of fracture with the martensite volume fraction.

The friction and oxidative wear characteristics of the normalised steel and dual phase steels under different normal loads and at a constant sliding velocity could be determined under dry sliding conditions in atmospheric air, using a pin-on-disc wear testing machine. This will help in revealing the effect of microstructure and normal load on the friction and wear behaviour of these steels.

An effort will be made for the first time to take into account the effect of the second phase (martensite) to predict the wear rate of the dual phase steels by evolving an oxidative wear model for two phase materials. To fulfill this objective the studies on the friction and wear characteristics of Armco iron could be undertaken to simulate friction and wear characteristics of ferrite phase. Fully martensitic steel could be used to simulate the friction and wear in martensite phase of the dual phase steel. Another estimate of the wear rate and coefficient of friction could be carried out on the basis of load sharing between the constituent phases and the rule of mixture.

The surfaces of the worn specimens of Armco iron, normalised steel, dual phase steels and fully martensitic steel and the nature of the wear debris after sliding could be studied to confirm the nature of wear and the mechanisms. The subsurface structure of the worn specimens could be examined to identify subsurface deformation and delamination and their contribution to the observed wear.

In summary, the present investigation is aimed to understand experimentally the friction and oxidative wear in plain carbon dual phase steel with variation in martensite content and compare it with predictions based on (a) extension of Quinn's model of oxidative wear in two phase material and (b) the model based on load sharing between the constituent phases and the rule of mixture.

Chapter 3

EXPERIMENTAL WORK

This chapter describes the experimental procedures used in the present investigation in respect of heat treatment to develop dual phase and fully martensitic structure in the plain carbon steels and characterisation of mechanical and tribological behaviour of the dual phase steels and fully martensitic steel thus produced.

3.1 SELECTION OF STEEL SAMPLES

The low and medium carbon hypoeutectoid steel rods of commercial grade of 6.25 mm diameter and Armco iron have been used for the present investigation. The steel has been procured from local market and Armco iron has been supplied by Steel Authority of India Limited (SAIL).

3.2 DETERMINATION OF CHEMICAL COMPOSITION OF STEEL

The chemical analysis of the plain carbon steels and Armco iron used in the present study has been carried out through the spectrophotometer and the results of the analysis are given in Chapter 5 of the present study.

3.3 EXPERIMENTAL SET-UP FOR HEAT TREATMENT

For production of dual phase and fully martensitic structure by heat-treatment, an experimental set-up shown schematically in Fig. 3.1 has been locally fabricated. Essentially, it consists of a tubular electric resistance furnace; a device for suspending steel samples in the furnace tube for heat treatment and a quenching device. A vertical tubular electric resistance furnace is locally fabricated using a sintered alumina tube, with both ends open, of internal diameter 6.5 cm and length 67 cm by winding non-inductive Kanthal wire of 18 SWG gauge and resistance of ~30 ohm as to yield in the centre of the furnace a uniform temperature zone (UTZ) of approximately 20 cm length. A circular sheet of asbestos, acted as a cover for the top end of alumina tube and had three openings-one for passing a chromel-alumel thermocouple encased in protective refractory sheath, to measure temperature in the UTZ, the second for another chromel-alumel thermocouple also encased in protective refractory sheath and placed in the UTZ and connected to a on-off type temperature controller (range 0^0C to 1200^0C) and the third for suspending pin shaped steel sample in the UTZ for heat treatment. Immediately below the furnace, is placed a quenching bath-a cylindrical steel tank containing water as the quenching medium. The lower end of the tube is submerged in the water for the instantaneous quenching of the specimen. Quenching is carried out by cutting the wire from which the sample is suspended thus allowing the heated specimen to fall directly into the quenching bath placed just below the furnace tube.

The furnace is supplied with single phase 220 volt a.c. power through an automatic solid state a.c. Servo-Voltage Stabiliser (NELCO make, 7.5 KVA, 175-266 V range, maximum current 30 amp.), a variable resistance (ESCORP make, Variac-240V, 28 amp. maximum load) and an automatic on-off type relay-operated temperature controller with

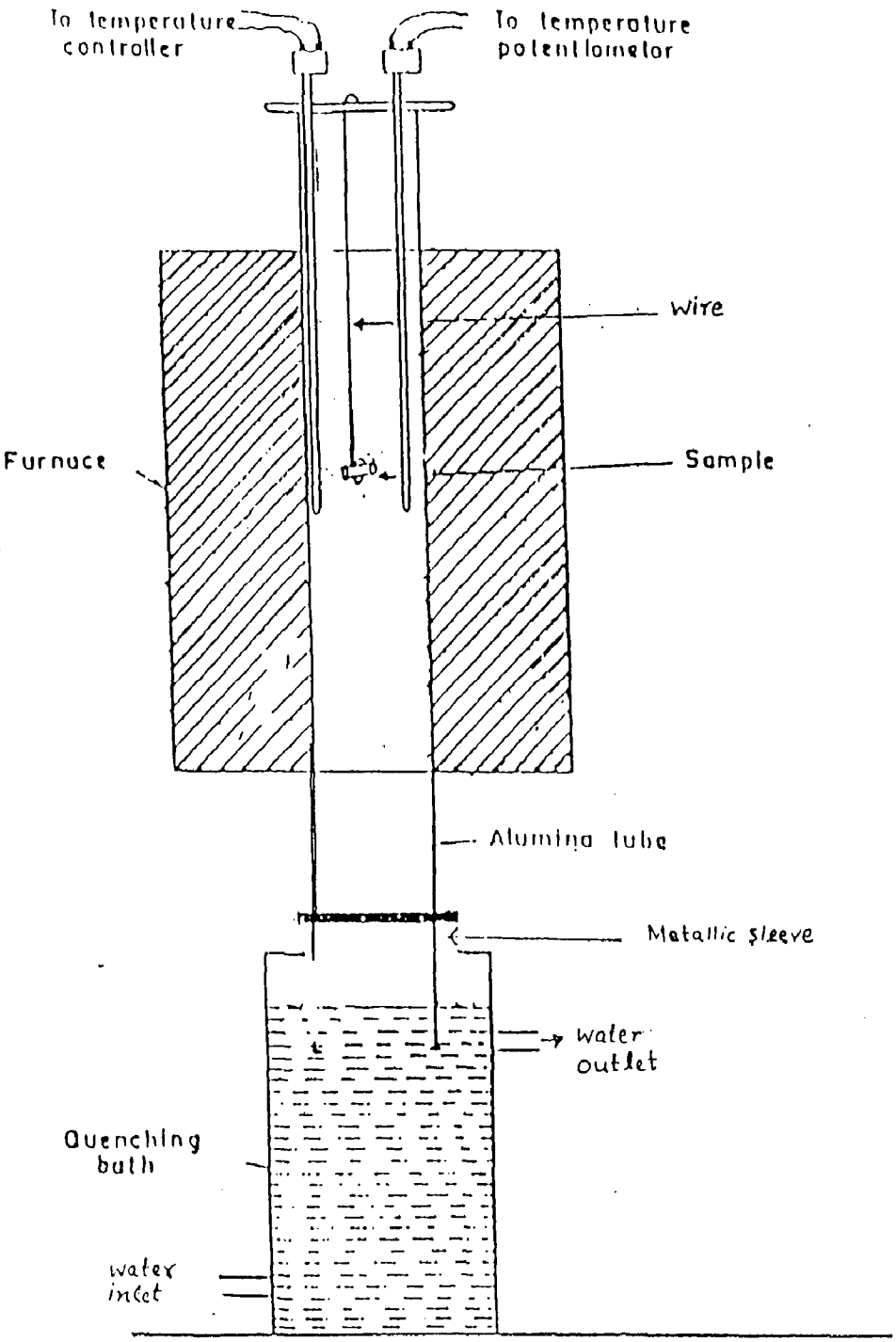

Fig. 3.1 Schematic view of the vertical tube furnace used for the intercritical heat treatment.

indicator (APLAB make-Applied Electronics, Thane, India, range upto 1200 ^{0}C), all mounted on a control panel with suitable indicator lights and electrical fuses and switches to enable precise temperature control upto ± 5^{0}C in the UTZ of the furnace. For temperature measurement, a Leads-Northup type 8694 potentiometer, has been used.

3.4 HEAT TREATMENT VARIABLES AND PROCEDURE

(a) Normalising

Cylindrical pin samples (30 mm X 6.25 mm ϕ) of low carbon steel and (30 mm X 4.0 mm ϕ) of the medium carbon steel have been used in the present study as shown in Fig. 3.2. The diameter has been reduced to 4 mm by the turning operation on the lathe. Sample diameter has been reduced to 4 mm to attain the sufficient hardenability in the quenched samples. All specimens are then normalised in a muffle furnace. Normalising has been carried out at a temperature of 950^{0}C for 15 minutes for the low carbon steel samples followed by air cooling whereas the same treatment has been carried out for the medium carbon steel samples at a temperature of 860^{0}C for 20 minutes. This normalising treatment is done in batches comprising of four (4) samples per batch.

(b) Intercritical Annealing

In the present investigation one parameter viz., intercritical annealing time has been varied at a fixed intercritical annealing temperature for obtaining different martensite volume fraction (MVF) in the dual phase steels. A close examination of available published literature on production of dual phase steels (Davies, 1978; Koo *et al*, 1980; and Nath, 1989) reveals

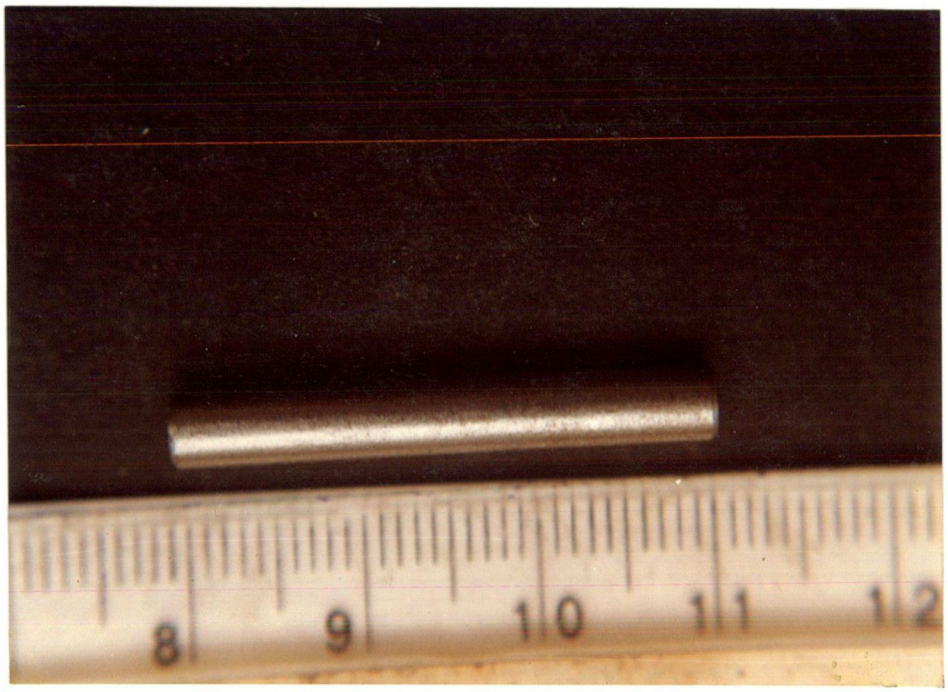

Fig. 3.2 Photograph showing the pin specimen used in the present investigation.

that, in general, the intercritical annealing time used has been either 10 minutes or 15 minutes at any one intercritical annealing temperature to obtain a fixed martensite volume fraction (MVF) in dual phase steels. These are the time duration for a plain carbon steel having carbon from 0.08 to 0.2 wt pct. However, the objective of present study is to have the dual phase steels with varying microstructure having different volume fraction of martensite, so as to analyse the effect of the martensite volume fraction on the wear and frictional behaviour of dual phase steels.

For obtaining dual phase structure, the pin shaped specimen is suspended by a wire in the UTZ of the vertical tube furnace and the top end of the alumina tube is covered with the asbestos sheet in order to prevent heat loss. The temperature of the furnace drops during charging of the sample inside the furnace. Therefore, the start of the intercritical time is considered from the moment the furnace temperature regains the original desired Intercritical Annealing (ICA) temperature. After the lapse of specified soaking time for each heat treatment, the wire is cut and the specimen is made to fall directly into the quenching water bath placed just below the furnace tube.

The samples of low carbon steel have been intercritically annealed to develop the desired dual phase structure of martensite and ferrite. The intercritical annealing has been conducted at a temperature of 740^0C for 5 minutes followed by water quenching. Intercritical annealing for five minutes is not long enough to attain equilibrium and annealing time in this range, could be used as a variable to control the amount of phases (Nath *et al*, 1994).

The samples of the medium carbon steel have also been heat treated at the specified intercritical annealing temperature of 740^0C for different holding times viz., 2.0, 2.5, 3.0 and

3.5 minutes followed by water quenching to obtain different volume fraction of martensite in the dual phase structures.

For developing fully martensitic structure in the steel the sample is heated at 920^{0}C for 20 minutes followed by water quenching.

3.5 METALLOGRAPHIC STUDIES

For metallographic examination, samples are first prepared using hot mounting in plastic granules employing a CISCO, Agra, make mounting machine. These mounted samples are next manually polished following the standard metallographic procedures described below. The surface of the specimen that is to be examined is first made plane by means of a specially designed motor–driven emery belt. The sharp edges of the specimen are then beveled to avoid the tearing of the emery paper in the subsequent polishing. The specimens were then polished manually using the SiC metallographic emery papers (120, 240, 400 and 600 grit). During polishing on each emery paper the direction of grinding was such as to introduce scratches at right angles to those introduced by the preceding paper. The final polishing is carried out on a sylvet-cloth using 0.1 μm size alumina powder suspension on a MPE, Mumbai, make polishing machine. After polishing, all the samples are etched with 2 pct nital (2 pct HNO_3 + 98 pct Methanol), washed, dried and finally examined under MeF_3 Reichert-Jung optical microscope made in Austria. Typical microstructural features of all the samples are photographed. These optical micrographs are presented and discussed in Chapter-5.

Quantitative measurements of microstructural features have been carried out to determine the volume fraction and the size of the islands of the phases present in the microstructures. Volume fraction of the martensite is measured by point-counting technique. A grid containing 100 points is inserted into the eye-piece of the microscope. The magnification of the microscope is so adjusted that maximum resolution could be attained and at the same time the condition of having not more than one grid point on one particle is satisfied. The number of grid points falling on the martensite islands is counted at random locations. For each sample, 20 such observations have been taken. The volume fraction of martensite, V_m is then calculated from the relationship,

$$V_m = \frac{\sum_{i=1}^{20} N_i}{20 \times 100} \qquad (3.1)$$

Where, N_i is the number of grid-points falling in martensite islands in any particular observation.

The size of the ferrite grains in Armco Iron, prior austenite grain size in normalised steel and the size of ferrite and martensite islands in dual phase steels has been measured by intercept method with a microscale inserted into the eye-piece of the microscope. The microscale is first calibrated with a given standard at the magnification of study. One division of scale corresponds to 6.25 μm of the object at a magnification of 80 X where as the value of one division is 2.6 μm at a magnification of X 200. At least 20 measurements are done randomly to estimate the average grain size. Results of the quantitative measurements are presented and discussed in Chapter-5.

3.6 MEASUREMENT OF MECHANICAL PROPERTIES

3.6.1 Hardness Measurement

The Vickers and Brinell hardness of the Armco Iron, normalised steel, dual phase steels and fully martensitic steel have been measured. For Armco iron the load applied during the Vickers hardness measurement is 20 kg while for the Brinnel hardness it is 16.25 kg. For rest of the steels the measurements are taken at a load of 30 kg for the Vickers hardness and at a load of 62.5 kg for the Brinell hardness. The load is applied for 30 seconds on a sample and then the diameter of indentation is measured from a projection of the indentation on a screen with the help of an optical lens provided in the hardness tester type Dia Tester 2RC supplied by Blue Star Co. The time of application of load should be such as to ensure that the plastic flow of the metal in the area under indentation has ceased. The load is removed to allow elastic recovery and the round impression was measured in millimeters to the nearest 0.01 mm using a low-power microscope. To eliminate any error in the measurements due to deviation from sphericity, measurements are taken along two diameters at 90^0 to each other. Hardness was determined by taking the mean diameter of the indentation. The Brinell or Vickers hardness number has been estimated from the diameter of indentation at the applied load on each sample, at least eight indentations for hardness measurement are made at different locations and the average of these readings is reported as the hardness of the steel.

Vickers microhardness tests have been carried out on the samples of both normalised and dual phase steels. The samples have been polished using the emery paper up to 4/0 grade. The hardness has been measured at a load of 10 g for 30 seconds by using a square base pyramid shape diamond indentor with an angle of 136^0. The diagonals of the square

indentation are measured under optical microscope at a magnification of X 500 provided with the microhardness Leitz Wetzler 721464 tester and the average of the two diagonals is used to find out the corresponding microhardness. At least five readings are taken on the martensite islands and the ferrite phase respectively. Average of these readings for each sample is reported as the microhardness of the martensite and ferrite in dual phase steels.

3.6.2 Tensile Testing

The tensile tests have been carried out at ambient temperature for the Armco Iron, normalised steel, dual phase steels and fully martensitic steel developed out of the medium carbon steel. The dimension of the tensile specimens, conforming to ASTM specification, is shown schematically in Fig. 3.3. The tensile tests have been performed on a tensometer, having maximum capacity of 25 kN supplied by Hounsfield Test Equipment Ltd., England. It has an arrangement for the computerised printing of the load *vs.* extension curve. The diameter and the gauge length of each specimen are measured prior to and after the tensile test. The ultimate tensile strength of the specimens has been estimated by dividing the maximum tensile force by the initial cross-sectional area of the specimens in units of MN/m^2 or MPa. After fracture of the specimen, the increase in gauge length is measured and the engineering fracture strain has been estimated as a change in gauge length per unit initial gauge length of 20 mm.

The yield stress in case of dual phase steels has been calculated by adopting the 0.2 pct offset proof stress method. The engineering stress *vs.* engineering strain curves have been plotted from the load extension curves.

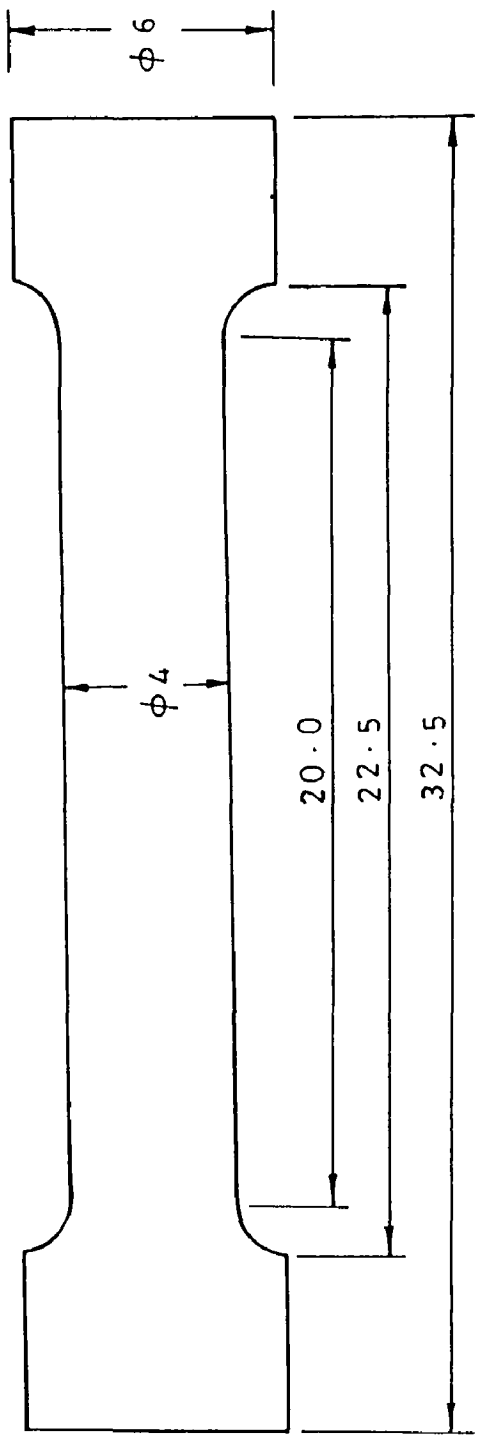

Fig. 3.3 Dimensions of the tensile test specimen.

3.7 FRACTOGRAPHIC STUDIES

The fractographic studies have been carried out on the broken tensile test specimens of Armco Iron, normalised steel, dual phase steel and fully martensitic steel. To have knowledge of the operating mode of fracture, all these samples are examined under LEO, 435 VP scanning electron microscope (SEM) and the salient features have been photographed.

3.8 DRY SLIDING FRICTION AND WEAR TESTING

Dry sliding wear tests for the Armco Iron, normalised steels both low and medium, dual phase steels and fully martensitic steels have been conducted using a sturdy pin-on-disc machine model TR-20E, supplied by M/S DUCOM, Bangalore (India) shown schematically in Fig 3.4. A complete photograph of the set up of the machine is shown in Fig. 3.5. The tests have been conducted in air having relative humidity in range from 40 to 75 pct. Wear tests have been conducted using pin samples that had flat surfaces in the contact region and the rounded corner. The pin is held stationary against the counterface of a 100 mm diameter rotating disc made of En-32 steel hardened to 62 to 65 HRC as provided in the pin-on-disc machine. The composition of the material of the steel disc is given in Table 3.1. The En-32 steel is a plain carbon steel case hardened to attain a hardness of 62–65 HRC.

Table 3.1

Chemical composition of the En–32 steel disc

C	Si	Mn	S	P
0.42 (max)	0.05-0.35	0.40–0.70	0.05 (max)	0.05 (max)

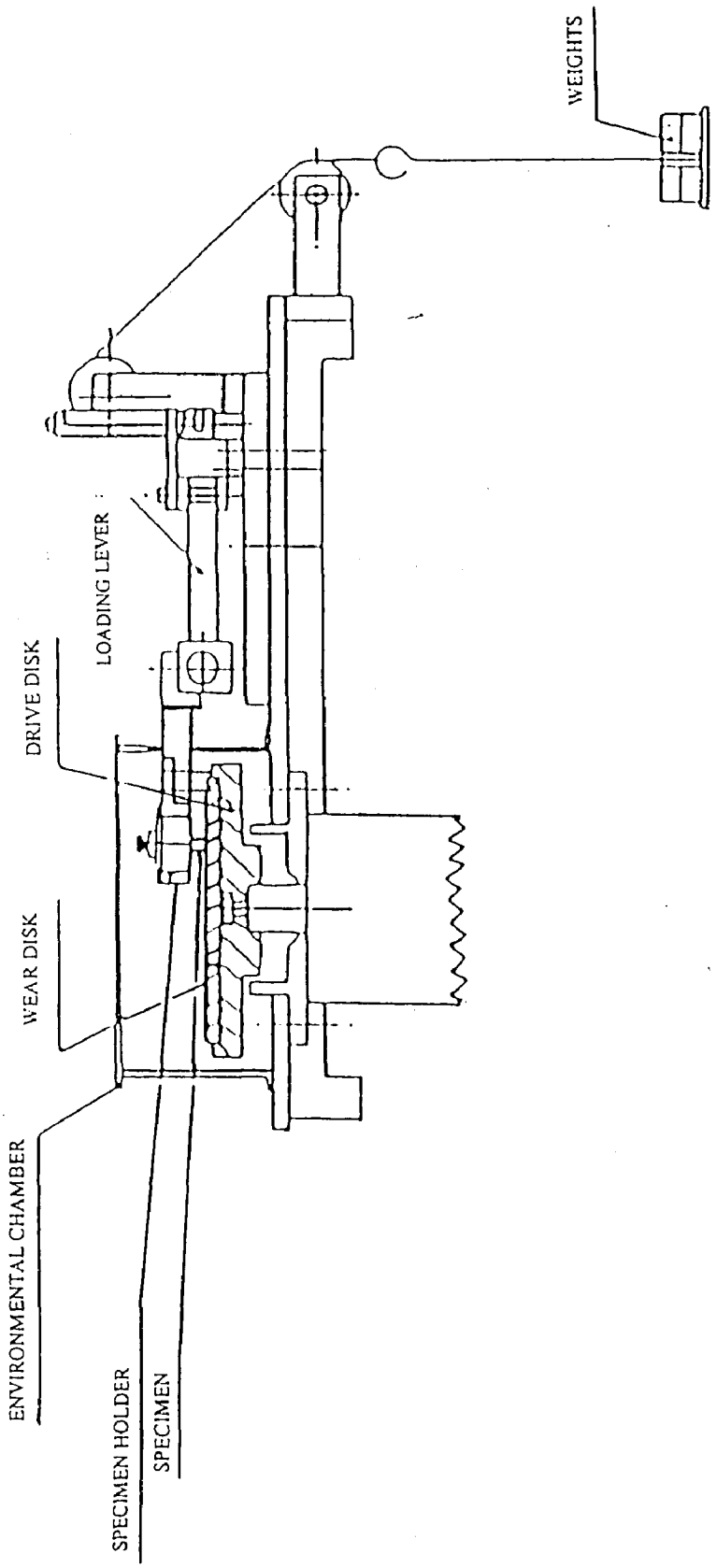

Fig. 3.4 Schematic view of the pin-on-disc wear testing machine.

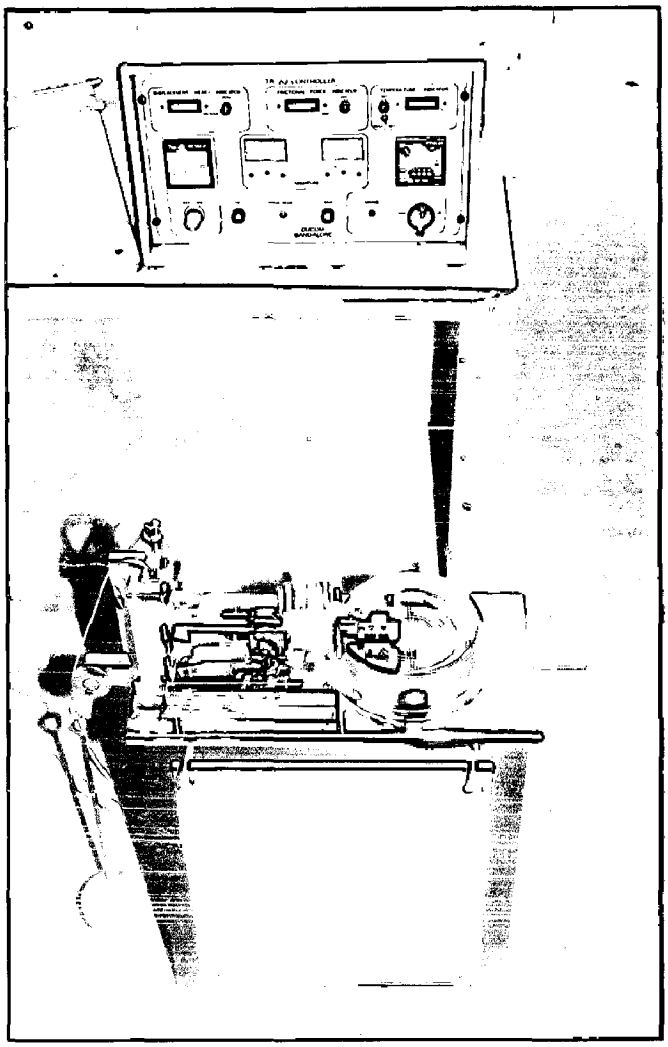

Fig. 3.5 Photograph showing the complete set-up of the wear testing machine and the control panel.

The pins have been polished up to 4/0-grade emery paper and both the disc and the pin were cleaned by acetone and dried before carrying out the test. The pin is loaded against the disc through a dead weight loading system. The wear tests for low carbon normalised steel and dual phase steel have been conducted under three normal loads of 14.7, 24.5 and 34.3 N and at a fixed sliding velocity of 1.15 m/s. However, five different normal loads of 14.7,19.6, 24.5, 29.4 and 34.3 N are used for conducting the dry sliding wear tests on the Armco iron, medium carbon normalised steel, dual phase steels and fully martensitic steel developed from the medium carbon steel in the present study. The track radii for the pin are kept at 35, 40, 45and 50 mm. The rpm of the rotation of disc is adjusted so as to keep the linear sliding speed at a constant value of 1.15 m/s. A variation of ±5 rpm is observed in the rpm of the disc. Each wear test has been carried out for a total sliding distance of about 39.74 km. Tangential force is monitored continuously during the wear test. Pin weight losses have been measured at different intervals of time to determine wear loss. Weight loss data has been converted to volume loss data using a steel density of 7800 kg/m^3 for the low carbon steel and 7760 kg/m^3 for the medium carbon steel (Glaeser, 1992). The pin is removed from the holder after each run, cooled to room temperature, brushed lightly to remove loose wear debris, weighed and fixed again in exactly the same position in the holder so that the orientation of the sliding surface remained unchanged. The weight has been taken in a semi-micro balance to within an accuracy of 1 x 10^{-7} kg. Initially, the pin weight is measured four times, once after every 10 minutes of sliding and then twice after every 20 minutes of sliding, throughout an 80-minutes period. Thereafter the weight is measured at the end of 125, 185, 275, 395 and 575 minutes of sliding. Hence, the total run for each sample for each load at the selected sliding speed of 1.15 m/s is 9 hours and 35 minutes. During this period, a total of 11 individual data on weight loss have been obtained for 11 different sliding distances. Each test

at a given load and sliding velocity has been repeated three times and the average data for volume loss after each interval of time has been used for the analysis of wear rate.

The torque on the sample is calibrated in terms of friction force as indicated on the machine, using a fixed distance of lever arm of the apparatus. The friction coefficient has been determined from the friction force and the normal loads; only precalibrated dead loads have been used.

3.9 MICROSCOPIC EXAMINATIONS

3.9.1 Examination of Sliding Surfaces and Subsurface

The sliding surfaces of Armco Iron, normalised steels both low and medium carbon, dual phase steels and fully martensitic steel have been examined under the MeF_3 Model Reichert-Jung optical microscope made in Austria. To examine the condition of subsurface after the wear test the transverse section of the sliding surface has also been studied by suitably mounting the specimen in the plastic mould. The mounted samples are then prepared by following the standard metallographic procedure, etched with 2 pct nital. The surface and the subsurface of specimens after the wear testing have been examined under LEO, 435 VP scanning electron microscope (SEM) and the salient features in each have been photographed.

To examine the deformation in the subsurface layer the samples of the Armco Iron, normalised steels, dual phase steels and fully martensitic steel have been mounted in a taper of 1:10 after the sliding wear tests under the normal loads of 14.5, 24.5 and 34.3 N. These

specimens are polished by employing standard metallographic procedure and then examined under the optical microscope. The distinguishing features of the specimens have been photographed.

3.9.2 Examination of Wear Debris

'The examination of the nature of wear debris provides basic information regarding the degree of work hardening or the composition of the transferred layer. The debris material generated during wear experiments was carefully collected during dry sliding wear of all the specimens e.g., Armco Iron, normalised steel, dual phase steels and fully martensitic steel. These samples of wear debris are examined under Zeiss stereo-microscope and scanning electron microscope and the salient features have been photographed.

3.10 MEASUREMENT OF TEMPERATURE OF SLIDING SURFACE

The temperatures of the normalised and dual phase steel samples were measured while the wear test was being carried out. A fine chromel-alumel thermocouple was brazed just 3 mm above the wear surface of the sample and the thermo e.m.f generated was measured with the help of milli-volt meter to determine temperature.

3.11 X-RAY DIFFRACTION ANALYSIS OF WEAR DEBRIS

The wear debris generated during sliding at different normal loads for short sliding and long sliding distances has been collected. To collect the wear debris a paper is wrapped around the rotating disc protruding out about 1 mm so that the debris could not fell out of the

disc due to the centrifugal force. X-ray diffraction studies have been carried out on the wear debris of Armco iron, normalised steels both low and medium carbon and dual phase steel samples. X-ray diffraction patterns are obtained separately for the wear debris corresponding to the short and long sliding distances. X-ray diffraction study has been conducted using an iron target and nickel filter at a current of 20 mA under a voltage of 35 kV. The diffraction pattern is automatically scanned by a Phillips X-ray diffractometer, model PW 1140/90, in the angle range (2θ) between 20^0 and 120^0. The intensity of diffracted beam against 2θ is recorded at a chart speed of 1 *cm/min* and the Goniometer speed is $1^0/min$. For all the intensity peaks and corresponding values of 2θ, the interplanner spacing, d, has been calculated using Bragg's law,

$$2d \sin\theta = n\lambda \tag{3.2}$$

Where, λ is the wave length of FeK_α radiation used for the diffraction and is taken as 1.973 $\mathring{A}$ for estimating the 'd' values which is finally used for identification of various phases with the help of inorganic ASTM X-ray diffraction data cards.

Chapter 4

MODELLING OF OXIDATIVE WEAR IN TWO PHASE MATERIAL

Wear behaviour in homogeneous materials has so far been understood in terms of Archard's law, derived on the basis of a very simple model. In spite of significant deviations from the assumptions involved, the wear behaviour predicted by this model is obeyed in a large variety of situations even involving the heterogeneous materials. This model has been used as the basis by the Quinn (1967) to develop another model for oxidative wear for a single phase material. In this chapter, models have been developed to describe wear in heterogeneous two phase materials like dual phase steel starting from the models proposed by Archard (1953) and Quinn (1967). These models described in this chapter will provide the basis for understanding the experimental results on friction and wear of dual phase steels.

4.1 ARCHARD'S LAW AND WEAR IN TWO PHASE MATERIAL

Archard (1953) in his model for adhesive wear has assumed that the metal surfaces are initially clean, the junction formed at the asperity contacts are circular and the wear particles formed during wear are of hemispherical shape. The actual contact takes place on an area called real area of contact, relatively smaller compared to the apparent area of contact. If a is the radius of each junction and n is the total number of junctions, then the real area of contact is given by,

$$A_r = n \pi a^2 \tag{4.1}$$

For a junction of diameter $2a$, the distance traversed for breaking one junction by a tangential pull is taken as $2a$. Since the total number of asperity-junctions getting disengaged by sliding through a distance $2a$ is n, the junctions getting disengaged per unit sliding distance, n_u, is given by,

$$n_u = \frac{n}{2a} \tag{4.2}$$

Substituting n from Eq. (4.1) into Eq. (4.2) one may get,

$$n_u = \frac{A_r}{2a \pi a^2} \tag{4.3}$$

It does not follow that all the junctions which get disengaged will form a wear particle. Therefore, assuming that K_1 is the probability that a wear particle forms at a junction, the wear rate, W, i.e., wear volume per unit sliding distance, may be written as,

$$\begin{aligned} W &= K_1 \, n_u \, (\textit{volume of a hemisperical wear particle}) \\ &= K_1 \, \frac{A_r}{2\pi a^3} \times \frac{2}{3} \pi a^3 \\ &\approx K_1 \, A_r \end{aligned} \tag{4.4}$$

It has been assumed that the wear particle generated at a junction is hemispherical with radius a. The factor 1/3 that is coming due to the hemispherical shape has been taken into the constant K_1 which is equal to one third of the earlier K_1.

At the junctions, the asperities of the hard mating surface indents the relatively softer surface and the situation is similar to that encountered during measurement of indentation hardness. The hardnes, H, is defined as

$$H = \frac{L}{A} \tag{4.5}$$

Where L is the applied load on the indenter and A is the area of indentation. Assuming that a similar relation is valid, one may write that the real area of contact, A_r, is given by

$$A_r = \frac{L}{H} \tag{4.6}$$

Where L is the applied normal load and H is the hardnessof the relatively softer mating surafce. The wear rate given in Eq. (4.4) may thus be written as,

$$W = \frac{V}{S} = K_1 \frac{L}{H} \tag{4.7}$$

Where V is the volume of the material worn after sliding through a distance S. This is the law given by Archard (1953) for estimating the wear rate in a single phase material and K_1 is called the wear coefficient.

The wear rate for a two phase material like dual phase steel may be estimated by the method based on the estimated load sharing between the constituent phases i.e., ferrite and martensite in the dual phase steel. Here, it has been explored whether the wear rate in two phase materials could be estimated in terms of wear behaviour of the constituent phases in the framework of Archard's law given in Eq. (4.7). This law originally proposed for single phase materials, works fairly well for multiphase alloys. For a two phase material like dual phase steel, it is assumed that the wear rate is the sum of wear rates of its constituent phases and the wear rate of two phase material like DP steel may be expressed as,

$$\left(\frac{V}{S}\right)_{DP} = K_f \frac{L_f}{H_f} + K_m \frac{L_m}{H_m} \tag{4.8}$$

Where, $(V/S)_{DP}$ is the wear rate of dual phase steel, K_f is the wear coefficient of ferrite in DP steel and K_m is the wear coefficient of martensite in DP steel. H_f is the microhardness of ferrite in the DP steel and H_m is the microhardness of the martensite in DP steel. L_f and L_m are the normal contact loads shared by the matrix of ferrite and the martensite islands, respectively, in dual phase steel.

The contact loads of L_f and L_m may be estimated as follows. If total normal load applied to the dual phase steel is L, then

$$L = L_f + L_m \tag{4.9}$$

From the definition of hardness, one may write that

$$H_m = \frac{L_m}{A_{rm}} \tag{4.10}$$

$$H_f = \frac{L_f}{A_{rf}} \tag{4.11}$$

Where, A_{rf} and A_{rm} are the real areas of contact in the ferrite matrix and martensite, respectively. Substituting the values of L_m and L_f from Eqs. (4.10) and (4.11) in Eq. (4.9), one gets,

$$L = A_{rf}\ H_f + A_{rm}\ H_m \tag{4.12}$$

It is reasonable to assume that the counterface has uniform distribution of asperities and distribution of real area of contact in the two phases will be in proportion to their relative area or volume fraction in the two phase material. Therefore, one may write,

$$\frac{A_{rf}}{A_{rm}} = \frac{(1 - V_m)}{V_m} \tag{4.13}$$

Where, V_m is the volume fraction of dispersed phase in a two phase material and it is assumed to be equal to its area fraction on the surface. This assumption is strictly valid if the distribution of the dispersed phase is random. Substituting the value of A_{rf} from Eq. (4.13) in Eq. (4.12) one gets,

$$L = A_{rm} \frac{H_f (1-V_m) + H_m V_m}{V_m} \tag{4.14}$$

Thus, one may estimate A_{rm} and A_{rf} as

$$A_{rm} = \frac{L V_m}{H_f (1-V_m) + H_m V_m} \tag{4.15}$$

$$A_{rf} = \frac{L (1-V_m)}{H_f (1-V_m) + H_m V_m} \tag{4.16}$$

Substituting the values of A_{rm} and A_{rf} from Eqs. (4.15) and (4.16) in Eqs. (4.10) and (4.11), respectively, one may arrive at the estimates of loads shared by the matrix and the dispersed martensite island as,

$$L_f = \frac{L H_f (1-V_m)}{H_f (1-V_m) + H_m V_m} \tag{4.17}$$

$$L_m = \frac{L H_m V_m}{H_f (1-V_m) + H_m V_m} \tag{4.18}$$

Now by substituting the values of L_f and L_m in Eq. (4.8) the expression for the wear rate in a dual phase steel becomes,

$$\left(V/S\right)_{DP} = \frac{L}{\left[H_f (1-V_m) + H_m V_m\right]} \left[K_f (1-V_m) + K_m V_m\right] \tag{4.19}$$

The values of H_f and H_m are experimentally determined. The volume fraction of martensite, V_m, is estimated from the microstructure by point counting technique. The wear rate in the dual phase steel may thus be estimated using Eq. (4.19) by putting the values of wear coefficients of the constituents known a priori for different stages of wear by carrying out wear tests on ferrite and martensite samples. The results based on the above calculations are presented and compared with the experimental results obtained, in Chapter 6 in the present investigation.

The coefficient of friction may also be estimated by the method based on the estimated load sharing between the ferrite and martensite phases in a two phase material like dual phase steel. Here, the coefficient of friction in two phase materials has been explored in terms of the frictional behaviour of the constituent phases.

Let F be the total frictional force generated due to sliding under a normal load of L. If F_f, is the frictional force shared by the ferrite and F_m is the frictional force shared by the martensite phase, one may write,

$$F = F_m + F_f \tag{4.20}$$

From the definition of the coefficient of friction, one may write,

$$F = \mu_{DP}\, L\,; \qquad F_m = \mu_m\, L_m\,; \qquad F_f = \mu_f\, L_f \tag{4.21}$$

Where, μ_{DP} is the coefficient of friction of dual phase steel. μ_m and μ_f are the coefficients of friction, respectively, of the martensite and the ferrite phases in dual phase steel. L_m and L_f are the loads shared by the martensite and ferrite in dual phase steel. Hence, from Eqs. (4.20) and (4.21), one may write,

$$\mu_{DP}\, L = \mu_f\, L_f + \mu_m\, L_m \tag{4.22}$$

Now by putting the values of L_f and L_m from Eqs. (4.17) and (4.18) in Eq. (4.22) and rearranging the terms, one gets the expression for the coefficient of friction of DP steel as,

$$\mu_{DP} = \mu_f \left[\frac{H_f\,(1-V_m)}{H_f\,(1-V)_m + H_m\,V_m}\right] + \mu_m \left[\frac{H_m\,V_m}{H_f\,(1-V_m) + H_m\,V_m}\right] \tag{4.23}$$

The values of μ_f and μ_m are taken to be the same as those observed experimentally for ferritic and martensitic steel. The results based on the above expression have been presented and discussed in Chapter 6 of the present investigation.

4.2 EXTENSION OF ARCHARD'S LAW FOR OXIDATIVE WEAR

In actual practice, the conditions prevailing at the sliding surface are quite different from that assumed to derive Archard's law. The surfaces of the metals are not generally clean and so the probability K_1 in the Archard's model needs to be modified accordingly. For developing models of oxidative wear, it is assumed that there is a thin layer of oxide on the sliding surface all the time. According to the oxidational theory of wear proposed by Quinn (1967), the oxide grows in thickness at the contact temperature, T, until the oxide film thickness reaches a critical value of ξ_c, at which it becomes mechanically unstable and gets detached from the substrate to eventually generate wear debris. Since by definition of K_1, the number of encounters $1/K_1$ is necessary to generate a particle of wear debris, which is by dislodging the oxide film in oxidative wear, one may determine its value as follows.

Let Δt be the time of contact for a single encounter. Then, the total time, t, required to build up a critical thickness is

$$t = \frac{\Delta t}{K_1} \tag{4.24}$$

Also, if d is the sliding distance for a single encounter and v is the sliding velocity, then

$$\Delta t = \frac{d}{v} \tag{4.25}$$

From Eqs. (4.24) and (4.25) one gets,

$$t = \frac{d}{v K_1} \tag{4.26}$$

Assuming that the growth of oxide follows a parabolic relationship with time, the mass of oxygen uptake by the oxide film per unit area, Δm, in time t, required to build up critical thickness, is given by,

$$(\Delta m)^2 = \beta t \tag{4.27}$$

Where β is oxidation rate constant. However, the mass gain of oxygen per unit area may also be written as,

$$\Delta m = f \xi_c \rho_0 \tag{4.28}$$

Where, f is the mass fraction of oxygen in oxide, ξ_c, is the critical oxide thickness and ρ_0 is the density of the oxide. Hence, from Eqs. (4.27) and (4.28), one may estimate t as,

$$t = \frac{f^2 \xi_c^2 \rho_0^2}{\beta} \tag{4.29}$$

Equating the Eqs. (4.26) and (4.29), one gets the value of K_1, as,

$$K_1 = \frac{\beta d}{v f^2 \xi_c^2 \rho_0^2} \tag{4.30}$$

Substituting this value of K_1 in Eq. (4.4), the wear rate, W, is given by

$$W = \frac{\beta d}{v f^2 \xi_c^2 \rho_0^2} A_r = \frac{\beta d}{v f^2 \xi_c^2 \rho_0^2} \frac{L}{H} \tag{4.31}$$

The oxidation rate constant β is given by the Arrhenius type equation

$$\beta = \beta_0 e^{\frac{-Q}{RT}} \tag{4.32}$$

Where β_0 is the Arehenius constant, Q the activation energy of the reaction and T is the temperature of the asperity contact.

Substituting the value of the β in Eq. (4.31) the wear rate becomes,

$$W = \frac{\beta d}{\nu f^2 \xi_c^2 \rho_0^2} e^{\frac{-Q}{RT}} \quad A_r = \frac{\beta d}{\nu f^2 \xi_c^2 \rho_0^2} e^{\frac{-Q}{RT}} \frac{L}{H} \tag{4.33}$$

This is the expression of the wear rate in case of the oxidative wear given by Quinn (1967), for a single phase material.

4.3 OXIDATIVE WEAR IN TWO PHASE MATERIAL

The model of oxidative wear proposed by Quinn (1967) has been extended for the two phase materials like dual phase steels. The real areas of contact in the two phase materials are assumed to be formed in each of the constituent phases and their extent may be estimated by considering the microhardness of the constituent phases. The applied normal load is also shared between these phases.

Case I.

In this model it is assumed that the critical thickness of the oxide layer is the same for both the phases i.e., ferrite and martensite, and also, the same probabitlity, K_1, holds for the removal of the this oxide layer in both these phases.

The applied normal load L is expressed in Eq. (4.9) in terms of the loads L_m, and L_f shared by the martensite island and ferrite matrix. Let a be the radius of the circular junction, then the real area of contact of each junction will be πa^2. If a total of n junctions are there, the total real area of contact, A_r, is given by

$$A_r = n \pi a^2 = A_{rf} + A_{rm} \tag{4.34}$$

Where, A_{rf} and A_{rm} are the real areas of contact in the ferrite and the martensite phases respectively. Similarly, the apparent area of contact, A_a, may be written as,

$$A_a = A_{af} + A_{am} \tag{4.35}$$

Where, A_{af} and A_{am} are the apparent areas of contact in the ferrite and the martensite phases respectively.

It is assumed that the junction density is the same in both the phases throughout the apparent area of contact. Let N be the number of the junctions per unit apparent area of contact, the load shared by the martensite phase, L_m, may be estimated as,

$$L_m = N A_{am} \pi a^2 H_m \tag{4.36}$$

and the load shared by the ferrite phase, L_f, may also be similarly estimated as,

$$L_f = N A_{af} \pi a^2 H_f \tag{4.37}$$

Total number of junctions n, is given by

$$n = N A_{af} + N A_{am} = N A_a \tag{4.38}$$

Substituting the values of L_f, L_m and N from Eqs. (4.36), (4.37) and (4.38) in Eq. (4.9), one gets,

$$L = L_m + L_f = \pi a^2 N (A_{af} H_f + A_{am} H_m)$$
$$= \frac{n \pi a^2}{A_a} (A_{af} H_f + A_{am} H_m) \quad (4.39)$$

From Eqs. (4.34) and (4.39), one may estimate L as,

$$L = \frac{A_r}{A_a} \left[A_{af} H_f + A_{am} H_m \right] \quad (4.40)$$

Thus, the real area of contact may be estimated as,

$$A_r = \frac{L A_a}{\left[A_{af} H_f + A_{am} H_m \right]} = \frac{L}{\left[\frac{A_{af}}{A_a} H_f + \frac{A_{am}}{A_a} H_m \right]} \quad (4.41)$$

It is reasonable to assume that the counterface has uniform distribution of asperities. The distribution of the apparent area of contact in the two phases will be in proportion to their relative area or volume fraction in the two phase material. Therefore, one may write,

$$\frac{A_{am}}{A_a} = V_m \quad and \quad \frac{A_{af}}{A_a} = (1 - V_m) = V_f \quad (4.42)$$

Where V_m and V_f are the volume fractions, respectively, of the martensite and the ferrite phases in dual phase steel.

From Eqs. (4.41) and (4.42), one gets the real area of contact as,

$$A_r = \frac{L}{[V_f H_f + V_m H_m]} \tag{4.43}$$

Substituting this value of A_r in Eq. (4.33) , the wear rate may be expressed as,

$$W = \frac{L d \beta_0}{v f^2 \xi_c^2 \rho_0^2 [V_f H_f + V_m H_m]} e^{\frac{-Q}{RT}} \tag{4.44}$$

This is the expression for the wear rate in two phase material when the critical thickness of the oxide layer and the probability of generating wear particle are same for each of the constituent phases.

Case II.

In the model developed here, it is assumed that the critical thickness of the oxide layers and the probability of their removal are different for both the phases.

Let the critical thicknesses of oxide for ferite and martensite are ξ_{cf} and ξ_{cm} and the probabilities of their removal are K_{1f} and K_{1m}, respectively.Then Eq. (4.4) will become

$$W = K_{1f} A_{rf} + K_{1m} A_{rm} \tag{4.45}$$

Using Eqs. (4.13) and (4.34), one may estimate A_{rm} and A_{rf} as,

$$A_{rm} = V_m \; A_r \quad and \quad A_{af} = (1 - V_m) \; A_r = V_f \; A_r \tag{4.46}$$

The values of K_{1f} and K_{1m} may be estimated by using Eq. (4.30) as,

$$K_{1f} = \frac{\beta \, d}{v \, f^2 \, \xi_{cf}^2 \, \rho_0^2} \tag{4.47}$$

and

$$K_{1m} = \frac{\beta \, d}{v \, f^2 \, \xi_{cm}^2 \, \rho_0^2} \tag{4.48}$$

Substituting the values of K_{1f}, K_{1m} from above and A_{rf} and A_{rm} from Eq. (4.46) in Eq. (4.45), one gets,

$$\begin{aligned} W &= \frac{\beta \, d}{v \, f^2 \, \xi_{cf}^2 \, \rho_0^2} \; V_f \; A_r + \frac{\beta \, d}{v \, f^2 \, \xi_{cm}^2 \, \rho_0^2} \; V_m \; A_r \\ &= \frac{\beta \, d}{v \, f^2 \, \rho_0^2} \left[\frac{V_f}{\xi_{cf}^2} + \frac{V_m}{\xi_{cm}^2} \right] A_r \end{aligned} \tag{4.49}$$

Putting the value of A_r from Eq. (4.43) into Eq. (4.49), one gets the expression of the wear rate W, as,

$$W = \frac{\beta \, d \, L}{v \, f^2 \, \rho_0^2 \, [V_f \, H_f + V_m \, H_m]} \left[\frac{V_f}{\xi_{cf}^2} + \frac{V_m}{\xi_{cm}^2} \right] \tag{4.50}$$

This expression gives the wear rate in a two phase material in terms of the different critical thicknesses of the oxide layers for the constituent phases.

The wear rates calculated from the above expressions have been presented in Chapter 6 and compared with those observed experimentally in the dual phase steels in different stages of wear. The results have also been discussed in the light of the variations of wear rates with normal load and martensite volume fraction in these steels.

Chapter 5

MICROSTRUCTURE AND MECHANICAL PROPERTIES

This chapter describes the results on qualitative and quantitative metallography of Armco iron, normalised steels both medium and low carbon, fully martensitic steel and dual phase steels having different volume fractions of martensite developed through intercritical annealing. The materials have been characterised on the basis of their microstructure and grain size. The results on the mechanical properties of these materials are also presented in this chapter. In the end, the results have been discussed in the context of existing literature so as to develop an understanding of these steels in terms of their properties as it emerges after this study.

5.1 RESULTS

5.1.1 Chemical Composition

The chemical composition of the test materials i.e., Armco iron, medium and low carbon steels as analysed through the spectroscopy is given in Tables 5.1, 5.2 and 5.3 respectively.

Table - 5.1

Chemical Composition of Armco iron (Weight Percent)

C	Mn	Si	S	P
0.026	0.01	0.02	0.035	0.004

Table - 5.2

Chemical Composition of Medium Carbon Steel (Weight Percent)

C	Mn	Si	S	P
0.42	0.62	0.15	0.04	0.04

Table - 5.3

Chemical Composition of Low Carbon Steel (Weight Percent)

C	Mn	Si	S	P
0.14	0.56	0.04	0.014	0.034

5.1.2 Microstructure

The microstructures of Armco iron, normalised steels, dual phase steels and FMS developed through intercritical annealing have been examined under optical microscope to find the amount and the distribution of phases in the microstructure.

(a) Armco Iron

The optical micrograph of Armco iron is shown in Fig. 5.1. This is a typical single-phase structure showing grains of ferrite, an interstitial solid solution of carbon in α–iron. However, small amount of impurities as black regions is visible along the grain boundary. The average grain size is 105 μm.

(b) Normalised Steel

(i) Medium carbon steel

The optical micrograph of the normalised steel (860^0C, 20 minutes, air-cooled) is shown in Fig. 5.2 and this steel is designated throughout this text as N steel. It has bright areas of proeutectoid ferrite and dark areas of pearlite, which is resolved in certain locations marked by arrow, into alternate lamellas of ferrite and cementite. The volume fraction of pearlite estimated by point counting technique is 52 pct and the rest i.e., 48 pct, is proeutectoid ferrite.

(ii) Low carbon steel

Figure 5.3 shows the microstructure of the low carbon normalised steel (950^0C, 15 minutes, air-cooled) designated as LCN steel throughout this text. The microstructure of LCN steel has bright areas of ferrite and dark areas of pearlite, which was confirmed by resolving the alternate lamellae of ferrite and cementite at higher magnification. The volume fraction of pearlite in LCN steel is approximately 19 pct.

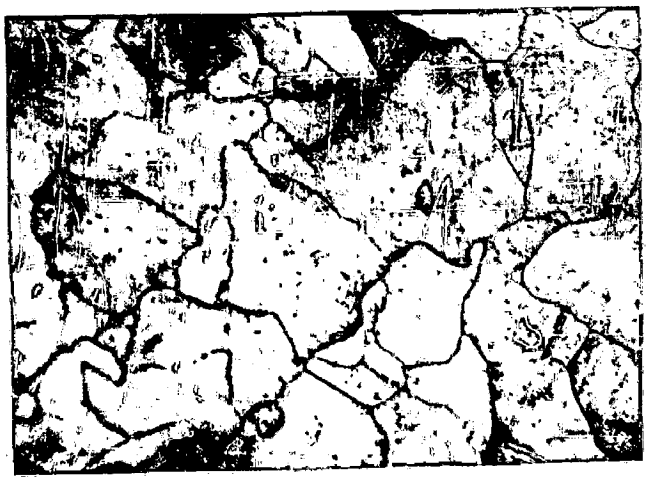

Fig. 5.1 Optical micrograph of the Armco iron showing large sized ferrite grains, X 80.

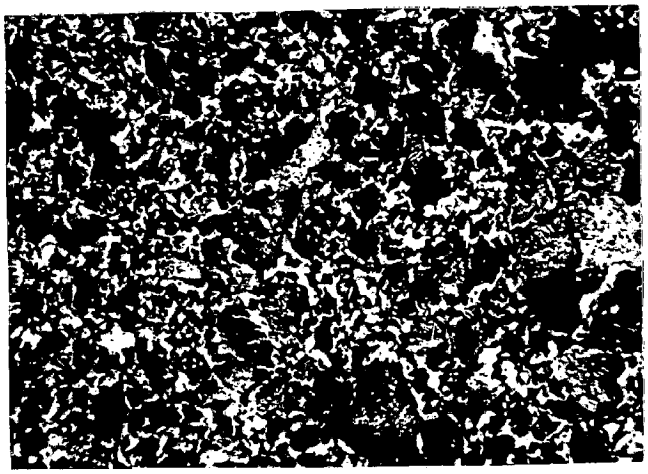

Fig. 5.2 Optical micrograph of normalised (N) steel showing dark regions of pearlite and bright regions of ferrite, (etchant 2 pct nital) X 390.

Fig. 5.3 Optical micrograph of low carbon normalised (LCN) steel showing dark regions of pearlite and bright regions of ferrite, (etchant 2 pct nital) X 200.

(c) Dual Phase Steels

The optical micrographs of dual phase steels developed from medium carbon normalised steel by intercritical annealing at 740^0C for varying times followed by water quenching are shown in Figs. 5.4 to 5.7.

Figures 5.4 (a) and (b) show the optical micrographs at lower and higher magnification respectively, of dual phase steel developed at 740^0C for 2.0 minutes of intercritical annealing followed by water quenching (designated as DP1). The structure has dark etching martensite islands in the bright regions of ferrite. There could be small amount of retained austensite associated with martensite and it is not visible in the micrograph. At higher magnification, martensite needles in the dark areas could be resolved as indicated by arrow in Fig. 5.4 (b). The volume fraction of martensite is approximately 42 pct.

Figure 5.5 shows the optical micrograph of dual phase steel developed at 740^0C for 2.5 minutes of intercritical annealing followed by water quenching. (designated as DP2). Here, the dark areas are martensite and bright areas are ferrite as in the microstructure of DP1 given in Fig. 5.4. Small amount of retained austensite may also be associated with martensite and it is not visible in the micrograph. The volume fraction of martensite is approximately 51 pct.

Figure 5.6 shows the optical micrograph of dual phase steel developed at 740^0C for 3.0 minutes of intercritical annealing followed by water quenching (designated as DP3). In this micrograph also the dark areas are martensite and the bright areas are ferrite as in the microstructure of DP1 steel given in Fig. 5.4. Small amount of retained austensite may also be associated with martensite and it is not visible in the micrograph. The volume fraction of martensite is approximately 59 pct.

friction coefficient in the run-in stage fluctuates around a mean level, then lessens and stabilizes after a certain period. It is further observed that with increasing load the friction coefficient decreases. The friction coefficient attains a value of 0.50, 0.48, 0.46, 0.45 and 0.44 at the maximum sliding distance of 39.74 km as the load increases from 14.7 N to 34.3 N in steps of 4.9 N. These values of the friction are lower than the values attained in case of the Armco iron but higher compared to the FMS.

(ii) Variation of coefficient of friction with normal load

Figure 6.32 shows the variation of the coefficient of friction averaged over the distance slid by the specimen corresponding to the run-in stage, with the applied normal load for Armco iron, FMS, N steel and DP steels. It is observed that at a fixed sliding velocity of 1.15 m/s, the average coefficient of friction decreases linearly as the load increases from 14.7 to 34.3 N. All the materials having different microstructures, investigated in the present study have been found to follow a similar trend. The Armco iron shows the highest values of the average coefficient of friction at all the loads whereas the corresponding values for the FMS are the lowest. The average coefficient of friction for N steel and DP steels is found to lie in-between those of Armco iron and FMS.

Figure 6.33 shows the variation of the coefficient of friction averaged over the distance slid by the specimen corresponding to the steady state of wear, with the applied normal load for Armco iron, FMS, N steel and DP steels. It is observed that at a fixed sliding velocity of 1.15 m/s, the average coefficient of friction decreases linearly as the load increases from 14.7 to 34.3 N. All the materials investigated in the present study have been found to follow a similar trend. The Armco iron shows the highest values of the average coefficient of friction in the steady state at all the loads whereas the corresponding values for

the FMS are the lowest. The average coefficient of friction for N steel and DP steels is found to lie in between those of Armco iron and FMS.

(iii) Estimation of the coefficient of friction

The coefficient of friction has been calculated from the expression given by Liu *et al* (1993) for a composite,

$$\mu_{DP} = \mu_f + (\mu_m - \mu_f) V_m \tag{6.1}$$

Where μ_{DP}, is the coefficient of friction of dual phase steel, μ_f, is the coefficient of the ferrite matrix in the dual phase steel, μ_m, is the coefficient of friction of the martensite phase and V_m, is the volume fraction of the martensite in the dual phase steel. The variation of the coefficient of friction in the steady state calculated by using Eq. (6.1), with normal load has been shown by a symbol of dark square in Figs. 6.34 (a) and (b).

The coefficient of friction has also been calculated on the basis of (i) estimated sharing of load between the constituent phases and (ii) the observed friction coefficients of fully ferritic Armco iron and fully martensitic FMS following Eq. (4.23). The variation of the calculated coefficient of friction with normal load has been shown by a symbol of hollow square in Figs. 34 (a) and (b).

Figures 6.34 (a) and (b) show the variation of the calculated and the observed values of the average coefficient of friction in the steady state with martensite volume fraction at the loads of 14.7 and 34.3 N, respectively. The calculated values of the coefficient of friction obtained by using Eq. (6.1) are found to be a little higher than the observed values whereas, the values of the friction coefficient obtained by using Eq. (4.23) have been found to be

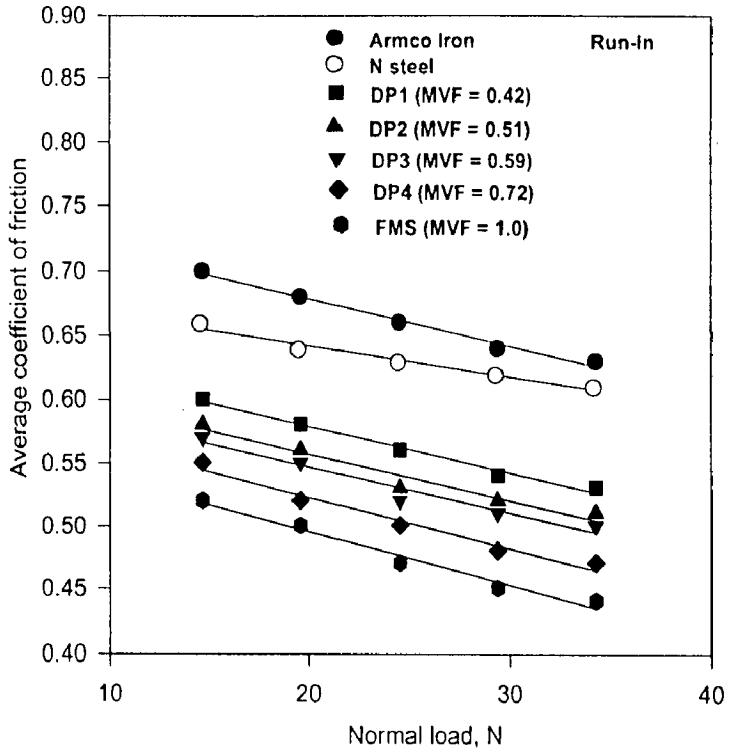

Fig. 6.32 Variation of coefficient of friction averaged over the distance of sliding during run-in stage of wear with load in Armco iron, FMS, N steel and DP steels.

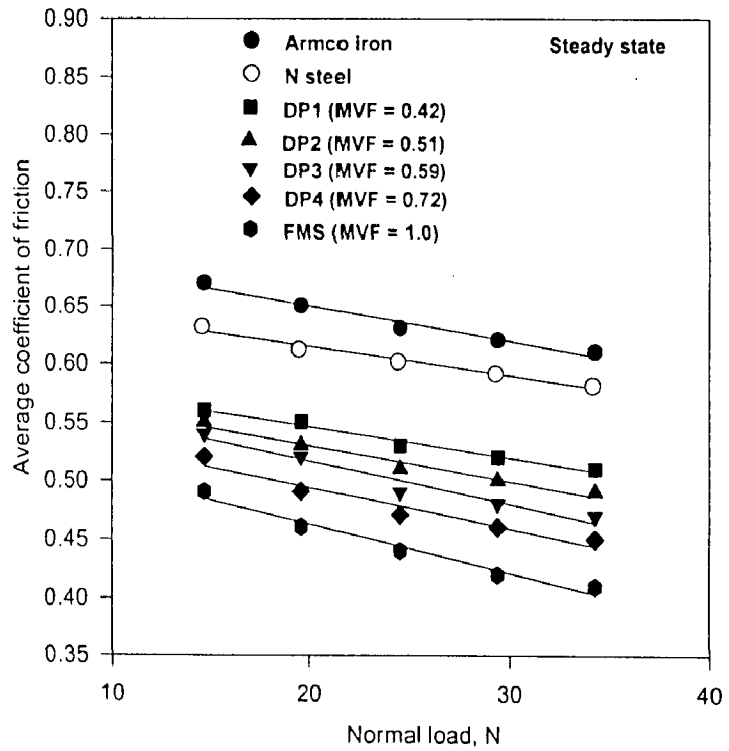

Fig. 6.33 Variation of coefficient of friction averaged over the distance of sliding during steady state of wear with load in Armco iron, FMS, N steel and DP steels.

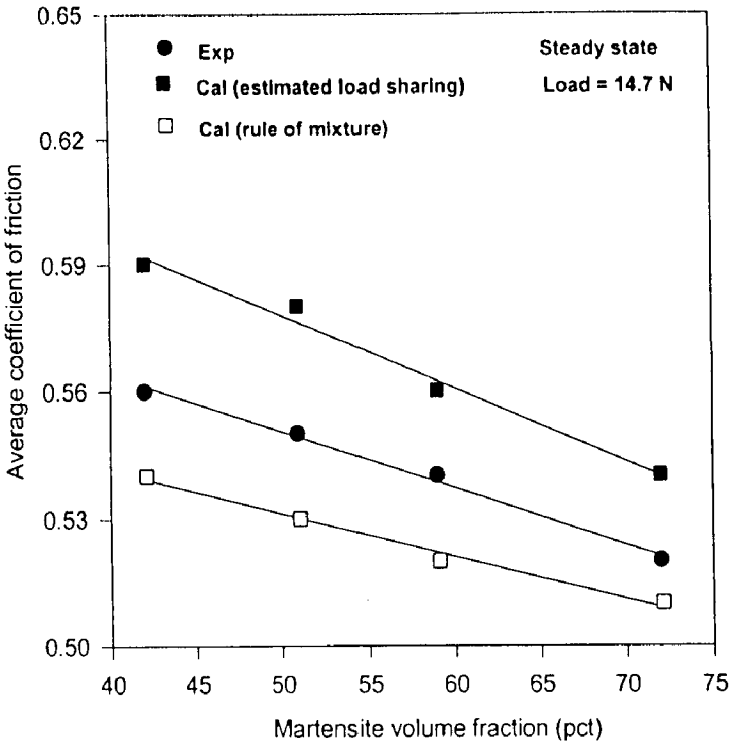

(a)

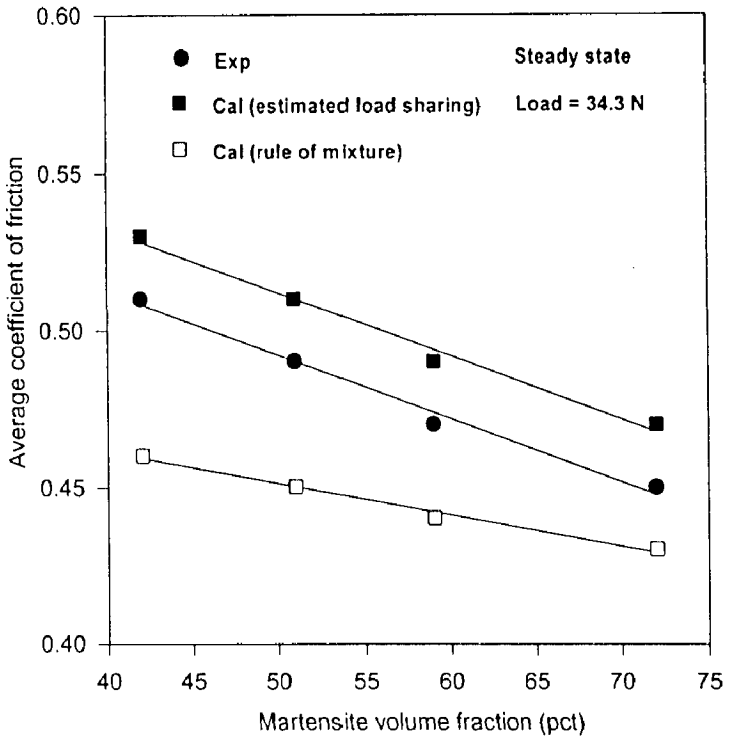

(b)

Fig. 6.34 The variation of calculated and experimental coefficient of friction with martensite volume fraction in steady state for dual phase steels, at the normal loads of (a) 14.7 N and (b) 34.3 N.

lower than the observed values at all the normal loads used in the present study. However, the average coefficient of friction, both estimated and observed decreases linearly with increasing volume fraction of martensite in dual phase steels. The difference in the calculated and the observed values of the coefficient of friction is relatively larger at the lower loads but becomes smaller at the higher loads when the volume fraction of martensite increases. It can further be observed that average coefficient of friction is lower at a higher load of 34.3 N as compared to the lower load of 14.7 N and this can be seen from a comparison of the Figs. 6.34 (a) and (b). A similar trend could be observed in coefficient of friction at the other loads of 19.6, 24.5 and 29.4 N used in the present study, but the plots are not shown here.

(iv) Variation of coefficient of friction with hardness

The variation of the average coefficient of friction in steady state with hardness, at different loads of 14.7, 19.6, 24.5, 29.4 and 34.3 N for Armco iron, N steel, DP steels with increasing volume fraction of martensite from DP1 to DP4 and FMS is shown in Fig.6.35. It is observed that for a particular load say 14.7 N the average coefficient of friction decreases almost linearly as the hardness of the materials increases. A similar trend is observed to be followed at the other loads also. It is further observed that the average coefficient of friction at a particular hardness decreases with increasing load, which is also shown in Fig. 6.35.

(v) Variation of coefficient of friction with real area of contact

Figure 6.36 (a) shows the variation of the average coefficient of friction in the steady state with theoretical real area of contact (load/initial hardness of the material) for Armco iron. It is seen that average coefficient of friction decreases linearly with a higher slope as real area of contact increases upto a value of almost 0.03 mm^2 but beyond this value it is observed to decrease with a smaller slope. The variation of the average coefficient of friction

in the steady state with theoretical real area of contact (load/initial hardness of the material) for N steel, DP steels with increasing volume fraction of martensite from DP1 to DP4 and FMS has been shown in Fig. 6.36 (b). The average coefficient of friction is found to decrease linearly with increasing real area of contact. However, the decrease in the average coefficient of friction is observed to be steep in the fully martensitic steel as compared to the other steels.

6.1.2 Examination of Sliding Surfaces

(i) Armco Iron

The Scanning Electron (SEM) micrographs of the wear surfaces of the specimens of Armco iron after sliding through a distance of 3.46 km (50 minutes) at the normal loads of 14.7, 24.5 and 34.3 N, corresponding to the first linear segment (run-in) of Fig. 6.1 are shown in Figs. 6.37 (a) to (c) respectively. The scoring marks along with a transfer layer of oxide can be seen on the surface as shown in Fig. 6.37 (a), for a normal load of 14.7 N. For a load of 24.5 N well formed scoring marks can clearly be observed from the Fig. 6.37(b). However, patches of the transfer layer of oxide partially covering the scoring marks can also be observed in some regions. For a load of 34.3 N tracks are not clearly distinguished because of the heavy protective cover provided by the transfer layer of oxide as seen from the Fig. 6.37 (c).

The SEM micrographs of the wear surfaces of the specimens of Armco iron after sliding through a distance of 39.74 km (9 hours and 35 minutes) i.e., the maximum sliding distance used, at the normal loads of 14.7, 24.5 and 34.3 N are shown in Figs. 6.38 (a) to (c), respectively. Deeper tracks in the region where the metallic surface is exposed for sliding are seen in Fig. 6.38 (b) as compared to Fig. 6.38 (a) because of the higher load of 24.5 N as

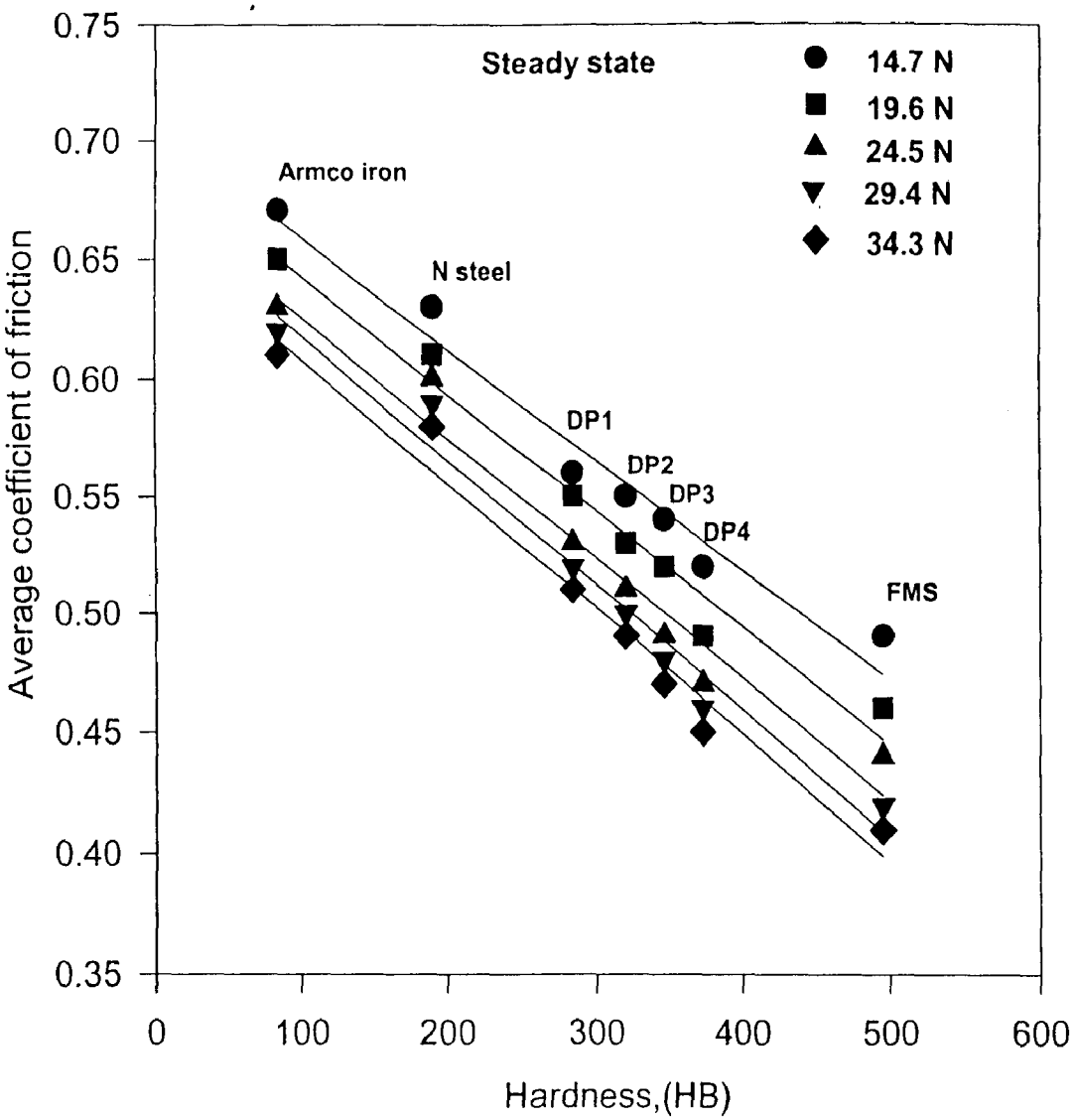

Fig. 6.35 The Variation of the average coefficient of friction in the steady state with hardness under different normal loads for Armco iron, N steel, DP steels and FMS.

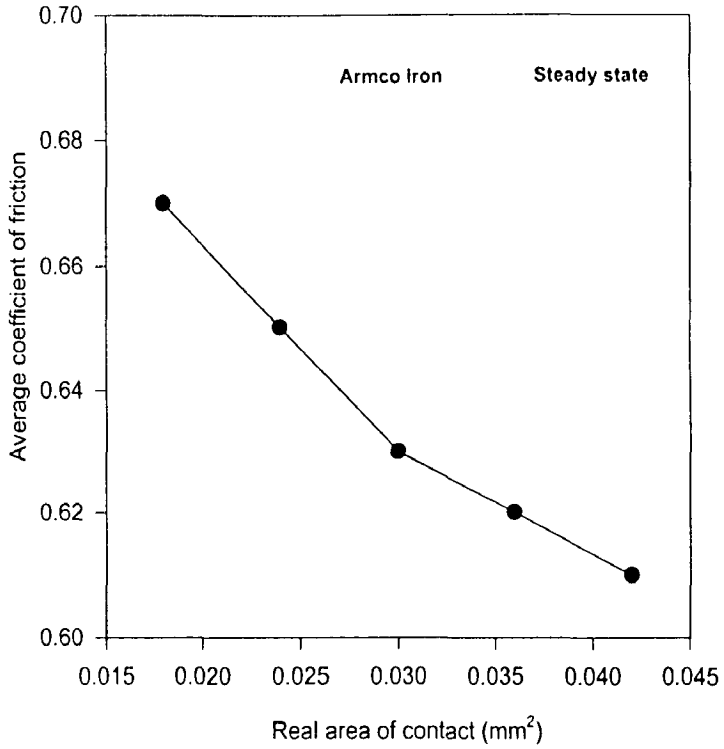

Fig. 6.36 (a) The variation of the average coefficient of friction in steady state with theoretical real area of contact for Armco iron.

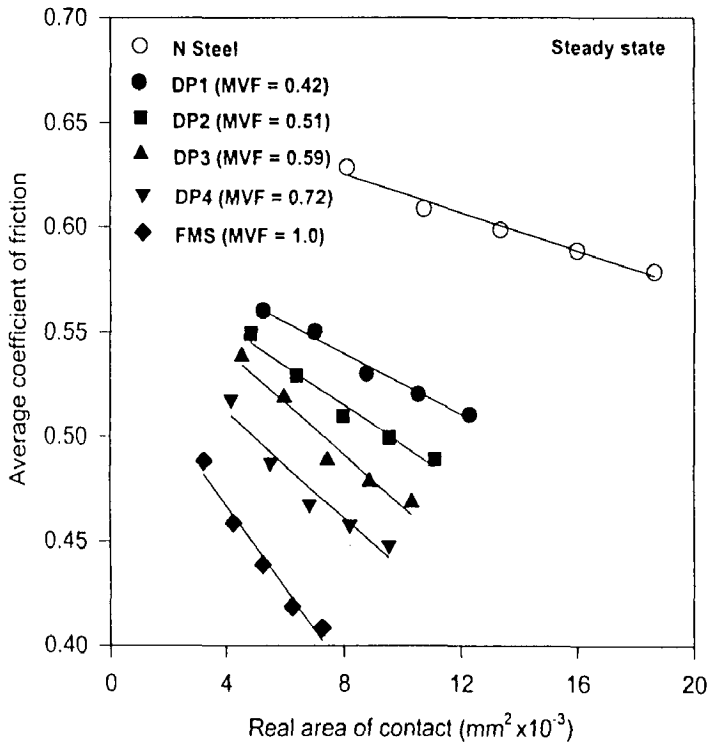

Fig. 6.36 (b) The variation of the average coefficient of friction in steady state with theoretical real area of contact for N steel, DP steels and FMS.

(a)

(b)

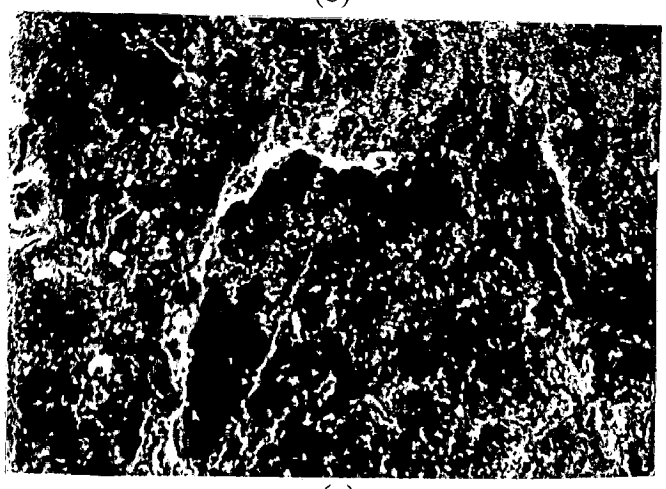

(c)

Fig. 6.37 Wear surfaces of the specimens of Armco iron after sliding through a distance of 3.46 km corresponding to the run-in stage at the normal loads of (a) 14.7 N, X 200 (b) 24.5 N, X 200 and (c) 34.3 N, X 200.

(a)

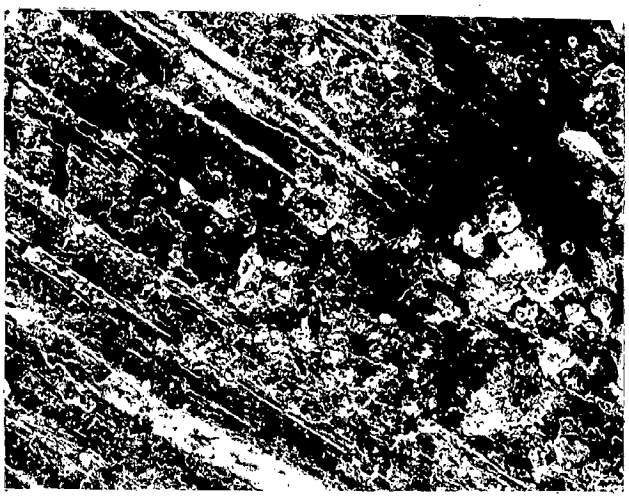

(b)

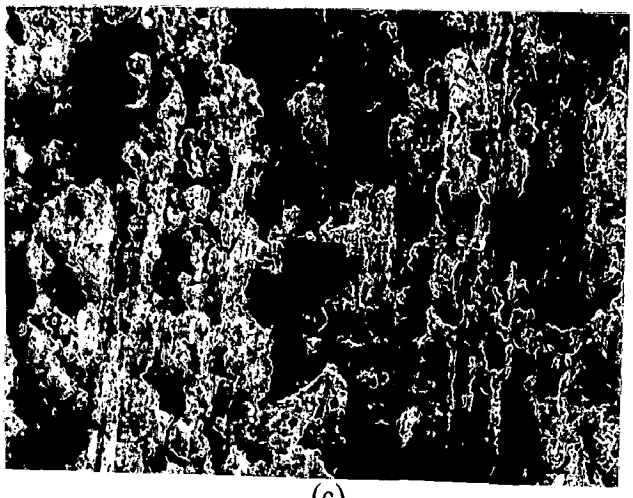

(c)

Fig. 6.38 Wear surfaces of the specimens of Armco iron after sliding through a distance of 39.74 km corresponding to the steady state at the normal loads of (a) 14.7 N, X 200 (b) 24.5 N, X 200 and (c) 34.3 N, X 200.

compared to 14.7 N in Fig. 6.38 (a). Whereas at a still higher load of 34.3 N the deeper tracks are not always visible because of the cover provided by the transfer layer of oxide as can be observed from Fig. 6.38 (c).

(ii) Fully Martensitic Steel (FMS)

The SEM micrographs of the wear surfaces of the specimens of fully martensitic steel after sliding through a distance of 3.46 km (50 minutes) at the normal loads of 14.7, 24.5 and 34.3 N, corresponding to the first linear segment (run-in) of Fig. 6.2 are shown in Figs. 6.39 (a) to (c), respectively. Deeper and wider scoring marks can be observed on the surface for a load 24.5 N compared to that observed at 14.7 N load, as shown in Figs. 6.39 (b) and (a), respectively. However, the scoring marks are not visible at a load of 34.3 N due to the protective cover provided by the highly compacted transfer layer of oxide as shown in Fig. 6.39 (c).

The SEM micrographs of the wear surfaces of the specimens of fully martensitic steel after sliding through a distance of 39.74 km (9 hours and 35 minutes) i.e., the maximum sliding distance used, at the normal loads of 14.7, 24.5 and 34.3 N are shown in Figs. 6.40 (a) to (c), respectively. It is observed that the surface is fully covered by the transfer layer of oxide and the wear tracks are not visible. The wear tracks must have formed with increasing load but these are not visible due to the cover provided by the transfer layer of oxide as seen from the Figs. 6.40 (a) to (c). The extent of cover provided by the transfer layer of oxide is observed to increase with the load as one moves from the Figs. 6.40 (a) to (c).

(iii) Normalised Steel

The SEM micrographs of the wear surfaces of the specimens of normalised (N) steel after sliding through a distance of 3.46 km (50 minutes) at the normal loads of 14.7, 24.5 and

34.3 N, corresponding to the first linear segment (run-in) of the Fig. 6.3 are shown in Figs. 6.41 (a) to (c), respectively. The scoring marks can be clearly observed in Fig. 6.41 (a) for a load of 14.7 N but these are less visible in Fig. 6.41 (b) at a normal load of 24.5 N due to the partial covering by the transfer layer of oxide. For a load of 34.3 N very few scoring marks are seen because of the heavy protective cover of oxide as shown in Fig. 6.41 (c).

The SEM micrographs of the wear surfaces of the specimens of N steel after sliding through a distance of 39.74 km (9 hours and 35 minutes) i.e., the maximum sliding distance used, under the normal loads of 14.7, 24.5 and 34.3 N are shown in Figs. 6.42 (a) to (c), respectively. The scoring marks can be clearly observed in Fig. 6.42 (a) for a load of 14.7 N but the scoring marks are not so clearly visible at a load of 24.5 N as shown in the Fig. 6.42 (b) due to the partial covering by the transfer layer of oxide. For a load of 34.3 N the very few scoring marks are seen because of the presence of the highly compacted layer of oxide as shown in Fig. 6.42 (c).

(iv) Dual Phase Steels

The SEM micrographs of the wear surfaces of the specimens of DP2 steel, containing 51 pct martensite, after sliding through a distance of 3.46 km (50 minutes) at the normal loads of 14.7, 24.5 and 34.3 N, corresponding to the first linear segment (run-in) of the Fig. 6.5 are shown in Figs. 6.43 (a) to (c), respectively. The scoring marks along with a compacted transfer layer of oxide can be observed on the surface for a load of 14.7 N as shown in Fig. 6.43 (a). But the marks are not visible at the higher loads of 24.5 and 34.3 N because of the presence of a highly compacted transfer layer of oxide as shown in Figs. 6.43 (b) and (c). The extent of cover provided by the transfer layer of oxide is observed to increase with increasing load as one moves from the Figs. 6.43 (a) to (c).

(a)

(b)

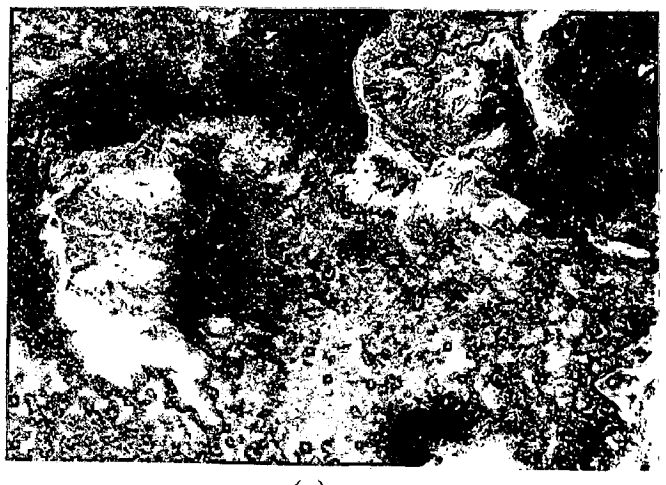

(c)

Fig. 6.39 Wear surfaces of the specimens of fully martensitic steel (FMS) after sliding through a distance of 3.46 km corresponding to the run-in stage at the normal loads of (a) 14.7 N, X 200 (b) 24.5 N, X 200 and (c) 34.3 N, X 200.

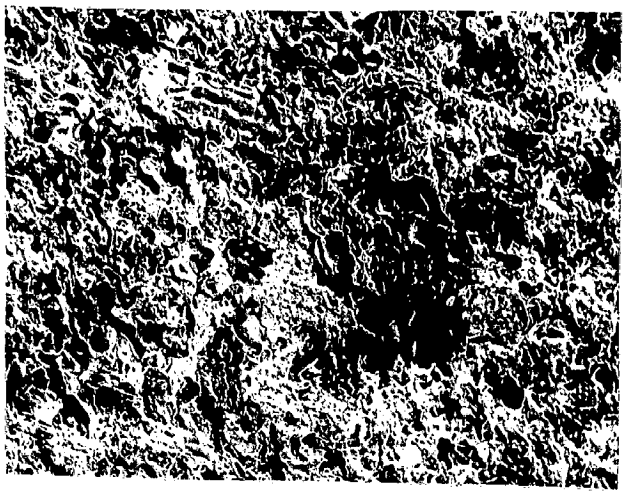

(a)

(b)

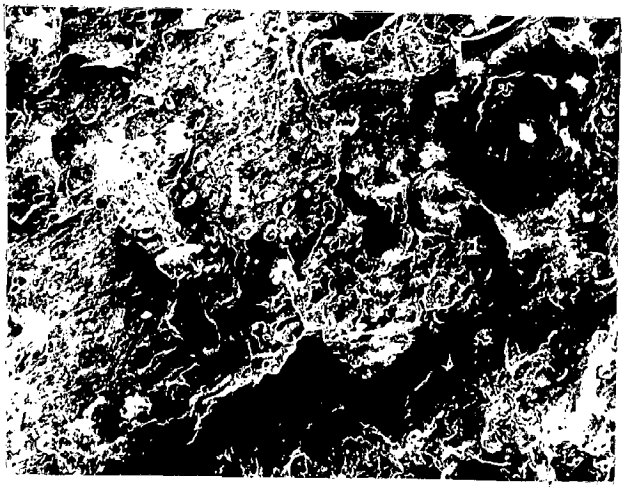

(c)

Fig. 6.40 Wear surfaces of the specimens of fully martensitic steel (FMS) after sliding through a distance of 39.74 km corresponding to the steady state at the normal loads of (a) 14.7 N, X 200 (b) 24.5 N, X 200 and (c) 34.3 N, X 200.

(a)

(b)

(c)

Fig. 6.41 Wear surfaces of the specimens of normalised (N) steel after sliding through a distance of 3.46 km corresponding to the run-in stage at the normal loads of (a) 14.7 N, X 200 (b) 24.5 N, X 200 and (c) 34.3 N, X 200.

(a)

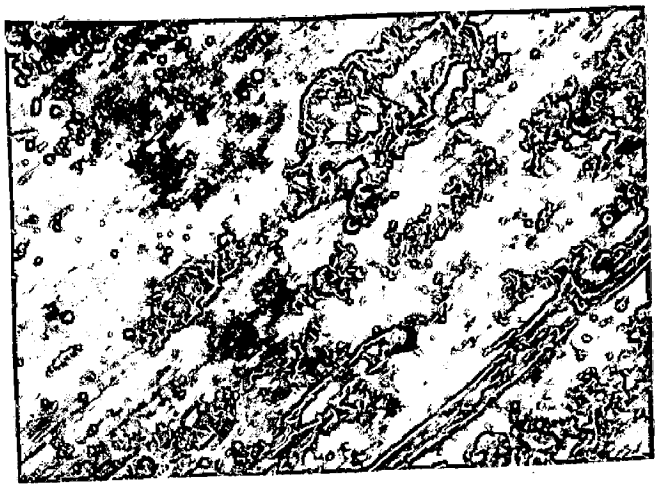

(b)

(c)

Fig. 6.42 Wear surfaces of the specimens of normalised (N) steel after sliding through a distance of 39.74 km corresponding to the steady state at the normal loads of (a) 14.7 N, X 200 (b) 24.5 N, X 200 and (c) 34.3 N, X 200.

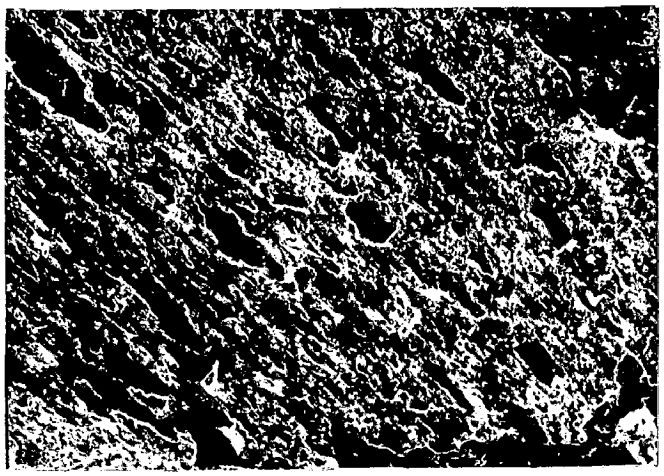

(a)

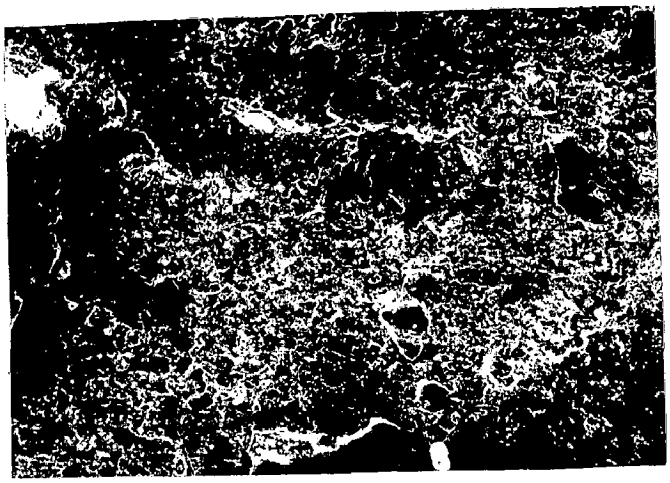

(b)

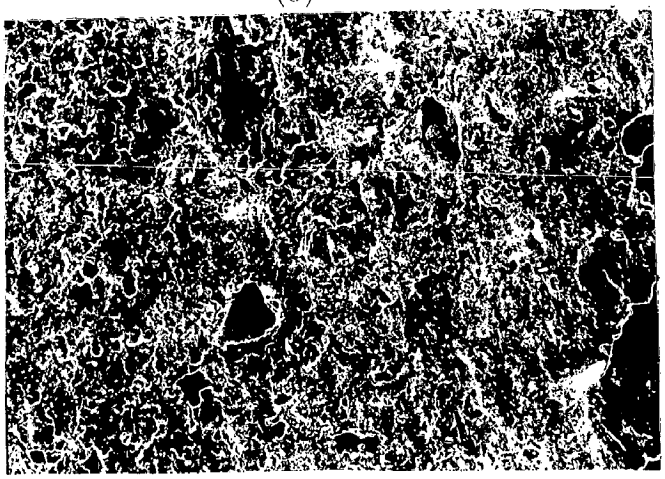

(c)

Fig. 6.43 Wear surfaces of the specimens of dual phase steel, DP2, after sliding through a distance of 3.46 km corresponding to the run-in stage at the normal loads of (a) 14.7 N, X 200 (b) 24.5 N, X 200 and (c) 34.3 N, X 200.

The SEM micrographs of the wear surfaces of the specimens of DP1, DP3 and DP4 steels after sliding through a distance of 3.46 km (50 minutes) at the normal load of 34.3 N corresponding to the first linear segment (run-in) are shown in Figs. 6.44 to 6.46, respectively. Wear tracks are observed to be present on the surface of the specimen of DP1 steel containing 42 pct martensite as shown in Fig. 6.44. The wear tracks are not seen on the surface of the specimens of the DP3 steel containing 51 pct martensite and DP4 steel containing 72 pct martensite because of the presence of a highly compacted transfer layer of oxide as shown in Figs. 6.45 and 6.46.

The SEM micrographs of the wear surfaces of the specimens of DP2 steel after sliding through a distance of 39.74 km (9 hours and 35 minutes) i.e., the maximum sliding distance used, at the normal loads of 14.7, 24.5 and 34.3 N are shown in Figs. 6.47 to 6.49 respectively. A highly compacted transfer layer of oxide is observed to be present on the sliding surface at all the loads and the extent of cover provided by the transfer layer is observed to increase with the increasing load from 14.7 to 34.3 N as shown in Figs. 6.47 (a), 6.48 (a) and 6.49 (a). The wear tracks along with transfer layer are also observed in the other regions of the surface and deeper wear tracks are observed for a load of 24.5 N as compared to those observed under a load of 14.7 N as shown in Figs. 6.48 (b) and 6.47 (b). At a higher load of 34.3 N the wear tracks are present but are covered by the transfer layer of oxide as can be seen from the Fig. 6.49 (b).

The SEM micrographs of the wear surface of the specimen of DP1 steel after sliding through a distance of 39.74 km (9 hours and 35 minutes) i.e., the maximum sliding distance used at a normal load of 34.3 N are shown in Figs. 6.50 (a) and (b). Figure 6.50 (a) shows the presence of transfer layer of compacted oxide on the surface whereas, the wear tracks along with the transfer layer can be seen in Fig. 6.50 (b).

Figures 6.51 (a) and (b) show SEM micrographs of the wear surface of the specimen of DP3 steel after sliding through a distance of 39.74 km (9 hours and 35 minutes) at a normal load of 34.3 N. Figure 6.51 (a) shows the presence of a transfer layer of compacted oxide on the surface whereas, both the wear tracks and the transfer layer of oxide can be seen in Fig. 6.51 (b).

The SEM micrographs of the wear surface of the specimen of DP4 steel after sliding through a distance of 39.74 km at a normal load of 34.3 N are shown in Figs. 6.52 (a) and (b). Figure 6.52 (a) shows the presence of transfer layer of compacted oxide on the surface whereas, the wear tracks along with the transfer layer can be seen in Fig. 6.52 (b).

It is further observed that the extent of cover provided by the transfer layer of oxide increases with increasing volume fraction of martensite in dual phase steels at a constant load of 34.3 N as seen from the micrographs shown in Figs. 6.50 (a), 6.49 (a), 6.51(a) and 6.52 (a) for the DP1, DP2, DP3 and DP4, respectively.

6.1.3 Examination of Subsurface

In this section optical micrographs of the tapered section and the SEM micrographs of the transverse section of the worn specimens (etched with 2 pct nital) of fully ferritic Armco iron, martensitic FMS, N steel and dual phase steels have been shown and described. The deformed metal layer and the cracks in the subsurface region have been marked by arrows wherever required.

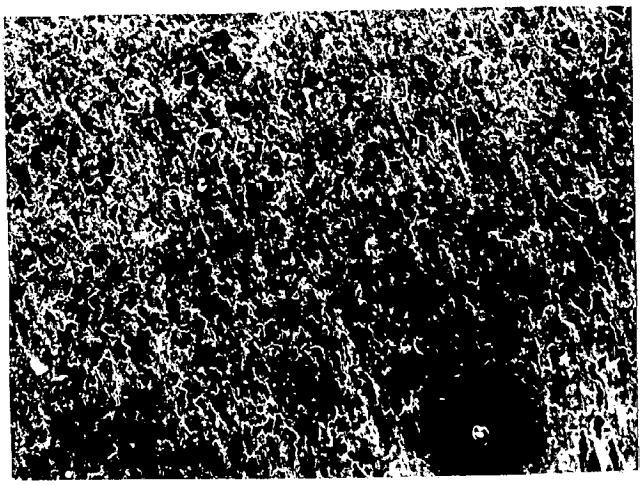

Fig. 6.44 Wear surface of the specimen of dual phase steel, DP1, after sliding through a distance of 3.46 km corresponding to the run-in stage at the normal load 34.3 N, X 200.

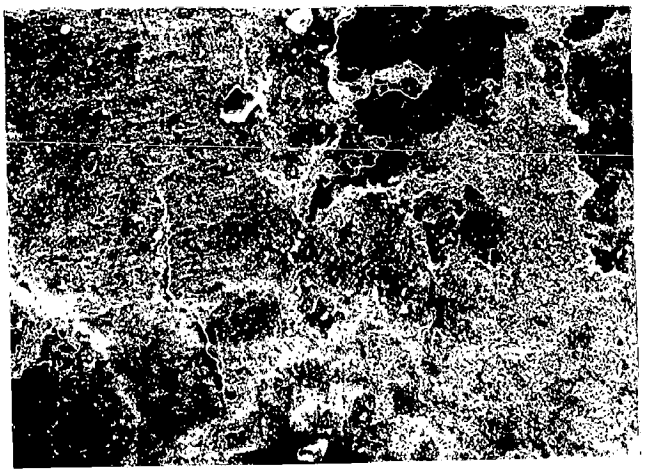

Fig. 6.45 Wear surface of the specimen of dual phase steel, DP3, after sliding through a distance of 3.46 km corresponding to the run-in stage at the normal load 34.3 N, X 200.

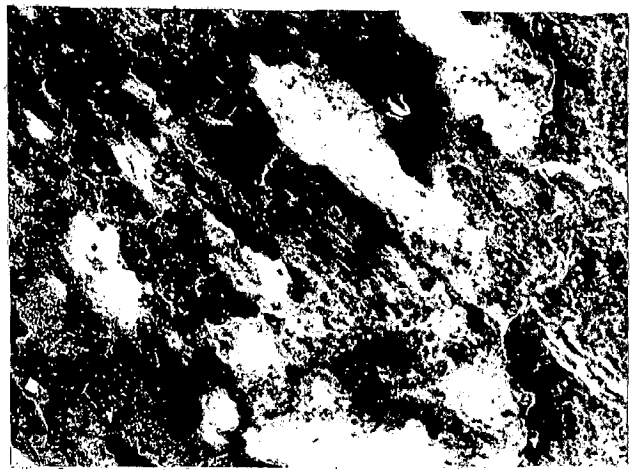

Fig. 6.46 Wear surface of the specimen of dual phase steel, DP4, after sliding through a distance of 3.46 km corresponding to the run-in stage at the normal load 34.3 N, X 200.

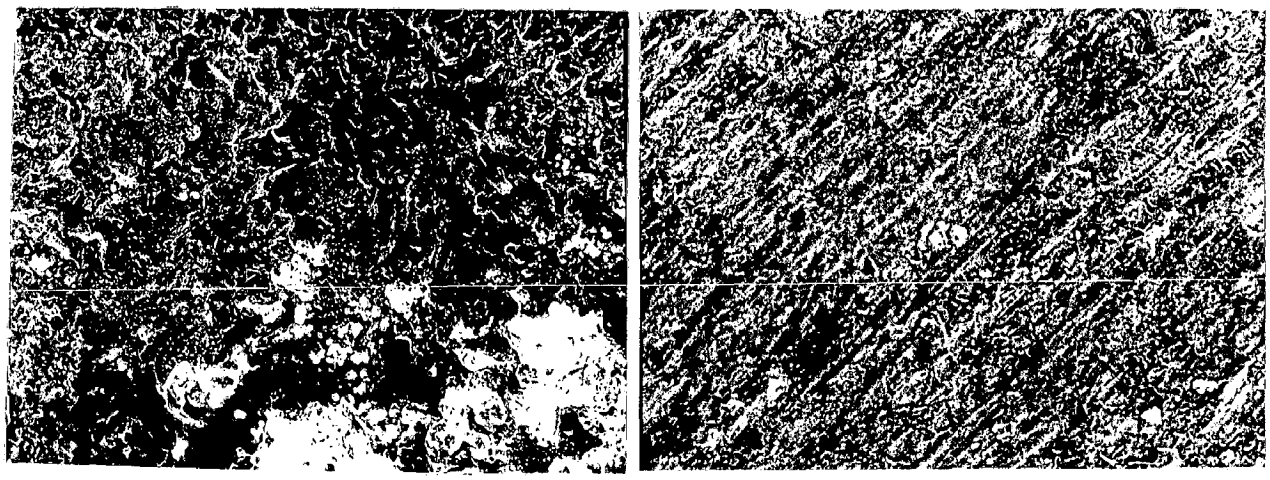

(a) (b)

Fig. 6.47 Wear surface of the specimen of dual phase steel, DP2, after sliding through a distance of 39.74 km corresponding to the steady state at a normal load 14.7 N, (a) X 200 and (b) X 200.

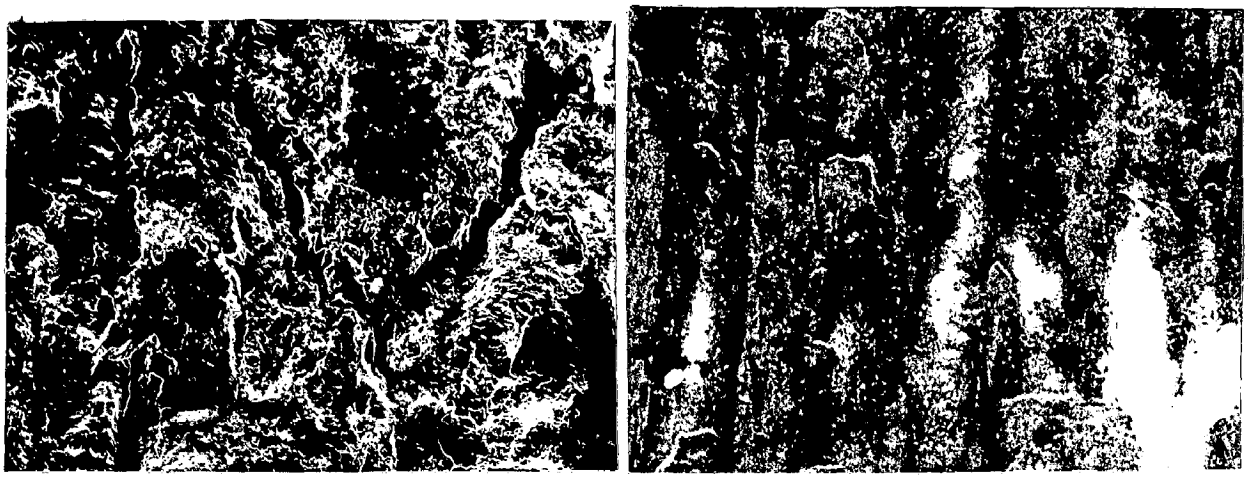

(a) (b)

Fig. 6.48 Wear surface of the specimen of dual phase steel, DP2, after sliding through a distance of 39.74 km corresponding to the steady state at a normal load 24.5 N, (a) X 200 and (b) X 200.

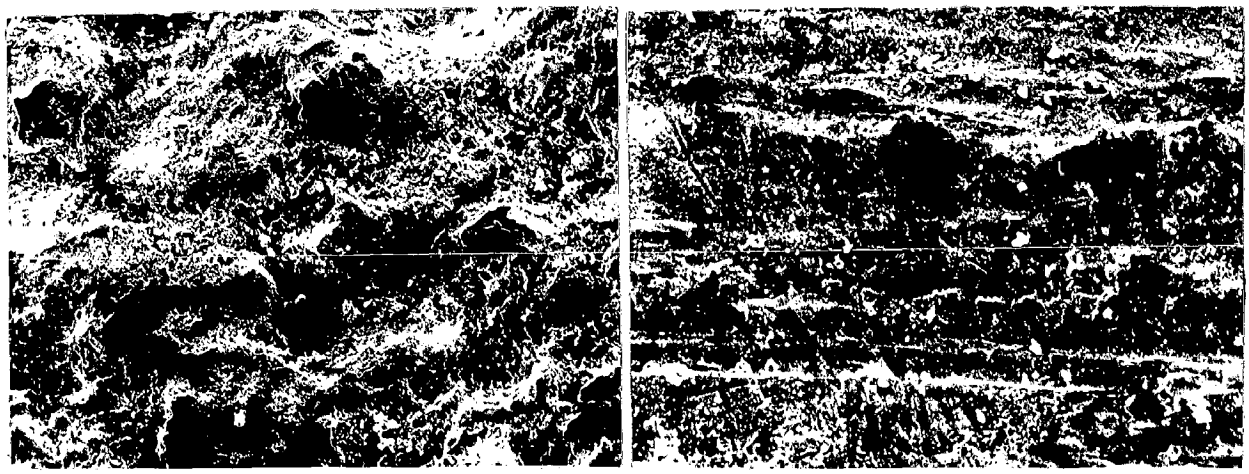

(a) (b)

Fig. 6.49 Wear surface of the specimen of dual phase steel, DP2, after sliding through a distance of 39.74 km corresponding to the steady state at a normal load 34.3 N, (a) X 200 and (b) X 200.

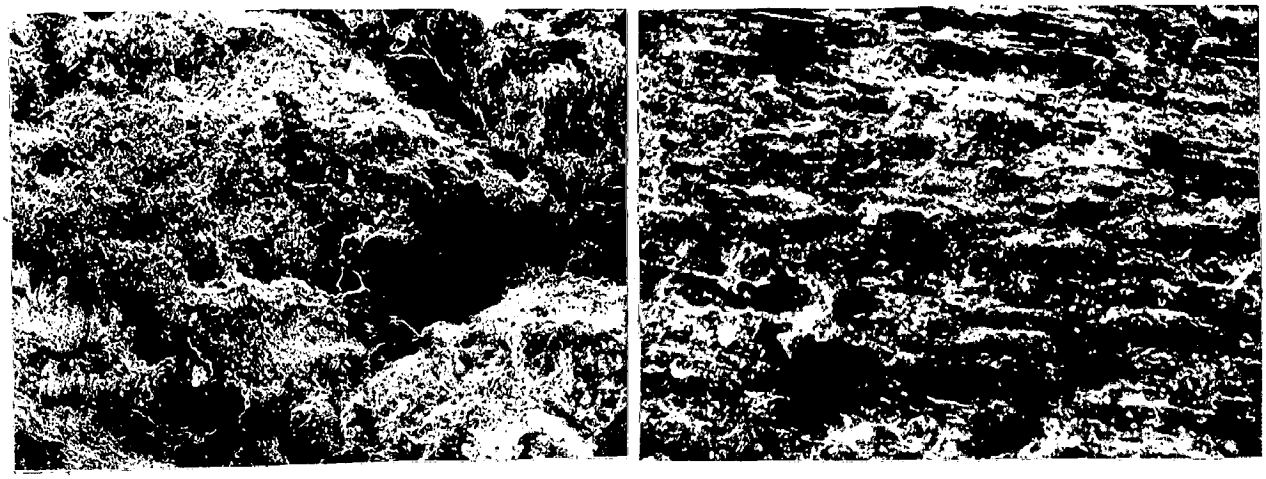

(a) (b)

Fig. 6.50 Wear surface of the specimen of dual phase steel, DP1, after sliding through a distance of 39.74 km corresponding to the steady state at a normal load 34.3 N, (a) X 200 and (b) X 200.

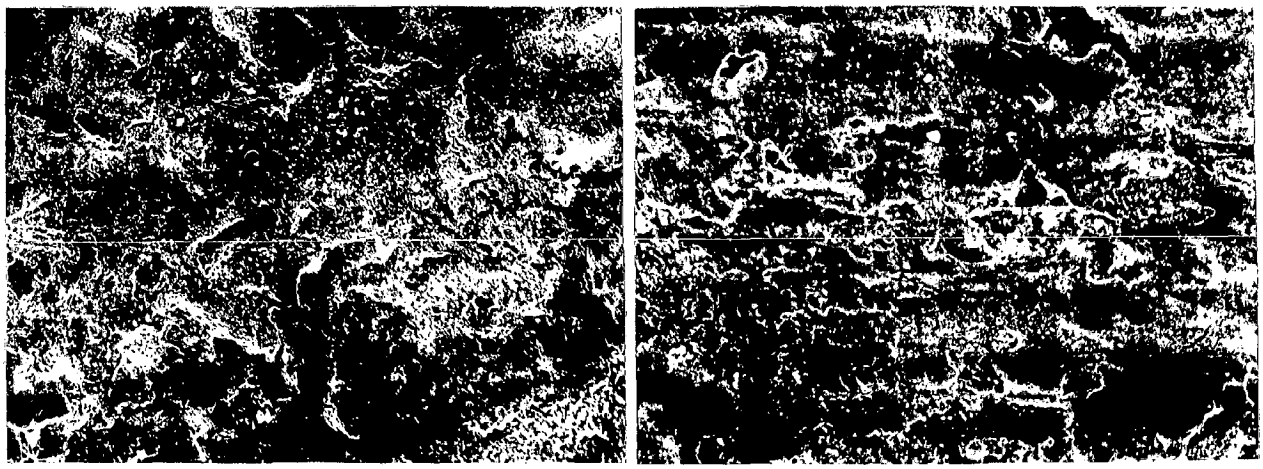

(a) (b)

Fig. 6.51 Wear surface of the specimen of dual phase steel, DP3, after sliding through a distance of 39.74 km corresponding to the steady state at a normal load 34.3 N, (a) X 200 and (b) X 200.

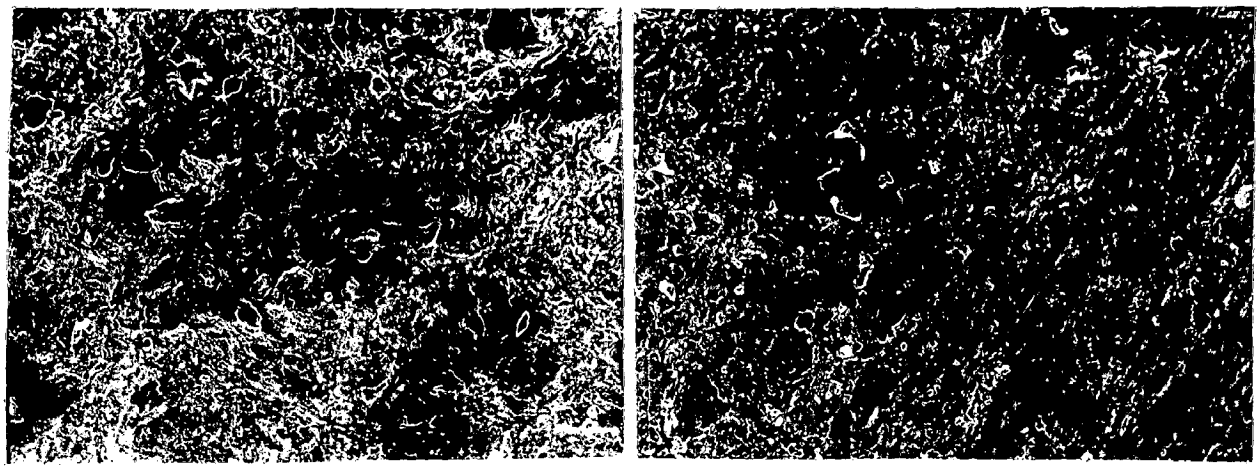

(a) (b)

Fig. 6.52 Wear surface of the specimen of dual phase steel, DP4, after sliding through a distance of 39.74 km corresponding to the steady state at a normal load 34.3 N, (a) X 200 and (b) X 200.

(i) Armco Iron

The optical micrographs of the subsurface of the specimen of Armco iron after sliding through a distance of 39.74 km under the normal loads of 14.7, 24.5 and 34.3 N and at a fixed sliding velocity of 1.15 m/s are shown in the Figs. 6.53 (a) to (c). The flow of the deformed material is clearly visible in the subsurface region as shown by arrows in respective micrographs. It observed that extent deformed layer increases with increasing load from 14.7 to 34.3 N as evident from Figs. 6.53 (a) to (c).

The SEM micrograph of the subsurface of the specimen of Armco iron after sliding through a distance of 39.74 km under a normal load of 24.5 N is also shown in Fig. 6.54. The cracks generated at the subsurface can be seen in the micrograph and are marked by arrows.

(ii) Fully Martensitic Steel (FMS)

Subsurface microstructures of the fully martensitic steel after sliding through a distance of 39.74 km under the normal loads of 14.7, 24.5 and 34.3 N and at a fixed sliding velocity of 1.15 m/s are shown in Figs. 6.55 to 6.57.

Figure 6.55 shows the SEM micrograph of the fully martensitic steel after sliding through a distance of 39.74 km under a normal load of 14.7 N. In this micrograph flow of the metal can easily be distinguished in the subsurface region as compared to the region which is below the subsurface.

Figures 6.56 (a) and (b) show the optical micrographs of the tapered section of the specimens of FMS after sliding through a distance of 39.74 km under the normal loads of

24.5 and 34.3 N, respectively. Deformed layer of the material is clearly visible in the subsurface region as marked by the arrows.

The SEM micrograph of the specimen of fully martensitic steel after sliding through a distance of 39.74 km under a load of 34.3 N is shown in the Fig. 6.57. A well deformed region in the subsurface can easily be distinguished as it etches darker compared to the region which has no effect of work hardening. The subsurface cracks are also visible in Fig. 6.57, marked by arrow.

(iii) Normalised Steel

Figure 6.58 (a) shows the optical micrograph of the tapered section of the specimen of normalised (N) steel after sliding through a distance of 39.74 km under a normal load of 14.7 N. It can be seen that there is a change in the microstructure in the subsurface region and the flow lines of the deformed material are clearly visible. Similar effect is observed for the specimen worn at a normal load of 24.5 N as can be seen from the optical micrograph shown in Fig. 6.58 (b).

Figure 6.59 shows the SEM micrograph of the transverse section of the specimen of N steel after sliding through a distance of 39.74 km under a load of 34.3 N. A well deformed subsurface layer is clearly seen here which can be judged by a change in the microstructure in deformed layer. The subsurface cracks generated due to sliding are also visible and are shown by the arrow in the micrograph.

(a)

(b)

(c)

Fig. 6.53 Optical micrographs showing subsurface microstructure of Armco iron after sliding through a distance of 39.74 km at the normal loads of (a) 14.7 N, X 200, (b) 24.5 N, X 200 and (c) 34.3 N, X 200. Arrow indicates the deformed layer of material.

Fig. 6.54 SEM micrograph of the subsurface of the specimen of Armco iron after sliding through a distance of 39.74 km under a load of 24.5 N, X 1560, showing cracking below the subsurface (marked by arrow).

Fig. 6.55 SEM micrograph of the subsurface of the specimen of fully martensitic steel after sliding through a distance of 39.74 km under a load of 14.7 N, X 1810.

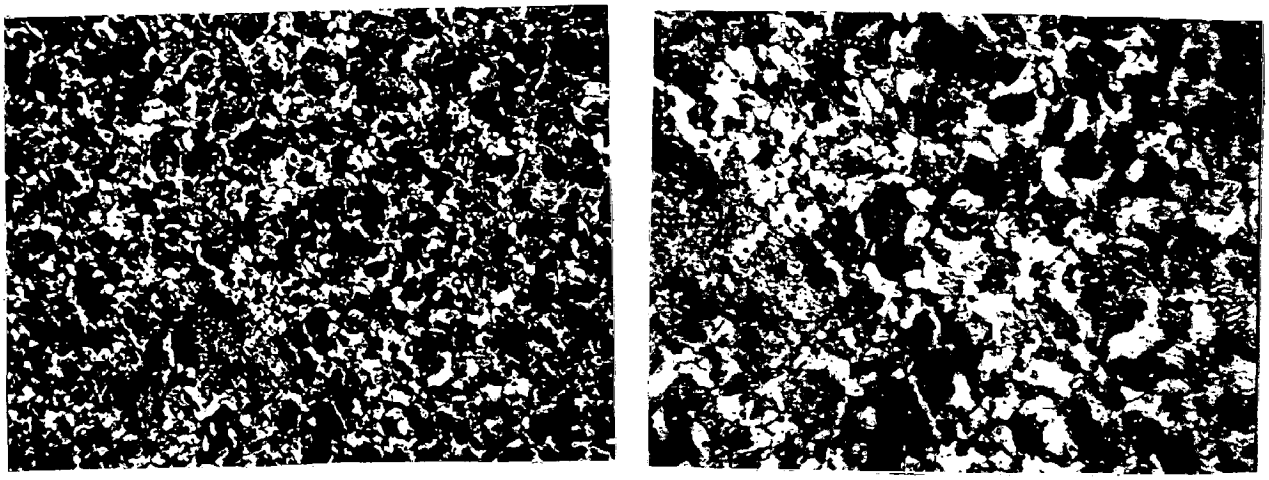

(a) (b)

Fig. 5.4 Optical micrograph of dual phase steel, DP1, showing dark regions of martensite and bright regions of ferrite, (etchant 2 pct nital) (a) X 390 and (b) X 780.

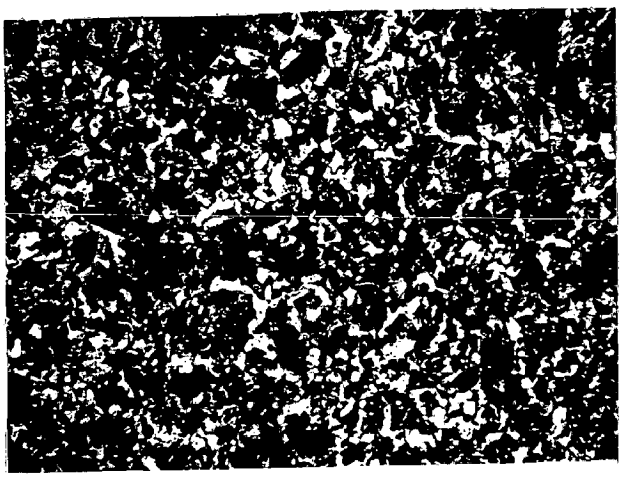

Fig. 5.5 Optical micrograph of dual phase steel, DP2, showing dark regions of martensite and bright regions of ferrite, (etchant 2 pct nital), X 390.

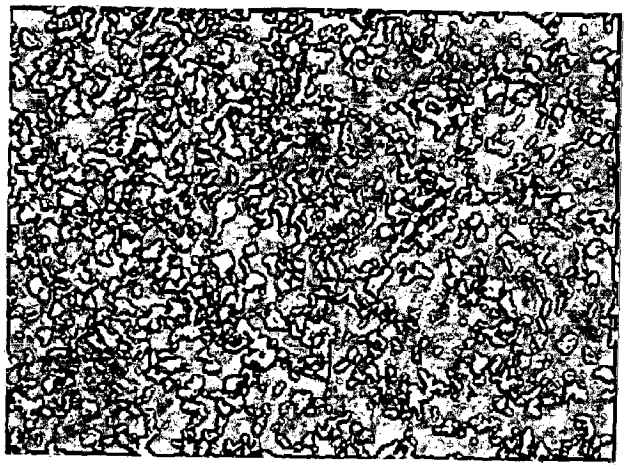

Fig. 5.6 Optical micrograph of dual phase steel, DP3, showing dark regions of martensite and bright regions of ferrite, (etchant 2 pct nital), X 390.

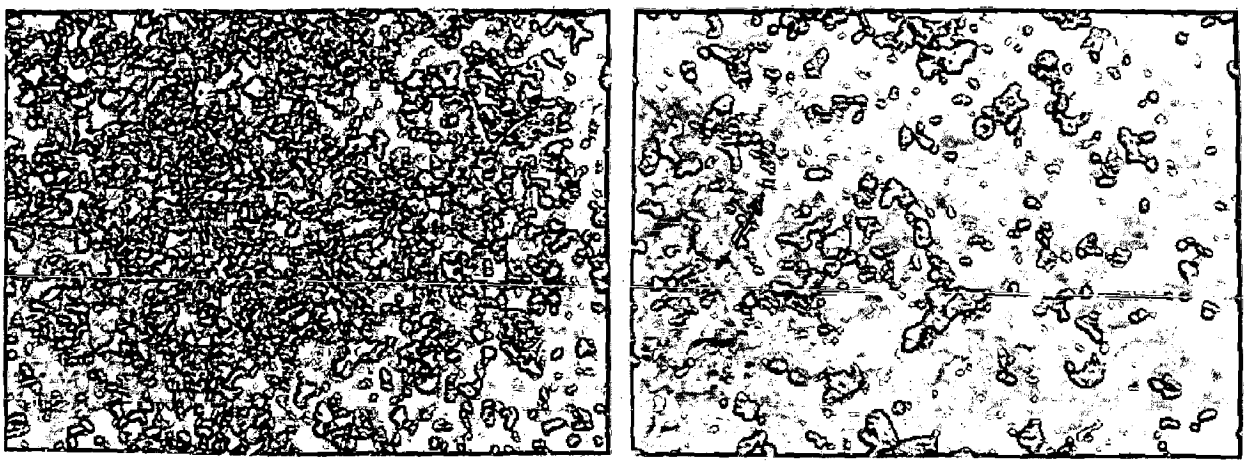

(a) (b)

Fig. 5.7 Optical micrograph of dual phase steel, DP4, showing dark regions of martensite and bright regions of ferrite, (etchant 2 pct nital) (a) X 390 and (b) X 780.

Figures 5.7 (a) and (b) show the optical micrographs at lower and higher magnification respectively, of dual phase steel developed at 740^0C for 3.5 minutes of intercritical annealing followed by water quenching (designated as DP4). Here also, the structure has dark etching martensite islands in the bright regions of ferrite. There could be small amount of retained austensite associated with martensite and it is not visible in the micrograph. At higher magnification, martensite needles in the dark areas could be resolved as indicated by arrow in Fig. 5.7 (b). The volume fraction of martensite is approximately 72 pct.

Figure 5.8 shows the optical micrograph of dual phase steel developed from the low carbon normalised steel at 740^0C for 5 minutes of intercritical annealing followed by water quenching (designated as DP). The microstructure has dark areas of martensite in bright regions of ferrite. The volume fraction of martensite in DP steel is approximately 8 pct.

(d) Fully Martensitic Steel

The optical micrograph of the pure martensite developed from the same medium carbon normalised steel used for developing dual phase steels, is shown in Fig. 5.9. The steel has been austenitized at 910^0C for 20 minutes followed by water quenching. Martensite is visible as small needles in the microstructure and retained austenite associated with martensite appears white.

5.1.3 Evolution of Microstructure and Intercritical Annealing

The variation of martensite volume fraction as determined by quantitative metallography from the micrographs has been plotted with intercritical annealing (ICA) time in Fig. 5.10. It is observed that as the intercritical annealing time increases at a constant temperature of 740^0C, martensite (austensite transformed on water quenching) volume

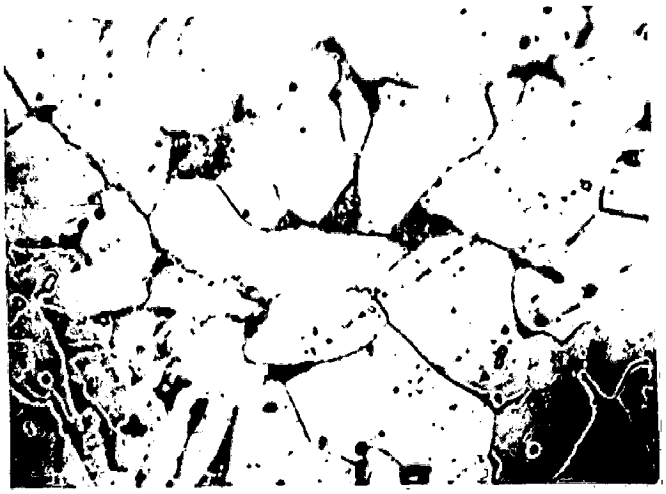

Fig. 5.8 Optical micrograph of dual phase steel, DP, showing dark regions of martensite and bright regions of ferrite, (etchant 2 pct nital), X 200.

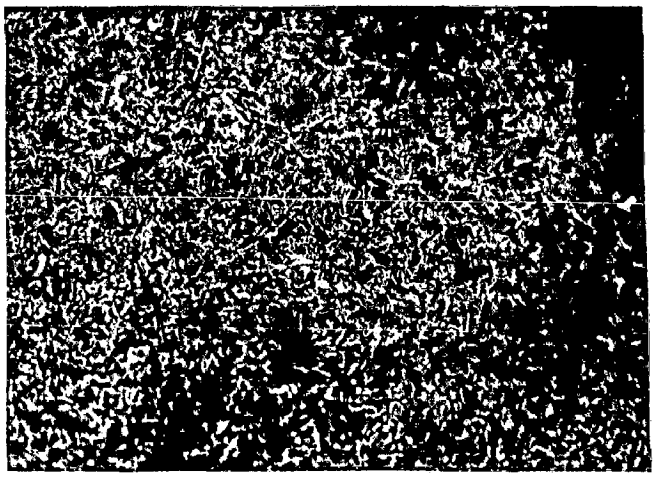

Fig. 5.9 Optical micrograph of fully martensitic steel (FMS) showing needles of martensite, (etchant 2 pct nital), X 400.

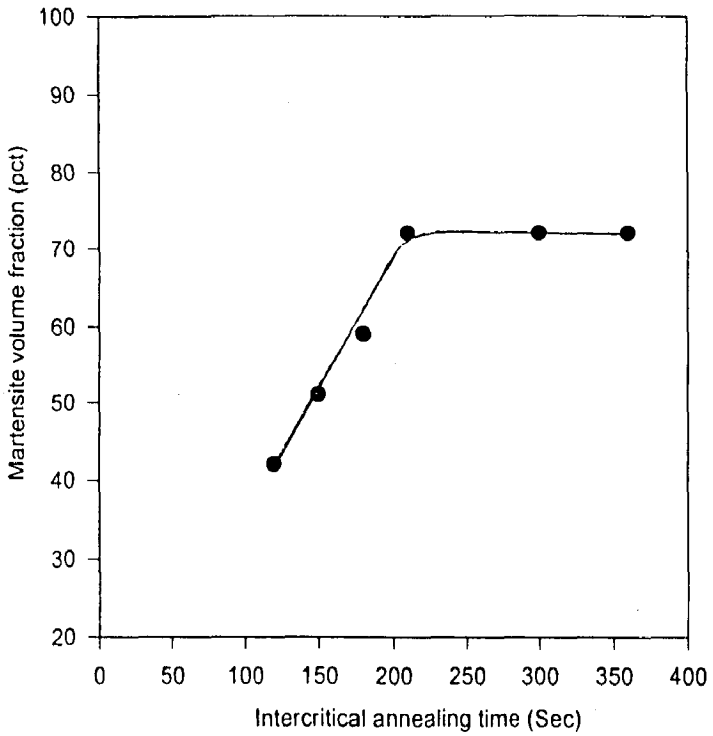

Fig. 5.10 Variation of martensite volume fraction in dual phase steels with intercritical annealing (ICA) time.

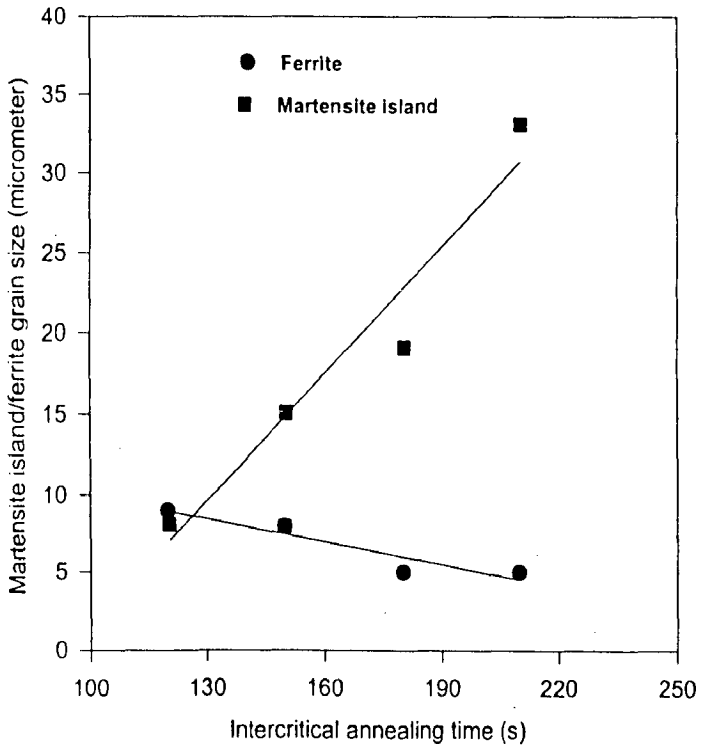

Fig. 5.11 Variation of average martensite island/ferrite grain size with intercritical annealing time in dual phase steels.

fraction increases before it saturates at long annealing times. It has been observed that martensite volume fraction increases from 42 pct (2.0 min. ICA time) to 72 pct (3.5 min. ICA time). It is further observed that increasing the intercritical annealing time beyond 3.5 minutes does not increase the martensite volume fraction significantly.

The volume fractions of the martensite obtained in the dual phase steels after different holding times, the size of martensite islands and the grain size of the ferrite phase in the steels have been given in Table A.1 in the appendix. The variation of the average size of martensite islands and ferrite grains with intercritical annealing time is shown in Fig. 5.11. The martensite island size increases linearly whereas the ferrite grain size decreases linearly with intercritical annealing time.

5.1.4 Mechanical Properties

The measured values of the macrohardness, microhardness, yield strength, tensile strength, ductility (expressed in terms of percentage elongation and percentage reduction in the area of cross section) and strain hardening index are reported in this subsection. The variation of the mechanical properties of Armco iron, dual phase steels and FMS with volume fraction of martensite is also described in this subsection.

(a) Hardness

The macrohardness has been measured and expressed in terms of the Brinell number for Armco iron, N steel, DP steels FMS as reported in Table A.2 given in the appendix. The hardness of Armco iron has been found to be 84 HB, whereas it is observed to be 190 HB for the normalised steel. The hardness of dual phase steels with increasing volume fraction of

martensite - DP1, DP2, DP3 and DP4 are 284, 320, 343 and 373 HB, respectively. The macrohardness of the fully martensitic steel (FMS) is found to be 495 HB.

The variation of the macrohardness with martensite volume fraction (expressed in percent) in Armco iron, dual phase steels and FMS is shown in Fig. 5.12. The hardness has been observed to vary linearly from 284 HB for DP1 steel to 495 HB for FMS. When this line is extrapolated to zero martensite the hardness there is slightly above that of Armco iron. This could be due to very low carbon content of this material.

The microhardness of the phases present in the normalised and the dual phase steels have also been measured and expressed in terms of Vickers hardness. These are given in Table A.3 in the appendix. The variation of the microhardness of martensite/ferrite with intercritical annealing time is shown in Fig. 5.13. It is observed that the microhardness of martensite decreases linearly whereas the microhardness of ferrite increases linearly with increasing intercritical annealing time.

The macrohardness of the low carbon normalised (LCN) steel is 136 HV and that of the DP steel is 215 HV. The Microhardnesses of the phases present in LCN and DP steel are given in Table A.4 in the appendix.

(b) Yield Strength and Tensile Strength

The engineering stress-strain curves of Armco iron, N steel, are shown in Figs. 5.14 (a) and (b). A discontinuous type of stress strain curve is observed for Armco iron and N steel, as there is a yield point phenomenon in the corresponding curves. Figures 5.14 (c) to (f) show the stress-strain curves of the DP steels with increasing volume fraction of martensite from DP1 to DP4. It is observed that all the DP steels show a continuous type of yielding

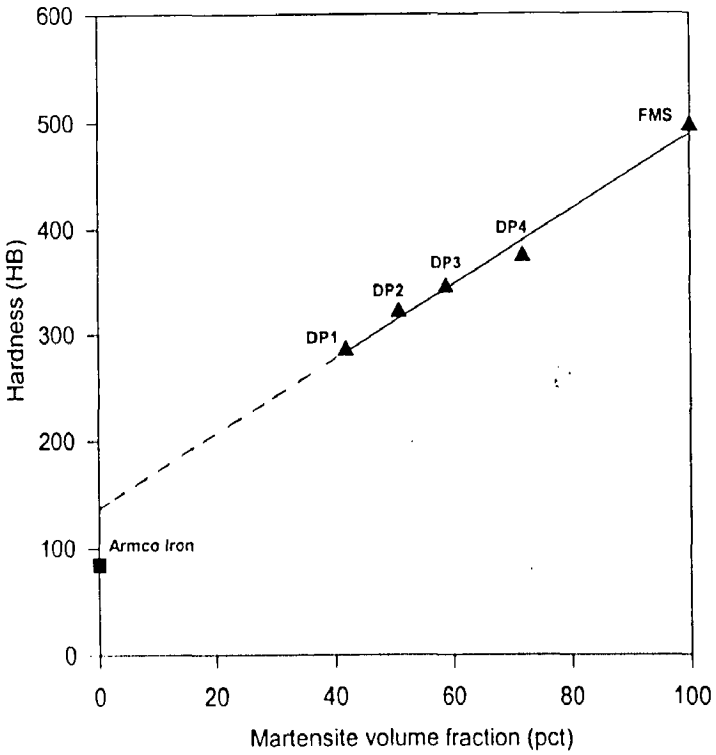

Fig. 5.12 Variation of hardness with martensite volume fraction in dual phase steels.

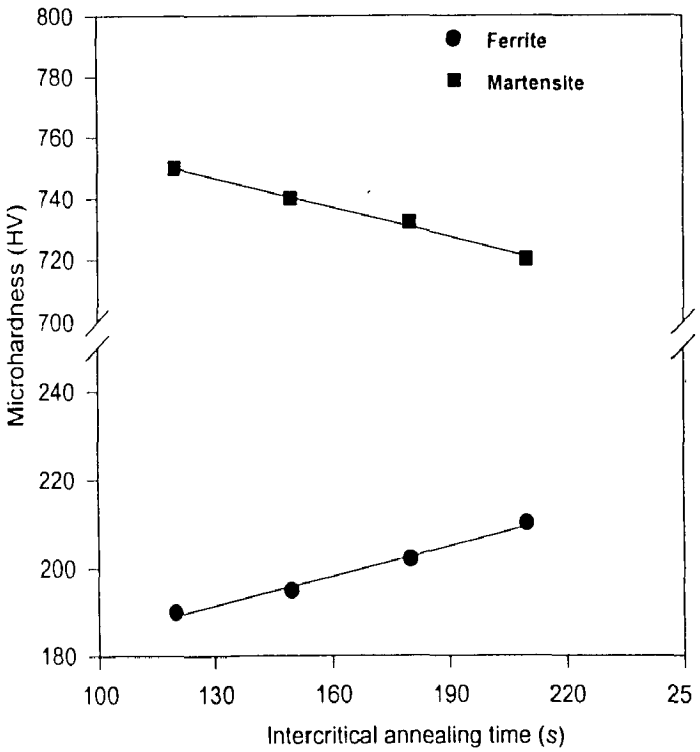

Fig. 5.13 Variation of microhardness of martensite/ferrite with intercritical annealing time in dual phase steels.

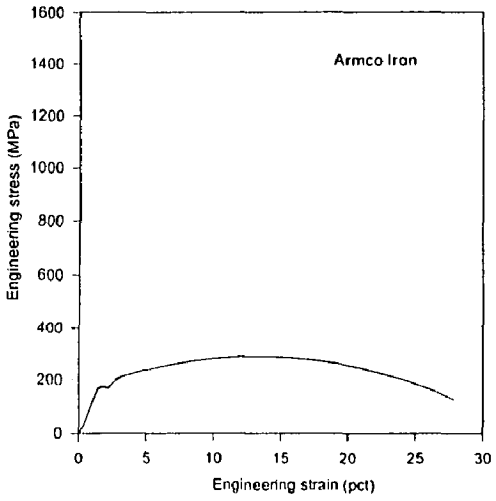
Armco Iron
Engineering stress (MPa)
Engineering strain (pct)
0
200
400
600
800
1000
1200
1400
1600
0
5
10
15
20
25
30

(a)

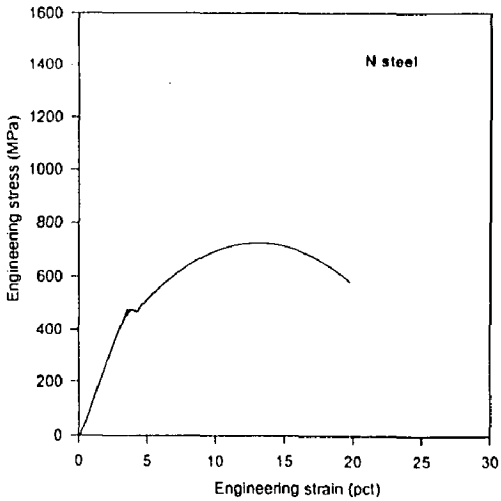
N steel
Engineering stress (MPa)
Engineering strain (pct)
0
200
400
600
800
1000
1200
1400
1600
0
5
10
15
20
25
30

(b)

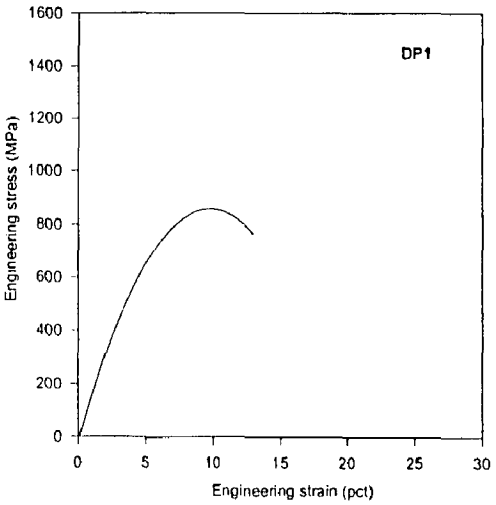
DP1
Engineering stress (MPa)
Engineering strain (pct)
0
200
400
600
800
1000
1200
1400
1600
0
5
10
15
20
25
30

(c)

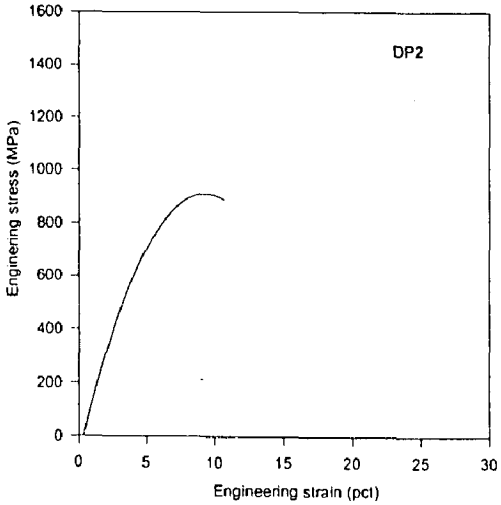
DP2
Enginering stress (MPa)
Engineering strain (pct)
0
200
400
600
800
1000
1200
1400
1600
0
5
10
15
20
25
30

(d)

Contd.

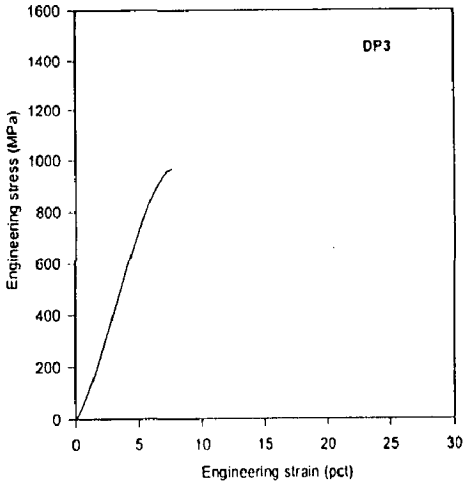

(c)

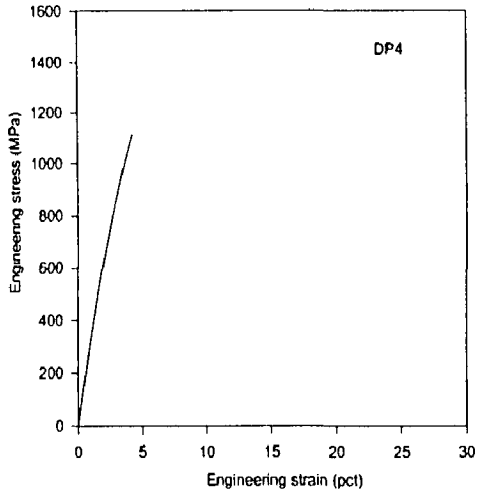

(f)

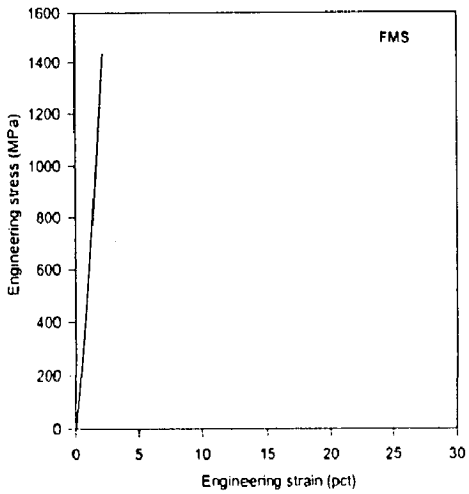

(g)

Fig. 5.14 The engineering stress-strain curve for (a) Armco iron, (b) N steel, (c) DP1, (d) DP2, (e) DP3, (f) DP4 and (g) FMS.

which can be judged from the absence of the yield point in the curves shown in Figs. 5.14 (c) to (f). The stress-strain curve of fully martensitic steel (FMS) as shown in Fig. 5.14 (g) is same as that of a brittle material. The yield stress, UTS and fracture stress is the same.

The yield and tensile stresses for Armco iron and medium carbon steels are reported in the Table A.2 given in the appendix. The variation of yield strength (YS) and ultimate tensile strength (UTS) with martensite volume fraction (expressed in percent) is shown in Fig. 5.15. The yield and tensile strength has been found to increase linearly with increasing martensite volume fraction from 42 to 72 vol pct in dual phase steels. The gap between the YS and UTS decreases as the volume fraction of martensite increases from 42 to 72 vol pct at which point the values of YS and UTS coincide.

(c) Ductility

Ductility has been expressed in terms of the percentage elongation and percentage reduction in the area of cross section. The percentage elongation has been calculated by measuring the elongation in gauge length from the broken tensile test specimens. The percentage elongation for Armco iron is found to be the highest having a value of 28 pct whereas, it is found to be the lowest for the FMS with a value of only 3 pct. The variation of percentage elongation of the dual phase steels with martensite volume fraction (expressed in percent) is shown in Fig. 5.16. It can be inferred from the curve that percentage elongation decreases linearly from 13 to 4 pct as the volume fraction of martensite increases from 42 to 72 vol pct in dual phase steels. When extrapolated to zero martensite the percentage elongation there is same as that of Armco iron but extrapolation to 100 pct martensite shows a negative value of the percentage elongation there.

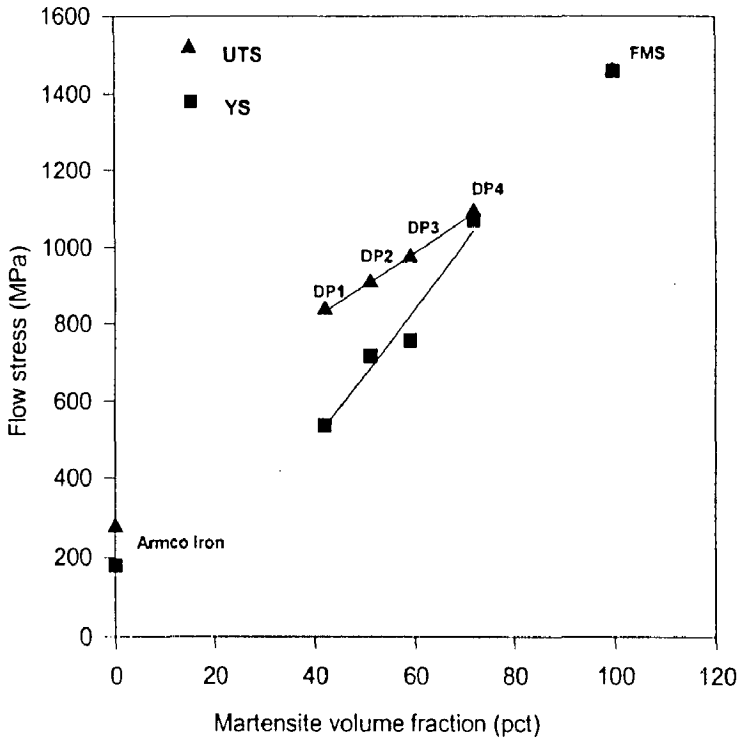

Fig. 5.15 Variation of flow stress with martensite volume fraction in dual phase steels.

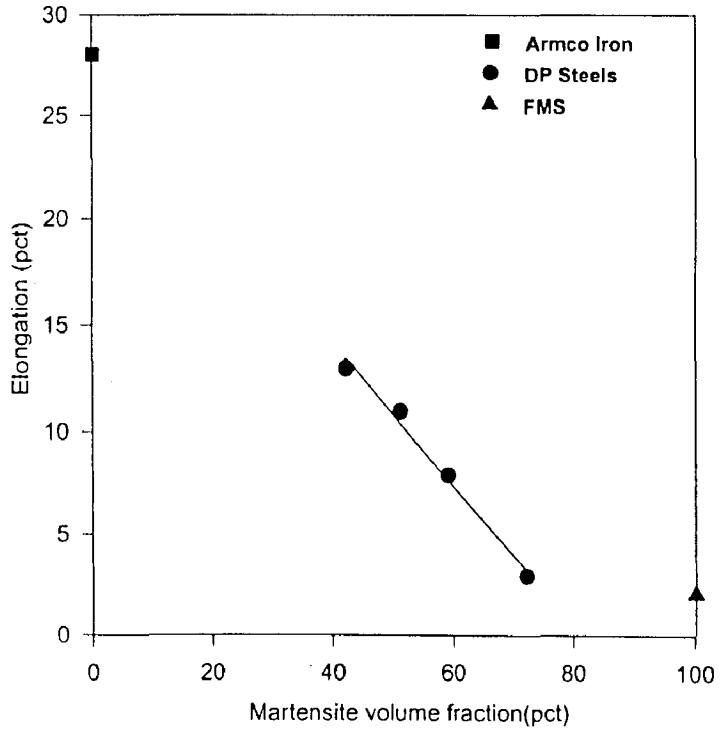

Fig. 5.16 Variation of percentage elongation (ductility) with martensite volume fraction in dual phase steels.

The variation of percentage reduction in the area of cross section with martensite volume fraction is shown in Fig. 5. 17. It is observed that the area reduction decreases linearly from 22 to 5 pct as the volume fraction of martensite increases from 42 to 72 pct in dual phase steels. When extrapolated to zero martensite, there the value of the percentage reduction in area is much lower than that for the Armco iron.

(d) Strain Hardening Index (*n*)

The strain hardening index has been estimated from the true uniform strain for the materials investigated in the present study. The true strain has been obtained from the engineering strain measured from the stress-strain curves. The strain hardening index for fully ferritic Armco iron, normalised steel, fully martensitic steel (FMS) and dual phase steels is reported in the Table A.2 in the appendix. Figure 5.18 shows the variation of strain hardening index with the martensite volume fraction. It is observed that the strain hardening index decreases linearly with increasing volume fraction of martensite from fully ferritic Armco iron to fully martensitic (FMS) containing 100 pct martensite.

5.1.5 Variation of the Area under Stress-Strain curve with Martensite Volume Fraction

The energy absorbed by the material per unit volume before fracture is given by the area under stress-strain curve. The variation of the area under stress-strain curve with martensite volume fraction for Armco iron, DP steels and FMS is shown in Fig. 5.19. For the normalised steel the area is the highest, about twice that of Armco iron. The area under the stress-strain curve is found to be the highest for the normalised steel and the lowest for the fully martensitic steel. The area under stress-strain curve initially increases in DP steel as

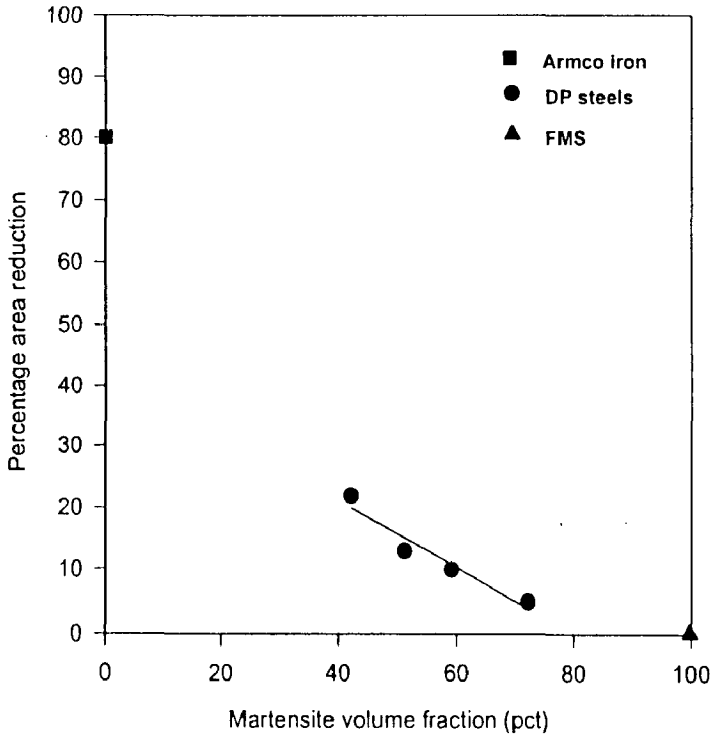

Fig. 5.17 Variation of percentage reduction in area with martensite volume fraction in dual phase steels.

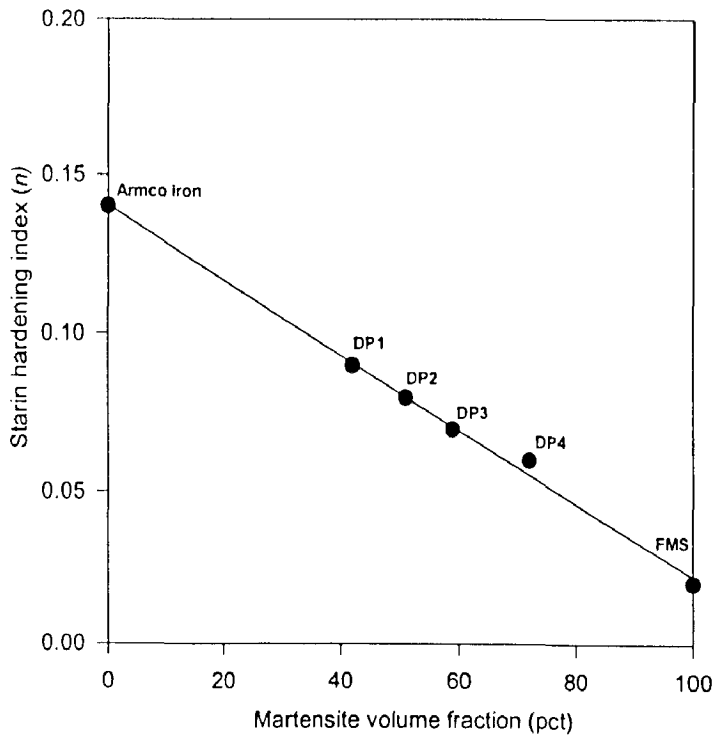

Fig. 5.18 Variation of strain hardening index with martensite volume fraction.

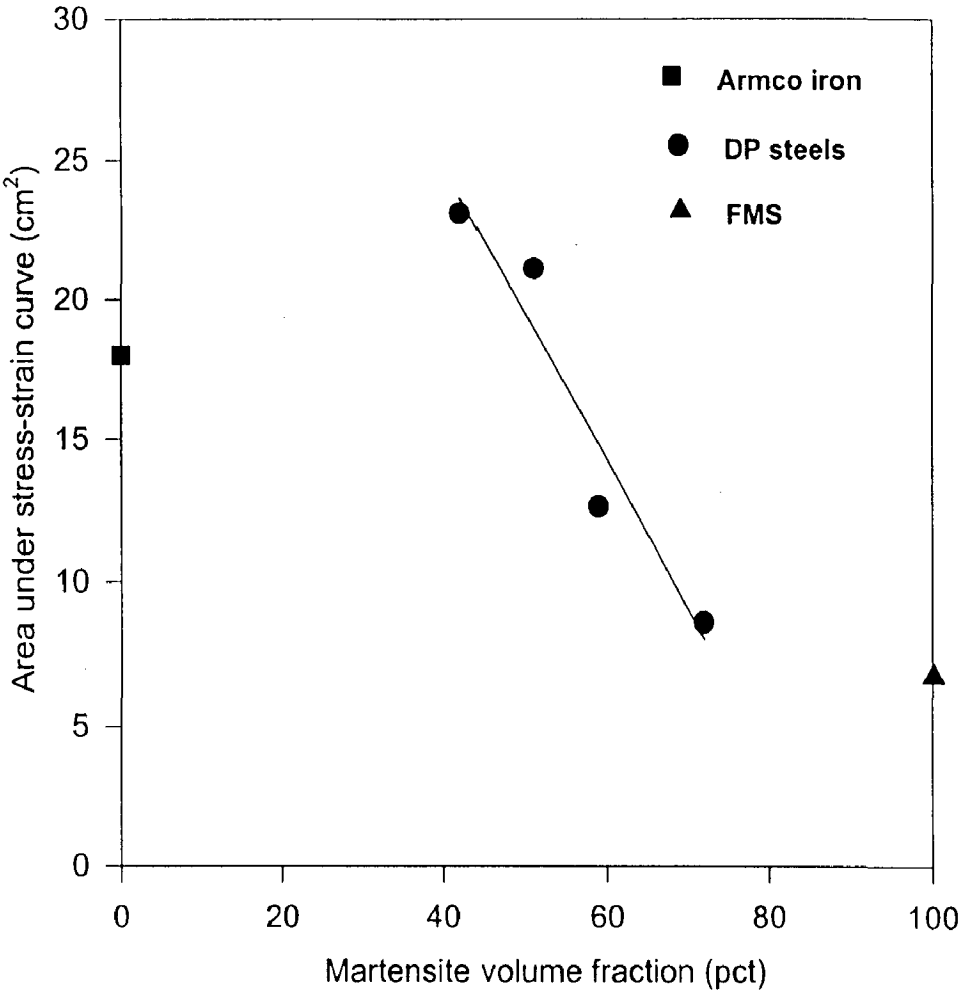

Fig. 5.19 Variation of area under stress strain curve with martensite volume fraction for Armco iron, dual phase steels and fully martensitic steel.

compared to Armco iron but decreases linearly with increasing volume fraction of martensite in the range 42 to 72 pct corresponding to DP1 and DP4 steel.

5.1.6 Fractography

The fractured surfaces of the tensile test specimens of Armco iron, N steel, DP steels with increasing volume fraction of martensite from DP1 to DP4 and FMS, have been studied under Scanning Electron Microscope (SEM) and the results are presented in this subsection.

Figure 5.20 shows the micrograph of the fractured surface of the Armco iron as observed under SEM. The micrograph shows a typical dimpled fracture surface which is characteristic of a ductile fracture. The average dimple size measured is approximately 18 μm. Figure 5.21 shows the SEM fractograph of normalised steel. Dimples are visible indicating a ductile mode of fracture in normalised steel. The average dimple size measured is approximately 2.3 μm.

The micrographs of the fractured surface of tensile specimen of dual phase steel, DP1, containing 42 vol pct of martensite are shown in Figs. 5.22 (a) and (b), respectively, at lower and higher magnification. The presence of dimples could be seen in both of these micrographs indicating a ductile mode of fracture in this steel. Figure 5.22 (b) shows a fully dimpled structure without the presence of any cleavages, or facets, which are characteristics of a brittle fracture. The average size of the dimples measured is approximately 1.8 μm, which is lower than Armco iron but similar to that observed for N steel.

Figures 5.23 (a) and (b) show the micrographs of the fractured surface at lower and higher magnification respectively, of the DP2 steel containing 51 vol pct martensite as

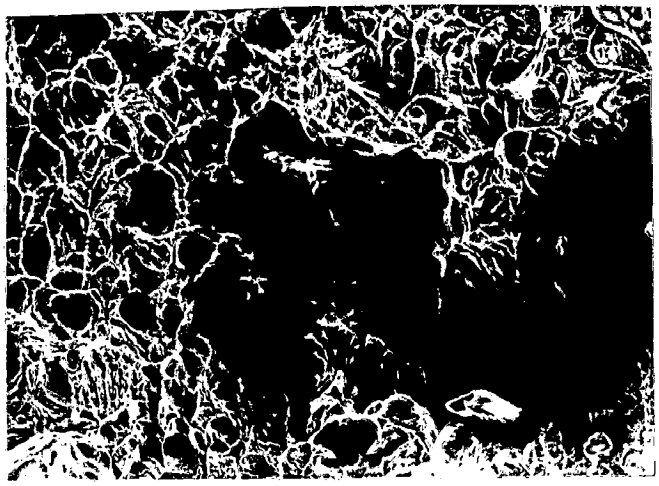

Fig. 5.20 SEM fractograph showing tensile fracture surface of Armco iron, X 217.

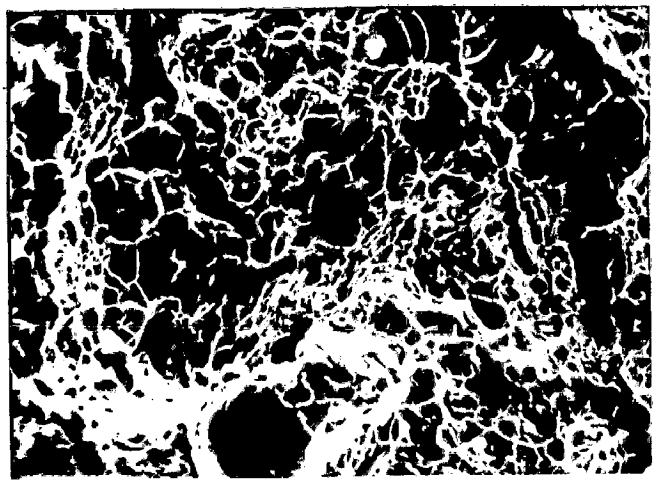

Fig. 5.21 SEM fractograph showing tensile fracture surface of normalised steel, X 2190.

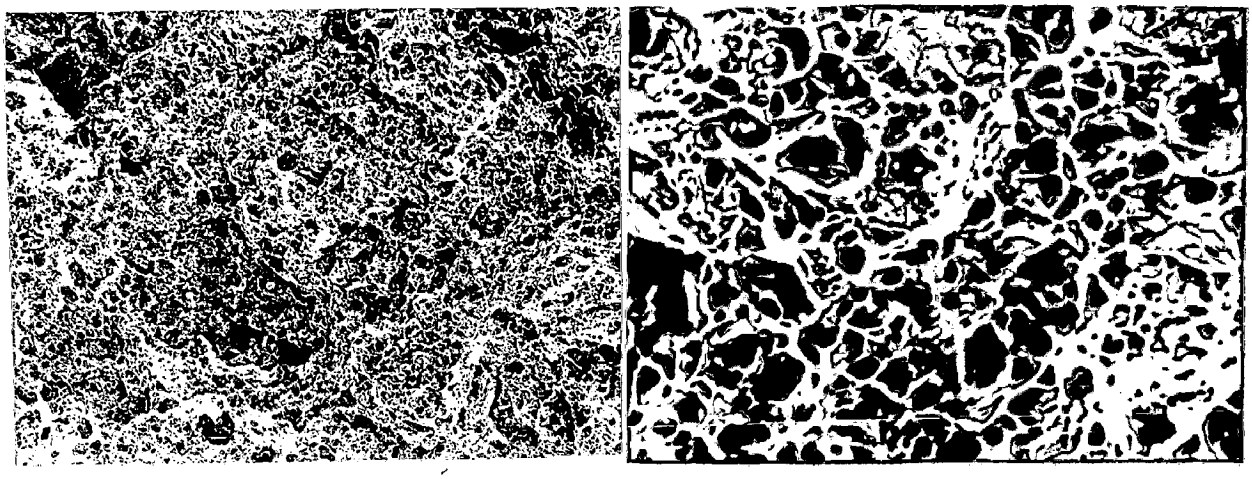

(a) (b)

Fig. 5.22 SEM fractographs showing tensile fracture surface of dual phase steel, DP1, (a) X 218 and (b) X 2320.

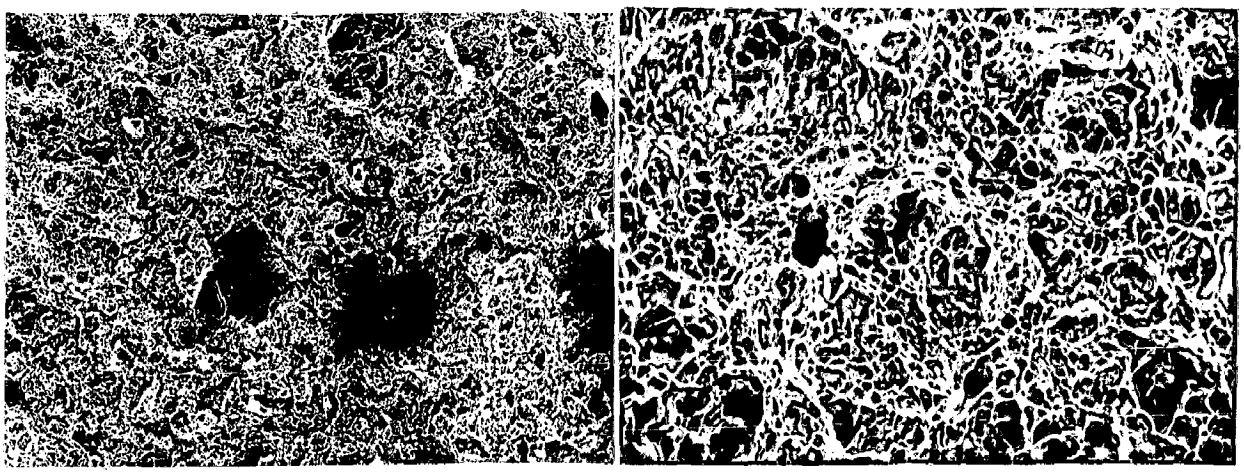

(a) (b)

Fig. 5.23 SEM fractographs showing tensile fracture surface of dual phase steel, DP2, (a) X 219 and (b) X 1270.

observed under SEM. Both the micrographs show a typical dimpled fracture surface which is characteristic of a ductile fracture. Figure 5.23 (b) shows a fully dimpled structure without the presence of any cleavages, or facets, which are characteristics of a brittle fracture. The average size of the dimples measured is approximately 1.6 μm.

Figures 5.24 (a) and (b) show the micrographs of the fractured surface at lower and higher magnification respectively, of the DP3 steel containing 59 vol pct martensite as observed under SEM. Both the micrographs show the presence of the smaller size dimples and the facets indicating a mixed (ductile + brittle) mode of fracture. The dimples and the cleavages could be observed more clearly at higher magnification as shown in Fig. 5.24 (b). The average size of the dimples measured is approximately 1.6 μm.

The SEM micrographs of the fractured surface of the DP4 steel containing 72 vol pct martensite as shown in Figs. 5.25 (a) and (b) at lower and higher magnification respectively, indicate a mixed mode of fracture in this steel also. Both the micrographs show the presence of the smaller size dimples and facets indicating a mixed (ductile + brittle) mode of fracture. The dimples and the cleavages could be observed more clearly at higher magnification as shown in Fig. 5.25 (b). The average size of the dimples measured is approximately 0.9 μm.

The SEM micrograph of the fractured surface of tensile specimen of fully martensitic steel (FMS) containing 100 pct martensite is shown in Fig. 5.26. It shows a cleavage fracture, which is characteristic of a typically brittle fracture and it can be judged from the presence of the facets all over the fracture surface. A very few smaller size dimples could also be seen in the fractograph and the average size of the dimples measured is approximately 0.4 μm.

The variation of the average dimple size with the martensite volume fraction in Armco iron, dual phase steels and fully martensitic steel is shown in Fig. 5.27. It is observed

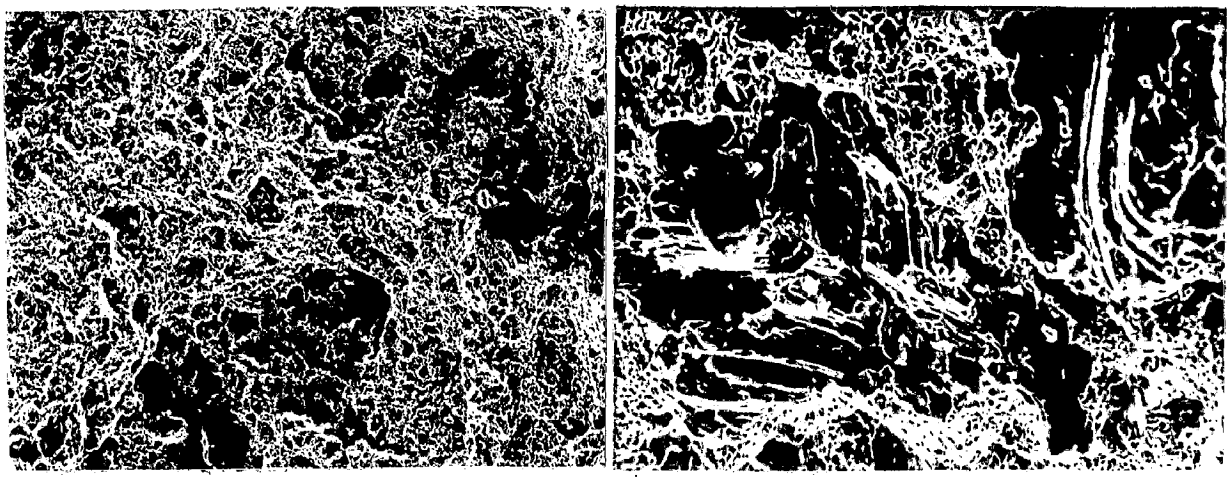

(a) (b)

Fig. 5.24 SEM fractographs showing tensile fracture surface of dual phase steel, DP3, (a) X 217 and (b) X 624.

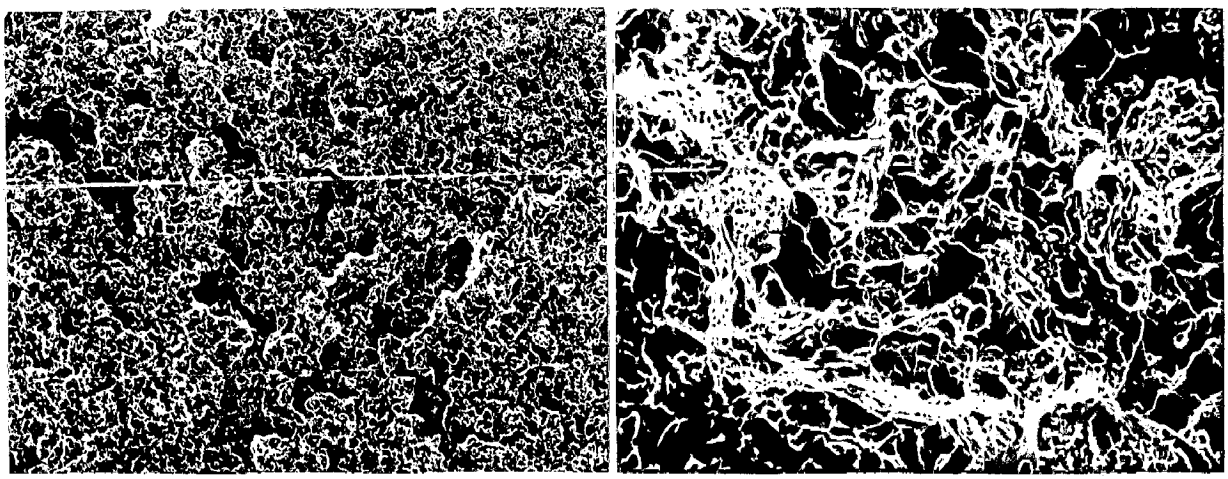

(a) (b)

Fig. 5.25 SEM fractographs showing tensile fracture surface of dual phase steel, DP4, (a) X 218 and (b) X 1060.

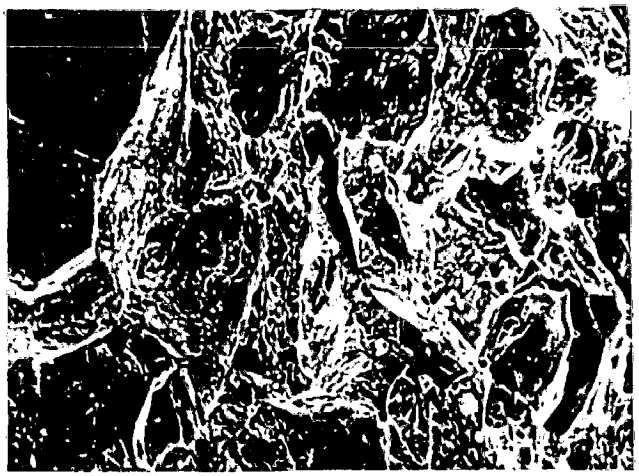

Fig. 5.26 SEM fractograph showing tensile fracture surface of fully martensitic steel, X 1500.

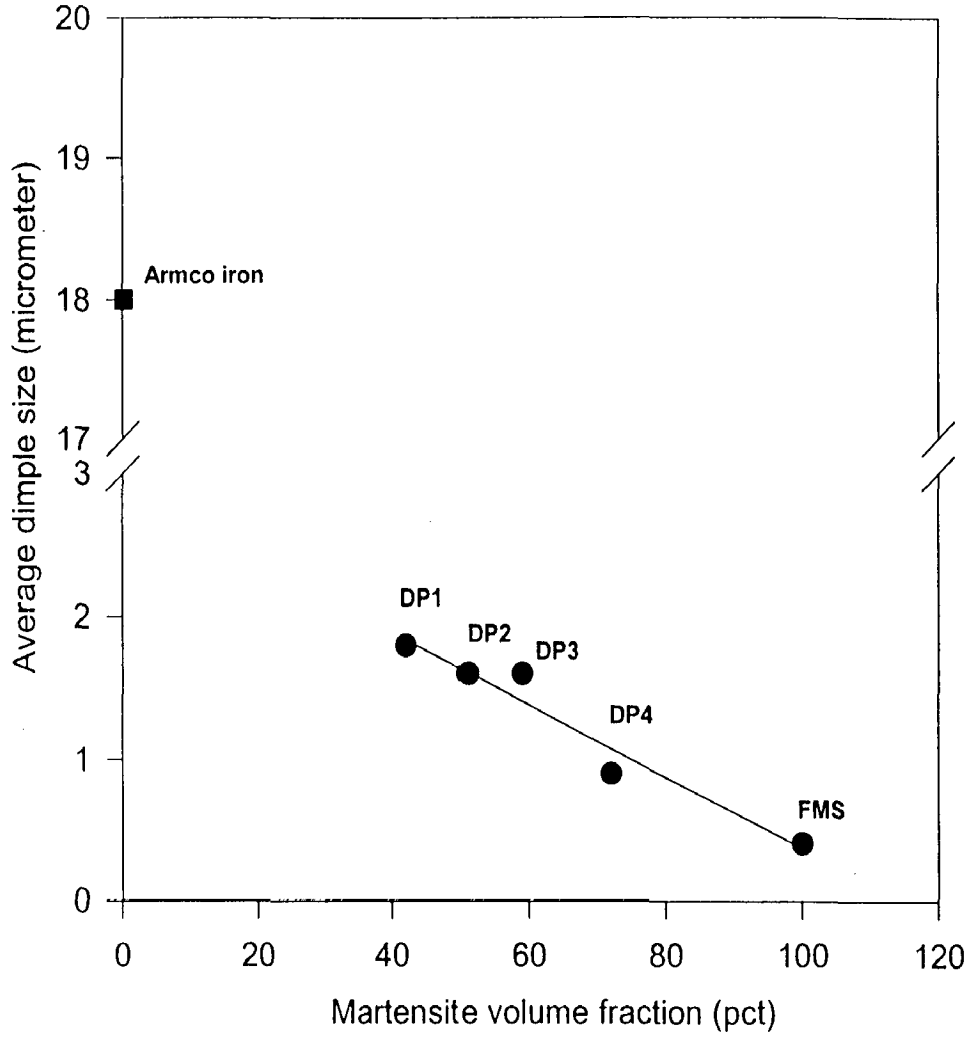

Fig. 5.27 Variation of average dimple size with martensite volume fraction in Armco iron, dual phase steels and FMS.

that the average dimple size decreases linearly as the volume fraction of martensite increases from 42 to 100 pct When extrapolated to zero martensite the dimple size there, is much lower than that observed for the ferritic Armco iron. This could be due to very less carbon in this material.

5.2 DISCUSSSION

The continuous yielding behaviour observed in tensile stress-strain curves of hypoeutectoid plain carbon dual phase steels DP1, DP2, DP3 and DP4 in the present investigation are shown in Fig. 5.14 (c) to (f), which are in agreement with the observation of Rashid (1976), Davies (1978), Ramos *et al* (1979) and Nath (1989). The non occurrence of yield point in these ferrite- martensite dual phase steels is attributed to the high dislocation density and residual stresses generated in the ferrite phase immediately surrounding the martensite islands. The transformation of the islands of austenite in ferrite matrix is accompanied by approximately 4 pct expansion in volume, which is accommodated in the ferrite phase itself resulting in its plastic deformation and increase in dislocation density. However, yield point phenomenon has been observed in Armco iron and N steel. The occurrence of the yield point in N steel as shown in Fig. 5.14 (b) is in agreement with the results of Rashid (1976), Davies (1978), Ramos *et al* (1979), Nath *et al* (1994). The yield point could not be observed in FMS due to its poor ductility.

The increase in the hardness, yield strength (YS) and ultimate tensile strength (UTS) of dual phase steels with an increase in the intercritical annealing time (ICA-time) at a particular intercritical annealing temperature is attributed to the formation of increased amount of the austenite during austenitization and martensite on subsequent quenching. As indicated in the Table A.1 and Fig. 5.10, the intercritical annealing at a fixed temperature of 740^0C for 2, 2.5, 3 and 3.5 minutes yields respectively, 42, 51, 59 and 72 pct martensite

volume fraction in the dual phase steels containing 0.42 wt pct carbon. There is no further increase in martensite volume fraction beyond 3.5 minutes of intercritical annealing of this steel. However, for steel containing 0.14 wt pct carbon 8 pct of martensite is obtained after 5 minutes of intercritical annealing at 740^0C as shown in Fig. 5.8. The increase in volume fraction of austenite/martensite with increase in intercritical annealing time can be explained on the basis of the mechanism of the austenite formation and its kinetics (Speich *et al*, 1981; Garcia *et al*, 1981). In the initial stage of the austenitization dissolution of carbide and the formation of high carbon austenite takes place simultaneously. The austenite grows into the supersaturated ferrite of originally the pearlitic region. In the end all the pearlite is replaced by the austenite and the amount of resulting austenite becomes approximately equal to that of pearlite in the original microstructure. There may be a little change in the amount of high carbon austenite over that observed in the microstructure because of the change in carbon content of ferrite at the intercritical annealing temperature. The growth of austenite with intercritical annealing time has been observed by the measurement of the martensite island size as shown in Fig. 5.11. At a fixed temperature of intercritical annealing the hardness of the martensite (transformed austenite on quenching) appears to decrease and that of ferrite appears to increase with increasing time of holding as shown in Fig. 5.12. Ultimately, the austenite volume fraction becomes constant depending on the time of holding during intercritical annealing at a particular temperature. The volume fraction of austenite is expected to increase with annealing time until it attains the equilibrium at the temperature of the intercritical annealing, for the given carbon content of the steel. This austenite is transformed to martensite on the water quenching resulting in a dual phase structure of ferrite and martensite. The effect of the increasing holding time is also reflected in the microstructures of the dual phase steels as shown in Figs. 5.4 to 5.7. In these figures one can clearly see the increase in martensite (darker regions) content as the holding time increases from 2.0 minute (DP1 $\approx$ 42 pct martensite) to 3.5 minutes (DP4 $\approx$ 72 pct martensite). The martensite islands become increasingly interconnected with increasing volume fraction of

martensite. The increase in hardness, yield strength and tensile strength with increasing intercritical annealing time has been attributed to the increase in the volume fraction of martensite which is a strong load-bearing phase in the dual phase steels, as shown in Figs. 5.12 and 5.15.

The decreasing ductility of the dual phase steels with increasing martensite volume fraction as shown in Figs. 5.16 and 5.17, is also in agreement with the results obtained by Rashid (1976), Davies (1978), Ramos *et al* (1979) and Nath (1989). With increase in the intercritical annealing time at a fixed temperature, the martensite volume fraction increases till its equilibrium amount is reached. Since martensite is a phase, which is hard and brittle, it imparts the hardness and strength to the steel at the expense of its ductility. Therefore, it is not surprising that the ductility diminishes with the increasing volume fraction of the martensite. It can also be seen from these figures that the ductility of the fully martensitic steel is also very poor due to the same reason.

The decrease in the strain-hardening coefficient with increase in martensite volume fraction as shown in Fig. 5.18 is in agreement with the work of Davies (1978). The decrease in strain hardening coefficient may be explained on the basis of the theory of work hardening proposed by Ashby (1966) which states that the rate of work hardening increases with increasing martensite volume fraction and decreasing martensite island size in dual phase steels. In the present study although there is an increase in the volume fraction of martensite but the size of martensite is also observed to increase therefore the net effect is a decrease in the strain hardening coefficient with increase in martensite volume fraction.

The Armco iron shows a ductile fracture shown in Fig. 5.20, indicated by the presence of the larger size dimples, characteristic of a ductile material. The normalised steel also shows a similar ductile fracture but the dimple size is smaller compared to the Armco

iron as can be seen from Fig. 5.21. An examination of the fractographs of the tensile specimens of the DP1 and DP2, shown in Figs. 5.22 (a) and (b) and Figs. 5.23 (a) and (b), indicates ductile fracture. The dimples, which are the characteristics of a ductile fracture, can be observed in these fractographs. Fractographs of DP3 and DP4 steels as shown in Figs. 5.24 (a) and (b) and Figs. 5.25 (a) and (b) exhibit a mixed (ductile + brittle) mode of fracture as both the dimples and the facets can be clearly observed. The presence of dimples may be attributed to the microvoids nucleated at the sites of localised strain discontinuity, such as that associated with second-phase particles, inclusions and dislocation pile-ups. As the strain in the material increases, the microvoids grow, coalesce and eventually form a continuous fracture surface showing numerous cuplike depressions commonly referred to as dimples. The size of the dimples on a fracture surface is governed by the number and distribution of microvoids that are nucleated. When the nucleation sites are few and widely spaced, the microvoids grow to a larger size before coalescing and result in a fracture surface that contains large dimples (Kerlins, 1992). The presence of the large size dimples on the surface of the Armco iron as shown in Fig. 5.20 may be attributed to the presence of inclusions and tertiary cementite because microvoids nucleate at the interface of ferrite and inclusions and ferrite and tertiary cementite. In contrast to this the small size dimples are formed on the surface when numerous nucleating sites are activated at the ferrite-martensite boundaries and adjacent microvoids join before they have an opportunity to grow to a larger size, fracture occurs. This seems to be a probable case in DP steels with increasing amount of second-phase particles i.e., martensite islands, which act as the nucleation sites for the microvoids resulting in a decreasing dimple size with increasing volume fraction of martensite as shown in Fig. 5.27. The decrease in the dimple size with increasing volume fraction of martensite also indicates the role of ferrite/martensite interface in nucleating microvoids. The fractograph of the FMS given in Fig. 5.26 shows a few small sized dimples apart from a large number of facets thus indicating a brittle fracture. It may be attributed to the higher amount of martensite, which inhibits the microvoids coalescence resulting in

decreased dimple size. The dimple size that is observed in the N steel fractrograph is similar to the dimple size observed in the DP1 steel fractrograph.

The study presented above outlines the results on the heat treatment variables and their effects on the microstructure and the mechanical properties of a typical two phase metallic material like dual phase steel. The increasing time of intercritical annealing at fixed temperature results on quenching, an increasing amount of martensite in dual phase steel but beyond a certain intercritical annealing time, the amount of martensite does not increase anymore and reaches a steady level depending upon the carbon content of steel. This steady level of martensite results presumably by the transformation of equilibrium amount of austenite at the intercritical annealing temperature. The presence of second phase i.e., martensite, in dual phase steel improves the mechanical properties in terms of hardness and tensile strength. The hardness and the tensile strengths are observed to increase linearly with increasing volume fraction of martensite, which is a hard and brittle phase. The ductility measured in terms of percentage elongation and percentage reduction in area, decreases linearly with increasing volume fraction of martensite in dual phase steels. Increasing amount of martensite is accompanied by a decrease in strain hardening coefficient and it has been attributed to the dominating influence of increasing size of martensite islands. The mode of fracture under uniaxial tension has also been observed to change from a typically ductile to brittle mode with increasing volume fraction of martensite.

Chapter 6

TRIBOLOGICAL BEHAVIOUR OF MEDIUM CARBON DUAL PHASE STEEL

The tribological behaviour of Armco iron, normalised (N) steel, dual phase (DP) steels (DP1, DP2, DP3 and DP4) and fully martensitic steel (FMS) has been investigated in terms of the friction and dry sliding wear against the counterface of steel. The primary focus of this study is to understand the role of microstructure and normal load on the wear and friction characteristics of these materials having different microstructures. The results have also been discussed to develop a coherent understanding of the tribological characteristics of these materials in terms of their correlation with the microstructure and mechanical properties of these materials as it has emerged from this study.

6.1 RESULTS

6.1.1 Dry Sliding Wear and Friction

(a) Dry Sliding Wear

(i) Variation of cumulative wear volume with sliding distance

The variation of cumulative wear volume with sliding distance under different normal loads and at a fixed sliding velocity of 1.15 m/s is shown in Figs. 6.1 to 6.7 respectively, for

fully ferritic Armco iron, fully martensitic steel (FMS), normalised (N) steel and dual phase (DP) steels i.e., DP1, DP2, DP3 and DP4.

The cumulative wear volume loss with sliding distance under different normal loads of 14.7, 19.6, 24.5, 29.4 and 34.3 N has been plotted on a log-log scale and it has demonstrated a sublinear variation, with coefficients of correlation exceeding 0.98 and 0.99 at all the normal loads, for Armco iron, FMS, N steel and DP steels i.e., DP1, DP2, DP3 and DP4. The values of the slopes and the coefficients of correlation are given in Table A.5 in the appendix. However, the data could also be analysed using two separate stages of wear behavior characterised by two linear segments, which also allows the relationship to remain within the framework of Archard's law. The change in slope has been observed after the first six experimental points (first stage-run-in), fitted by one line, and the latter six points have been fitted with another line with the sixth point common between them. The slope is observed to change to a lower value after sliding through a distance of 5.53 km. Both the lines have been determined by the linear least square fit. The wear rate is given by the line slope. The procedure followed helps establish the run-in period rate separately from the long-term steady state rate (second stage). This procedure is followed in all the cumulative wear volume *vs.* sliding distance variations with respect to all the materials having different microstructures, used in the present study.

Figure 6.1 shows the cumulative wear volume loss with sliding distance under different normal loads of 14.7, 19.6, 24.5, 29.4 and 34.3 N for fully ferritic Armco iron. The cumulative wear volume is found to increase with sliding distance at particular load say 14.7 N. The variation at a given load has been expressed by two linear segments. The slope of the first linear segment (run-in) is found to be higher as compared to the second linear segment (steady state). The similar trend of variation of cumulative wear volume with sliding distance is also observed for other normal loads i.e., 19.6, 24.5, 29.4 and 34.3 N. The cumulative wear

volume is also observed to increase with the increase in normal load as can be seen from the Fig. 6.1. For a maximum sliding distance of 39.74 km the cumulative wear volume at a normal load of 14.7 N is 87 x 10^{-1} mm^3. Similarly, for the other normal loads of 19.6, 24.5, 29.4 and 34.3 N the cumulative wear volumes are 126, 165, 219, and 271 x 10^{-1} mm^3 respectively, for the same maximum sliding distance.

Figure 6.2 illustrates the variation of cumulative wear volume with sliding distance under different normal loads of 14.7, 19.6, 24.5, 29.4 and 34.3 N for fully martensitic steel (FMS) containing 100 pct martensite. The cumulative wear volume is found to increase with sliding distance at a particular load say 14.7 N. The variation at a given load has been expressed by two linear segments. The first linear segment (run-in) is found to be steeper compared to the second linear segment (steady state). The slope is observed to change to a lower value after sliding through a distance of 5.53 km. The similar trend of variation of cumulative wear volume with sliding distance is also observed for other normal loads i.e., 19.6, 24.5, 29.4 and 34.3 N. The cumulative wear volume is also observed to increase with the increase in normal load as can be seen from Fig. 6.2. For a maximum sliding distance of 39.74 km the cumulative wear volume at a normal load of 14.7 N is 30 x 10^{-2} mm^3. Similarly, for the other normal loads of 19.6, 24.5, 29.4 and 34.3 N the cumulative wear volumes are 44, 65, 80, and 105 x 10^{-2} mm^3 respectively, for the same maximum sliding distance. The cumulative wear volume for fully martensitic (FMS) is found to be much lower than that for the fully ferritic Armco iron, at all the normal loads.

Figure 6.3 indicates the variation of cumulative wear volume with sliding distance under different normal loads of 14.7, 19.6, 24.5, 29.4 and 34.3 N for normalised (N) steel. The cumulative wear volume is found to increase with sliding distance at a particular load say 14.7 N. The variation at a given load has been expressed by two linear segments. The first linear segment (run-in) is found to be steeper compared to the second linear segment

(steady state). The slope is observed to change to a lower value after sliding through a distance of 5.53 km. The similar trend of variation of cumulative wear volume with sliding distance is also observed for other normal loads i.e., 19.6, 24.5, 29.4 and 34.3 N. For a maximum sliding distance of 39.74 km the cumulative wear volume at a normal load of 14.7 N is 323 x 10^{-2} mm^3. Similarly, for the other normal loads of 19.6, 24.5, 29.4 and 34.3 N the cumulative wear volumes are 444, 577, 776, and 975 x 10^{-2} mm^3 respectively, for the same maximum sliding distance. The cumulative wear volume for N steel is found to be much lower as compared to the Armco iron, but very high as compared to the FMS at all the normal loads.

The variation of cumulative wear volume with sliding distance under different normal loads of 14.7, 19.6, 24.5, 29.4 and 34.3 N for dual phase (DP1) steel containing 42 vol pct martensite is shown in Fig. 6.4. The cumulative wear volume is found to increase sliding distance at a particular load say 14.7 N. The variation at a given load has been expressed by two linear segments. The first linear segment (run-in) is found to be steeper compared to the second linear segment (steady state). The slope is has been observed to change to a lower value after sliding through a distance of 5.53 km. The similar trend of variation of cumulative wear volume with sliding distance is also observed for other normal loads i.e., 19.6, 24.5, 29.4 and 34.3 N. The cumulative volume is also observed to increase with increasing normal load. For a maximum sliding distance of 39.74 km the cumulative wear volume at a normal load of 14.7 N is 183 x 10^{-2} mm^3. Similarly, for the other normal loads of 19.6, 24.5, 29.4 and 34.3 N the cumulative wear volumes are 277, 376, 489 and 625 x 10^{-2} mm^3 respectively, for the same maximum sliding distance. The cumulative wear volume for DP1 steel is found to be much low as compared to both Armco iron and normalised steel, but high as compared to the FMS at all the normal loads approximately by a factor of six.

Figure 6.5 shows the cumulative wear volume loss with sliding distance under different normal loads of 14.7, 19.6, 24.5, 29.4 and 34.3 N for dual phase (DP2) steel containing 51 vol pct martensite. The cumulative wear volume is found to increase with sliding distance at a particular load say 14.7 N. The variation at a given load has been expressed by two linear segments. The first linear segment (run-in) is found to be steeper as compared to the second linear segment (steady state). The slope is observed to change to a lower value after sliding through a distance of 5.53 km. The similar trend of variation of cumulative wear volume with sliding distance is also observed for other normal loads i.e., 19.6, 24.5, 29.4, and 34.3 N. The cumulative volume is also observed to increase with increasing normal load. For a maximum sliding distance of 39.74 km the cumulative wear volume at a normal load of 14.7 N is 142 x 10^{-2} mm^3. Similarly, for the other normal loads of 19.6, 24.5, 29.4 and 34.3 N the cumulative wear volumes are 217, 292, 378 and 468 x 10^{-2} mm^3 respectively, for the same maximum sliding distance. The cumulative wear volume for DP2 steel is found to be much low as compared Armco iron, but high as compared to the FMS at all the normal loads approximately by a factor of five.

Figure 6.6 shows the variation of cumulative wear volume with sliding distance under different normal loads of 14.7, 19.6, 24.5, 29.4 and 34.3 N and at a fixed sliding velocity of 1.15 m/s, for dual phase (DP3) steel containing 59 vol pct martensite. The cumulative wear volume is found to increase with both normal load and sliding distance. However, the variation at a given load say 14.7 N has been expressed by two linear segments. The first linear segment (run-in) is found to possess a higher slope as compared to the second linear segment (steady state). The slope is observed to change to a lower value after sliding through a distance of 5.53 km. The similar trend of variation of cumulative wear volume with sliding distance is also observed for other normal loads i.e., 19.6, 24.5, 29.4 and 34.3 N. The cumulative volume is also observed to increase with increasing normal load. For a maximum sliding distance of 39.74 km the cumulative wear volume at a normal load of 14.7 N is

105 x 10^{-2} mm^3. Similarly, for the other normal loads of 19.6, 24.5, 29.4 and 34.3 N the cumulative wear volumes are 158, 216, 282 and 369 x 10^{-2} mm^3 respectively, for the same maximum sliding distance. The cumulative wear volume for DP3 steel is found to be much low as compared Armco iron, but around three to four times high as compared to FMS at all the normal loads.

Wear volume loss with sliding distance under different normal loads of 14.7, 19.6, 24.5, 29.4 and 34.3 N for dual phase (DP4) steel containing a martensite volume fraction of 72 pct, is shown in Fig. 6.7. The cumulative wear volume is found to increase with sliding distance at a particular load say 14.7 N. The variation at a given load has been expressed by two linear segments. The slope of the first linear segment (run-in) is found to be higher as compared to the second linear segment (steady state). The slope is observed to change to a lower value after sliding through a distance of 5.53 km. The similar trend of variation of cumulative wear volume with sliding distance is also observed for other normal loads i.e., 19.6, 24.5, 29.6 and 34.3 N. The cumulative volume is also observed to increase with increasing normal load as can be seen from Fig. 6.7. For a maximum sliding distance of 39.74 km the cumulative wear volume at a normal load of 14.7 N is 75 x 10^{-2} mm^3. Similarly, for the other normal loads of 19.6, 24.5, 29.4 and 34.3 N the cumulative wear volumes are 103, 145, 183 and 242 x 10^{-2} mm^3 respectively, for the same maximum sliding distance. The cumulative wear volume for DP4 steel is found to be much low as compared Armco iron, but high as compared to the FMS at all the normal loads.

(ii) Variation of wear rate with normal load

The wear rate, i.e., volume loss in wear per unit sliding distance at a given load, has been determined from the slope of the linear least square fit lines at different loads given in Figs. 6.1 to 6.7. The variation of the wear rate with normal load corresponding to both the

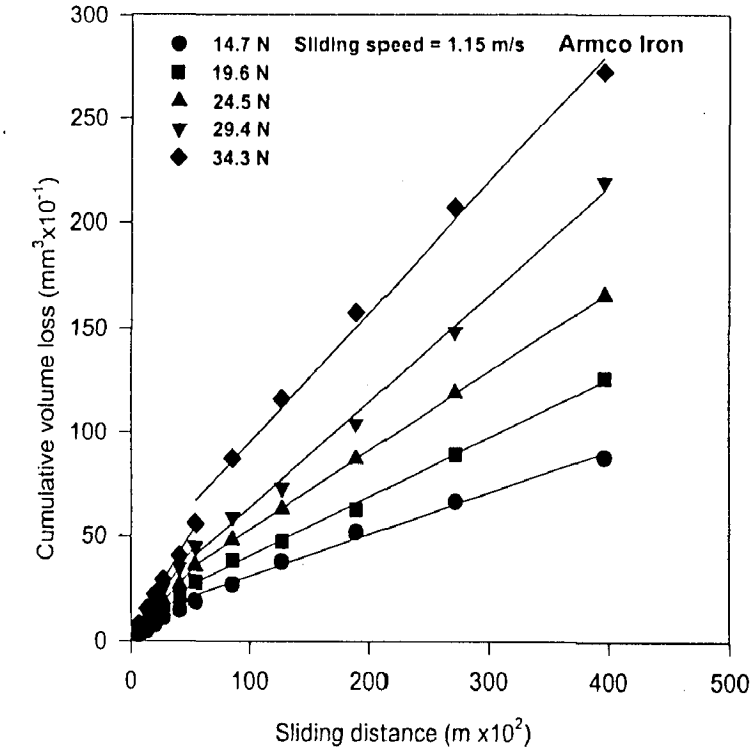

Fig. 6.1 Cumulative wear volume with sliding distance at different loads in Armco iron.

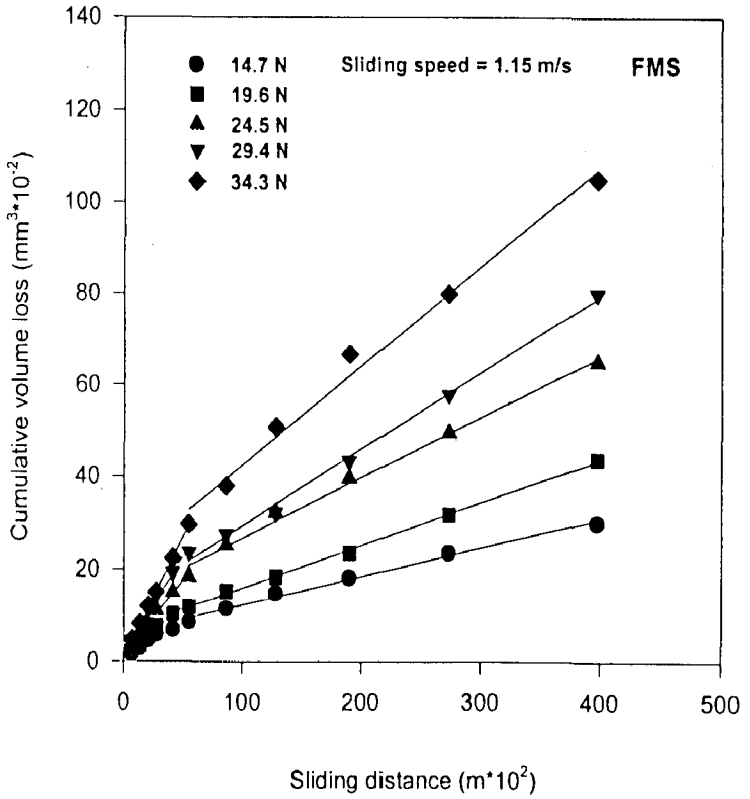

Fig. 6.2 Cumulative wear volume with sliding distance at different loads in fully martensitic steel (FMS).

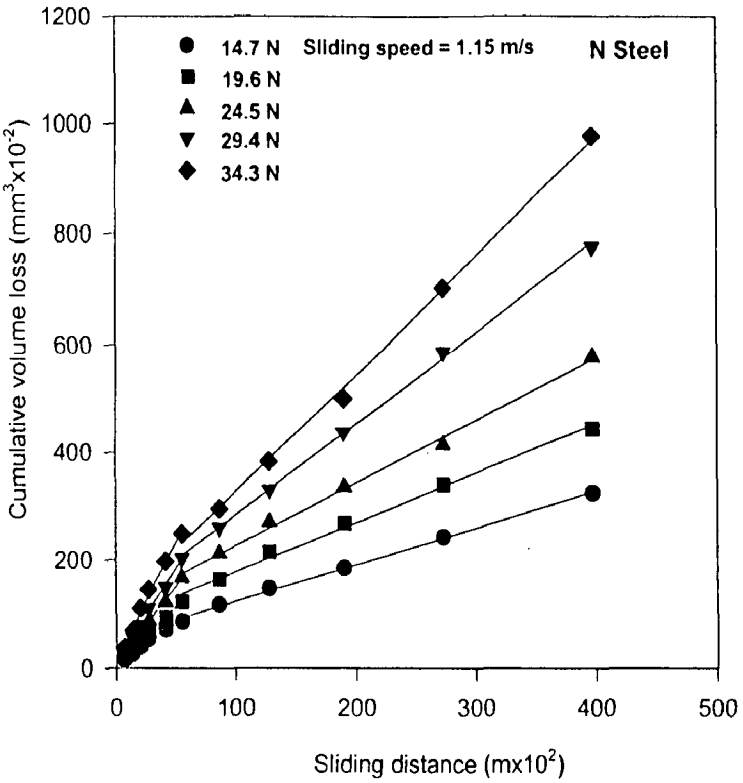

Fig. 6.3 Cumulative wear volume with sliding distance at different loads in normalised (N) steel.

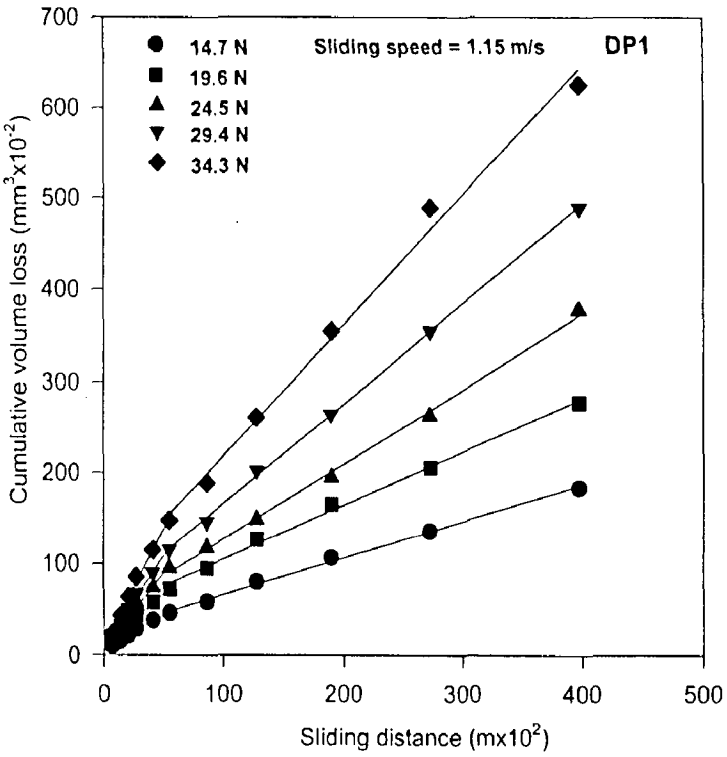

Fig. 6.4 Cumulative wear volume with sliding distance at different loads in dual phase steel, DP1, containing 42 pct martensite.

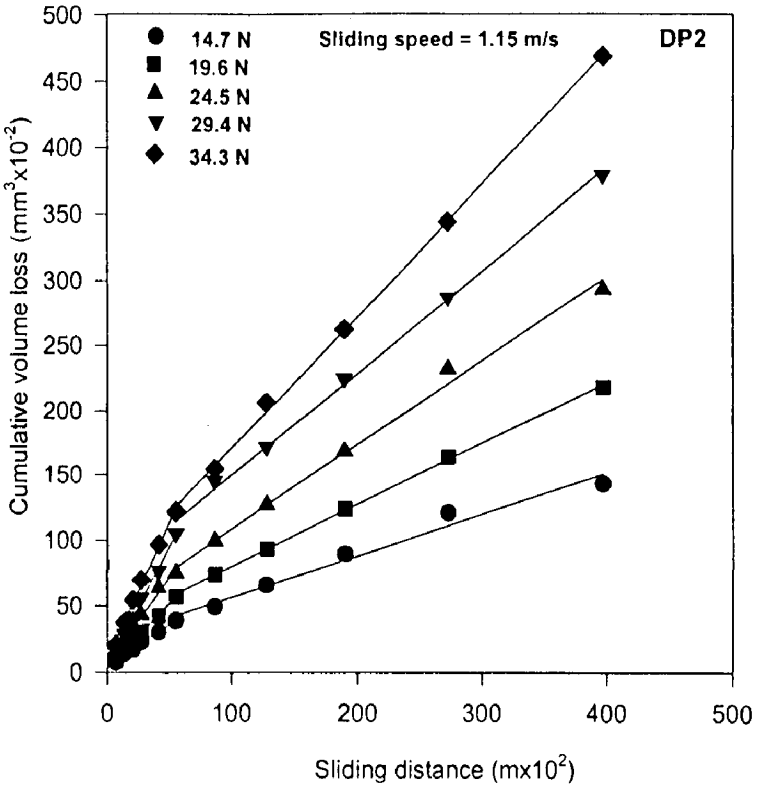

Fig. 6.5 Cumulative wear volume with sliding distance at different loads in dual phase steel, DP2, containing 51 pct martensite.

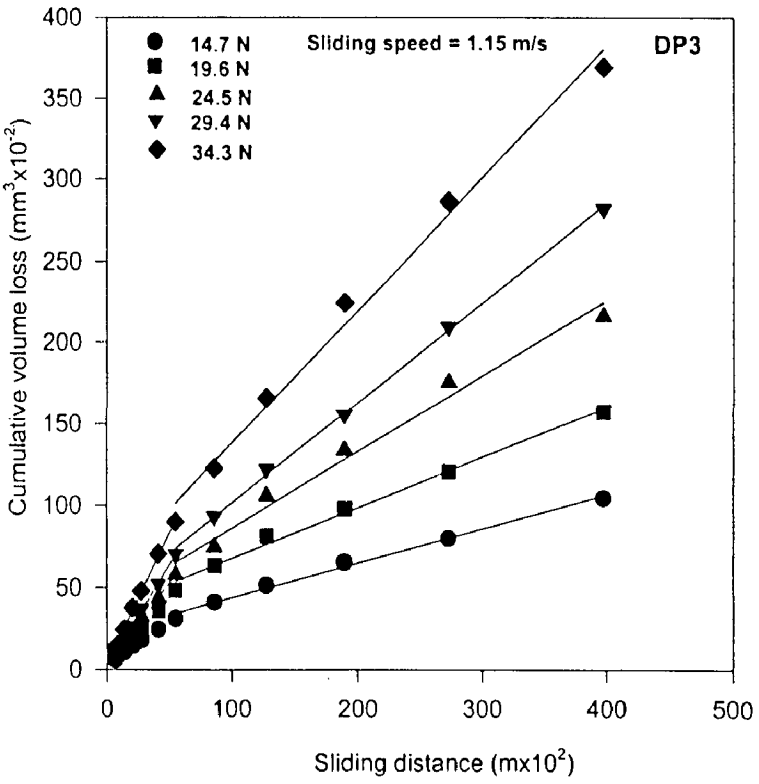

Fig. 6.6 Cumulative wear volume with sliding distance at different loads in dual phase steel, DP3, containing 59 pct martensite.

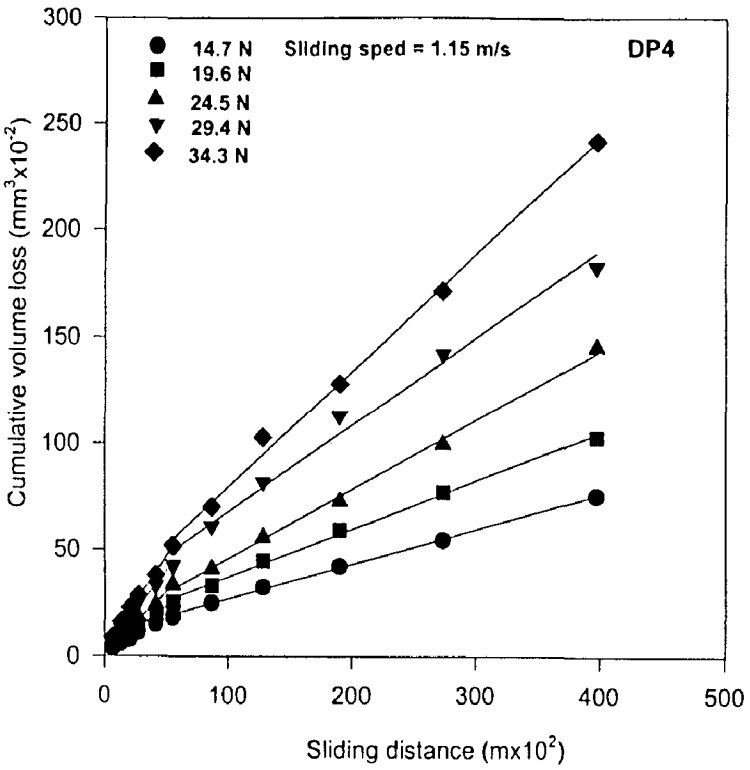

Fig. 6.7 Cumulative wear volume with sliding distance at different loads in dual phase steel, DP4, containing 72 pct martensite

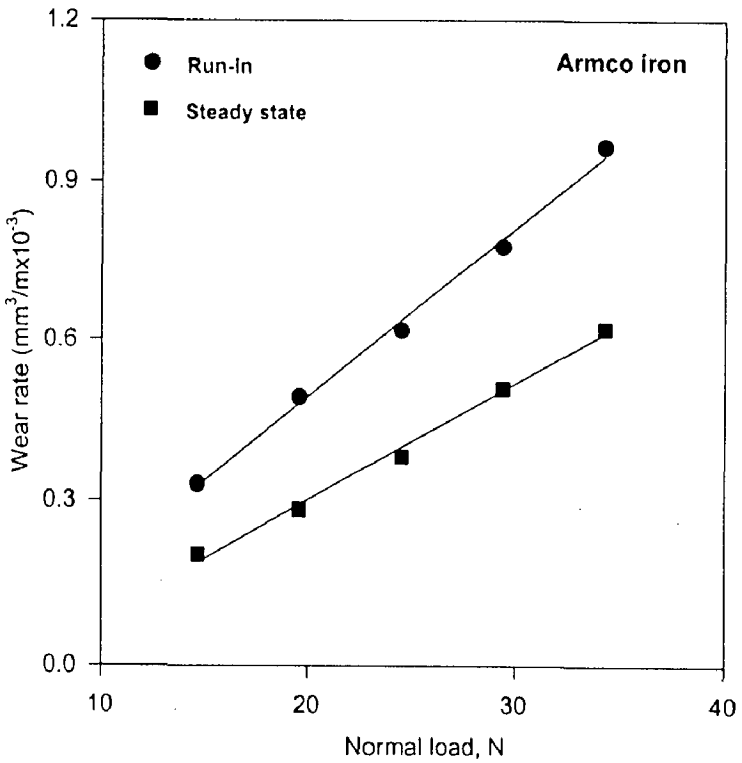

Fig. 6.8 Variation of wear rate with normal load in Armco iron for both run-in and steady state of wear.

linear segments are shown in Figs. 6.8 to 6.14 for the ferritic Armco iron, fully martensitic steel (100 vol pct martensite), normalised steel and dual phase steels i.e., DP1, DP2, DP3 and DP4 containing 42, 51, 59, and 72 vol pct martensite, respectively. The wear rate is observed to increase more or less linearly in the range of load between 14.7 N to 34.3 N for Armco iron as shown in Fig. 6.8. The wear rate corresponding to second linear segment (steady state) is found to be low as compared to the first linear segment (run-in). The wear rate is found to increase from 0.33 to 0.966 X 10^{-3} mm^3/m in the load range from 14.7 N to 34.3 N, for the run-in stage of wear. The wear rate in the steady state wear varies from 0.2 to 0.62 X 10^{-3} mm^3/m as the normal load changes from 14.7 N to 34.3 N.

Figure 6.9 shows the variation of wear rate with normal load for the fully martensitic steel (FMS). The wear rate is observed to increase linearly with normal load for both the run-in and the steady state of wear as determined from Fig. 6.2. The wear rate in the run-in stage increases from 0.137 to 0.514 X 10^{-4} mm^3/m as the load increases from 14.7 N to 34.3 N, whereas, for the same increase in load, the wear rate increases from 0.061 to 0.217 X 10^{-4} mm^3/m for the steady state of wear behaviour.

Figure 6.10 shows the variation of wear rate with normal load for the normalised (N) steel corresponding to both the run-in and the steady state of wear as seen from the Fig. 6.3. It is observed that the wear rate increases linearly with load in both the stages. Wear rate increases from 1.42 to 2.15 X 10^{-4} mm^3/m at the corresponding loads of 14.7 and 34.3 N in the run-in stage. The wear rate in the steady state increases linearly from 0.69 X 10^{-4} mm^3/m to 1.17 X 10^{-4} mm^3/m when the load increases from 14.7 to 24.5 N but the wear rate increases with a higher slope as the load changes from 24.5 to 34.3 N.

The wear rates for the Armco iron, normalised (N) steel, dual phase steels – DP1 to DP4 and fully martensitic steel are under different loads of 14.7, 19.6, 24.5, 29.4 and 34.3 N are reported in Tables A.6 to A.10 respectively, in the appendix.

(iii) Variation of wear rate with martensite volume fraction (MVF)

The wear rates of the DP steels at different loads for both the run-in and the steady state of wear are given in Table A.11 in the appendix. Figures 6.11 to 6.14 show the variation of wear rate with normal load for dual phase steels - DP1, DP2, DP3 and DP4, with increasing volume fraction of martensite, as observed in both run-in and steady state of wear behaviour. It is observed that the wear rate increases linearly with the normal load in both the stages for all the dual phase steels in the entire load range. Among the dual phase steels investigated, the wear rate has been found to be minimum for DP4 containing 72 vol pct martensite in respect of both the stages whereas wear rate is maximum for DP1 containing 42 vol pct martensite. The values of the wear rates for DP2 and DP3 are found to lie in-between those of DP1 and DP4.

Figure 6.15 shows a comparison of wear rate with normal load in the run-in stage of wear for the fully ferritic Armco iron, dual phase steels and FMS. The variation of the wear rate is represented by diverging lines of least square fit as one moves from a lower load of 14.7 N to a higher load of 34.3 N. The wear rate at a given load decreases as the volume fraction of martensite increases. This effect in the run-in stage of wear has been directly demonstrated in Fig. 6.16 which shows the variation of the wear rate with the martensite volume fraction at the minimum and maximum normal loads of 14.7 and 34.3 N used for this investigation. The wear rate decreases with increasing volume fraction of martensite. The wear rate decreases almost linearly in martensite range of 42 to 72 pct corresponding to DP1 and DP4 steel as can be seen from Fig. 6.16. Thereafter, the wear rate appears to saturate

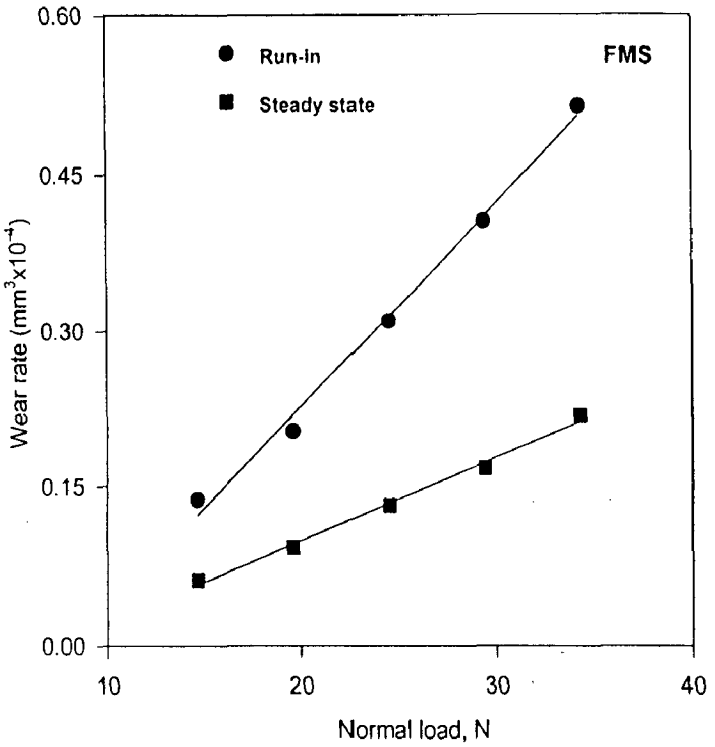

Fig. 6.9 Variation of wear rate with normal load in fully martensitic steel for both run-in and steady state of wear.

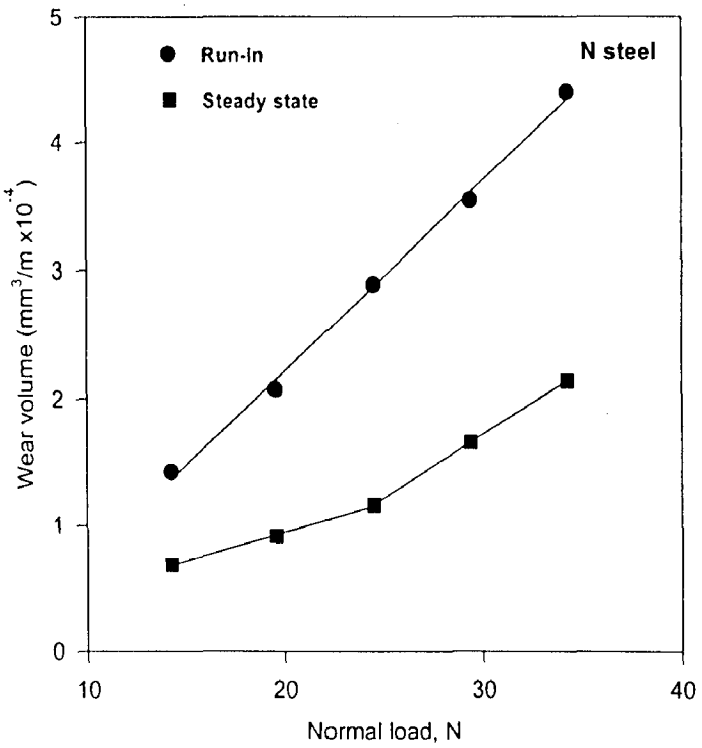

Fig. 6.10 Variation of wear rate with normal load in normalised steel for both run-in and steady state of wear.

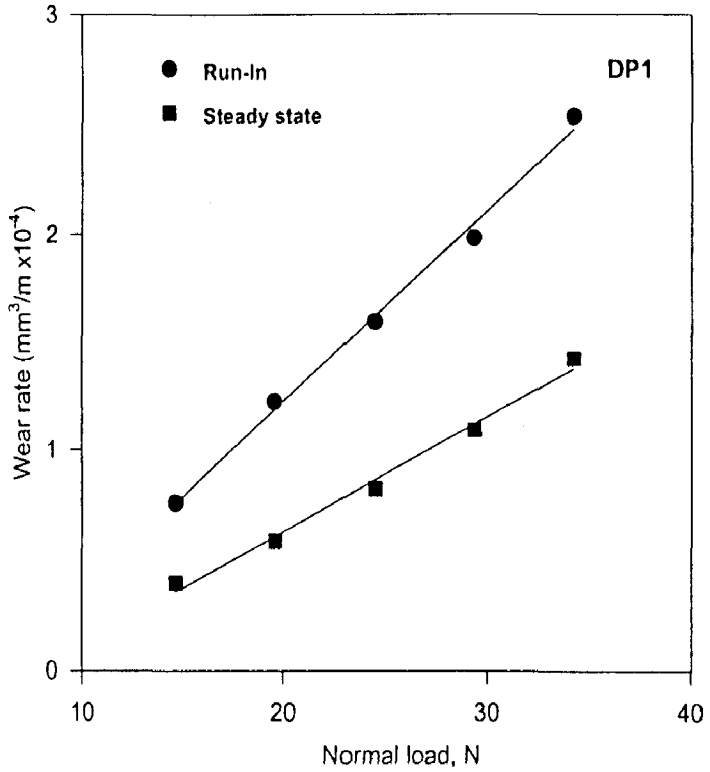

Fig. 6.11 Variation of wear rate with normal load in dual phase steel, DP1, containing 42 pct martensite for both run-in and steady state of wear.

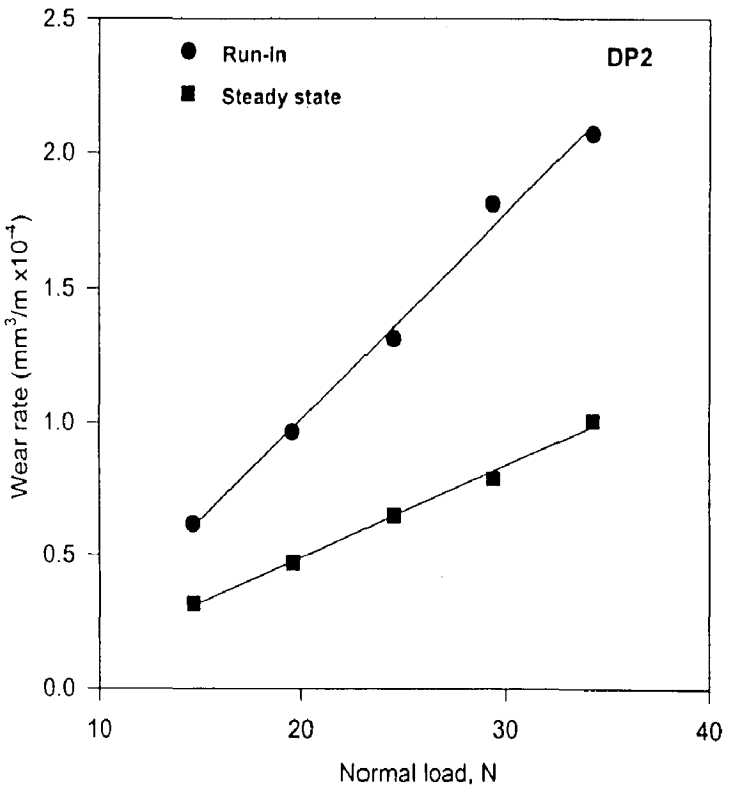

Fig. 6.12 Variation of wear rate with normal load in dual phase steel, DP2, containing 51 pct martensite for both run-in and steady state of wear.

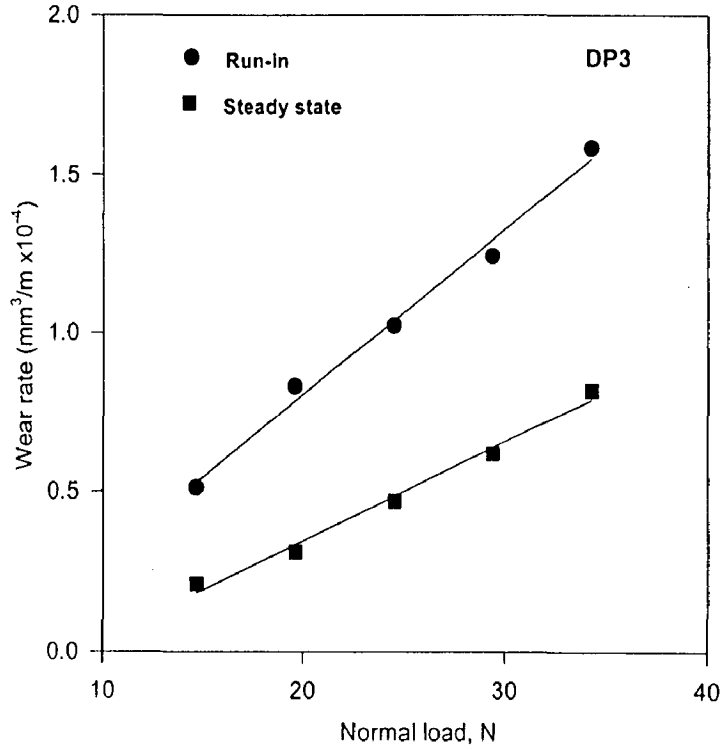

Fig. 6.13 Variation of wear rate with normal load in dual phase steel, DP3, containing 59 pct martensite for both run-in and steady state of wear.

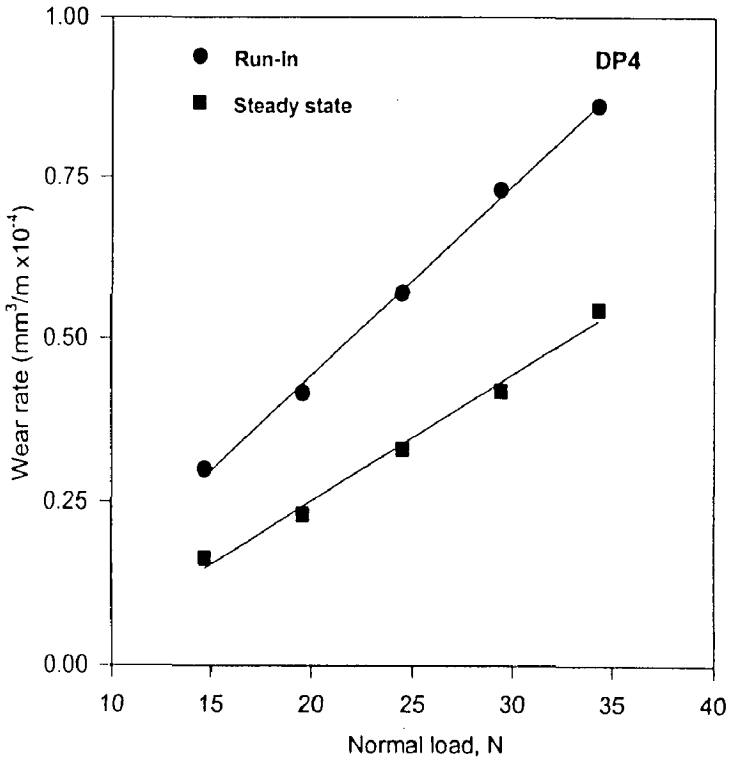

Fig. 6.14 Variation of wear rate with normal load in dual phase steel, DP4, for both run-in and steady state of wear.

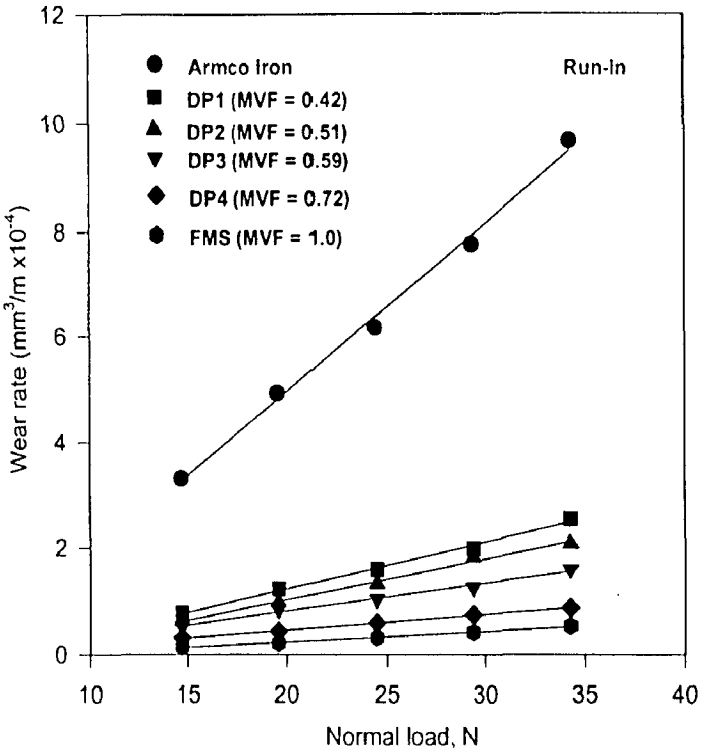

Fig. 6.15 Variation of wear rate with normal load in Armco iron, dual phase steels and FMS corresponding to first linear segment (run-in stage).

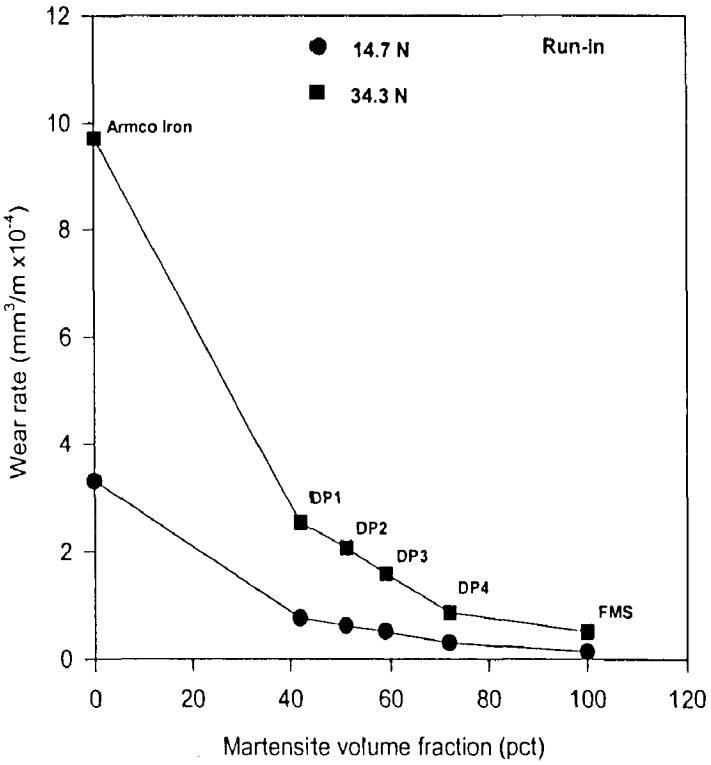

Fig. 6.16 Variation of wear rate with martensite volume fraction at the normal loads of 14.7 and 34.3 N in the run-in stage.

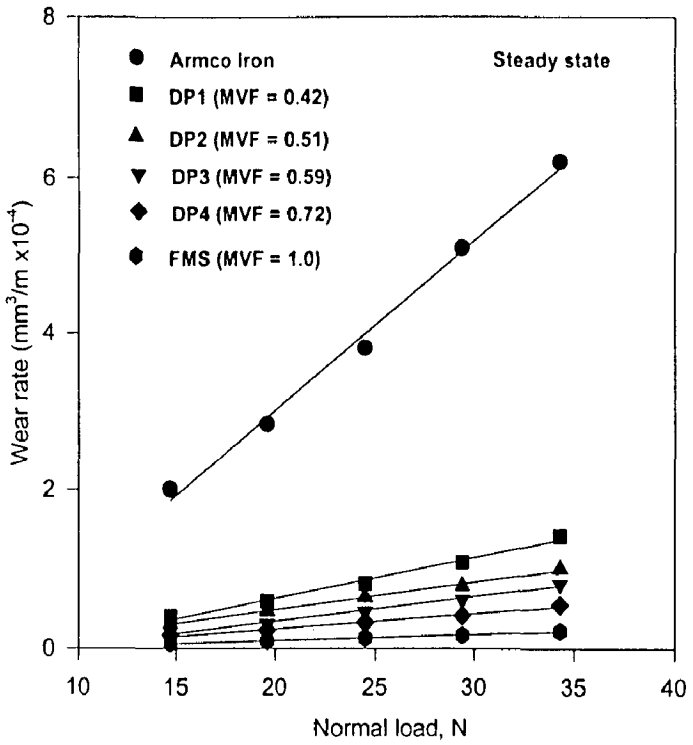

Fig. 6.17 Variation of wear rate with normal load in Armco iron, dual phase steels and FMS corresponding to second linear segment (steady state).

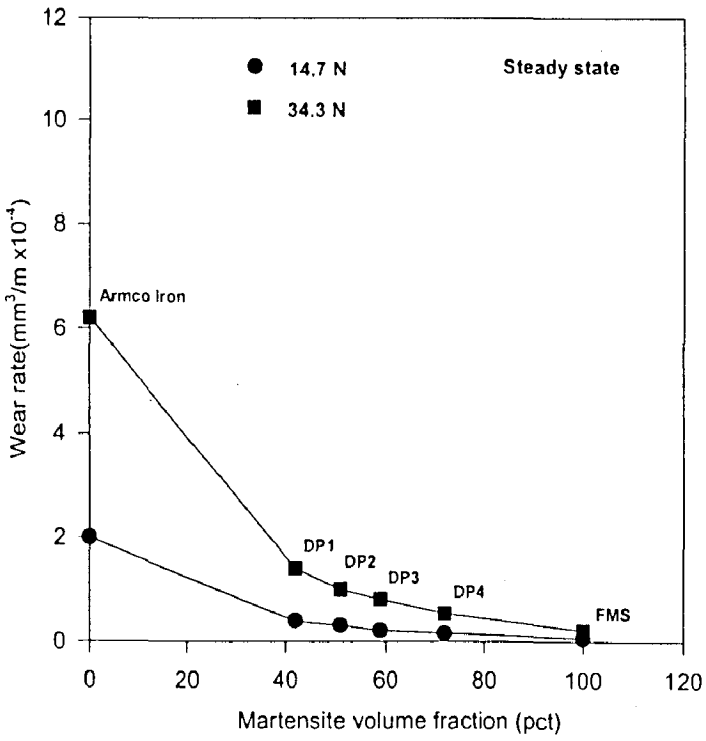

Fig. 6.18 Variation of wear rate with martensite volume fraction at the normal loads of 14.7 and 34.3 N in the steady state.

with further increase in the martensite volume fraction beyond 72 pct. It is further observed that the decrease in wear rate with martensite volume fraction is relatively more at a higher load of 34.3 N as compared to the lower load of 14.7 N.

Figure 6.17 shows a comparison of wear rate with normal load in the steady state of wear for the Armco iron, dual phase steels - DP1 to DP4 and FMS. The variation of the wear rate is represented by diverging lines of least square fit as one moves from a lower load of 14.7 N to a higher load of 34.3 N. The wear rate decreases with increasing martensite volume fraction at the same normal load. This effect has been directly demonstrated for the steady state of wear in Fig. 6.18 which shows the variation of the wear rate with the martensite volume fraction at the minimum and maximum loads of 14.7 and 34.3 N used for this investigation. The wear rate decreases with increasing volume fraction of martensite. The wear rate decreases linearly in the martensite range between 42 to 72 pct corresponding to DP1 and DP4 steel as can be seen from Fig. 6.18. Thereafter, the wear rate appears to saturate with further increase in volume fraction of martensite beyond 72 pct. It is further observed that the decrease in wear rate with martensite volume fraction is relatively more at a higher load of 34.3 N as compared to that at the lower load of 14.7 N.

(iv) Estimation of wear rate

The wear rates for both the run-in and the steady state have been estimated on the basis of (i) estimated load sharing between constituent phases and (ii) the observed wear coefficients of ferritic Armco iron and martensitic FMS by using Eq. (4.19). The calculated and observed variations of wear rate with normal load in run-in stage of wear for dual phase steels DP1, DP2, DP3 and DP4 containing the martensite volume fractions of 42, 51, 59 and 72 pct are shown in Figs.6.19 (a) to (d), respectively. The calculated wear rate increases linearly with the load for all the DP steels. The calculated wear rate shows a good matching

with the observed wear rate at lower loads but has increasingly larger difference with the observed values at increasing loads. The slope of the variation of wear rate with normal load decreases with increasing volume fraction martensite for both the estimated and observed variations as can be seen from Figs. 6.19 (a) to (d). The estimated and observed values of wear rate become closer at higher loads when the volume fraction of martensite increases.

The calculated (using Eq. (4.19)) and observed variations of wear rate with normal load in the steady state for dual phase steels DP1, DP2, DP3 and DP4 containing the martensite volume fractions of 42, 51, 59 and 72 pct are shown in Figs.6.20 (a) to (d), respectively. The slope of the variation of wear rate with normal load decreases with increasing volume fraction martensite for both the estimated and the observed variations. The calculated wear rates show a good matching with the experimentally observed wear rates at lower loads but have increasingly larger difference with the observed values at increasing loads. However, the difference between calculated and observed wear rates decreases and their values become closer at the higher loads when the volume fraction of martensite increases. The difference between estimated and observed wear rates is much less in the steady state as compared to that in the run-in stage of wear as can be seen from Figs. 6.19 (a) to (d) and Figs. 6.20 (a) to (d). In DP3 and DP4 steels the least square fit lines for calculated and experimental wear rates appear to cross at some intermediate load with values of calculated and experimental wear rates falling in the same band.

The wear rates have also been estimated using the oxidative wear model proposed in Chapter 4 where it is assumed that the critical thickness of oxides and probability of their removal are same in both the constituent phases i.e., ferrite and martensite in the dual phase steel following Eq. (4.44). The average critical thickness has been assumed to be 1 μm on the basis of the work Sullivan *et al* (1980) in which they have reported that the critical thickness of oxide decreases as the sliding velocity decreases. The oxidation rate constant has been

assumed to be the same as given by Kubaschewaski and Hopkins (1962) for the static oxidation of iron to Fe_2O_3. The values of the fraction of oxygen, f, in oxide and the density of the oxide have also been taken from the work of the Sullivan *et al* (1980). The variations of calculated and observed wear rate with normal load in both run-in and steady state wear for dual phase steels DP1, DP2, DP3 and DP4 containing the martensite volume fractions of 42, 51, 59 and 72 vol pct are shown in Figs.6.21 (a) to (d), respectively. The line of the least square fit for the calculated wear rate is same for both the run-in and the steady state of wear. The calculated wear rate increases linearly with the load for all the DP steels and the calculated values are found to be much higher than experimentally observed values in both run-in and steady state as shown in Figs. 6.21 (a) to (d). However, if the oxidation rate is taken lower or the critical thickness of oxide layer is taken higher the estimated wear rate may match the observed wear rate. The lines of the least square fit are almost parallel for DP1 and DP2 steel in the run-in stage as can be seen from the Figs. 6.21 (a) and (b) but the estimated variation has a higher slope than those observed for DP3 and DP4 steels as shown in Figs. 6.21 (c) and (d). The estimated variation has higher slope in the steady state for all the dual phase steels and the difference in slope increases with the increasing volume fraction of martensite as seen from the Figs. 6.21 (a) to (d).

The wear rates in both run-in and steady state have also been estimated by using Eq. (4.50). It has been assumed that the critical thickness of the oxide layer and the probability for its removal are different for both the phases i.e., ferrite and martensite in the dual phase steel. The average values of the critical thickness of the oxide layer for ferrite and martensite have been determined from the experimentally observed wear rates of the fully ferritic Armco iron and fully martensitic steel simulating the ferrite and martensite phase, respectively, in the dual phase steel. Figures 6.22 (a) to (d) show the variations of calculated and observed wear rates with normal load in run-in stage of wear for dual phase steels DP1, DP2, DP3 and DP4 containing the martensite volume fractions of 42, 51, 59 and 72 vol pct

respectively. The calculated wear rates are found to be consistently lower at all the loads in DP1, DP2 and DP3 steels but the difference is more particularly at higher loads. The slope of variation of wear rate with load increases with decreasing martensite volume fraction in both the estimated and observed variations. The estimated and observed values of wear rate become closer at higher load when volume fraction of martensite increases as shown in Figs. 6.22 (a) to (d).

The calculated (using Eq. (4.50)) and observed variations of wear rate with normal load in the steady state for dual phase steels DP1, DP2, DP3 and DP4 containing the martensite volume fractions of 42, 51, 59 and 72 vol pct are shown in Figs.6.23 (a) to (d), respectively. The calculated wear rate increases linearly with the load for all the DP steels. The calculated wear rates show a good matching with the experimentally observed wear rates at the lower loads but have increasing larger difference with the observed values at increasing loads. However, the difference is relatively small for the DP3 and DP4 steels as shown in Figs. 6.23 (c) and (d) and within the limits of the error the calculated and the experimental values show a good matching. At lower loads the calculated and experimental values are found to be almost same in DP1 and DP2 steels but their difference increases as the load increases from 14.7 to 34.3 N, as shown by the diverging lines of least square fit in Figs. 6.23 (a) and (b). In DP3 and DP4 steels, the least square fit lines for calculated and experimental wear rates appear to cross at some intermediate load with values of calculated wear rate being higher than the experimental values below this load and being lower than the experimental values beyond this load as shown in Figs. 6.23 (c) and (d). The slope of variation of wear rate with normal load decreases as the volume fraction of martensite increases for both the estimated and the observed variations. However, the estimated and the observed values of wear rate become closer as the volume fraction of the martensite increases as can be seen from Figs. 6.23 (a) to (d).

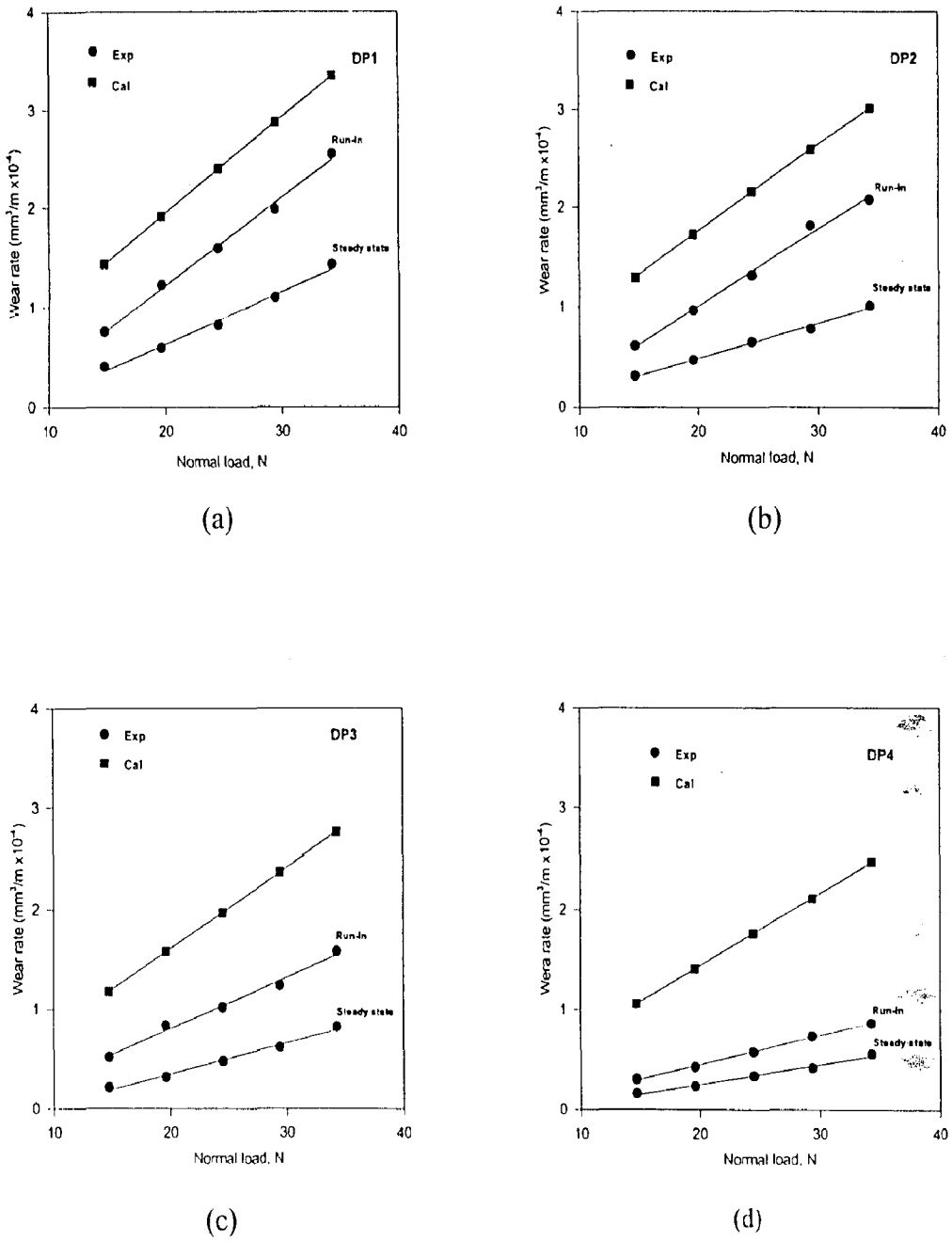

Fig. 6.19 The variation of calculated and experimental wear rate with normal load in run-in stage for dual phase steels (a) DP1, (b) DP2, (c) DP3 and (d) DP4, estimated on the basis of load sharing.

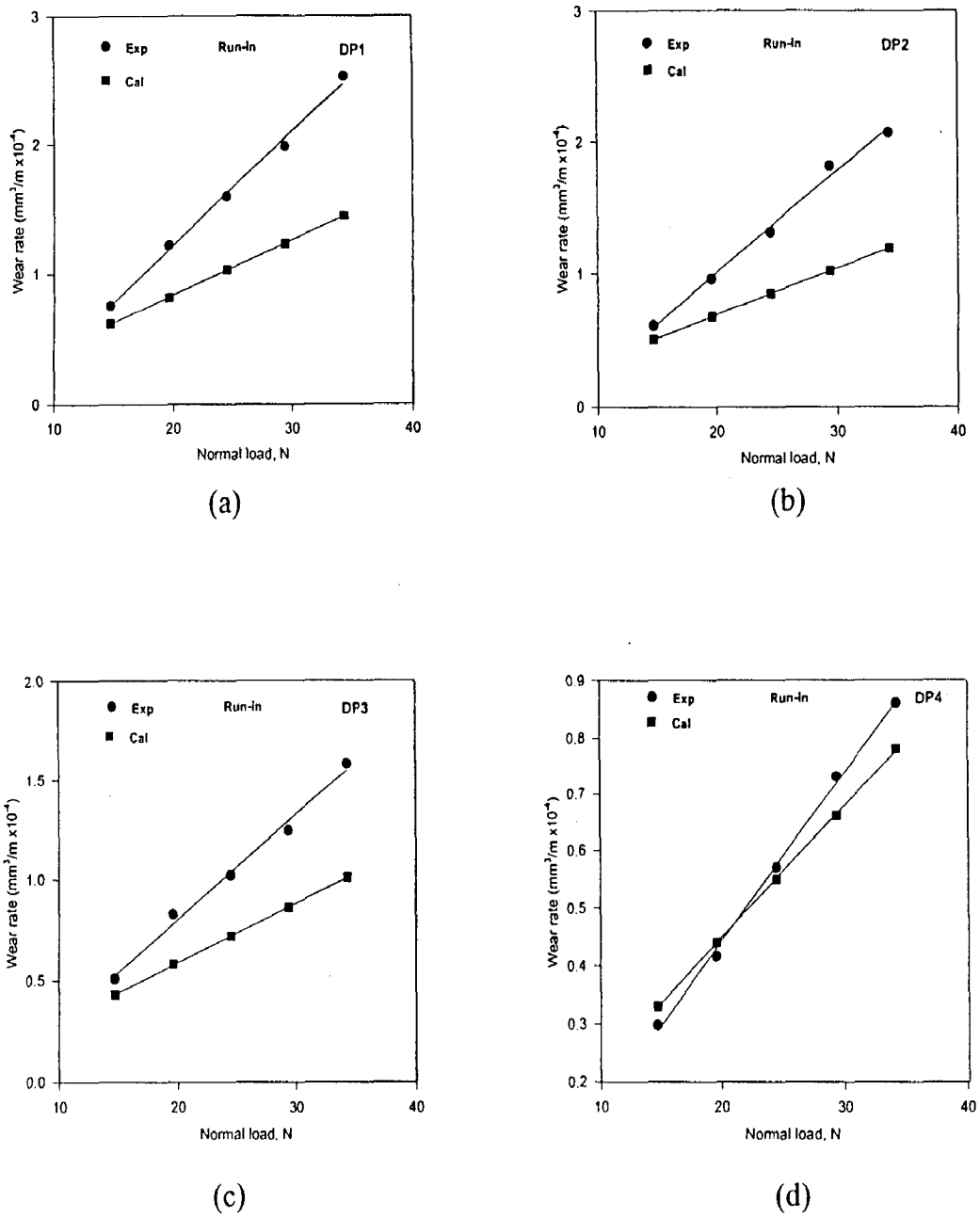

Fig. 6.20 The variation of calculated and experimental wear rate with normal load in steady state for dual phase steels (a) DP1, (b) DP2, (c) DP3 and (d) DP4, estimated on the basis of load sharing.

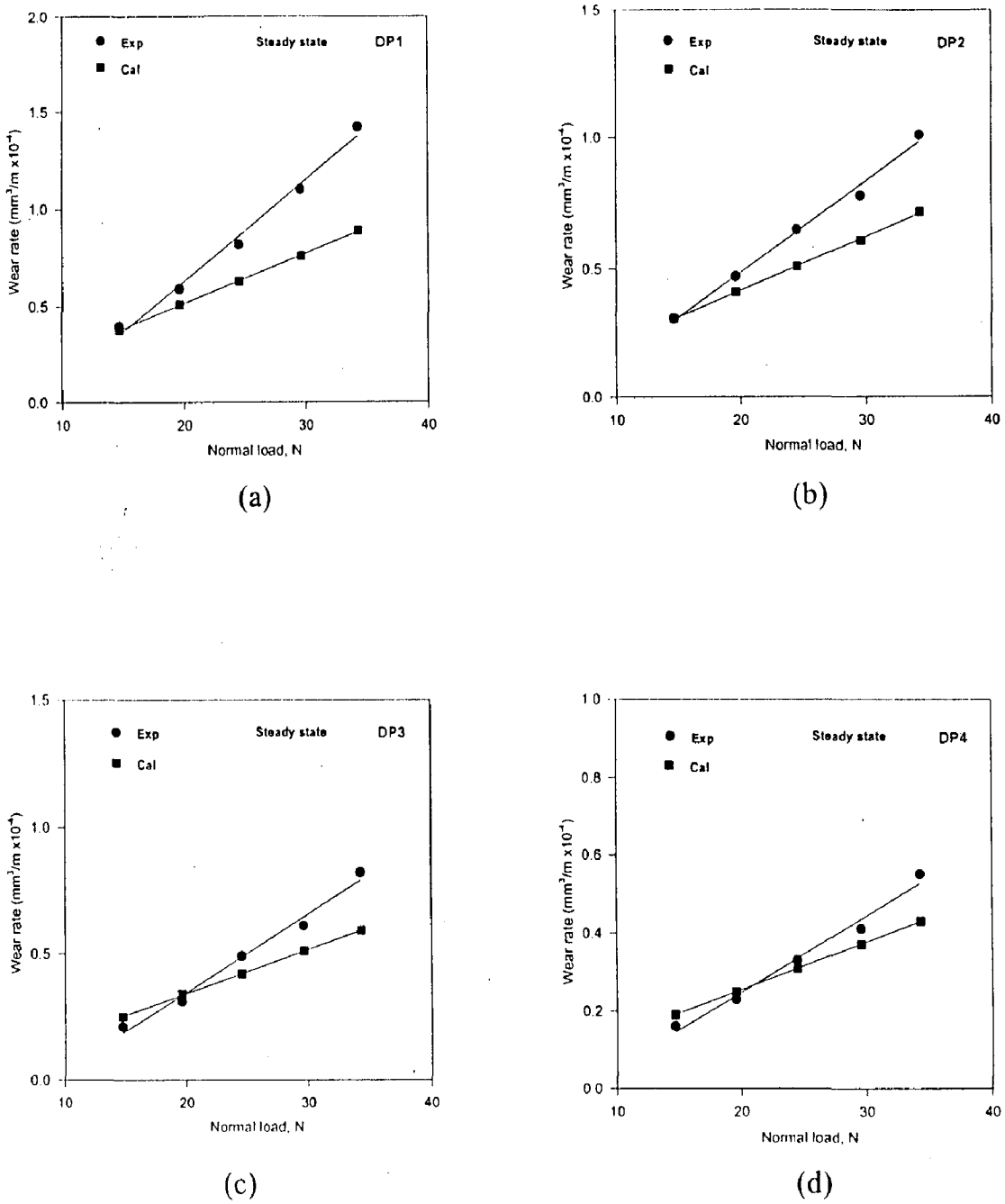

Fig. 6.21 The variation of calculated and experimental wear rate with normal load for both the run-in and the steady of wear for dual phase steels (a) DP1, (b) DP2, (c) DP3 and (d) DP4, estimated by oxidative wear model assuming the same critical thickness and probability of removal of oxide for both the phases.

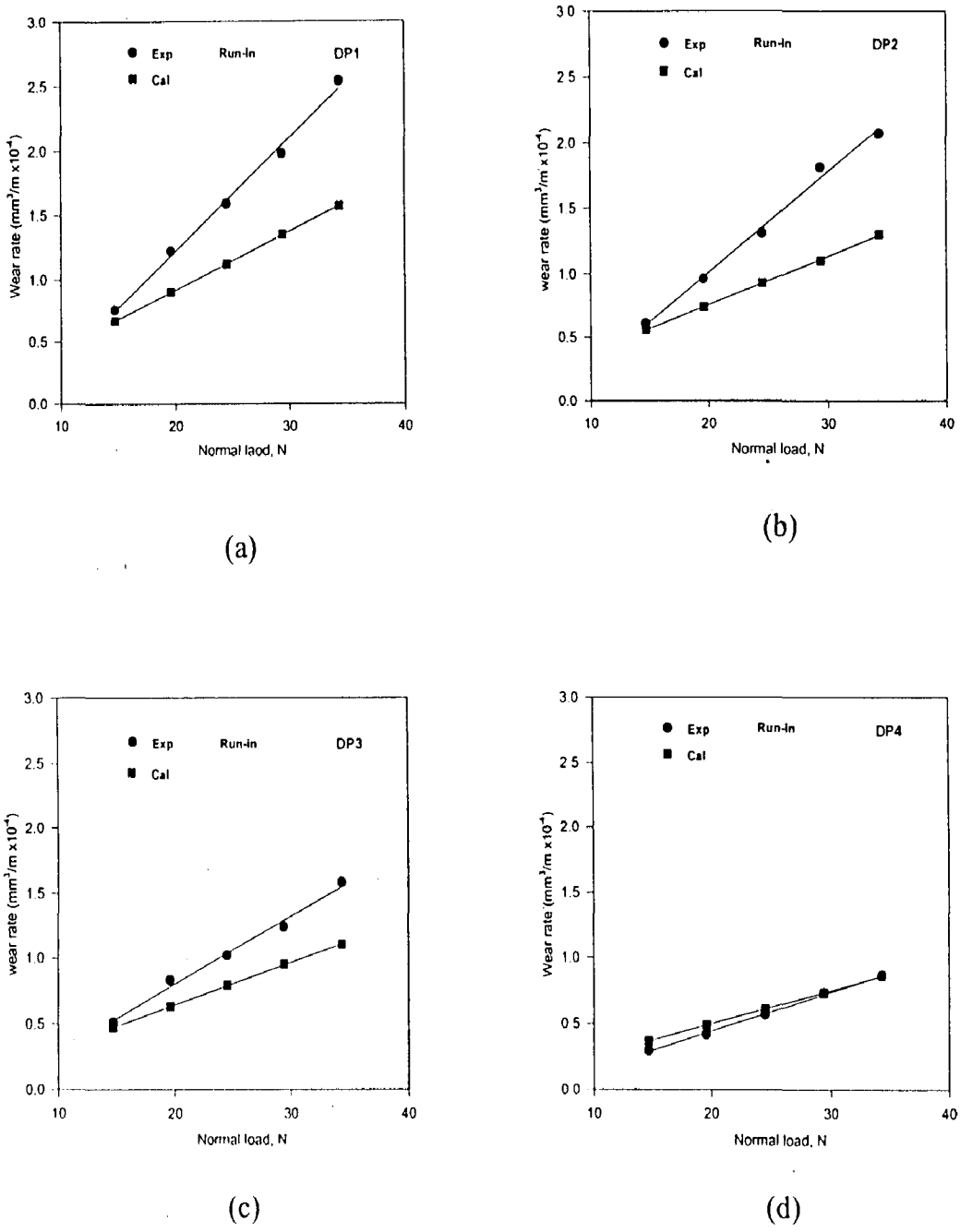

Fig. 6.22 The variation of calculated and experimental wear rate with normal load in run-in stage for dual phase steels (a) DP1, (b) DP2, (c) DP3 and (d) DP4, estimated on the basis of the oxidative wear model with different critical thickness and probability of removal of oxide for both the phases.

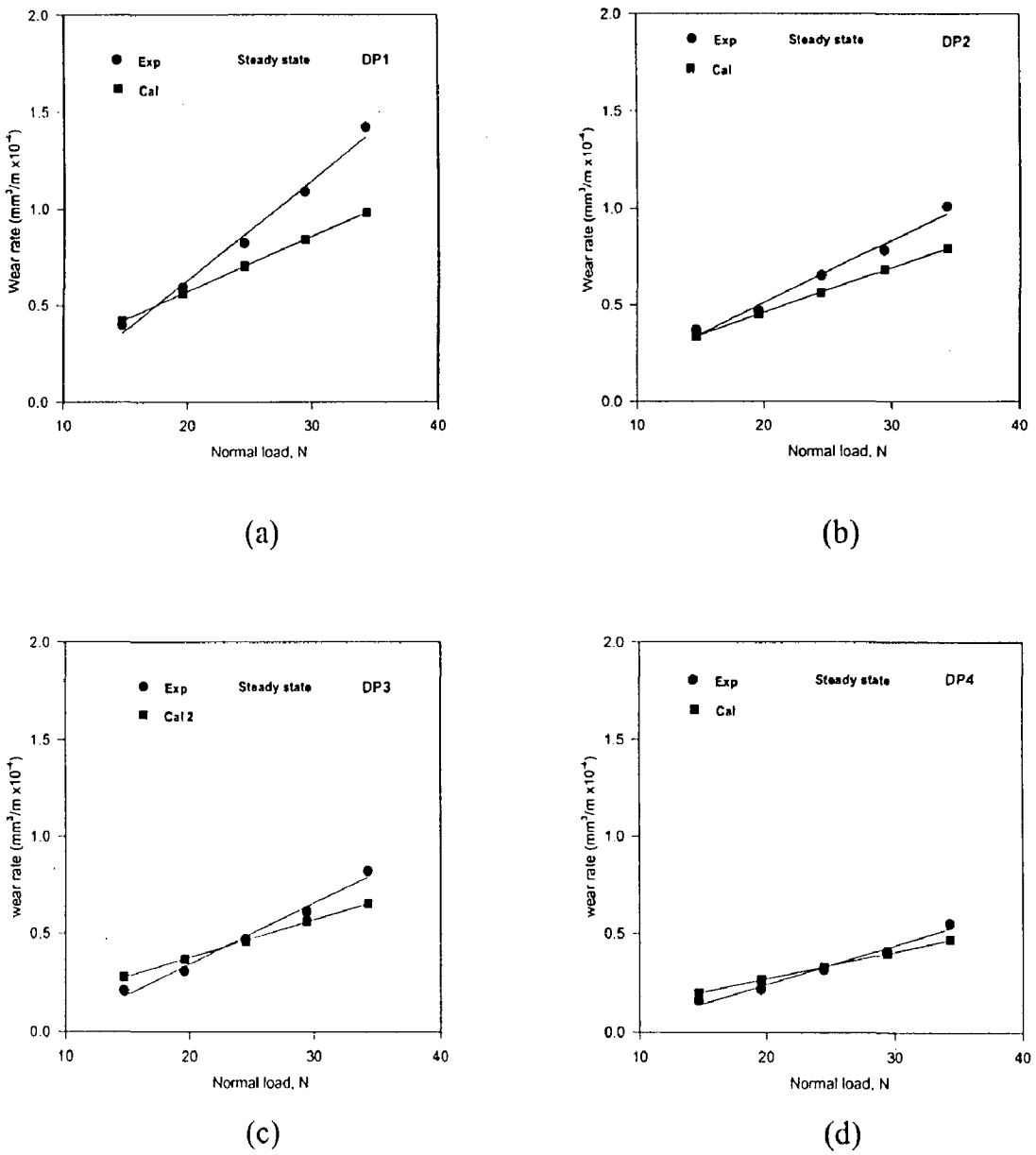

Fig. 6.23 The variation of calculated and experimental wear rate with normal load in steady state for dual phase steels (a) DP1, (b) DP2, (c) DP3 and (d) DP4, estimated on the basis of the oxidative wear model with different critical thickness and probability of removal of oxide for both the phases.

(v) Variation of wear coefficient with hardness

The wear coefficient has been estimated from the slope of the linear variation of wear rate with load, by multiplying it with the initial hardness of the corresponding pin material. The wear coefficients under different loads for Armco iron, N steel, DP steels and FMS for both the run-in and the steady state of wear are given in Tables A.6 to A.10 in the appendix. However, the average wear coefficients in both the run-in and the steady state of wear for Armco iron, N steel, DP steels and FMS are given in Table A.12 in the appendix. Figure 6.24 shows the variation of the wear coefficient with hardness corresponding to both the run-in and the steady state of wear for Armco iron, N steel, DP1, DP2, DP3, DP4 and FMS. It is observed that the wear coefficient changes relatively less in the hardness range from 84 to 320 HB which correspond to Armco iron and DP2 steel containing 51 vol pct martensite. However, beyond this value of hardness, there is a sharp decrease in the wear coefficient with increase in hardness in the range between from 320 and 373 HB corresponding to DP2 steel and DP4 steel containing 72 vol pct martensite. After a hardness of 373 HB, the decrease in wear coefficient is observed to be less again. Both the run–in and the steady state wear coefficient changes similarly but the magnitude of change in the hardness range between 320 and 373 HB appears to be more for run-in stage than for steady state of wear.

(b) Dry Sliding Friction

(i) Variation of coefficient of friction with sliding distance

Figures 6.25 to 6.31 show the variation of coefficient of friction with sliding distance under different normal loads of 14.7, 19.6, 24.5, 29.4 and 34.3 N for Armco iron, FMS, N steel and DP steels with increasing volume fraction of martensite - DP1, DP2, DP3 and DP4,

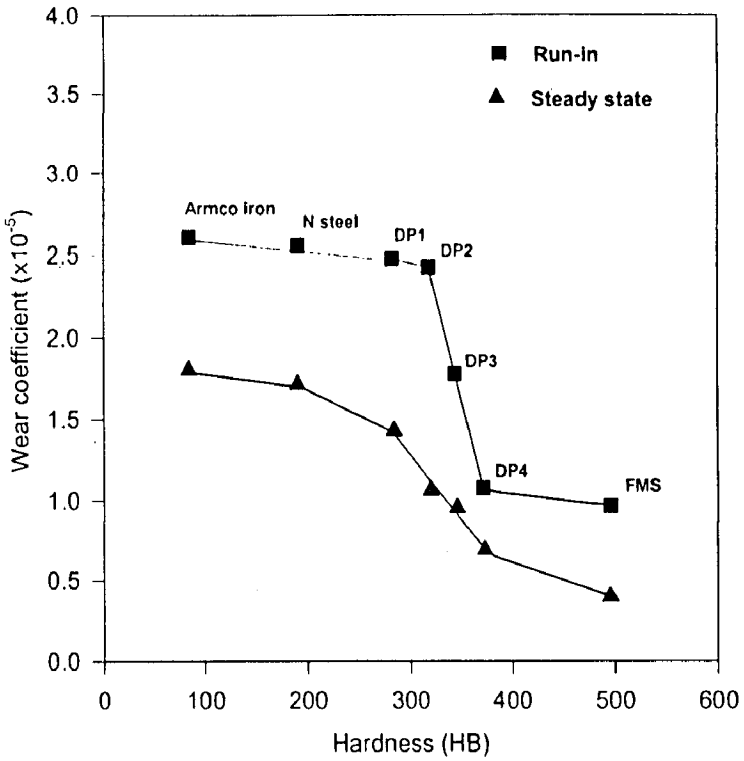

Fig. 6.24 The variation of the wear coefficient with hardness in both the run-in and the steady state of wear for Armco iron, N steel, DP1, DP2, DP3, DP4 and FMS.

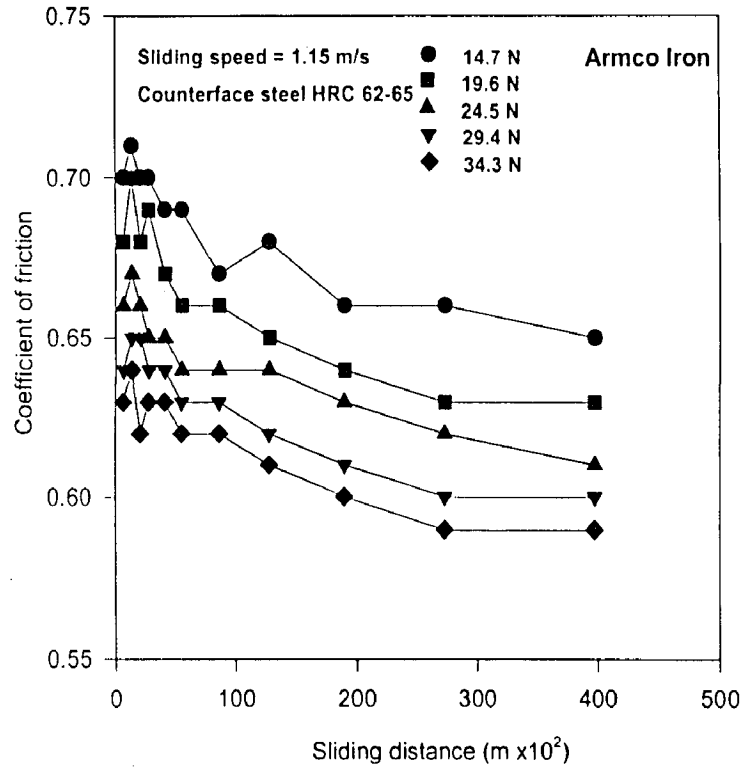

Fig. 6.25 Variation of sliding friction coefficient with distance of sliding at different loads in Armco iron.

respectively. Figure 6.25 shows the variation of the friction coefficient with sliding distance for Armco iron and it may be noted that at a given load friction coefficient in the run-in stage fluctuates around a mean level, then lessens and stabilizes after a certain period. It is further observed that with increasing load, the friction coefficient decreases. For example the friction coefficient attains a value of 0.65, 0.63, 0.61, 0.60 and 0.59 at the maximum sliding distance of 39.74 km as the load increases from 14.7 N to 34.3 N in steps of 4.9 N.

Figure 6.26 shows the variation of the friction coefficient with sliding distance for the fully martensitic steel (FMS) and it can be observed that at a given load the friction coefficient in the run-in stage fluctuates around a mean level, then lessens and stabilizes after a certain period. It is further observed that with increasing load the friction coefficient decreases. The friction coefficient attains a value of 0.47, 0.44, 0.42, 0.40 and 0.39 at the maximum sliding distance of 39.74 km as the load increases from 14.7 N to 34.3 N in steps of 4.9 N. These values of the friction are much less than the values attained in case of the Armco iron.

Figure 6.27 shows the variation of the friction coefficient with sliding distance for the normalised (N) steel and it may be noted that at a given load the friction coefficient in the run-in stage fluctuates around a mean level, then lessens and stabilizes after a certain period. It is further observed that with increasing load the friction coefficient decreases. The friction coefficient attains a value of 0.61, 0.60, 0.58, 0.56 and 0.55 at the maximum sliding distance of 39.74 km as the load increases from 14.7 N to 34.3 N in steps of 4.9 N. These values of the friction are lesser than the values attained in case of the Armco iron but higher compared to the FMS.

Figure 6.28 shows the variation of the friction coefficient with sliding distance for the DP1 steel containing 42 vol pct martensite and it may be noted that at a given load the

friction coefficient in the run-in stage fluctuates around a mean level, then lessens and stabilizes after a certain period. It is further observed that with increasing load the friction coefficient decreases. The friction coefficient attains a value of 0.54, 0.53; 0.51, 0.50 and 0.48 at the maximum sliding distance of 39.74 km as the load increases from 14.7 N to 34.3 N in steps of 4.9 N. These values of the friction are lower than the values attained in case of the Armco iron but higher as compared to the FMS.

Figure 6.29 shows the variation of the friction coefficient with sliding distance for the DP2 steel containing 51 vol pct martensite and it may be noted that at constant load the friction coefficient in the run-in stage fluctuates around a mean level, then lessens and stabilizes after a certain period. It is further observed that with increasing load the friction coefficient decreases. The friction coefficient attains a value of 0.53, 0.51, 0.50, 0.49 and 0.48 at the maximum sliding distance of 39.74 km as the load increases from 14.7 N to 34.3 N in steps of 4.9 N. These values of the friction are lower than the values attained in case of the Armco iron but as higher compared to the FMS.

Figure 6.30 shows the variation of the friction coefficient with sliding distance for the DP3 steel containing 59 vol pct martensite and it may be noted that at constant load the friction coefficient in the run-in stage fluctuates around a mean level, then lessens and stabilizes after a certain period. It is further observed that with increasing load the friction coefficient decreases. The friction coefficient attains a value of 0.53, 0.50, 0.48, 0.47 and 0.44 at the maximum sliding distance of 39.74 km as the load increases from 14.7 N to 34.3 N in steps of 4.9 N. These values of the friction are lower than the values attained in case of the Armco iron but higher compared to the FMS.

Figure 6.31 shows the variation of the friction coefficient with sliding distance for the DP4 steel containing 72 vol pct martensite and it may be noted that at constant load the

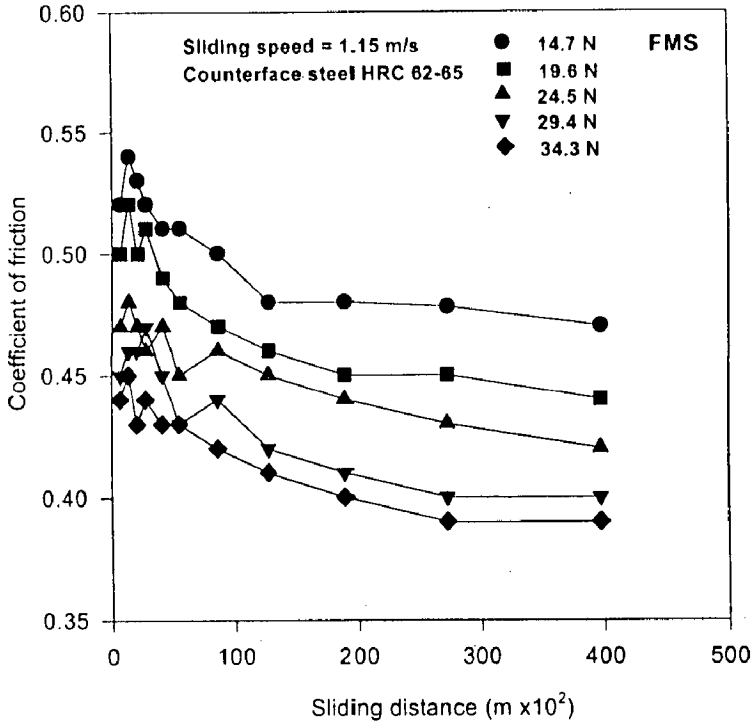

Fig. 6.26 Variation of sliding friction coefficient with distance of sliding at different loads in fully martensitic steel.

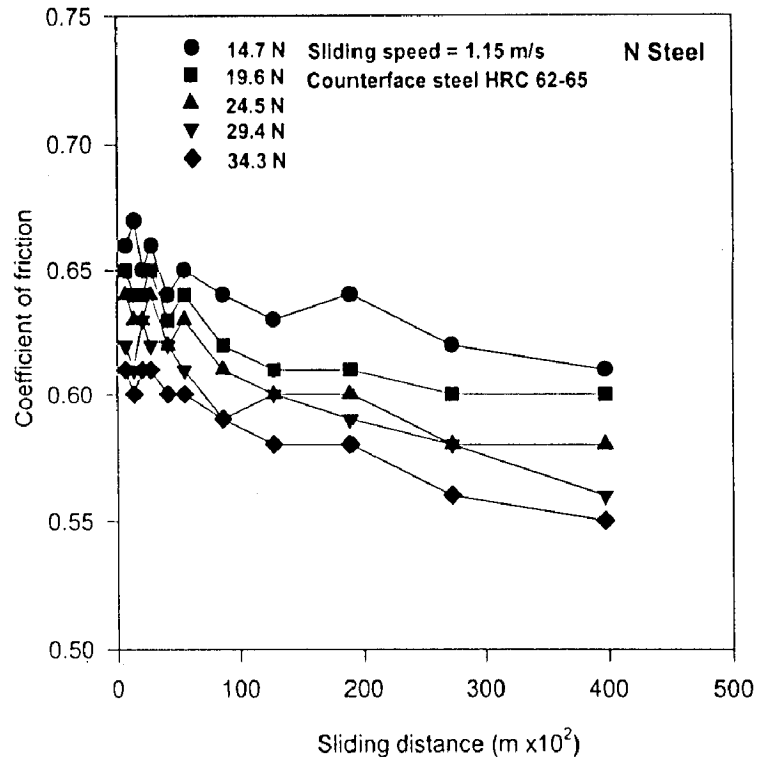

Fig. 6.27 Variation of sliding friction coefficient with distance of sliding at different loads in normalised steel.

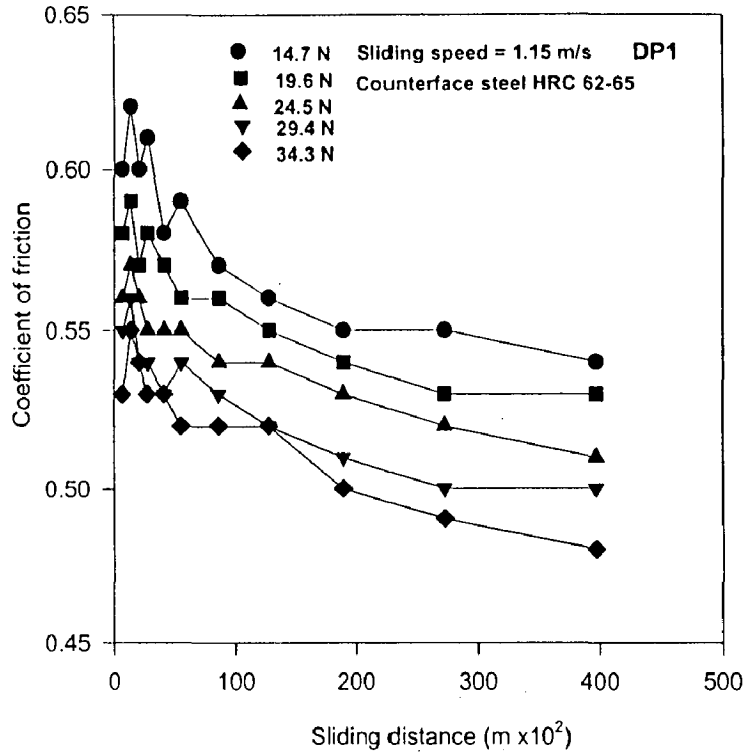

Fig. 6.28 Variation of sliding friction coefficient with distance of sliding at different loads in dual phase steel, DP1, containing 42 pct martensite.

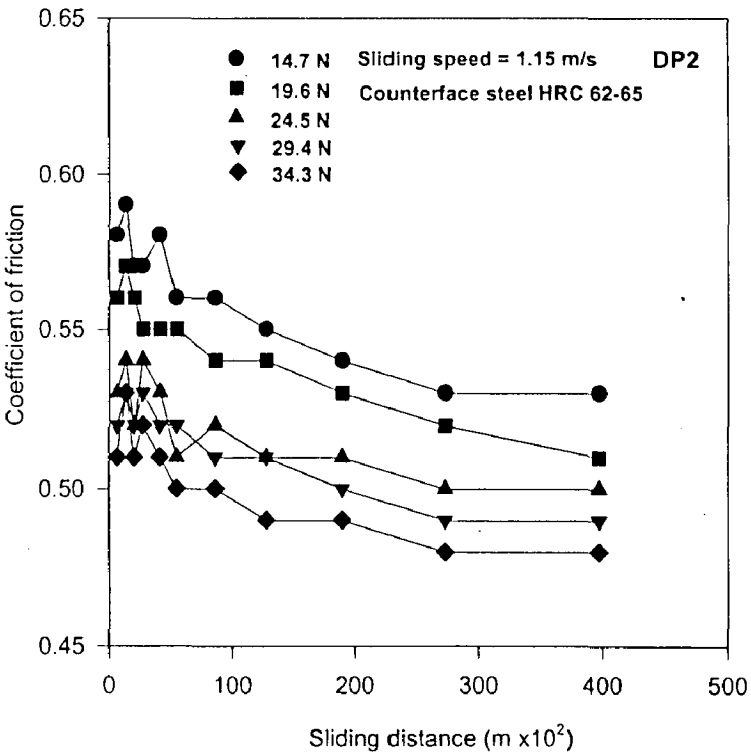

Fig. 6.29 Variation of sliding friction coefficient with distance of sliding at different loads in dual phase steel, DP2, containing 51 pct martensite.

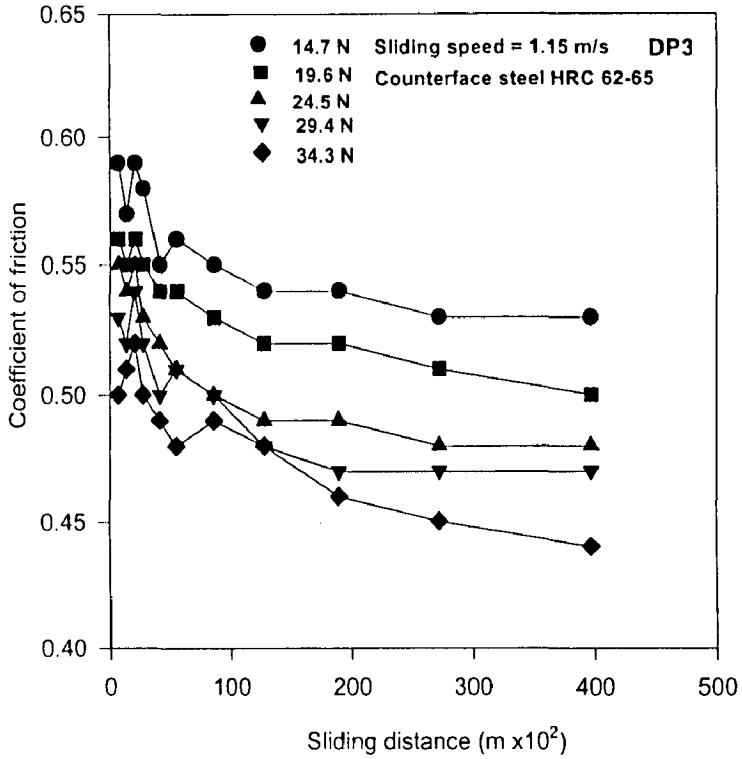

Fig. 6.30 Variation of sliding friction coefficient with distance of sliding at different loads in dual phase steel, DP3, containing 59 pct martensite.

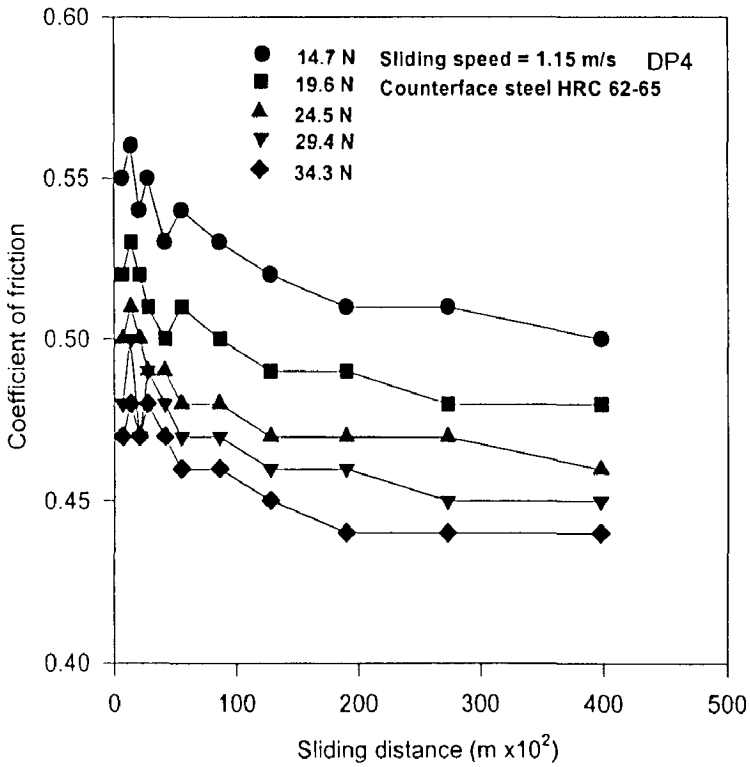

Fig. 6.31 Variation of sliding friction coefficient with distance of sliding at different loads in dual phase steel, DP4, containing 72 pct martensite.

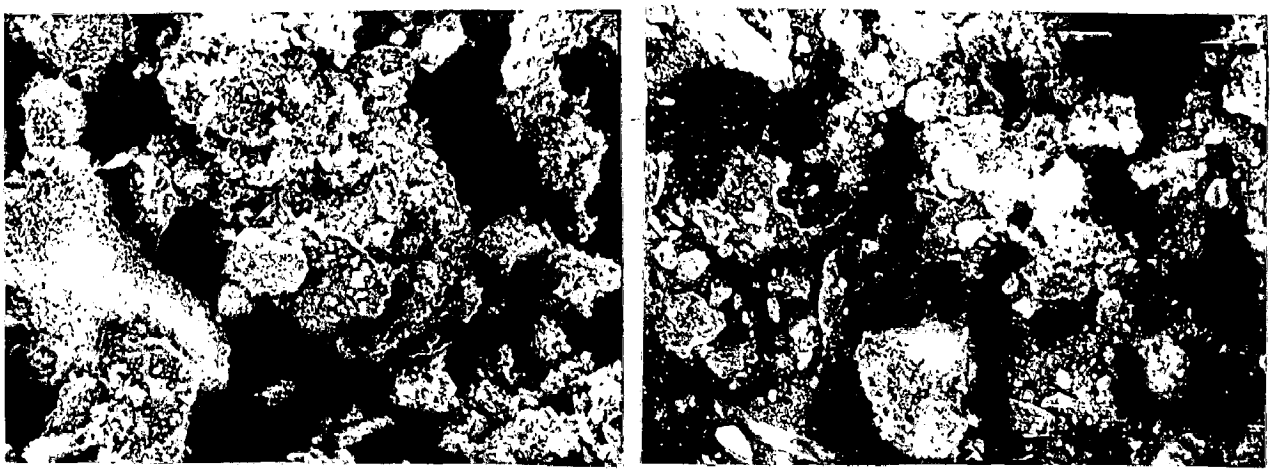

(a) (b)

Fig. 6.79 SEM micrographs showing wear debris of DP2 steel (a) corresponding to the run-in stage, X 150 and (b) corresponding to the steady state, X 400.

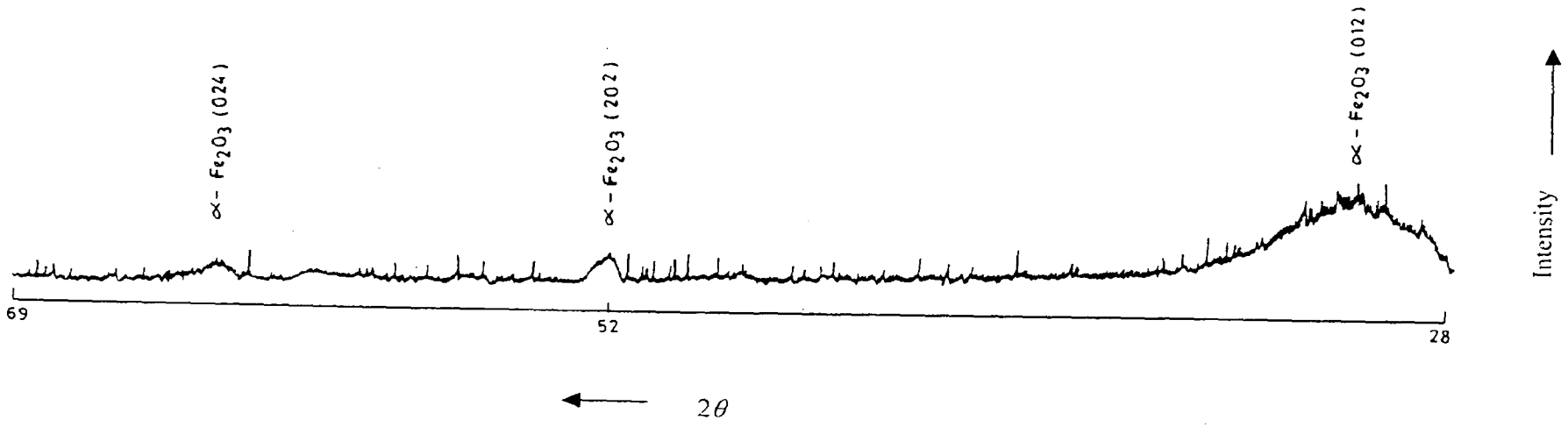

Fig. 6.80 X-ray diffraction patterns of the wear debris of Armco iron generated at a normal load of 34.3 N and collected from the disc counterface.

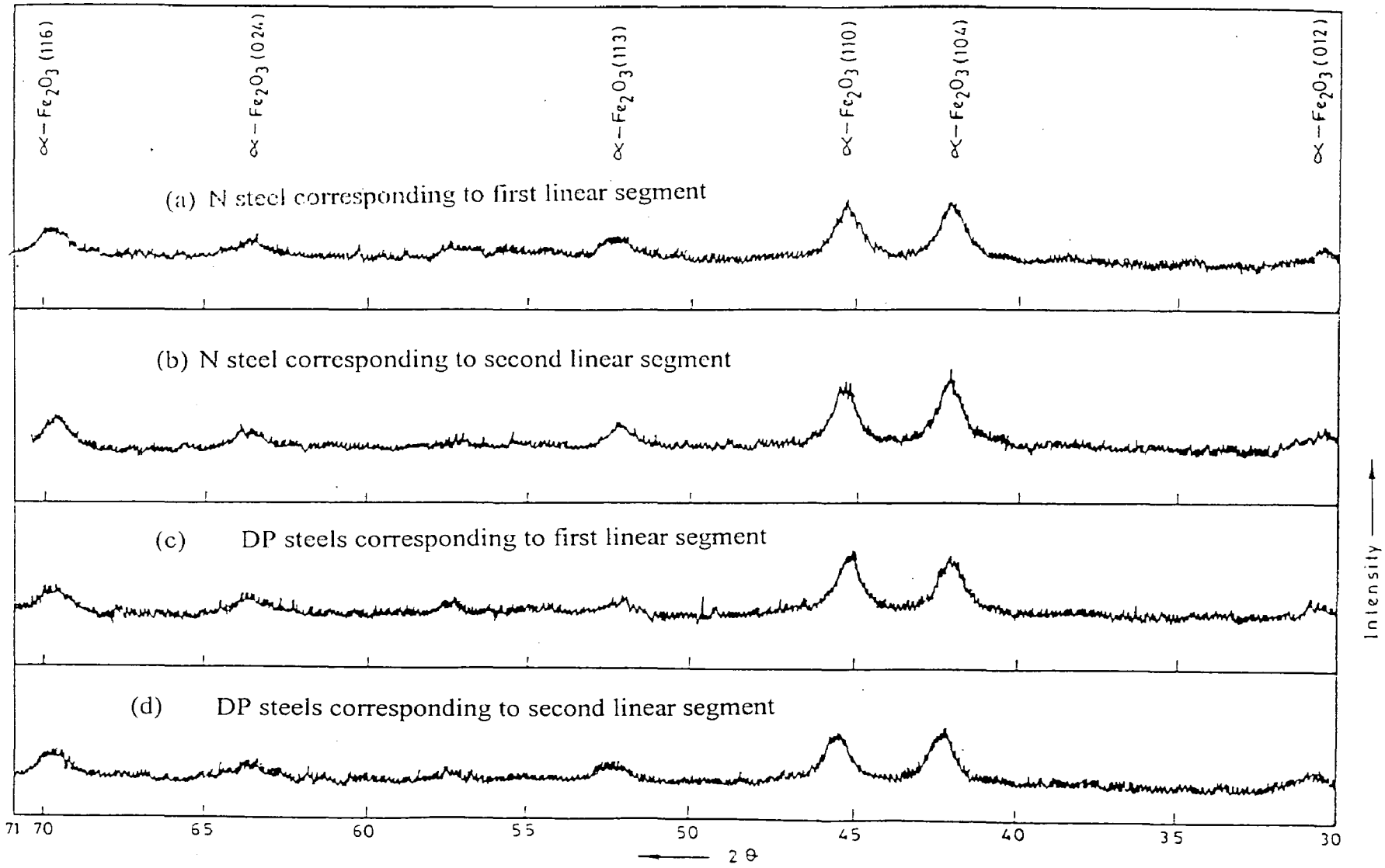

Fig. 6.81 X-ray diffraction patterns of the wear debris for both normalised and dual phase steels generated at a normal load of 34.3 N and collected from the disc counterface.

Figures 6.81 (a) to (d) show the X ray diffraction patterns of the wear debris of N and DP steels. Figures 6.81 (a) and (b) show the X-ray diffraction pattern of the wear debris of N steel that corresponds to first and second linear segments respectively, generated under a normal load of 34.3 N. Figures 6.81 (c) and (d) show the X-ray diffraction pattern of the wear debris of DP steel that corresponds to first and second linear segments, respectively, also under the same load of 34.3 N.

All the peaks in the patterns correspond to those belonging to α-Fe_2O_3. The corresponding $Sin\theta$ and d values are reported in Tables A.14 and A.15 in the appendix.. The miller indices of planes (hkl), giving rise to diffraction peaks, are shown in Figures 6.80 and 6.81 (a) through (d). However, no peak was observed for iron. When iron was present, it was not detected because of its small quantity.

6.1.6 Temperature of Sliding Surface

The rise in the temperature of the pin samples has been measured during wear with a fine chromel-alumel thermocouple brazed on the pin side about 3 mm above the mating surface and is monitored by a milivoltmeter. The temperature as measured by the above method is about 70^0C.

The theoretical bulk temperature at the surface of the specimen, calculated on the basis of the model given by Lim and Ashby (1987), is found to 338 K, i.e., 65^0C, which is almost the same as the temperature measured 3 mm above the sliding surface. The contact temperature of the sliding surface, calculated by using the heat flow equations given by Alpas and Ames (1995), is 688 K, i.e., 415^0C.

6.2 DISCUSSION

The dry sliding friction and wear are known to be sensitive to the working conditions (i.e., load, sliding speed, environment, temperature etc.), the nature of the sliding system, the microstructure and the properties of the mating materials in the sliding contact. In a two phase material, the incorporation of the hard phase affects the sliding wear by hardening and thereby, reducing the real area of contact between the sliding body of this material and counterface (Ramesh *et al*, 1992). Dual phase steels offer an opportunity for an *in situ* incorporation of a hard phase of martensite in a relatively softer phase of ferrite. A hard phase like martensite in a relatively softer phase like ferrite may satisfy the requirements of a good bearing material. The soft phase is expected to adjust itself to the contour of the mating body to establish conditions for hydrodynamic lubrication whereas, the hard phase bears the load. Also the incorporation of the hard phase helps in imparting the required strength to the softer matrix which provides the required ductility to the two phase material.

In the present investigation the cumulative volume loss in the ferritic Armco iron, martensitic FMS, N steel, DP1, DP2, DP3 and DP4 steels increases linearly with the sliding distance at a given load. After an initial distance covering the run-in stage, the slope generally decreases establishing steady state wear. A similar variation is observed under different loads, which follows Archard's law predicting linear variation of cumulative volume loss in wear with sliding distance, as shown in Figures 6.1 to 6.7. The observed variation has been fitted by the least square lines in two segments, to establish the effect of run-in period separately from the steady state. The slope of the lines of least square fit in Figs. 6.1 to 6.7 give the wear rates separately, in the run-in and the steady state of wear under different loads. The trend observed here is in agreement with the work of Archard and Hirst (1956), Clayton (1980), Wayne and Rice (1983), Smith (1986, 1988), Iwabuchi *et al* (1988) who have also

observed a discontinuous transition from the run-in to the steady state with sliding distance in steels.

A higher cumulative volume loss, which gives rise to a higher wear rate in the run-in stage as compared to that in the steady state in fully ferritic material of Armco iron as shown in Fig. 6.8, may be explained on the basis of the initial surface roughness of the wearing material. When two previously unworn surfaces are first brought into contact and slid relative to one another, mechanical, thermal, chemical and microstructural changes begin to occur in and adjacent to the contact interface Blau (1981). It is well known that the surfaces of the engineering components are rough and have asperities, which are gentle undulations protruding out of the surface. As the relative motion of sliding between the two bodies takes place, the contact occurs at these asperities and the surfaces evolve to attain better conformity to each other at the end of run-in stage. The wear in this stage occurs by the removal of high asperities and the removal of initial oxide layers and surface contaminants. Consequently, the material loss is higher in the run-in stage of wear. Therefore, the wear rate, given by the slope of the line in Fig. 6.1, is also high in run-in stage as shown in Fig. 6.8. In the run-in stage the oxide layer may be in the formative stage during sliding and eventually evolves to the steady state providing an extent of cover determined by the conditions of load, sliding velocity and environmental conditions. The onset of the steady state, shown by second linear segment in Fig. 6.1, may be explained on the basis of attaining steady state in respect of the real area of oxide contact and at the same time, the evolution of mating surfaces to better conformity. The oxide contact at junctions depends both on the oxidation of metal on the sliding surface and on the formation of compacted transfer layer of the wear debris generated during sliding. Figures 6.37 (a) and (b) and Figs. 6.38 (a) to (c) show the SEM micrographs of the wear surfaces of Armco iron worn under different loads in both the run-in and the steady state respectively. Some exposed metallic surface apart from the transfer layer of oxide is visible in all these micrographs. However, it is observed that in the run-in stage, the transfer layer

starts cracking at places at the highest load of 34.3 N used in the present study as shown in Fig. 6.37 (c) giving rise to flaked off particles and agglomerates from the transfer layer. Thus, the wear debris may contain both fine oxide particles and flaked off oxide agglomerates as shown in Figs. 6.65 (a) to (c) and 6.66 (a) to (c) for the wear debris generated under the loads of 14.7, 24.5 and 34.3 N respectively for the run-in and the steady state. The amount of flaked off agglomerates increases with increasing load as indicated by widespread cracking of transfer layer at higher load as shown in Fig. 6.37 (c). At the loads used in the present investigation the wear is primarily mild oxidative in nature in both the run-in and the steady state of wear in Armco iron as is evident from the transfer layer and the wear debris. The oxidative nature of wear is further confirmed by the X-ray diffraction pattern of the wear debris generated during steady state as shown in Fig. 6.80. All the peaks in the pattern correspond to those belonging to α-Fe_2O_3. The Miller indices of the planes (*hkl*), which have given rise to the diffraction peaks, are shown in Fig. 6.80. However, no peak has been observed for metallic iron. Therefore, metallic wear particles, even if present, could be beyond the detection limit of X-ray diffraction. Some cracking below the subsurface layer is also observed at a load of 24.5 N as shown in Fig.6.54, pointing towards a possibility of a delamination wear, but no trace of a metallic particle is observed in the X-ray diffraction pattern of the wear debris. Hence, it appears that the cracked particle gets oxidised before generating wear debris. Lim and Bruntun (1986) have also observed that in the load range of 2 to 30 N and sliding velocity ranging from 0.44 to 0.87 m/s the wear in pure iron occurs by a primarily mild oxidative mechanism. The range of loads used in the present investigation is similar to that used by Lim and Bruntun (1986) but a higher sliding velocity of 1.15 m/s has been used in the present work as compared to that used by them. A higher sliding velocity will generate higher frictional heat and cause more oxidation, hence, the observation of mild oxidative nature of the wear under conditions used in this study is in consonance with the observations of Lim and Bruntun (1986).

When a test sample is under dry sliding wear at relatively lower loads, the frictional heating helps atmospheric oxidation over the sliding surface, the oxide layer gets removed by repeated and multiple contacts and the wear debris of oxide particles is generated. The wear debris gets trapped between the sliding surfaces and is compacted into a layer. The continuing process of removal of the transfer layer and its reformation and thickening results in the fluctuation of friction coefficient, as observed in Fig. 6.25. At very short sliding distances, the fluctuation may also include the contribution resulting from the variation in contact that occurs when the sample and the counterface are evolving to develop a better surface conformity. The average coefficient of friction in both the run-in and the steady state is found to decrease linearly with increasing load for Armco iron as shown in Figs. 6.32 and 6.33. This may be attributed to the increased rate of oxidation and better compaction of the oxide caused by the enhanced frictional heating at higher loads. The junctions on oxidised area of surface will require relatively less energy to shear during sliding as compared to that for metallic junction. The average coefficient of friction in the run-in stage is also higher as compared to that in the steady state due to interlocking of high asperities in the run-in stage, which requires more energy to slide one asperity over the another and hence, the friction is higher in the run-in stage. But in the steady state, the area under the cover provided by the oxide and the transfer layer of oxides is more and the asperities have attained steady state height thereby reducing the friction in the steady state.

The wear rate in Armco iron increases linearly with increasing load in both the run-in and the steady state and this is in agreement with the work of Lim and Brunton (1986) who have also observed that the wear rate in Armco iron increases linearly with increasing load. However, wear rate is less in the steady state as compared to that in the run-in stage as shown in Fig. 6.8. As the sliding continues more and more debris is entrapped between the sliding surfaces and gets compacted due to repetitive sliding. A comparison of Figs. 6.37 (a) to (c) and 6.38 (a) to (c) for the run-in and the steady state respectively, clearly shows that the

extent of compaction of the transfer layer is more in the steady state as compared to that in the run-in stage of wear when it begins to form by compacting the wear debris trapped between sliding surfaces. This transfer layer protects the underlying metal and the wear rate decreases. Therefore, the wear rate is relatively lower in the steady state as compared to that in the run-in stage as shown in Fig. 6.8.

To examine the possibility of subsurface work hardening, the samples after the wear test were ground to a taper of 1:10 and Vickers macrohardness measurements were carried out from sliding surface along the taper. In Armco iron, the hardness near the sliding surface increased from 100 HV before sliding to 129, 152 and 174 HV after sliding under the normal loads of 14.7, 24.5 and 34.3 N respectively, applied during wear test. The increase in hardness could have resulted from the subsurface work hardening as revealed in the subsurface microstructures shown in Figs. 6.53 (a) to (c) worn under the loads of 14.7, 24.5 and 34.3 N respectively. A deformed layer of material in the subsurface region is clearly seen in all the micrographs and the extent of deformation increases with increasing load from 14.7 to 34.3 N. The decrease in friction at the higher loads with increasing theoretical real area of contact in Armco iron as shown in Fig. 6.36 (a) may also be contributed by increased work hardening of the surface during sliding. The increased hardness of the substrate due to work hardening is expected to lower the real area of contact, when one estimates the real area of contact from considerations similar to that in indentation hardness. But the ratio of the hardness of work hardened surface with respect to initial hardness of the material after sliding is less than the ratio of applied normal load. Thus, it may explain the lowering of friction with sliding at a given load but not the observed lowering of friction with increasing load. The extent of cover provided by the compacted transfer layer on the sliding surface may account for the decrease in friction at higher loads. Increased cover of transfer layer reduces the friction because of formation of relatively weaker junctions of lower shear strength in the oxide area.

The wear coefficient of Armco iron has been estimated from the slope of the linear variation of wear rate with load, *V/SL*, taken from Fig. 6.8 by multiplying it with the initial hardness of the material. Thus, the wear coefficient may be taken as the wear rate per unit real area of contact. In Armco iron, wear coefficients are 2.6×10^{-5} and 1.8×10^{-5} for the run-in and the steady state respectively. The lower wear coefficient in the steady state may be attributed to both a lower wear rate and a relatively lower real area of contact as compared to those in the run-in stage.

A higher cumulative volume loss and a relatively higher wear rate in the run-in stage as compared to that in the steady state in fully martensitic steel are shown in Figs. 6.2 and 6.9 and it could be explained on the basis of the development of the surface compatibility in the sliding contact as described for Armco iron. The SEM micrographs of the wear surfaces of FMS worn under the loads of 14.7 and 24.5 N in the run-in stage of wear as given in Figs 6.39 (a) and (b), show exposed metallic surface apart from the transfer layer of oxide. However, at the highest load of 34.3 N, the surface appears to be fully covered by the transfer layer and exposed metallic surface is hardly visible even in the late run-in stage as shown in Fig. 6.39 (c). Thus, it is apparent that the extent of compacted layer in the run-in stage depends both on the applied load and sliding time as it has also been observed for Armco iron. Figures 6.40 (a) to (c) show the wear surfaces of FMS after sliding through a distance of 39.74 km under different loads in the steady state in which the transfer layer of oxide is seen covering the entire area under the contact. The flaking off of this transfer layer of oxide generates larger agglomerates of oxide in the wear debris along with finer particles of oxide as observed in Figs. 6.69 (a) to (c) and 6.70 (a) to (c) showing the wear debris generated under the respective loads of 14.7, 24.5 and 34.3 N for the run-in and the steady state respectively. At the loads used in the present investigation the wear in FMS is primarily oxidative in nature in both the run-in and the steady state of wear in FMS, as is evident from

the transfer layer and the wear debris. The oxidative nature of the wear could further be confirmed by the visual examination of the wear surfaces, which showed the presence of reddish brown oxide on the pin surface all the time during sliding. Some cracking below the subsurface layer is also observed at a load of 34.3 N as shown in Fig.6.57 (marked by an arrow), indicating a possibility of a delamination wear, but no trace of a metallic particle is observed in the wear debris through microscopic examinations. Hence, it may be possible that the particle got oxidised before being detached as wear debris.

The continuing process of thickening, removal and reformation of the transfer layer may be responsible for the fluctuation of friction coefficient, as observed in Fig. 6.26. At very short sliding distances, the variation in contact that occurs when the sample and the counterface are evolving to develop a better surface conformity may also contribute to the fluctuation in friction coefficient. The average coefficient of friction in both the run-in and the steady state is found to decrease linearly with increasing load for FMS as shown in Figs. 6.32 and 6.33. The decreasing coefficient of friction with increasing load may be attributed to the increased rate of oxidation and better compaction of the wear debris resulting due to the higher frictional heating at higher loads similar to that in Armco iron.

The wear rate in FMS increases linearly with increasing load in both the run-in and the steady state of wear. However, wear rate is less in the steady state as compared to that in the run-in stage as shown in Fig. 6.9. A comparison of Figs. 6.39 (a) to (c) and 6.40 (a) to (c) for the run-in and the steady state respectively, clearly indicates that the transfer layer formed is more compacted in nature in the steady state as compared to that in the run-in stage of wear. Therefore, the wear rate is relatively lower in the steady state as compared to that in the run-in stage due to the protection provided by this transfer layer of compacted wear debris to the underlying metal as shown in Fig. 6.9.

Measurement of hardness in the subsurface region in FMS, indicate that the hardness just below the sliding surface increased from 725 HV before sliding to 742, 758 and 779 HV after sliding under the normal loads of 14.7, 24.5 and 34.3 N respectively, applied during wear test. This increase in hardness is also evident from the subsurface microstructures shown in Figs. 6.55 and 6.56 (a) and (b) for samples tested under the loads of 14.7, 24.5 and 34.3 N respectively. The decrease in friction at the higher loads with increasing theoretical real area of contact in FMS as shown in Fig. 6.36 (b) may also be attributed to the progressive work hardening of the surface during sliding. The continued increase in the hardness of the substrate due to work hardening may lower the real area of contact. However, it may not be solely responsible for the reduction of the friction at the higher loads. The extent of the compacted transfer layer may also account for the decrease in friction at higher loads.

The wear coefficients for FMS, as estimated from the slopes of the linear variation of wear rate with load, *V/SL*, taken from Fig. 6.9 by multiplying with the initial hardness of the material, are 0.95 X 10^{-5} and 0.38 X 10^{-5} for the run-in and the steady state respectively. The lower wear coefficient in the steady state may be attributed to the lower wear rate in this state as compared to the run-in stage.

A higher cumulative volume loss is also observed in the run-in stage as compared to that in the steady state in normalised (N) steel as shown in Fig. 6.3. Therefore, the wear rate, given by the slope of the line in Fig. 6.3, is also high in run-in stage as shown in Fig. 6.10. In the run-in stage the oxidation of the surface begins and progresses with frictional heating generated during sliding. The transfer layer of oxide may, thus, begin to form in the run-in stage and evolves to the steady state providing an extent of cover determined by the conditions of load, sliding velocity and environmental conditions. The second linear segment in Fig. 6.3 shows the steady state of wear, which as it has been described earlier, indicate

attaining of steady state in respect of (i) the evolution of mating surfaces to better conformity, (ii) the spread of oxide and compacted transfer layer and (iii) the real area of contact. Figures 6.41 (a) to (c) and Figs. 6.42 (a) to (c) show the SEM micrographs of the wear surfaces of N steel samples tested under different normal loads in both the run-in and the steady state respectively. Some exposed metallic surface apart from the transfer layer of oxide is observed in all these micrographs. It is observed that in the steady state, the transfer layer starts cracking at places even at the lowest load of 14.7 N used in the present study as shown in Fig. 6.42 (a) giving rise to flaked off particles and agglomerates from the transfer layer. Thus, the wear debris may contain both fine oxide particles and flaked off oxide agglomerates as shown in Fig. 6.72 (a) and (b) for the wear debris generated during sliding in the run-in and the steady state. Since the cracking behaviour of transfer layer has not been investigated systematically it is difficult to say anything definite. But it is possible that cracking may take place once the thickness of the transfer layer builds upto to a critical thickness. At the loads used in the present investigation the wear in N steel investigated is primarily oxidative in nature in both the run-in and the steady state of wear. The oxidative nature of wear is further confirmed by the X-ray diffraction of the wear debris generated during sliding in the run-in and the steady state as shown in Figs. 6.81 (a) and (b). All the peaks in the patterns correspond to those belonging to α-Fe_2O_3. This is in conformity with the results of Sullivan and Hodgson (1988). The Miller indices of the planes (*hkl*), which have given rise to the diffraction peaks, are shown in Fig. 6.81 (a) and (b). However, no peak has been observed for metallic iron. Therefore, metallic wear particles, even if present, could be beyond the detection limit of X-ray diffraction. Figure 6.59 shows the presence of subsurface cracks at a load of 34.3 N, which indicate towards a possible delamination type of wear mechanism also taking place, but no peak corresponding to a metallic particle is observed in X-ray diffraction pattern of the wear debris. Hence, it seems that the cracked particle gets oxidised before being detached as wear fragment.

Quinn *et al* (1980) have also observed oxidative mechanism of wear in low alloy steels in the load range 4 to 40 N and at sliding velocities ranging from 2 to 5 m/s. They also observed a change in the nature oxide from α-Fe_2O_3 to Fe_3O_4 to FeO, at well defined loads for every sliding velocity. Sullivan *et al* (1980) have also reported oxidative wear for the low alloy steels in the load range of 6 to 60 N and sliding velocities ranging from 2 to 5 m/s. They also observed a change in the nature of oxide during sliding. However, no change in the nature of oxide is found in the present investigation. Of the three types of the oxides of iron, α-Fe_2O_3 has been reported to be a low temperature oxide, which forms around a temperatures less than 450^0C. Fe_3O_4 forms between 450-600^0C, whereas FeO forms at the temperatures greater than 600^0C (Quinn *et al*, 1984). The flash temperature i.e., the instantaneous temperature at the contact points during sliding, which could be attained for a given material combination, depends upon the sliding and environmental conditions. It has also been reported by Quinn (1984) that the temperature at the contacts i.e., flash temperature during sliding is about 200^0C higher than the general surface temperature. Since in the present study the temperature measured at a distance of 3 mm from the sliding surface is 70^0C, it is reasonable to assume that the temperature of the contact will not exceed 450^0C and the formation α-Fe_2O_3 is in good agreement with earlier observations. The temperature estimated from the equations given by Alpas and Ames (1995) is also around 415^0C. The theoretical bulk temperature at the surface of the sample calculated on the basis of model given by Lim and Ashby (1987), is found to be 338 K i.e., 65 ^{0}C, which is the same as the temperature measured 3 mm away from the sliding surface. Therefore, the change in the nature of the oxide is not observed as evident from the X-ray diffraction patterns shown in the Figs. 6.81 (a) and (b).

The fluctuation of friction coefficient in N steel, as observed in Fig. 6.27 may be the result of the continuing process of removal of the transfer layer and its reformation and thickening. At very short sliding distances, the fluctuation may also include the contribution

resulting from the variation in contact that occurs when the sample and the counterface are evolving to develop a better surface conformity. The average coefficient of friction in both the run-in and the steady state is found to decrease linearly with increasing load for N steel as shown in Figs. 6.32 and 6.33. This may be attributed to the enhanced frictional heating and extent of compaction at higher loads as discussed earlier for Armco iron and FMS. The average coefficient of friction in the run-in stage is also higher as compared to that in the steady state and it may be attributed to the interlocking of high asperities in the run-in stage as described earlier for Armco iron and FMS. A relatively lower average coeficient of friction in the steady state may be explained on the basis of the extent of cover of the oxide cover and attainment of the steady state height by the asperities as discussed earlier for Armco iron and FMS.

The wear rate in N steel increases linearly with increasing load in both the run-in and the steady state as shown in Fig. 6.10 and this is in agreement with the work of Welsh (1965), Clayton (1980), Bhattacharyya (1980), Venkatesan and Rigney (1992), who have also observed that the wear rate in pearlitic steels increases linearly with increasing load. The wear rate in the steady state first increases as the load increases from 14.7 to 24.5 N and then further increases linearly with a higher slope as load increases from 24.5 to 34.3 N. The higher wear rate beyond a load of 24.5 N may be attributed to a higher cumulative volume loss at these loads which may be observed from relatively deeper wear tracks formed at the surface of the specimen worn under a load of 34.3 N as compared to those formed on the specimen worn under a load of 24.5 N as shown in Figs. 6.42 (c) and (b) respectively. The wear rate is less in the steady state as compared to that in the run-in stage as shown in Fig. 6.10. It may be explained on the basis of the more extent of cover of the transfer layer in the steady state as compared to that in the run-in stage of wear as observed form the comparison of Figs. 6.41 (a) to (c) and 6.42 (a) to (c) for the run-in and the steady state respectively. The cover provided by the transfer layer protects the underlying metal and the wear rate

decreases. Therefore, in the N steel the wear rate is relatively lower in the steady state as compared to that in the run-in stage as shown in Fig. 6.10.

In N steel, the hardness near the sliding surface increased from 243 HV before sliding to 278, 295 and 314 HV after sliding under the normal loads of 14.7, 24.5 and 34.3 N respectively, applied during wear test. The increase in hardness may be a result of the subsurface work hardening as revealed in the subsurface microstructures shown in Figs. 6.58 (a) and (b) worn under the loads of 14.7 and 24.5 N respectively. A deformed layer of material in the subsurface region can be clearly observed in both these micrographs with the extent of deformation being higher at 24.5 N load as compared to that at the 14.7 N load as shown in Figs. 6.58 (a) and (b). The decrease in friction at the higher loads with increasing theoretical real area of contact in N steel as shown in Fig. 6.36 (b) may also be explained on the basis of the progressive work hardening of the surface during sliding as discussed earlier for the Armco iron and FMS.

The wear coefficient has been estimated from the slope of the linear variation of wear rate with load, *V/SL*, taken from Fig. 6.10 by multiplying it with the initial hardness of the material. The wear coefficient in the run-in stage of wear is 2.56 X 10^{-5} for N steel. The wear coefficients in the steady state for N steel are 0.93 X 10^{-5} and 1.86 X 10^{-5}. The lower wear coefficient in the steady state may be attributed to both the lower wear rate and lower real area of contact in this state as compared to those in the run-in stage.

The variation of cumulative volume loss with sliding distance in the run-in and the steady state for dual phase steels - DP1 to DP4 is shown in Figs. 6.4 to 6.7 respectively. The wear behaviour during run-in period leading to higher volume loss compared to that in the study state of wear as observed in all the specimens investigated, has been attributed to the original topography and of sliding surfaces becoming smoother as argued by Shafia and Eyre (1980). All

engineering surfaces are rough and have asperities. When two surfaces are loaded against each other they touch only over a small part of their apparent area of contact (Archard, 1980). When two virgin surfaces are first brought into contact, the junctions (microwelds) are formed at the asperities and the relative motion of sliding causes deformation and shearing of these junctions as described earlier. The wear in the run-in stage occurs by the truncation of higher asperities and by the removal of pre-existing layers of oxide and other contaminants which gives rise to more material loss also for the DP steels in the run-in stage of wear. Therefore, the wear rate, given by the slope of the lines in Figs. 6.4 to 6.7, is also high in the run-in stage, similar to that observed in Armco iron, FMS and N steel, as shown in Fig. 6.11 to 6.14. Initially, the surface roughens due to the fracture of deformed asperities but after a short time, the frictional heating of the surface provides better conditions for softening the asperities and filling up the valleys by deformation which leads to a smoother surface and eventually evolves to a steady state of wear shown by the second linear segment Figs. 6.4 to 6.7. The evolution of steady state in dual phase steels may also be explained on the similar lines as described earlier for Armco iron, FMS and N steel. Figures 6.43 (a) to (c) and Figs. 6.47 (a) and (b) to Figs. 6.49 (a) and (b) show the SEM micrographs of the wear surfaces of DP2 steel samples after sliding under different normal loads in the run-in and the steady state respectively. Some exposed metallic surface apart from the transfer layer of oxide is visible in all these micrographs. Similar features are also observed in the micrographs of the wear surfaces of the other DP steels i.e., DP1, DP3 and DP4 after sliding under a normal load of 34.3 N as shown in Figs. 6.44 to 6.46 and Figs. 6.50 to 6.52 respectively, for both the run-in and the steady state of wear. However, it is observed that in the run-in stage, the transfer layer starts cracking at places at the highest load of 34.3 N used in the present study as shown in Fig. 6.45 giving rise to flaked off particles and agglomerates from the transfer layer. But the cracking behaviour has not been investigated thoroughly in the present investigation as indicated earlier. Thus, the wear debris may contain both fine oxide particles and flaked off oxide agglomerates as shown in Figs. 6.75 (a) and (b) to 6.78 (a) and (b) for the wear

debris generated in both the run-in and the steady state respectively, for DP1, DP2, DP3 and DP4. A comparison of the wear debris generated in the run-in and the steady state as shown in Figs. 6.75 (a) to 6.78 (a) and Figs. 6.75 (b) to 6.78 (b) indicates that the size of the flaked off agglomerates is relatively larger in the debris generated during the run-in stage as compared to that generated during the steady state. It may be due to the better compaction and subsequent churning of the compacted debris during sliding which results in relatively finer agglomerates of debris in the steady state. The wear is primarily oxidative in nature under the conditions used in the present study in both the run-in and the steady state of wear in DP steels, as is evident from the transfer layer and the wear debris. The oxidative nature of wear is further confirmed by the X-ray diffraction analysis of the wear debris generated during both the run-in and the steady state as shown in Figs. 6.81 (c) and (d) respectively. The Debye-Scherrer X-ray diffraction patterns from the wear debris show the lines consistent with the presence of α-Fe_2O_3 only. The Miller indices of the planes (*hkl*), which have given rise to the diffraction peaks, are shown in Fig. 6.81 (c) and (d). However, no peak for metallic iron has been observed which may be because of its quantity being so small that could not be detected by X-ray diffraction. Some cracking below the subsurface layer is also observed at a load of 34.7 N in all the DP steels but the cracks are seen to form around hard martensite islands as shown in Figs. 6.60 (c) to 6.63, suggesting a possibility of a delamination wear, but no trace of a metallic particle is observed in the X-ray diffraction patterns of the wear debris. Hence, it appears that even if the particle cracks, it gets oxidised before generating wear debris.

The fluctuations in the friction coefficient in dual phase steels as shown in Figs. 6.28 to 6.31 may be attributed to the continuous removal and reformation of the transfer layer of compacted debris and attaining a steady state in respect of the real area of contact as explained earlier for the Armco iron, FMS and N steel. The average coefficient of friction in both the run-in and the steady state has been observed to decrease linearly with increasing

load for all DP steels as shown in Figs. 6.32 and 6.33. The decrease in friction coefficient with increasing load may be explained on the basis of enhanced frictional heating and increasing extent of cover provided by the transfer layer as discussed earlier for Armco iron, FMS and N steel. A higher coefficient of friction in the run-in stage as compared to that in the steady state may be explained on the basis of the interlocking of high asperities and a relatively lower area under the oxide cover in the run-in stage as described earlier for the Armco iron, FMS and N steel.

The wear rate in all DP steels also increases linearly with increasing load in both the run-in and the steady state as shown in Figs. 6.11 to 6.14. However, wear rate is less in the steady state as compared to that in the run-in stage as shown in Figs. 6.11 to 6.14. A lower wear rate in the steady state as compared to that in the run-in stage for dual phase steels has also been reported by Sawa and Rigney (1987). A comparison of Figs. 6.43 (a) to (c) and 6.47 (a) to 6.49 (a) for DP2 steel in the run-in and the steady state respectively, clearly shows that the extent of cover provided by the transfer layer is more in the steady state as compared to that in the run-in stage of wear when it begins to form by compacting the wear debris trapped between sliding surfaces. This transfer layer of the compacted wear debris provides the protection to underlying metal and the wear rate decreases. A similar conclusion may be drawn from a comparison of the wear surfaces of specimens of DP1, DP2 and DP3 steels after sliding under a load of 34.3 N as shown in Figs. 6.44 to 6.46 and Figs. 6.50 (a) to 6.52 (a) for the run-in and the steady state respectively. Therefore, the wear rate is relatively lower in the steady state as compared to that in the run-in stage as shown in Figs. 6.11 to 6.14 for DP1, DP2, DP3 and DP4 respectively.

The possibility of the subsurface work hardening in DP steels has been explored by hardness measurements near the subsurface on the tapered specimens after the complete period of wear test. In DP1 steel the hardness increases from an initial value of 353 HV to

392 HV, 419 HV and 431 HV respectively, after sliding at loads of 14.7, 24.5 and 34.3 N. The hardness of the DP2 steel increases from 412 HV to 431, 449 and 467 HV respectively, after sliding under the normal loads of 14.7, 24.5 and 34.3 N, whereas for the DP3 steel the hardness is found to increase from 444 HV to 465 HV, 483 HV and 498 HV respectively, for the same loads and same sliding distance. The hardness of the DP4 steel increases from 503 HV to 518 HV, 532 and 549 HV respectively, after sliding at the loads of 14.7, 24.5 and 34.3 N. The subsurface work hardening as revealed in the SEM micrographs of the subsurface shown in Figs. 6.60 to 6.63 for DP1, DP2, DP3 and DP4 steel respectively, may be responsible for this increase in hardness. A deformed layer of material (marked by arrows) in the subsurface region is clearly visible in all the micrographs. The extent of deformation appears to increase with increasing load from 14.7 to 34.3 N as observed in the optical micrographs of the DP4 steel shown in Figs. 6.64 (a) to (c). The coefficient of friction in dual phase steels is observed to decrease with increasing theoretical real area of contact as shown in Fig. 6.36 (b). The increased hardness of the substrate due to work hardening is expected to lower the actual real area of contact, which may lower the friction coefficient. However, it may explain the lowering of the friction with sliding distance at a given load as shown in Figs. 6.28 to 6.31 but not the observed lowering of friction with increasing load. The extent of cover provided by the transfer layer of oxide on the sliding surface might be responsible for the decrease in friction at higher loads as indicated earlier also for the Armco iron, FMS and N steel.

The wear coefficient has been estimated from the slope of the linear variation of wear rate with load, *V/SL*, taken from Figs. 6.11 to 6.14 by multiplying it with the initial hardness of the corresponding dual phase steel. For DP1 steel the wear coefficients are 2.46×10^{-5} and 1.43×10^{-5} for the run-in and the steady state respectively, whereas the wear coefficients for DP2 steel are 2.41×10^{-5} and 1.07×10^{-5} in the corresponding stages of wear. The wear coefficients in the run-in and steady state are 1.76×10^{-5} and 0.96×10^{-5} respectively, for

DP3 steel and 1.06 X 10^{-5} and 0.70 X 10^{-5} for DP4 steel. A lower wear coefficient in the steady state in all the DP steels may be attributed to both a lower wear rate and a relatively lower area of contact as compared to those in the run-in stage.

It is observed that the cumulative wear volume for the Armco iron is the highest whereas it is the least for the FMS at all the normal loads used in the present study. The cumulative wear volume of the N and DP steels lie in-between those of Armco iron and FMS. The hardness follows an increasing trend from Armco iron to N steel, DP1, DP2, DP3, DP4 and FMS whereas the reverse is true for the cumulative volume loss. Since the hardness of the Armco iron is the lowest and that of the FMS is the highest, therefore, the real area of contact in the Armco iron should be the highest and that in the FMS should be the lowest at a given load. Thus, it is not surprising in the context of Archard's law that Armco iron has the highest cumulative volume loss and while FMS has the lowest volume loss. The higher volume loss in N steel as compared to the DP steels can also be explained on similar grounds.

In general a linearly increasing pattern of wear rate with increasing applied load is observed under the conditions of load and sliding velocity used in the present study for all the materials having different microstructures investigated. The wear rate is found to increase linearly with increasing load in all DP steels as shown in Figs. 6.15 and 6.17 respectively, in both the run-in and the steady state of wear. The DP4 steel has shown a lower wear rate compared to that observed in other DP steels consistently at all the loads used in the present study. The lower wear rate in DP4 steel reflects the effect of a higher martensite volume fraction (72 pct) in this steel as compared to DP1, DP2 and DP3 steels. However, the wear rate at a given load is observed to decrease linearly with increasing volume fraction of martensite in DP steels as shown in Figs. 6.16 and 6.18 for both the run-in and the steady state respectively. The decreasing wear rate with increasing volume fraction of martensite may be explained on the basis of the hardness imparted by the incorporation of the martensite

in these steels. The steel containing higher volume fraction of martensite will have lower real area of contact as a result of the increased hardness due to incorporation of a hard martensite phase. Since, the wear rate is directly proportional the real area of contact, the steel containing relatively higher percentage of martensite will show a lower wear rate as compared to those having lower amount of martensite. Hence, it is not surprising in the context of Archard's law that the FMS which contains 100 vol pct martensite shows the lowest wear rate and the Armco iron, which has no martensite at all, shows the highest wear rate. A similar explanation may hold for the DP4 steel showing the lower wear rate as compared to other DP steels investigated in the present study. The observed trend is in agreement with the observations of Basak *et al* (1998), who have also reported that the wear resistance of the dual phase steels increases with increasing volume fraction of martensite. The wear rate of N steel is low as compared to Armco iron but high as compared to the DP steels and FMS and it may be attributed to the relative difference in the real area of contact in these materials. The increasing difference in the wear rates in DP steels at higher loads as compared to the lower load as seen from the Figs. 6.15 and 6.17 may be explained on the basis better compaction and adhesion of transfer layer aided by frictional heating. It has been shown that a harder substrate is able to hold a thicker transfer layer of oxide more firmly as compared to a softer one (Saka *et al*, 1977). Therefore, the DP4 steel which is harder than other DP steels investigated may be able to hold a transfer layer of larger critical thickness firmly before it flakes off and hence, the difference in wear rates will be higher at higher loads. This effect is the maximum in FMS. The other factor contributing to the observed behaviour of wear rate may be the extent of cover provided by the transfer layer of oxide and nature of adhesion of the compacted transfer layer to the pin surface, which may flake off easily from a substrate of lower hardness. In other words, the critical thickness of the oxide may be lesser in a material of relatively lower hardness as compared to a material of relatively higher hardness. Hence, there will be a higher probability of the flaking off of this layer in Armco iron and N steel as compared to DP steels and FMS. Thus, a higher wear rate

in materials of comparatively lower hardness may be attributed to the increase in the flaking off of the transfer layer during sliding.

The observed average lower coefficient of friction in materials of higher hardness as shown in Fig. 6.35, may be attributed to a relatively lower real area of contact in these materials as compared to the materials of lower hardness used in the present study. This again reflects the effect of the increasing martensite content, which brings about an increase in hardness. The steel with higher martensite is expected to have a lower real area of contact resulting in a lower force of friction and therefore, a lower coefficient of friction. Thus, it is not surprising that FMS containing 100 pct martensite has the lowest friction coefficient and Armco iron containing no martensite has the highest friction coefficient. The coefficient of friction decreases linearly with the increasing hardness or the increasing volume fraction of martensite in DP steels as observed in Fig. 6.35 and it may also be attributed to the lower real area of contact as explained above. The N steel has a coefficient of friction lower than that of Armco iron but higher as compared to that observed for DP steels. This may also be attributed to a relatively lower real area of contact in N steel compared to that in Armco iron and a relatively higher real area of contact as compared to that in DP steels. The other factor contributing to the lower coefficient of friction in relatively harder materials may be the extent of the area under the oxide cover. The extent of the oxide cover is observed to be more in the harder materials as compared to the softer materials in the present study as indicated in the Figs. 6.38 (a) to (c), 6.40 (a) to (c), 6.42 (a) to (c), and 6.47 (a, b) to 6.52 (a, b). The junctions formed in the oxide contact will require less energy for shearing during sliding and will therefore, result in a lower friction coefficient. Thus, it was expected that a material with higher hardness will show a lower friction coefficient as compared to a material of lower hardness and the results reflect the expectations.

Apart from this the lower friction in DP steels as compared to that observed in N steel as shown in Figs. 6.32 and 6.33 in both the run-in and the steady state may reflect the difference in the oxidation behaviour of these materials having different microstructures but this has not been quantified in the present study. Blau (1981) has also found a higher friction in normalised steel as compared to that in DP steel having the same carbon content and has reported that it may be due to the difference in the oxidation characteristics of these steels. So the observations of the present study appears to be in good agreement with the observations of Blau (1981).

The wear coefficient which may be interpreted as wear rate per unit real area of contact, does not change significantly between the Armco iron and the dual phase steels (DP1 and DP2 containing 42 and 51 vol pct martensite respectively) and decreases sharply as one moves from DP2 (51 vol pct) to DP4 (72 vol pct martensite) in the run-in stage as shown in Fig. 6.24 and Table A.12. But in the steady state the wear coefficient decreases linearly with increasing volume fraction of the martensite. The decrease in wear coefficient may be attributed to the decreasing wear rate dominating over the decrease in real area of contact due to increasing hardness. For wear coefficient, because of its definition, decrease in real area of contact becomes a disadvantage. Hence, Wear coefficient as a sensitive discriminating wear parameter may not, therefore, be adequate in materials of similar property and structure and the wear rate may be a better indicator.

The wear rates calculated on the basis of (i) estimated load sharing between the constituent phases and (ii) the observed wear coefficients of fully ferritic Armco iron and martensitic FMS, using Eq. (4.19) are relatively higher than the observed wear rates in dual phase steels in both the run-in and the steady state of wear as shown in Figs. 6.19 (a) to (d) and 6.20 (a) to (d). The calculated wear rates are comparable to the observed wear rates at lower loads but have increasingly larger difference with increasing loads. However, when the

volume fraction of martensite increases, the difference between the estimated and the observed wear rates decreases even at higher loads. This difference between the estimated and the observed wear rates is relatively lower in the steady state compared to that in the run-in stage as shown in Figs. 6.19 (a) to (d) and Figs. 6.20 (a) to (d). In DP3 and DP4 steels the least square fit lines for the calculated and the experimental wear rates appear to cross at some intermediate load with their values falling in the same band. The difference in the calculated and the observed wear rates may be attributed to the flow of the softer phase of ferrite over the hard martensite islands resulting in easily oxidised junctions of low shear strength while maintaining the same real area of contact. The higher oxidative wear of this ferrite over that of martensite may lead to higher observed wear rates. This is evident from the much higher rate of oxidative wear observed for the Armco iron as compared that for the FMS in the present study. As the martensite volume fraction increases, the flow of ferrite gets restrained and thereby a better matching between the experimental and the calculated results is observed because the sliding surface has both ferrite and martensite in amounts as presumed in the calculation. At lower loads, the flow of ferrite is not significant and therefore, a better matching of the experimental and the calculated results is observed. But with increasing load the flow of ferrite becomes significant, resulting in higher observed wear rates in steels having a relatively lower martensite volume fraction.

The wear rates have also been estimated using the oxidative wear model proposed in Chapter 4 where it is assumed that the critical thickness of oxide and the probability of its removal are same in both the phases of ferrite and martensite in DP steels. The wear rates calculated following Eq. (4.44), are consistently higher than those observed experimentally at all the loads in both the run-in and the steady state respectively, as shown in Figs. 6.21 (a) to (d). The critical thickness of oxide layer ξ_c has been assumed to be 1 μm on the basis of the work of Sullivan *et al* (1980) and the oxidation rate constant β has been assumed to be the same as given by Kubaschewaski and Hopkins (1962) for the static oxidation of iron to

Fe_2O_3. The estimated wear rates could match the observed wear rates if one takes either a higher value of the critical thickness of oxide or a lower value of oxidation rate constant. The rate of oxidation under the conditions of dry sliding may be lower due to the limited supply of oxygen to the sliding surfaces. Quinn *et al* (1980) have reported a very high value of the oxidation rate constant in tribology and if the value reported by them is taken then the estimated wear rate will be orders of magnitude higher than the observed rates.

The wear rates have been estimated on the basis of different oxidation behaviour of the constituent phases of ferrite and martensite assumed for deriving Eq. (4.50) where the critical thickness of oxide layer and the probability of its removal are presumed different for both the phases in DP steels. The critical thickness of oxides and the probability of their removal for ferrite and martensite have been determined from the oxidative wear behaviour of ferritic Armco iron and martensitic FMS respectively. The calculated wear rates are comparable to the observed wear rates at lower loads in DP1, DP2 and DP3 steels but are increasingly higher at higher loads in both the run-in and the steady state of wear. However, when volume fraction of martensite increases the difference between the estimated and the observed wear rates decreases even at higher loads as it could be observed from Figs. 6.22 (a) to (c) and 6.23 (a) to (c). The difference in the estimated and the observed wear rates may be attributed to the flow of the softer ferrite over the hard martensite islands as described earlier. A good matching at the lower loads may be attributed to the insignificant flow of ferrite as the sliding surface has relative area fractions of ferrite and martensite as presumed. The increasing difference in the estimated and observed wear rates at higher loads may be due the higher area fraction of ferrite which has flown over the hard martensite islands and its relatively higher rate of oxidative wear. But an increase in the martensite volume fraction inhibits the flow of ferrite and the wear rate is also contributed by the oxidative wear of martensite, which wears at a relatively lower rate. Therefore, a better matching between the

estimated and the observed wear rates is obtained at higher martensite volume fractions as it could be observed from Figs. 6.22 (d) and 6.23 (d) for DP4 steel.

The coefficients of friction in the steady state, have been estimated on the basis of the rule of mixture and the observed friction coefficients of fully ferritic Armco iron and martensitic FMS, by using Eq. (6.1). The calculated friction coefficients are found to be a little higher than those observed experimentally in DP steels as shown in Figs. 6.34 (a) and (b) respectively, at normal loads of 14.7 and 34.3 N (marked by dark squares).

However, the coefficients of friction in the steady state, calculated on the basis of (i) estimated load sharing between the constituent phases and (ii) the observed friction coefficients of Armco iron and FMS by using the Eq. (4.23), are relatively lower than those observed experimentally in DP steels. But the difference between the calculated and the observed friction coefficients decreases with increasing volume fraction of martensite at a given load as it could also be observed from the Figs. 6.34 (a) and (b). The estimated friction coefficients are shown by the hollow squares in the above figures. The lower values of the estimated friction coefficients may be attributed to the flow of the softer phase of easily oxidised ferrite over the hard martensite islands in the DP steels, resulting in formation of the lower shear strength junction and consequently, a lower coefficient of friction. But in the steels with higher volume fraction of martensite the flow of ferrite is restrained and the friction is governed by the real area of contact, which determines the number of junctions and therefore, the friction coefficient. A lower real area of contact in steel with relatively higher amount of martensite results in a fewer number of junctions and thus, a lower coefficient of friction. Hence, there is better matching between the estimated and the experimental friction coefficients when the volume fraction of martensite increases.

The study of friction and wear presented above indicates that the microstructure plays a crucial role in dictating the tribological behaviour of a typical two phase metallic material like dual phase steel. The increasing amount of martensite in dual phase steels imparts hardness to these steels, which in turn, results in lowering of real area of contact during dry sliding. The lower is the real area of contact, the lower will be the wear rate. Hence, the wear rate is observed to decrease linearly with increasing volume fraction of martensite in dual phase steels. The extent of cover provided by the transfer layer of oxide increases with increasing volume fraction of martensite in dual phase steels and consequently, decreases the average coefficient of friction. The friction coeficient depends on the number and the shear strength of junctions formed during sliding contact. The decreasing coefficient of friction with increasing volume fraction of martensite is attributed to a relatively lower real area of contact resulting in a fewer number of junctions. The wear rates calculated on the basis of (i) estimated load sharing between the constituent phases and (ii) proposed models of oxidative wear show a good match with those observed experimentally at low loads but have difference at higher loads. It has been attributed to synergy between the two phases resulting from significant flow of easily oxidised ferrite over the martensite islands during sliding at higher loads. However, the estimated and the observed wear rates show a good match even at higher loads when volume fraction martensite increases and this has been attributed to a restricted flow of ferrite in dual phase steels containing higher amount of martensite. The coefficient of friction calculated on the basis of the estimated load sharing between constituent phases, are lower than those observed experimentally in dual phase steels but the difference between the calculated and the observed friction coefficients decreases with increasing volume fraction of martensite. It has been attributed to the flow of the softer phase of ferrite over the martensite islands during sliding, resulting in formation of the junctions of lower shear strength and consequently, a lower coeficient of friction. But at higher martensite content, the flow of ferrite gets restrained and the friction is governed by the real area of contact. The increasing amount of martensite results in decreasing real area of contact and thus, the number of

junctions. Hence, the calculated and the observed coefficients of friction match better when the volume fraction of martensite increases. The wear coefficients as observed, are found to be inadequate parameters in judging the wear resistance of materials.

Chapter 7

TRIBOLOGICAL BEHAVIOUR OF LOW CARBON DUAL PHASE STEEL

The tribological behaviour of low carbon normalised (LCN) steel and dual phase (DP) steel developed through intercritical annealing from the same normalised steel having 0.14 wt pct carbon has been investigated in terms of the friction and dry sliding wear against the counterface of steel. This chapter describes the results on the wear and friction characteristics of the low carbon normalised (LCN) steel and dual phase (DP) steel. In the end the results have been discussed.

7.1 RESULTS

7.1.1 Friction and Wear Characteristics

(a) Dry Sliding Wear

Wear volume losses of DP and LCN steels with distance under different loads at 1.15 m/s sliding speed are shown in Figs. 7.1 and 7.2 respectively. A log-log plot of wear volume against sliding distance demonstrated a linear variation with coefficient of correlation exceeding 0.98 and 0.99 for DP and LCN steels, respectively and their slopes indicate that, for both the LCN and the DP steels, the wear volume varies sublinearly with sliding distance. However, the data in Figs. 7.1 and 7.2 can also be analysed using two separate stages of wear behaviour. Two linear segments will also allow remaining within the framework of Archard's

law. The change in slope has been observed after the first six experimental points (first stage-run-in), fitted by one line, and the latter six points (steady state) have been fitted by another line with the sixth point common between them. Both the lines have been determined by the linear least square fit. The wear rate is given by the line slope. The procedure followed helps to establish the run-in period rate separately from the long-term steady state rate (second stage).

It is observed that, for a given load the cumulative wear volume increases with increasing distance of sliding for both the DP and LCN steels. There is increased scatter of data points in the second linear segment for the DP steel as compared to LCN steel. For all the three loads, the wear volume is considerably lower in the DP steel than that in N steel for the same load at a given sliding distance. The least square fit lines for the DP steel under loads of 24.5 and 34.3 N appear to cross at short sliding distances in the first linear segment, but that may be due to the lower wear volume resulting in a relatively larger contribution of the initial period to the cumulative loss.

The wear rates in two periods for both the DP and the LCN steels under different loads are reported in Table A.13 in the appendix. Figure 7.3 shows the variation of wear rate with load in both first segment (run-in) and second segment (steady state) in DP and LCN steels. It is observed that wear rate increases linearly with load for both the LCN and the DP steels. However, the run-in wear rate is higher in LCN steel and it also increases faster with load than that observed in DP steel. For longer sliding distances corresponding to the second linear segment (steady state), the wear rate for LCN steel appears to have nonlinear variation with load. In LCN steel the wear rate increases rapidly beyond 24.5 N load. Although there is only one data at higher load, the nonlinear variation is possibly a real effect in view of the fact that the basic cumulative volume loss with sliding distance for the second segment in LCN steel at different loads have relatively much less scatter as shown in Fig. 7.2. In DP steel, the wear rate increases more or less linearly with load in the range investigated and the

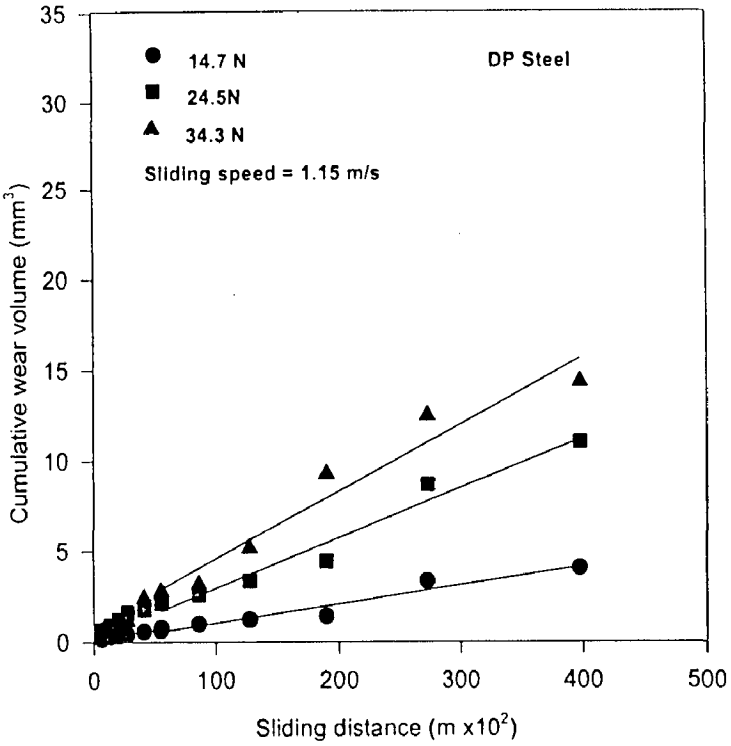

Fig. 7.1 Cumulative wear volume with sliding distance at different loads in dual phase steel, DP, containing 8 pct martensite.

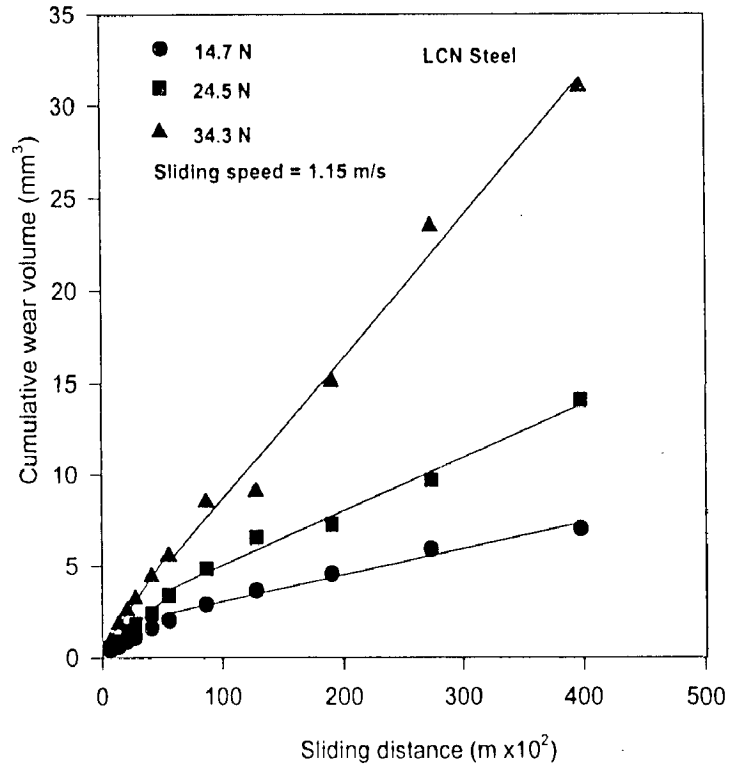

Fig. 7.2 Cumulative wear volume with sliding distance at different loads in normalised (LCN) steel.

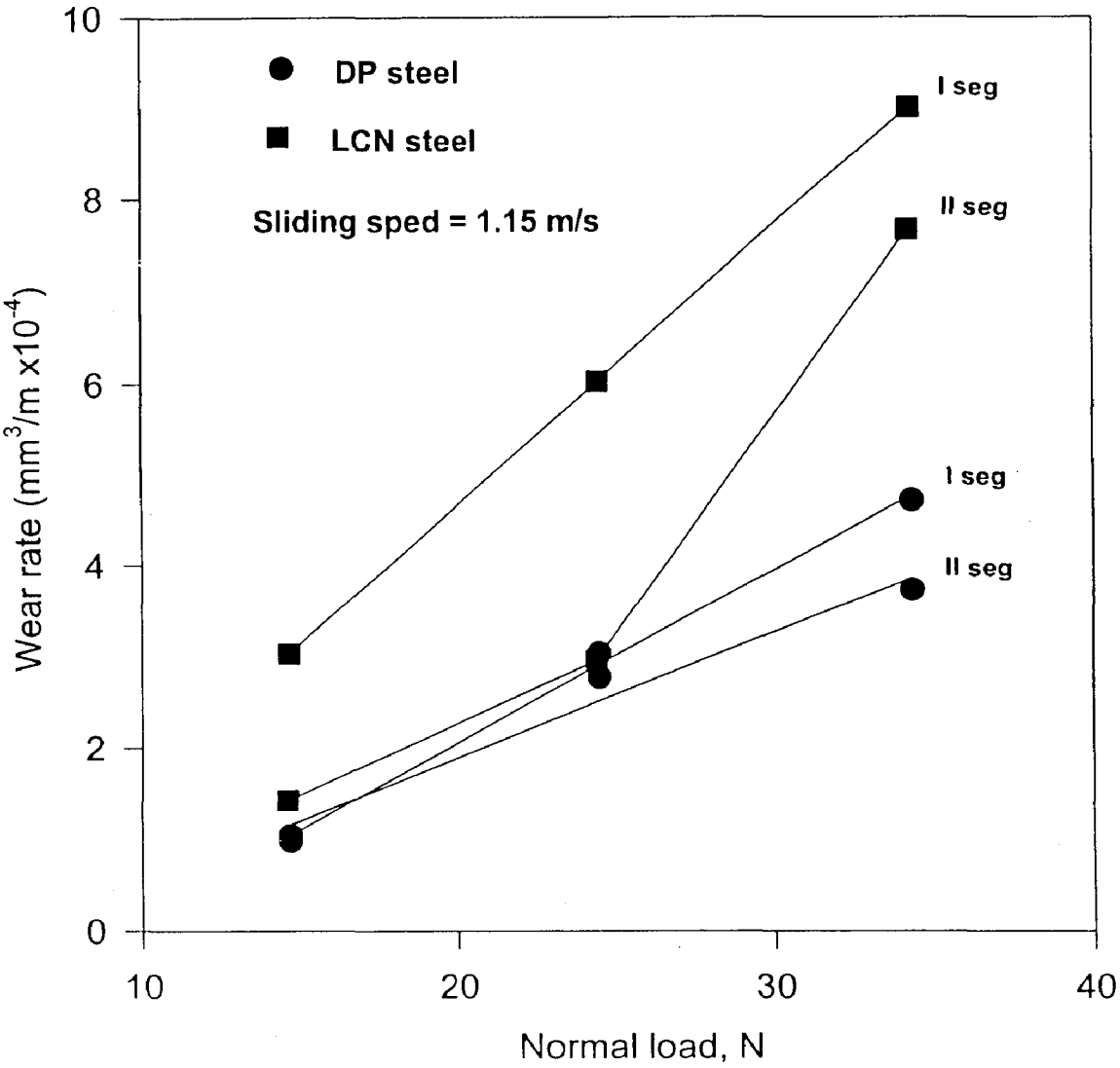

Fig. 7.3 Variation of wear rates with load in both DP and LCN steel corresponding to first and second linear segments.

wear rate in LCN steel is marginally higher than that for DP steel upto a load of 24.5 N. Beyond this load, the steady state wear rate in LCN steel increases rapidly with load. However, the wear rate corresponding to the first linear segment (run-in) in LCN steel is significantly higher than that in DP steel at all the loads as shown in Fig. 7.3. Further, the difference in wear rate between LCN steel and DP steel also appears to increase with load.

Figures 7.4 and 7.5 show the variation of wear rate with martensite volume fraction for both low and medium carbon dual phase steels at the minimum and maximum normal loads of 14.7 and 34.3 N used for this investigation respectively, for the run-in and the steady state of wear. It is observed that the wear rate in the run-in stage decreases linearly as the volume fraction of the martensite increases from 8 to 72 pct corresponding to DP and DP4 steel as shown in Fig. 7.4. The wear rate in the steady state of wear also decreases linearly with increasing volume fraction of martensite at a load of 14.7 N but the decrease in wear rate appears to be non-linear at a load of 34.3 N as shown in Fig. 7.5.

The wear coefficient, K, has been determined from Fig. 7.3 using Archard's equation as given below.

$$K = \frac{V\,H}{L\,S} \tag{7.1}$$

Where, V is the cumulative volume loss under a normal load of L, after a sliding distance of S. H is the initial hardness of the softer material (pin). The wear coefficient has been estimated from the slope of the linear variation of wear rate with load, V/SL, by multiplying it with the initial hardness of the corresponding pin material. For DP steel the wear coefficient is 0.39×10^{-4} but that for LCN steel it is 0.40×10^{-4} as determined from the first linear segment (run-in). However, the wear coefficient of DP steel corresponding to second linear

segment (steady state) is 0.29 x 10^{-4} determined from the slope in Fig. 7.3. The wear coefficients corresponding to the second linear segment of LCN steel are 0.21 x 10^{-4} and 0.64 x 10^{-4} . The wear coefficients for both DP steel and LCN steel are similar in both the wear regimes except for that observed at the second linear segment at loads exceeding 24.5 N.

(b) Dry Sliding Friction

Figures 7.6 (a) and (b) show the variation of coefficient of friction with sliding distance for different loads against the HRC 62-65 hardened steel disc for both the DP and the LCN steels. It is noted that friction coefficient in the run-in stage fluctuates around a mean level, then lessens and stabilizes after a certain period. This trend is similar in both types of steel. The fluctuations are relatively large in the run-in short sliding distances corresponding to first linear segment. Figure 7.7 shows the variation of average coefficient of friction over the entire sliding distance with load in both the DP and the LCN steels. It shows that as the load increases, the average coefficient of friction decreases to about 0.6 for both the steels, and remains at that level. The LCN steel shows a slightly higher value of friction consistently at all loads as compared to those observed for DP steel, but the difference of 1 to 2 pct is close to the uncertainty in the friction coefficient determination.

7.1.2 Examination of Sliding Surface and Subsurface

Figures 7.8 (a) to (c) show the SEM micrographs of worn surfaces of DP and LCN steels at different loads. It is observed that at a load of 24.5 N, apart from scoring marks, there is a highly compacted transfer layer of oxides which appears bright under SEM. There

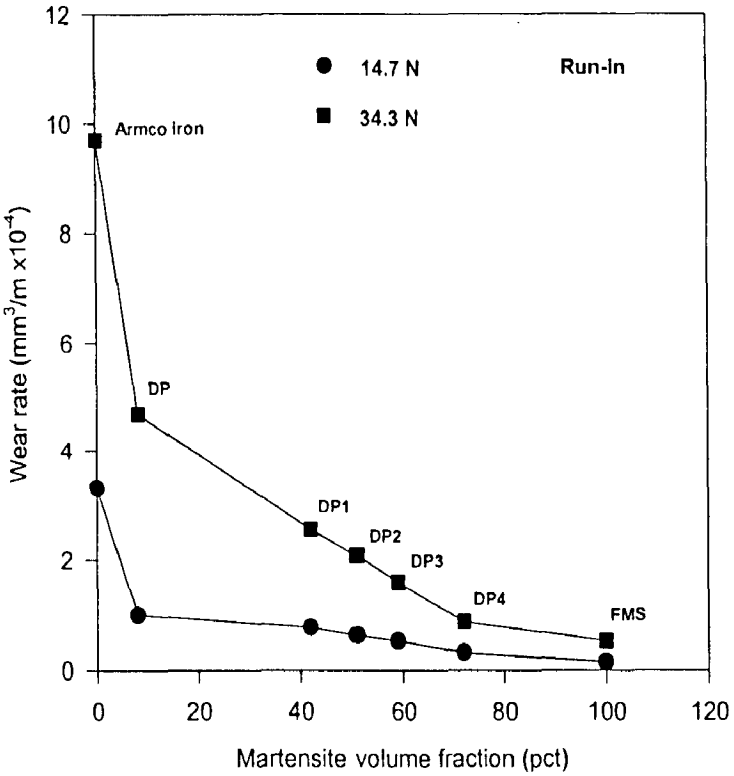

Fig. 7.4 Variation of wear rate with martensite volume fraction in low and mediu carbon dual phase steels at the normal loads of 14.7 and 34.3 N in the run-i stage.

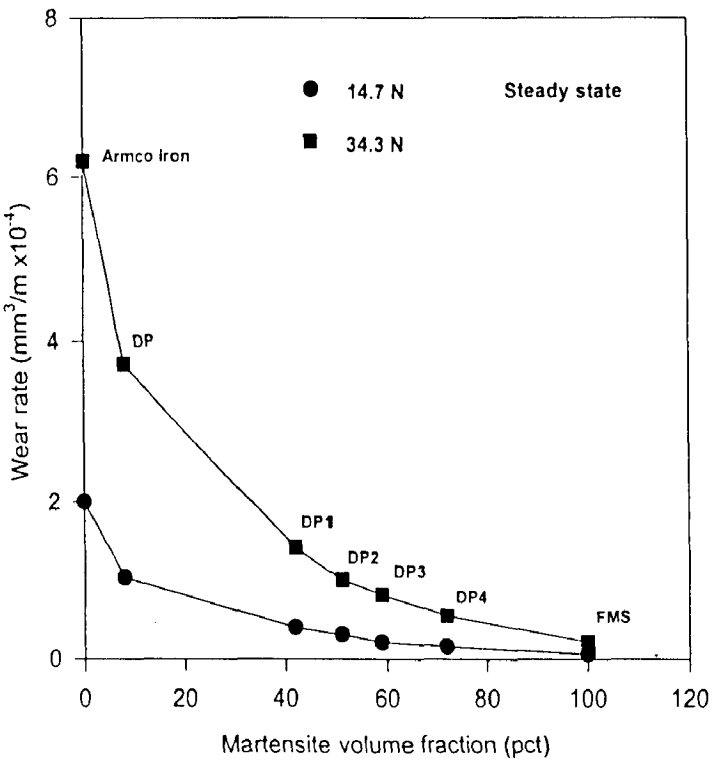

Fig. 7.5 Variation of wear rate with martensite volume fraction in low and medium carbon dual phase steels at the normal loads of 14.7 and 34.3 N in the steady state.

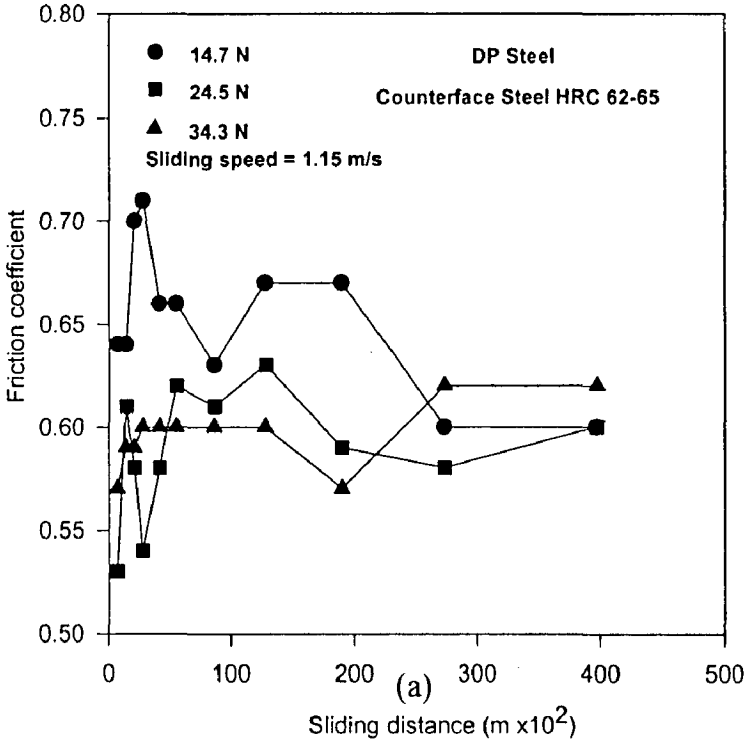

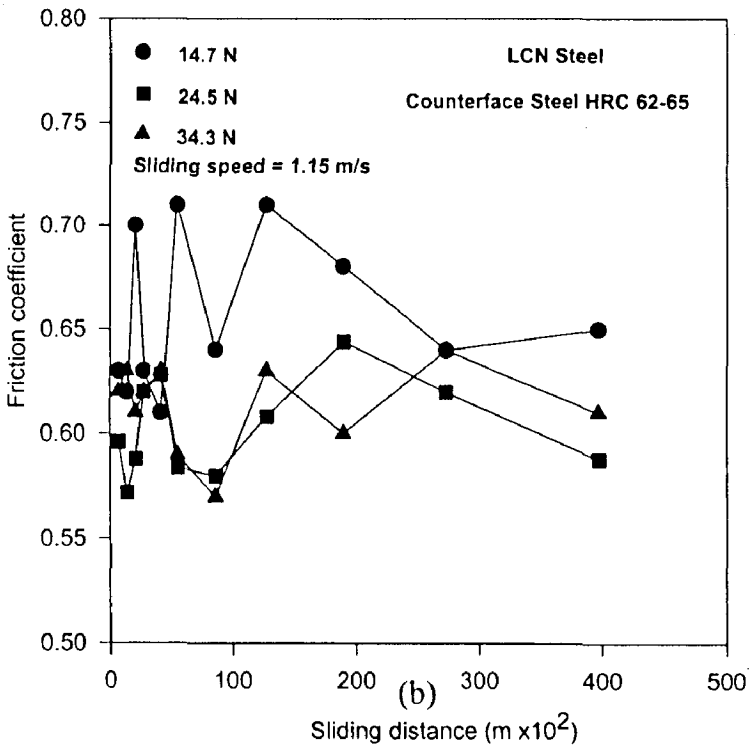

Fig. 7.6 Variation of sliding friction coefficient with sliding distance at different loads in (a) DP steel and (b) LCN steel.

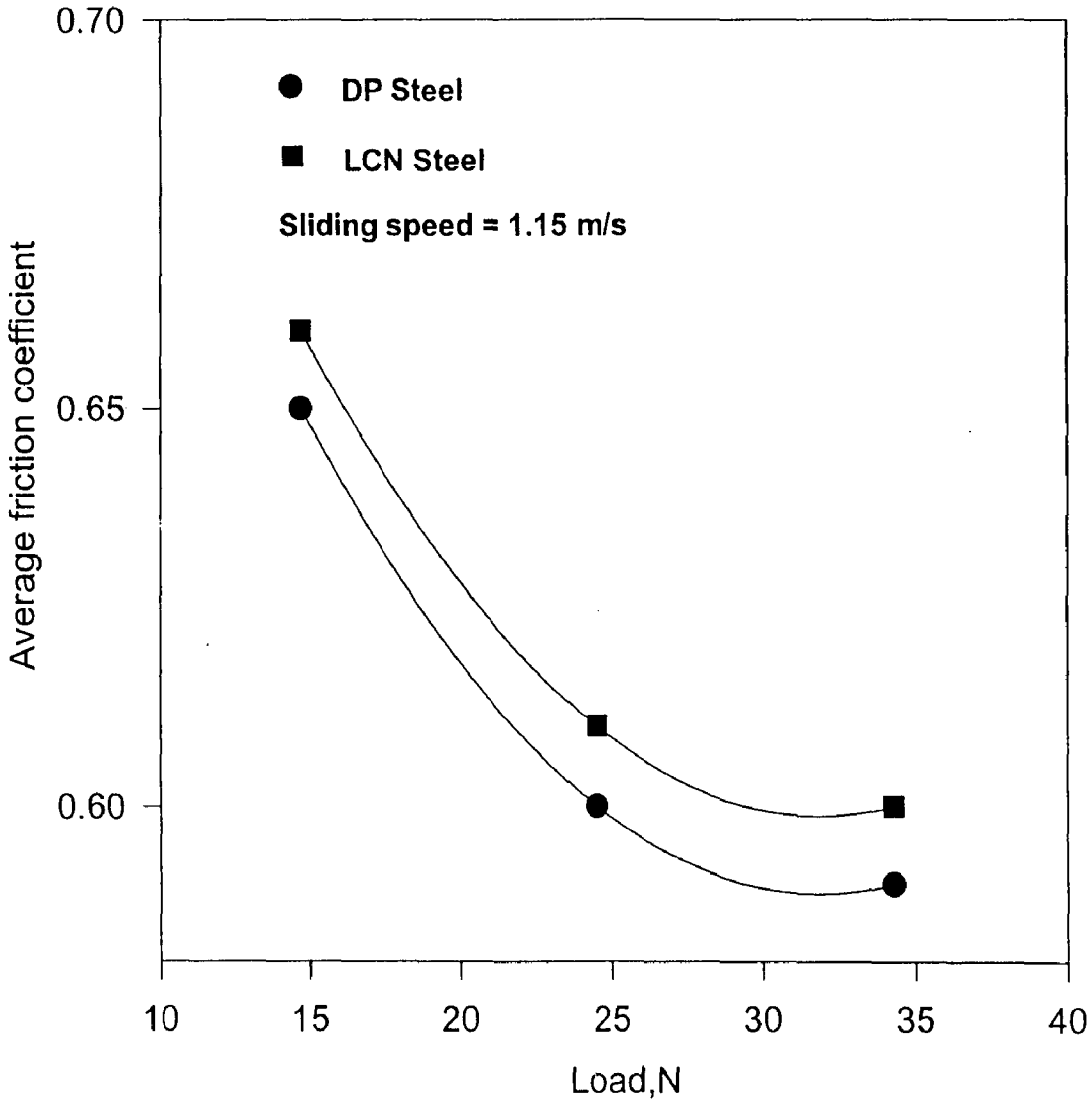

Fig. 7.7 Variation of the average coefficient of friction with load for both DP and LCN steel.

(a)

(b)

(c)

Fig. 7.8 Wear surfaces of specimens of (a) DP steel at 24.5 N, X 100, (b) DP steel at 14.7 N, X 100 and (c) LCN steel at 24.5 N, X 100, after sliding through a distance of 39.74 km.

are also a few craters from where metallic particles have possibly come into debris due to microwelding or delamination, as shown in Fig. 7.8 (c), marked by arrows.

Figures 7.9 (a) and (b) show the SEM micrographs of the subsurface of the DP and the LCN steels respectively. Some cracking below the subsurface can be observed in both these micrographs. In DP steel the cracks are appearing to form around hard martensite islands as shown by the arrow in Fig. 7.9 (a). However, the subsurface of the LCN steel clearly reveals a few locations where delamination could have taken place, as shown by the arrow in Fig. 7.9 (b).

The microstructures of the subsurface of both the DP and the LCN steels as examined under optical microscope, after sliding under a normal load of 34.3 N are shown in Figs. 7.10 (a) and (b) respectively. A change in microstructure in the subsurface can be clearly observed in DP steel as shown in Fig. 7.10 (a). In LCN steel a deformed layer of the material is clearly visible in the subsurface region as shown in Fig. 7.10 (b).

7.1.3 Examination of Wear Debris

Figures 7.11 (a) and (b) show the optical micrographs of the wear debris generated during sliding in the run-in stage of wear respectively, for both DP and LCN steels. The finer oxide particles apart from some larger agglomerates of the oxide could be observed in these micrographs. Figures 7.12 (a) and (b) show the optical micrographs of the wear debris generated during sliding in the steady state of wear respectively, for both the DP and LCN steels. The finer oxide particles apart from some larger agglomerates of the oxide are observed in these micrographs also.

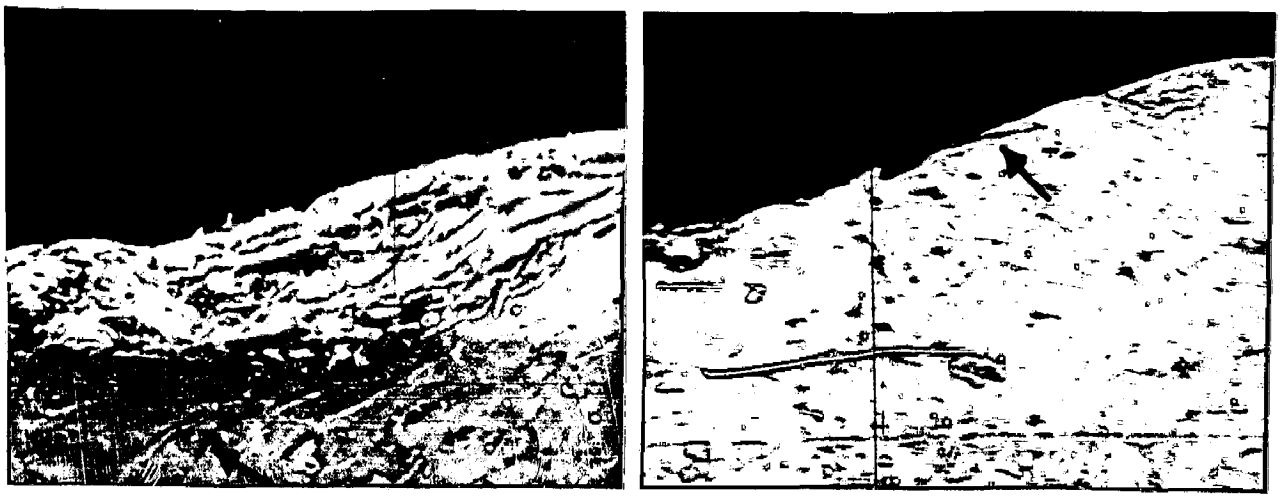

(a) (b)

Fig. 7.9 SEM micrographs of subsurface of specimens of (a) DP steel at 24.5 N, X 100 and (b) LCN steel at 14.7 N, X 100, after sliding through a distance of 39.74 km. Arrows indicate the formation of cracks.

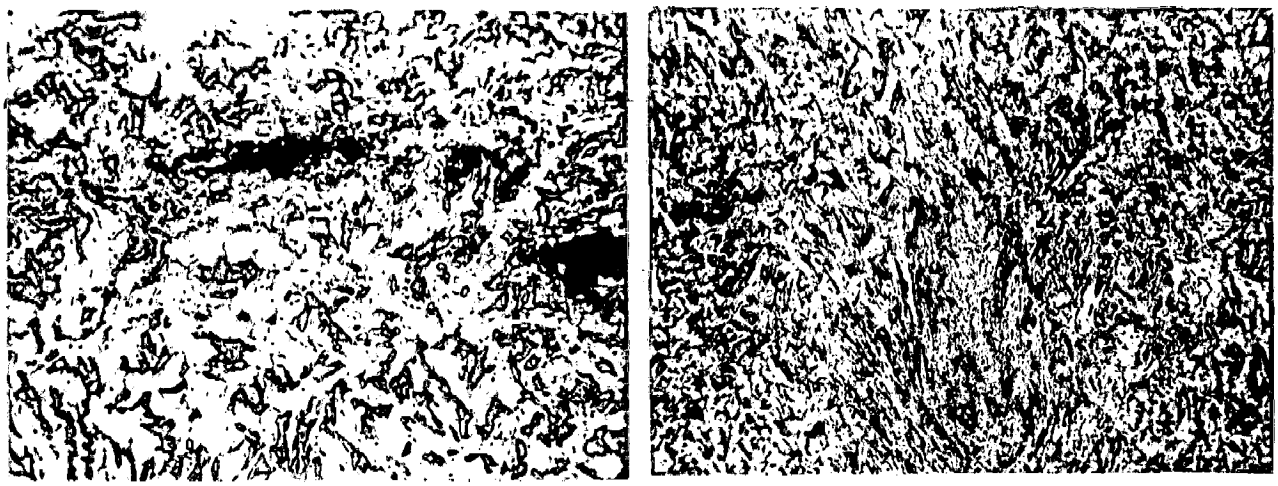

(a) (b)

Fig. 7.10 Optical micrographs showing subsurface microstructure of (a) DP steel, X 100 and (b) LCN steel, X 100, at a normal load of 34.3 N.

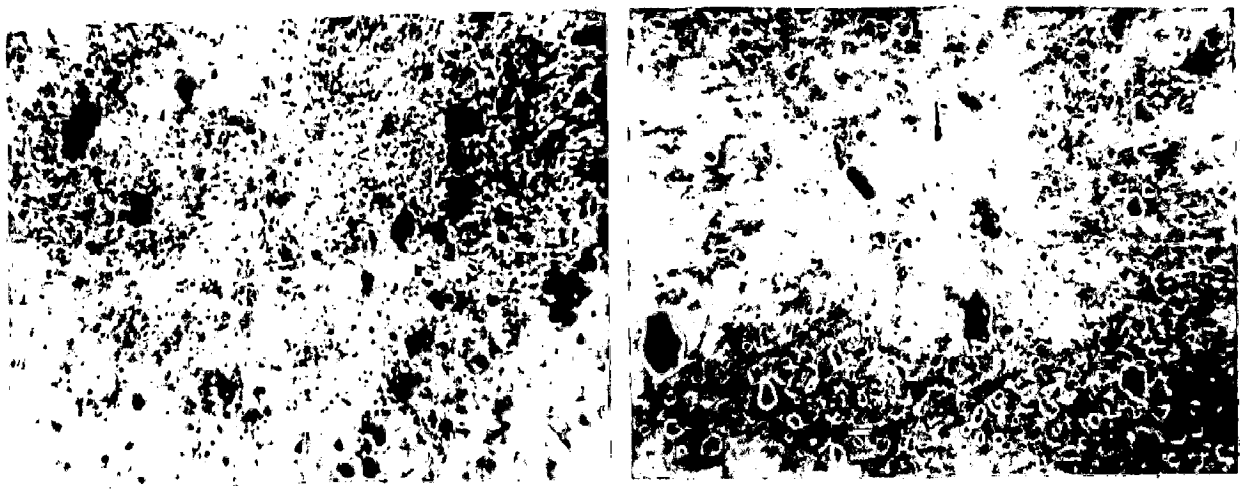

(a) (b)

Fig. 7.11 Optical stereo micrographs showing wear debris of (a) DP steel X 25 and (b) LCN steel, X 25 spread on white paper, for short sliding distances corresponding to the first linear segment.

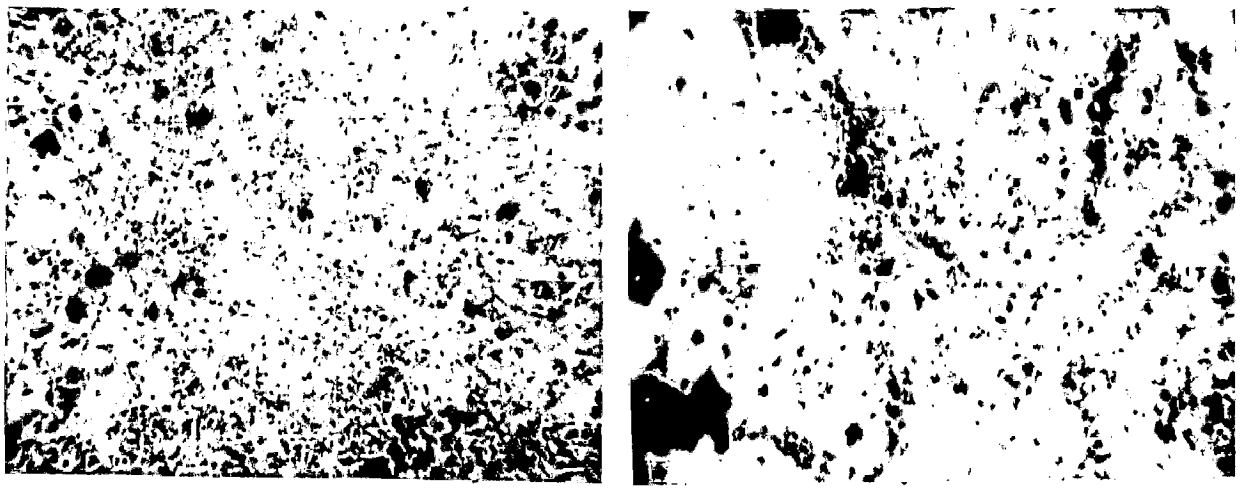

(a) (b)

Fig. 7.12 Optical stereo Micrographs showing wear debris of (a) DP steel, X.25 and (b) LCN steel, X 25 spread on white paper, for long sliding distances corresponding to the second linear segment.

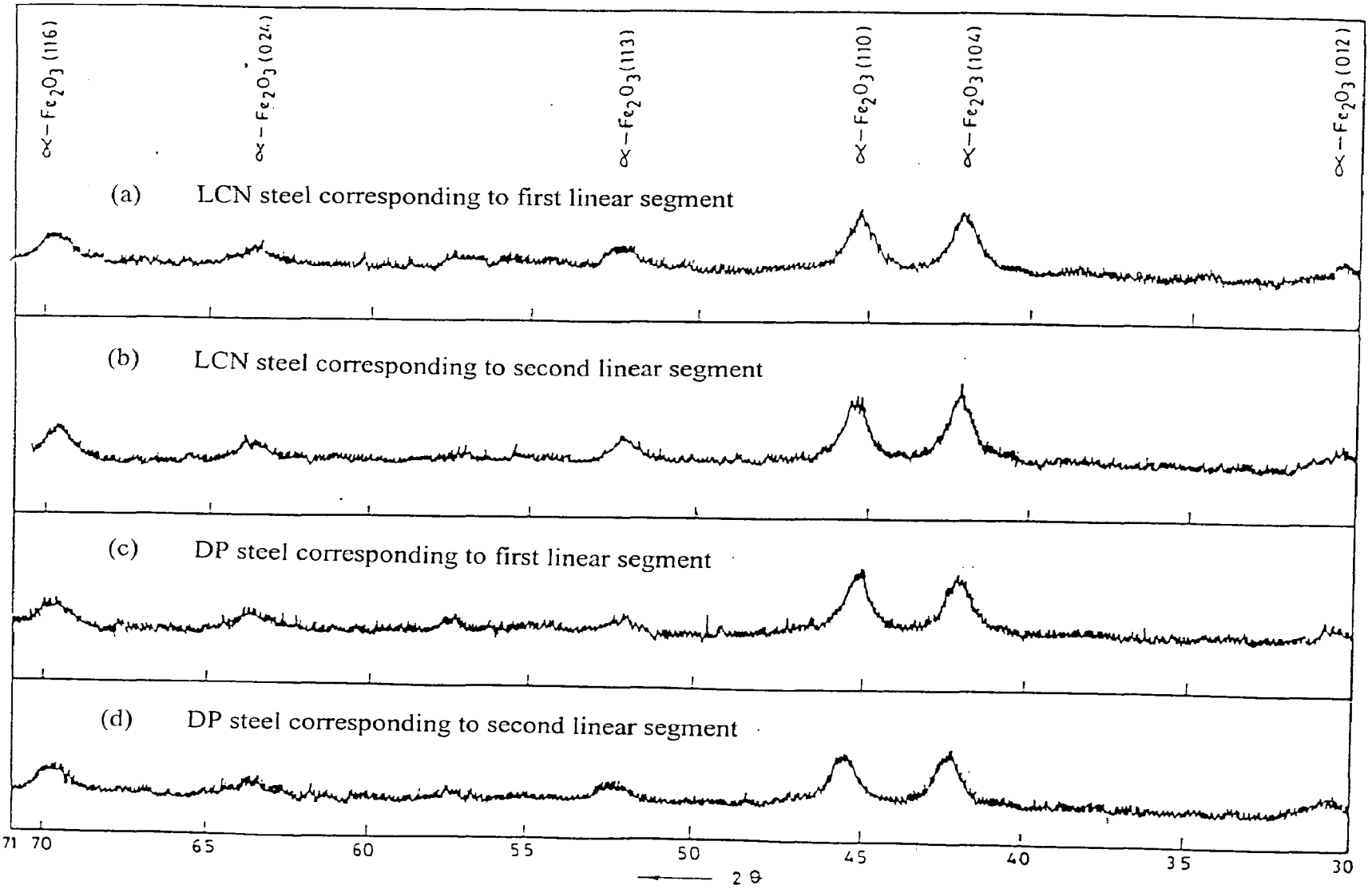

Fig. 7.13 X-ray diffraction patterns of the wear debris for both LCN and DP steels generated at a normal load of 34.3 N and collected from the disc counterface.

7.1.4 X-Ray Diffraction Analysis

The X-ray diffraction studies have been carried out on the wear debris of LCN and DP steel by using an iron target. The debris generated during the run-in stage of wear has been analysed separately from that generated during the steady state wear.

Figures 7.13 (a) to (d) show the X ray diffraction patterns of the wear debris of both the LCN and the DP steels. Figures 7.13 (a) and (b) show the X-ray diffraction patterns of the wear debris of LCN steel that corresponds to first and second linear segments respectively, generated under a normal load of 34.3 N. Figures 7.13 (c) and (d) show the X-ray diffraction patterns of the wear debris of DP steel that corresponds to first and second linear segments respectively, also under the same load of 34.3 N.

All the peaks in the patterns correspond to those belonging to α-Fe_2O_3. The corresponding $Sin\theta$ and d values are reported in Table A.15 in the appendix. The miller indices of planes (hkl), giving rise to diffraction peaks, are shown in Figs. 7.13 (a) through (d). However, no peak was observed for iron. When iron was present, it was not detected because of its small quantity.

7.2 DISCUSSION

The cumulative volume loss and the wear rate in the run-in stage are relatively higher compared to that observed in the steady state of wear for both the DP and the LCN steels as shown in Figs. 7.1, 7.2 and 7.3. The higher volume loss in the run-in stage may be attributed

to the initial roughness of the surfaces. All engineering surfaces are rough and have gentle undulations protruding out of the surface commonly known as asperities. When two nominally flat surfaces are brought together, the contact occurs at these asperities and imposition of a relative motion of sliding causes shearing of these asperities. The mating surfaces evolve to attain a better surface conformity with each other at the end of the run-in stage. The wear in the run-in stage occurs by the removal of high asperities and the pre-existing layers of oxides resulting in a relatively higher loss of material in this stage. Therefore, the wear rate, given by the slope of the line in Figs. 7.1 and 7.2, is also high in run-in stage as shown in Fig. 7.3. The onset of the steady state, shown by second linear segment in Figs. 7.1 and 7.2, may be explained on the basis of attaining steady state in respect of the real area of contact and at the same time, the evolution of mating surfaces to better conformity. Figures 7.8 (a) to (c) show the SEM micrographs of the worn surfaces of both DP and LCN steels under different loads. It is observed that at a load of 24.5 N, apart from scoring marks, there is a compacted transfer layer of oxide that appears bright under SEM. At the loads used in the present investigation, the wear appears to be primarily oxidative in DP steel, as is evident from the transfer layer. For short sliding times corresponding to the first linear segment, the oxidative nature of wear is further confirmed by examination of wear debris which shows fine oxide particles apart from a few larger oxide agglomerates, as shown in Fig. 7.11 (a). For short sliding times, when the wear is in the first linear segment of Fig. 7.2, the LCN steel has also shown similar mechanisms of wear as evident from Figs. 7.8 (c) and 7.11 (b). There are also a few craters from where metallic particles may have come into the wear debris due to microwelding or delamination, as shown in Fig. 7.8 (c). An examination of subsurface of LCN steel clearly reveals a few locations where delamination could have taken place, as shown in Fig. 7.9 (b), marked by arrow. In DP steel, the cracks may have formed around hard martensite islands as shown by arrow, in Fig. 7.9 (a). But no trace of metallic iron is observed in X-ray diffraction pattern. Therefore, it appears that cracked particle gets oxidised before generating wear debris.

An evaluation of wear particles shown in Figs 7.11 and 7.12, corresponding to the first and second linear segments in Figs. 7.1 and 7.2 for DP steel and LCN steel respectively, indicates that the wear mechanism involved is primarily oxidative wear. This is further confirmed by the X-ray diffraction patterns as shown in Figs. 7.13 (a) to (d) of the wear debris of both LCN and DP steels corresponding to first and second linear segments of Figs. 7.1 and 7.2. Figures. 7.13 (a) and (b) show the X-ray diffraction pattern for the wear debris of LCN steel corresponding to first and second linear segments, respectively, generated at a load of 34.3 N. Figures 7.13 (c) and (d) show the X-ray diffraction pattern for the wear debris of DP steel corresponding to first and second linear segments, respectively, at the same load of 34.3 N. All the peaks in the pattern correspond to those belonging to α-Fe_2O_3. The miller indices of planes (hkl), which have given rise to diffraction peaks, are shown in Figs. 7.13 (a) to (d). However, no peak was observed for iron. When present, it was not detected because of their small quantity.

The rate of wear in the first segment is higher compared to that in the steady state for both LCN and DP steels as shown in Fig. 7.3. In the second linear segment, the accumulated oxide in the wear debris gets compacted to form a transfer layer that protects the underlying metal and the wear rate decreases as shown in Fig. 7.3, for both DP and LCN steels. However, the transfer layer may not form to cover the entire contact surface and some direct metal-metal adhesion may also be taking place particularly at low loads which has resulted in higher coefficient of friction. The observed lower wear rate in DP steel in comparison to that in LCN steel as shown in Fig. 7.3, could be due to lower contact area in DP steel at a given load contributed by its higher hardness compared to that in LCN steel. The increasing difference in the wear rate between DP and LCN steels at higher loads could be due to the difference in microstructure. The ferrite in dual phase steel is relatively harder (Table-A.4) compared to the ferrite in LCN steel. At a higher load, the increasingly higher wear rate observed in LCN steel may be due to increase in flaking off of the transfer layer during

sliding, which depends on its extent of compaction and the nature of its adhesion on the pin surface. Higher hardness in the metallic area of DP steel may result in a compaction layer of higher integrity, which does not flake off so easily even with increasing load. Thus, the extent of transfer layer may also be higher in DP steel resulting in relatively lower friction at higher load in DP steel as compared to that in LCN steel. But the extent of transfer layer has not been quantified in this study.

The linear behaviour of load *vs.* wear rate in Fig. 7.3 is indicative of Archard's law. Quinn (1983) has shown that in case of constant oxidation rate resulting in linear growth of oxidation layer over time, the wear rate will be independent of time and will show a behaviour similar to Archard's law also for oxidative wear. Linear rate of layer growth is often observed in oxidation of metals when ion diffusion constraints are negligible (Batchelor *et al*, 1986). Tomashow (1986) has given examples of linear rate of layer growth in nonferrous metals. In these ferrous alloys under consideration, it is possible that the small layer of oxide cracks during sliding generating wear debris of oxide particles and allows further access of oxygen. Since the critical thickness of oxide necessary for its removal is small, it is not surprising that Archard's law of wear is being followed in the first linear segment of both DP and LCN steels.

The second linear segments for both DP and LCN steels as shown in Figs. 7.1 and 7.2, have different slopes compared to the first linear segment which may be due to formation of well compacted transfer layer of oxide. In individual measurements on a sample there is scatter from the linear variation of wear volume with sliding distance contributed by sudden flaking off the transfer layer resulting in larger aggregates of oxides in wear debris as shown in Figs. 7.12 (a) and (b). However, averaging of wear volume has significantly suppressed this scatter. But in DP steel, the scatter could still be observed even after averaging the wear volume, as revealed, particularly in the second linear segment in Fig. 7.1. The change in

slope of the linear segment during sliding has been observed earlier in ferrous alloys and it has been attributed to a change in the nature of oxides (Smith, 1986). But the study here indicates formation of α-Fe_2O_3 alone and change in the nature of oxide is not observed as shown in Fig.7.13.

When the test sample is under dry sliding wear, the frictional heating helps atmospheric oxidation over the sliding surface and the oxide layer gets removed by repeated and multiple contacts and wear debris of oxide particles are generated. The wear debris gets trapped between the sliding surfaces and is compacted into a layer. The competition between the removal of transfer layer and its reformation and thickening could result in fluctuation of friction coefficient, as observed in Figs. 7.6 (a) and (b). At very short sliding distances, the fluctuation may also include the contribution resulting from the variation of contact when the sample and the counterface develop better surface conformity. The amplitude of this initial fluctuation is reduced and a dynamic steady state is established eventually. At the steady state, it appears that the relative area under effective oxide cover increases due to increased frictional heating at higher loads. Thus, it is observed that the coefficient of friction tends to decrease with increasing load, as shown in Fig. 7.7. The first segment of the linear variation of cumulative volume loss with sliding distance could correspond to the period prior to attaining the steady state, which is indicated by the onset of the second linear segment. The readings have been taken at an interval of 10 minutes for the first four points, 20 minutes for the next two points and then, the time interval has been progressively increased in order to cover a longer total time. When a higher time interval is used, the temperatures prevailing in the sample due to frictional heating is expected to increase till steady temperature corresponding to thermal equilibrium between heat produced and heat lost has been attained. The bulk temperature of the test specimens as measured on the specimen side surface is about 70^0C and it increased to this temperature on sliding over a long time. Thus the variation of time period from 10 to 20 minutes may not have resulted any significant

temperature variation. The theoretical bulk temperature at the surface of the sample calculated on the basis of model given by Lim and Ashby (1987) is found to be 303 K i.e., 30^0C, which is significantly lower than the temperature measured 3 mm away from the sliding surface. The contact temperature of the sliding surface calculated by using the heat flow equations given by Alpas and Ames (1995) is 604 K i.e., 331^0C.

To examine the possibility of subsurface work hardening, the samples of DP and LCN steels tested for wear, have been ground to a taper of 1:10 and Vickers macro-hardness measurements have been carried out from the sliding surface along the taper. In LCN steel the hardness near the sliding surface has increased from 136 HV before sliding to 175, 156 and 195 HV respectively after sliding under the loads of 14.7, 24.5 and 34.3 N. For the DP steel, the hardness before sliding is 215 HV and it has increased to 251, 216 and 269 HV after sliding under the loads of 14.7, 24.5 and 34.3 N respectively, for the same total sliding time. This increase in hardness could have resulted due to subsurface work hardening as revealed in the subsurface microstructure shown in Figs. 7.10 (a) and (b) for DP and LCN steels respectively. For DP steel the variation of wear rate with load could be considered linear but for LCN steel, the wear rate increases significantly at higher load exceeding 24.5 N to result in a clearly nonlinear trend as shown in Fig. 7.3. The difference in subsurface hardening in both the DP and the LCN steels are similar and may not account for the larger difference in wear rates in both the run-in and the steady state of wear in these steels. The extent of transfer layer formed in these two steels may account for this difference but as it has already been mentioned the present study has not quantified this layer.

The results of wear coefficient for both the DP and the LCN steels are nearly similar as shown in Table A.13 in the run-in stage of wear although the wear rates are significantly different as shown in Fig. 7.3 and Table A.13. The slope of the wear rate with load is significantly higher in LCN steel compared to that in DP steel. Following Eq. (7.1) the wear

coefficient could be taken as wear rate per unit area of real contact. Since DP steel has a higher hardness compared to LCN steel, the former has a lower contact area compared to the LCN steel. Thus, inspite of a lower wear rate and its lower slope of variation with load, the wear coefficient of DP steel has become similar to that of LCN steel due to lower real area of contact. Similar effect may be observed for the wear coefficient in the second linear segment (steady state) particularly at higher load as shown in Table A.13. The wear coefficient as a sensitive, discriminating wear parameter may not, therefore, be adequate in materials of similar property and structure; the wear rate may be a better indicator.

A comparison of the steel having 0.14 wt pct carbon with a steel having 0.42 wt pct carbon in the normalised state shows that the wear rate, the coefficient of friction and the wear coefficient are relatively higher for a steel with lower carbon content under the conditions used in the present study. This may be attributed to the higher hardness of the steel having higher carbon content which results in a relatively lower area of contact and therefore, a lower wear rate and friction coefficient. Similar conclusions can be drawn by a comparison of the low carbon and medium carbon dual phase steels. Dual phase steel with higher carbon and higher martensite volume fraction results in lower wear rate and coefficient of friction because of the same reason as discussed above.

The wear rates corresponding to both the run-in and the steady state are found to decrease linearly with increasing volume fraction of martensite as shown in Figs. 7.4 and 7.5 at the normal loads of 14.7 and 34.3 N respectively. It may be attributed to the hardness imparted by the increasing amount of martensite, which results in a lower real area of contact, and therefore, a lower wear rate as described also in Chapter 6. It is interesting to note that the wear rate decreases linearly with increasing volume fraction of martensite irrespective of the carbon content of steel. Hence, it appears that in dual phase steels the wear rate is sensitive to the amount of the martensite only and not to the carbon content of steel.

The study presented above is to understand the friction and wear behaviour of a low carbon dual phase steel in the context of those observed in the normalised steel having the same carbon content. The mechanism of wear is primarily oxidative in nature in both of these steels which has been confirmed the X-ray diffraction analysis of the wear debris. The wear rates for both the dual phase and the normalised steels are found to increase linearly with increasing load following Archard's law. But the wear rate is lower for the dual phase steel as compared to that for the normalised steel. It has been attributed to a relatively higher hardness resulting in lower real area of contact in dual phase steel as compared to that in normalised steel having relatively lower hardness. The average coeficient of friction in dual phase steel is found to be marginally lower than that observed in normalised steel. It has been attributed to different oxidation characteristics of these steels, which have not been specifically investigated in this study. The wear coefficient as determined, is found to be an inadequate parameter for discriminating the wear resistance of materials.

Chapter 8

CONCLUSIONS

The present investigation on the chararteisation of medium and low carbon dual phase steels may be concluded in two sections corresponding to two aspects covered in this study (i) mechanical properties of dual phase steels developed by intercritical annealing (ii) tribological behaviour of the materials.

8.1 MECHANICAL PROPERTIES

(1) The martensite volume fraction in the dual phase steels increases initially with increasing time for intercritical annealing at 740^0C. However, the amount of martensite saturates after intercritical annealing for 3.5 minutes in medium carbon steel containing 0.42 wt pct carbon at a temperature of 740^0C.

(2) The Brinnel hardness, the yield strength and the ultimate tensile strength (UTS) in dual phase steels increase with increasing volume fraction of martensite, which is a hard and load bearing phase.

(3) However, the ductility measured in terms of percentage elongation and percentage reduction in area decreases with increasing martensite volume fraction.

(4) The microhardness of the martensite decreases whereas, that of the ferrite in dual phase steels increases with increasing time of intercritical annealing due to the

increased diffusion of carbon from austenite (which on water quenching transforms to martensite) to ferrite.

(5) The size of martensite islands increases while the size of the ferrite grains decreases with increasing time of intercritical annealing due to the growth of austenite into ferrite areas with diffusion of carbon.

(6) Increasing volume fraction of martensite in dual phase steels is accompanied by a decrease in the strain hardening coefficient which has been attributed to the dominating influence of increasing size of martensite islands.

(7) DP1 and DP2 steels containing 42 and 51 pct of martensite respectively, show the ductile fracture as it has been observed also in the Armco iron and N steel. However, DP3 and DP4 steels containing 59 and 72 pct of martensite respectively, have shown the mixed (ductile + brittle) mode of fracture whereas the fully martensitic steel has undergone a brittle mode of fracture.

(8) The dimple size is found to decrease linearly with increasing volume fraction of martensite. This has indicated the role of ferrite/martensite interface in nucleating microvoids.

8.2 TRIBOLOGICAL BEHAVIOUR

(9) At a constant load, friction coefficient in the run-in stage fluctuates around a mean level, then lessens and stabilizes after a certain period. This is true for all the low

carbon and medium carbon steels having different microstructures, investigated in the present study.

(10) The friction coefficient decreases with increasing normal load in both the run-in and the steady state of wear for all the low carbon and medium carbon steels having different microstructures, investigated in the present study which has been attributed to the enhanced frictional heating leading to increased rate of oxidation at the contacts and the lower shear strength of the junctions.

(11) However, the average coefficient of friction in the run-in stage is higher than that in the steady state for all the materials which has been attributed to the oxidation and formation of a well compacted transfer layer of the oxide on the surface in the steady state, covering more area where junctions of lower shear strength may form.

(12) At a given load, the coefficient of friction decreases with the increasing hardness of the materials containing increasing amount of martensite from ferritic Armco iron to fully martensitic steel (FMS). This has been attributed to the decreasing real area of contact and the extent of compaction of the transfer layer resulting in a decrease in the coeficient of friction.

(13) The coefficient of friction in the low carbon normalised (LCN) steel is marginally higher than that observed for the medium carbon normalised (N) steel. This may be attributed to the relatively higher hardness at higher carbon content resulting in a lower real area of contact.

(14) The coefficients of friction in the steady state, calculated on the basis of (i) estimated load sharing between the constituent phases and (ii) the observed friction coefficients of fully ferritic Armco iron and martensite (FMS) are relatively lower than those observed experimentally in DP steels. This difference between the calculated and the experimental friction coefficients decreasing with increasing martensite volume fraction has been attributed to the flow of the softer phase of easily oxidised ferrite over the hard martensite islands in the DP steels.

(15) The coefficients of friction calculated on the basis of the rule of mixture are consistently higher than those observed experimentally at all the loads in dual phase steels.

(16) The mechanism of wear is primarily oxidative in the range of loads and sliding speed used in the present study for low and medium carbon steels having different microstructures investigated, as evident from the wear debris and the transfer layers. However, some delamination caused by subsurface cracking could also be observed at a few places, particularly at higher loads.

(17) The wear debris of oxides, confirmed by the X-ray diffraction patterns, consists of α-Fe_2O_3 in the wear debris; no metallic particles or other oxides could be detected by X-ray diffraction.

(18) For a given load, the cumulative wear volume increases linearly with increasing sliding distance in the run-in stage but changes slope beyond certain sliding distance when steady state of wear sets in for all the materials used in the present investigation. Therefore, the wear volume-distance relationship has been represented by two linear segments in order to remain within the framework of Archard's law.

(19) The onset of the steady state after a short span of the run-in stage has been attributed to the attainment of a steady state on sliding surface in respect of the real area of contact, oxidation and the formation of a well compacted transfer layer of the oxide for a given condition of load and sliding velocity.

(20) The wear rate increases linearly with increasing load in both the run-in and the steady state of wear for all the low and medium carbon steels having different microstructures, investigated in the present study. In the steady state the wear rate increases with a higher slope beyond a certain load for both low carbon normalised (LCN) and medium carbon normalised (N) steels. However, the wear rate is less in the steady state as compared to that in the run-in stage of wear. This has been attributed to the cover provided by oxidation and the compacted transfer layer of oxide, which protects the underlying material.

(21) For a particular load, the wear rate in the dual phase steels decreases linearly with increasing volume fraction of martensite irrespective of the carbon content of steel. The highest wear rate has been observed in fully ferritic material of Armco iron and the lowest wear rate is observed in fully martensitic steel (FMS). This has been explained on the basis of higher hardness imparted by the increasing volume fraction of martensite, which results in a lower real area of contact and therefore, a lower wear rate.

(22) The wear rates in both the segments (run-in and steady state) are higher in the low carbon normalised (LCN) steel than in the low carbon DP steel. Similar results have been observed in medium carbon DP steels. This has been attributed to the relatively higher hardness in the DP steel.

(23) The wear rates in the low carbon normalised (LCN) steel are higher than those observed for the medium carbon normalised (N) steel in both the run-in and the steady state of wear. This may be attributed to the relatively higher hardness of the N steel having higher carbon content.

(24) The wear rates calculated on the basis of (i) estimated load sharing between the constituent phases and (ii) the observed wear coefficients of the ferritic Armco iron and martensitic (FMS), are relatively higher than the observed wear rates in dual phase steels in both the run-in and the steady state of wear. This difference has been attributed to the flow of the softer phase of ferrite over the hard martensite islands resulting in easily oxidised junctions of low shear strength, which has not been taken into account in the calculation.

(25) When the critical thicknesses of the oxides and the probabilities of their removal are presumed the same, the wear rates calculated on the basis of the proposed model of oxidative wear for multiphase material, are higher than those observed experimentally in DP steels. This has been attributed to the assumed values of the critical thickness of the oxides and the oxidation rate constant which may be different under the dry sliding condition due to limited supply of oxygen at the sliding surface.

(26) When the critical thicknesses of the oxides and the probabilities of their removal are presumed different for both the phases in DP steel the wear rates, estimated on the basis of the proposed model of oxidative wear for multiphase material are comparable to the observed wear rates at lower loads in DP1, DP2 and DP3 steels but are

increasingly higher at higher loads in both the run-in and the steady state of wear. This increasing difference in the estimated and the observed wear rates with load has been attributed to the flow of the softer ferrite over the hard martensite islands. However, the estimated and observed wear rates show a better matching for the DP4 steel containing the highest volume fraction of martensite. This has been attributed to the restricted flow of ferrite over the martensite islands.

(27) The wear coefficients are similar for DP1, DP2, fully ferritic Armco iron and medium carbon normalised (N) steel in the run-in stage of wear despite the difference in the wear rates. Similar results have been observed for both low carbon normalised (LCN) and dual phase (DP) steel. It appears that any decrease in the real area of contact has been compensated by a decreasing wear rate. But the wear coeficient decreases sharply for DP3 and DP4 containing higher amount of martensite indicating a higher decrease in wear rate compared to the decrease in the real area of contact. However, in the steady state the wear coefficient decreases linearly with increasing volume fraction of martensite in dual phase steels reflecting the effect of the decreasing wear rate dominating over the decreasing real area of contact.

APPENDIX

TABLE A.1

Metallographic Characterisation of the Specimens.

Sample Designation	Heat Treatment	Volume fraction of Martensite/pearlite (%)	Mean grain size of ferrite (μm)	Martensite island/Pearlite colony size (μm)
Armco iron	As received	-	105	-
N steel	Normalising at 860°C, 20 Min., Air cooled	52	-	19
DP1	Intercritical annealing at 740°C, 2.0 min, water quench	42	9	7.8
DP2	Intercritical annealing at 740°C, 2.5 min, water quench	51	8	16
DP3	Intercritical annealing at 740°C, 3.0 min, water quench	59	5	18
DP4	Intercritical annealing at 740°C, 3.5 min, water quench	72	5	33
FMS	Austenetizing at 920°C, 20 min, water quench	100	-	-

TABLE A.2

Mechanical Properties of the Armco iron, N steel, DP steels and FMS.

Sample Designation	Macrohardness (HB)	YS (MPa)	UTS (MPa)	% Elongation	% area reduction	Strain hardening index (n)
Armco iron	84	75	178	28	80	0.14
N steel	190	507	747	19	29	0.15
DP1	284	536	836	13	22	0.09
DP2	320	719	907	11	13	0.08
DP3	344	758	974	8	10	0.07
DP4	373	1070	1091	4	5	0.06
FMS	495	1460	1460	3		0.02

TABLE A.3

Microhardness of Phases in Medium Carbon Steel.

Steel Designation	Regions	Phases Identified	Average Microhardness (HV)
Normalised	Bright	Ferrite	152
	Dark	Pearlite	347
DP1	Bright	Ferrite	190
	Dark	Martensite	750
DP2	Bright	Ferrite	195
	Dark	Martensite	740
DP3	Bright	Ferrite	202
	Dark	Martensite	732
DP4	Bright	Ferrite	210
	Dark	Martensite	720

a. Load, 10 g (0.01 kg)

TABLE A.4

Microhardness of Phases in Low Carbon Steel.

Steel	Regions	Phases Identified	Average microhardness in HV[a]
DP	Bright	Ferrite	283
	Dark	Martensite	505
LCN	Bright	Ferrite	206
	Dark	Pearlite	311

a. Load, 10 g (0.01 kg)

TABLE A.5

Slopes and Coefficient of Correlation of Log-Log Plot of Cumulative Wear Volume *vs.* Sliding Distance for Armco iron, N steel, DP steels and FMS.

Sample Designation	Slope					Coefficient of Correlation				
	Load (N)					Load (N)				
	14.7	19.6	24.5	29.4	34.3	14.7	19.6	24.5	29.4	34.3
Armco iron	0.85	0.83	0.83	0.82	0.88	0.99	0.99	0.99	0.99	0.99
N steel	0.73	0.76	0.77	0.79	0.77	0.99	0.99	0.99	0.99	0.99
DP1	07.72	0.74	0.73	0.78	0.80	0.99	0.99	0.99	0.99	0.99
DP2	0.73	0.77	0.76	0.79	0.75	0.99	0.99	0.99	0.99	0.99
DP3	0.70	0.74	0.81	0.82	0.81	0.99	0.99	0.99	0.99	0.99
DP4	0.74	0.77	0.80	0.81	0.81	0.99	0.99	0.99	0.99	0.99
FMS	0.68	0.72	0.71	0.70	0.77	0.99	0.99	0.99	0.99	0.99

TABLE A.6

Wear Rates and Wear Coefficients for Armco Iron, N Steel, DP Steels and FMS at a Normal Load of 14.7 N.

Sample Designation	Wear Rate Run-in (mm^3/m)	Wear Coefficient (Run-in)	Wear Rate Steady-state (mm^3/m)	Wear Coefficient (Steady-state)
Armco iron	0.33×10^{-3}	1.85×10^{-5}	0.2×10^{-3}	1.12×10^{-5}
N steel	1.42×10^{-4}	1.80×10^{-5}	0.69×10^{-4}	0.87×10^{-5}
DP1	0.76×10^{-4}	1.43×10^{-5}	0.40×10^{-4}	0.76×10^{-5}
DP2	0.61×10^{-4}	1.31×10^{-5}	0.31×10^{-4}	0.67×10^{-5}
DP3	0.51×10^{-4}	1.17×10^{-5}	0.21×10^{-4}	0.48×10^{-5}
DP4	0.30×10^{-4}	0.74×10^{-5}	0.16×10^{-4}	0.41×10^{-5}
FMS	0.14×10^{-4}	0.45×10^{-5}	0.06×10^{-4}	0.20×10^{-5}

TABLE A.7

Wear Rates and Wear Coefficients for Armco Iron, N Steel, DP Steels and FMS at a Normal Load of 19.6 N.

Sample Designation	Wear rate Run-in (mm^3/m)	Wear Coefficient (Run-in)	Wear rate Steady-state (mm^3/m)	Wear Coefficient (Steady-state)
Armco iron	0.49×10^{-3}	2.07×10^{-5}	0.28×10^{-3}	1.19×10^{-5}
N steel	2.07×10^{-4}	1.97×10^{-5}	0.92×10^{-4}	0.87×10^{-5}
DP1	1.22×10^{-4}	1.73×10^{-5}	0.59×10^{-4}	0.84×10^{-5}
DP2	0.96×10^{-4}	1.54×10^{-5}	0.47×10^{-4}	0.67×10^{-5}
DP3	0.83×10^{-4}	1.38×10^{-5}	0.31×10^{-4}	0.54×10^{-5}
DP4	0.42×10^{-4}	0.78×10^{-5}	0.23×10^{-4}	0.42×10^{-5}
FMS	0.21×10^{-4}	0.52×10^{-5}	0.092×10^{-4}	0.23×10^{-5}

TABLE A.8

Wear Rates and Wear Coefficients for Armco Iron, N Steel, DP Steels and FMS at a Normal Load of 24.5 N.

Sample Designation	Wear rate Run-in (mm^3/ m)	Wear Coefficient (Run-in)	Wear rate Steady-state (mm^3/ m)	Wear Coefficient (Steady-state)
Armco iron	0.62×10^{-3}	2.08×10^{-5}	0.38×10^{-3}	1.28×10^{-5}
N steel	2.89×10^{-4}	2.19×10^{-5}	1.17×10^{-4}	0.89×10^{-5}
DP1	1.58×10^{-4}	1.8×10^{-5}	0.82×10^{-4}	0.93×10^{-5}
DP2	1.31×10^{-4}	1.68×10^{-5}	0.65×10^{-4}	0.83×10^{-5}
DP3	1.02×10^{-4}	1.41×10^{-5}	0.47×10^{-4}	0.65×10^{-5}
DP4	0.57×10^{-4}	0.85×10^{-5}	0.33×10^{-4}	0.49×10^{-5}
FMS	0.31×10^{-4}	0.61×10^{-5}	0.13×10^{-4}	0.26×10^{-5}

TABLE A.9

Wear Rates and Wear Coefficients for Armco Iron, N Steel, DP Steels and FMS at a Normal Load of 29.4 N.

Sample Designation	Wear rate Run-in (mm^3/ m)	Wear Coefficient (run-in)	Wear rate Steady-state (mm^3/ m)	Wear Coefficient (Steady-state)
Armco iron	0.78×10^{-3}	2.17×10^{-5}	0.51×10^{-3}	1.43×10^{-5}
N steel	3.54×10^{-4}	2.24×10^{-5}	1.67×10^{-4}	1.06×10^{-5}
DP1	1.98×10^{-4}	1.87×10^{-5}	1.09×10^{-4}	1.03×10^{-5}
DP2	1.81×10^{-4}	1.83×10^{-5}	0.78×10^{-4}	0.84×10^{-5}
DP3	1.24×10^{-4}	1.43×10^{-5}	0.64×10^{-4}	0.71×10^{-5}
DP4	0.73×10^{-4}	0.90×10^{-5}	0.41×10^{-4}	0.51×10^{-5}
FMS	0.41×10^{-4}	0.67×10^{-5}	0.18×10^{-4}	0.28×10^{-5}

TABLE A.10

Wear Rates and Wear Coefficients for Armco Iron, N Steel, DP Steels and FMS at a Normal Load of 34.3 N.

Sample Designation	Wear rate Run-in (mm^3/ m)	Wear Coefficient (run-in)	Wear rate Steady-state (mm^3/ m)	Wear Coefficient (Steady-state)
Armco iron	0.97×10^{-3}	2.31×10^{-5}	$0.62.\times 10^{-3}$	1.48×10^{-5}
N steel	4.39×10^{-4}	2.38×10^{-5}	2.15×10^{-4}	1.17×10^{-5}
DP1	2.54×10^{-4}	2.06×10^{-5}	1.42×10^{-4}	1.16×10^{-5}
DP2	2.07×10^{-4}	1.89×10^{-5}	1.01×10^{-4}	0.92×10^{-5}
DP3	1.58×10^{-4}	1.56×10^{-5}	0.82×10^{-4}	0.81×10^{-5}
DP4	0.86×10^{-4}	0.91×10^{-5}	0.55×10^{-4}	0.52×10^{-5}
FMS	0.51×10^{-4}	0.73×10^{-5}	0.22×10^{-4}	0.31×10^{-5}

TABLE A.11

Wear Rate Data for Dual Phase Steels Corresponding to Both Run-in and Steady State of Wear.

Normal load (N)	Wear rate in 1st segment(Run–in) (mm^3/m)			
	DP1	DP2	DP3	DP4
14.7	0.76×10^{-4}	0.61×10^{-4}	0.51×10^{-4}	0.30×10^{-4}
19.6	1.22×10^{-4}	0.96×10^{-4}	0.83×10^{-4}	0.42×10^{-4}
24.5	1.59×10^{-4}	1.31×10^{-4}	1.02×10^{-4}	0.57×10^{-4}
29.4	1.98×10^{-4}	1.81×10^{-4}	1.24×10^{-4}	0.73×10^{-4}
34.3	2.54×10^{-4}	2.07×10^{-4}	1.58×10^{-4}	0.86×10^{-4}
	Wear rate in 2nd segment (steady state) (mm^3/m)			
14.7	0.40×10^{-4}	0.32×10^{-4}	0.21×10^{-4}	0.16×10^{-4}
19.6	0.59×10^{-4}	0.47×10^{-4}	0.31×10^{-4}	0.23×10^{-4}
24.5	0.82×10^{-4}	0.65×10^{-4}	0.47×10^{-4}	0.33×10^{-4}
29.4	1.09×10^{-4}	0.78×10^{-4}	0.61×10^{-4}	0.41×10^{-4}
34.3	1.42×10^{-4}	1.00×10^{-4}	0.82×10^{-4}	0.55×10^{-4}

TABLE A.12

Average Wear Coefficient for the Armco iron, N steel, DP steels and FMS for both Run-in and Steady State.

Sample Designation	Wear Coefficient 1^{st} segment (run-in)	Wear Coefficient 2^{nd} segment (steady state)
Armco iron	2.60×10^{-5}	1.88×10^{-5}
N steel	2.56×10^{-5}	1.72×10^{-5}
DP1	2.46×10^{-5}	1.43×10^{-5}
DP2	2.41×10^{-5}	1.06×10^{-5}
DP3	1.76×10^{-5}	0.95×10^{-5}
DP4	1.07×10^{-5}	0.70×10^{-5}
FMS	0.95×10^{-5}	0.38×10^{-5}

Table A.13

Wear Rates and Wear Coefficients for Low Carbon Normalised and Dual Phase Steels.

Type of Steel	Load (N)	Wear rate 1^{st} segment (run-in) (mm^3/m)	Wear Coefficient (run-in)	Wear rate 2^{nd} segment (steady state) (mm^3/m)	Wear Coefficient (Steady State)
LCN	14.7	3.44×10^{-4}	0.31×10^{-4}	1.44×10^{-4}	0.13×10^{-4}
	24.5	5.83×10^{-4}	0.32×10^{-4}	2.96×10^{-4}	0.16×10^{-4}
	34.3	9.42×10^{-4}	0.37×10^{-4}	7.70×10^{-4}	0.30×10^{-4}
DP	14.7	0.99×10^{-4}	0.14×10^{-4}	1.04×10^{-4}	0.15×10^{-4}
	24.5	3.05×10^{-4}	0.26×10^{-4}	2.76×10^{-4}	0.24×10^{-4}
	34.3	4.69×10^{-4}	0.27×10^{-4}	3.72×10^{-4}	0.23×10^{-4}

Table A.14

X-Ray Diffraction Analysis for Wear Debris Generated During Sliding of Armco iron.

Sinθ	I/I_0	d	Phase	I/I_0 as in ASTM Chart
0.2638	100	3.670	α-Fe_2O_3	25
0.4384	25	2.209	α-Fe_2O_3	30
0.5239	17	1.8486	α-Fe_2O_3	40

Table A.15

X-Ray Diffraction Analysis for Wear Debris Generated During Sliding of Low and Medium Carbon Normalised and Dual Phase Steels.

Sinθ	I/I_0	d	Phase	I/I_0 as in ASTM Chart
0.2621	28	3.6944	α-Fe_2O_3	25
0.3599	100	2.6907	α-Fe_2O_3	100
0.3867	80	2.5048	α-Fe_2O_3	50
0.4415	42	2.1939	α-Fe_2O_3	30
0.5707	56	1.6973	α-Fe_2O_3	60
0.5786	50	1.6742	α-Fe_2O_3	25

REFERENCES

1. ***Abdalla***, A. J., Hein, L. R. O., Pereira, M. S. and Hashimoto, T. M., (1999), "Mechanical Behaviour of Strain Aged Dual Phase Steels," *Mater. Sc. and Tech.*, **Vol.** 15, pp. 1167-70.
2. ***Abrahamson***, E. P., Jahanmir, S., and Suh, N. P., (1975), "The Effect of Surface Finish on the Wear of Sliding Surfaces," *CIRP Annals*, International Institution of Production Engineering Research, **Vol.** 24, pp. 513-14.
3. ***Ames***, W. and Alpas, A.T., (1995), "Wear Mechanisms in Hybrid Composites of Graphite-20 Pct SiC in A356 Aluminium Alloy (Al-7 Pct Si-0.3 Pct Mg)," *Metall. Mater. Trans. A*, **Vol.** 26A, pp. 85-98.
4. ***Archard***, J. F., (1953), "Contact and Rubbing of Flat Surfaces," *J. of App. Phys.*, **Vol.** 24, pp. 981-88.
5. ***Archard***, J. F. and Hirst, W., (1956), "The Wear of Metals Under Unlubricated Conditions," *Proc. R. Soc. London, Ser. A*, pp. 397-410.
6. ***Archard***, J.F., (1980), "Wear Theory and Mechanisms," Wear Control Hand book, eds., M. B. Peterson, and W. O. Winer, *ASME*, NY, p. 35.
7. ***Archard***, J.F., (1986), "Friction Between Metal Surfaces," *Wear*, **Vol.** 113, pp. 3-16.
8. ***Ashby***, M.F., (1966), *Philosophical Magazine*, **Vol.** 14, p. 1157,
9. ***Ballinger***, N. K. and Gladman, T., (1981), *Metal Science*, pp. 95-108.
10. ***Barber***, J. R., (1969), "Thermoelastic Instabilities in the Sliding of Conforming Solids," *Proc. Roy. Soc. London. Ser. A*, **Vol.** 312, pp. 381-94.

11. ***Basak***, A., Reddy, D. C. and Kanth, D. V. K., (1998), "Computer Modelling of Wear Resistance for Plain Carbon Steels," *Material Sc. and Tech.*, **Vol.** 14, pp. 776-82.

12. ***Batchelor***, A. W., Stachowiak, G.W. and Cameron, A., (1986), "The Relationship Between Oxide Films and the Wear of Steels," *Wear*, **Vol.**113, pp. 203-23.

13. ***Bayer***, R. G., (1994), *Mechanical Wear Prediction and Prevention*, Marcel Dekker Inc., New York, USA.

14. ***Bhattacharyya***, S., (1980), "Wear and Friction in Steel, Aluminum and Magnesium Alloys I: Pearlitic and Spheroidized Steels," *Wear*, **Vol.** 61, pp. 133-41.

15. ***Blau***, P. J., (1981), "An Investigation of the Unlubricated Friction and Wear Break-in Behavior of a Dual-Phase Steel," *Wear*, **Vol.** 72, pp. 67-80.

16. ***Blau***, P. J., (1981), "Mechanisms for Transitional Friction and Wear Behavior of Sliding Metals," *Wear*, **Vol.** 72, pp. 55-66.

17. ***Blau***, P. J., (1997), "Fifty Years of Research on Wear of Metals," *Trib. Int.*, **Vol.** 30, No. 5, pp. 321-31.

18. ***Bowden***, F. P. and Tabor, D., (1954), *The Friction and Lubrication of Solids*, Part I, Clarendon Press, Oxford.

19. ***Bowden***, F. P. and Tabor, D., (1964), *The Friction and Lubrication of Solids*, Part II, Clarendon Press, Oxford.

20. ***Bucher***, J. H. and Hamburg E.G., (1977), "High-Strength Formable Sheet Steel," *SAE Reprint* 770164.

21. ***Buckley***, D. H., (1981), *Surface Effects in Adhesion, Friction, Wear and Lubrication*, Tribology Series 5, Elsevier Scientific Publishing Company.

22. ***Clayton***, P., (1980), "The Relations Between Wear Behaviour and Basic Material Properties for Pearlitic steels," *Wear*, **Vol.** 60, pp. 75-93.

23. ***Clayton***, P., Sawley, K. J., Bolton, P. J. and Pell, G. M., (1987), "Wear of Bainitic Steels," *Wear*, **Vol.** 120, pp. 199-220.

24. ***Coldren***, A. P., and Tither, G., (1978), "Development of Mn-Si-Cr-Mo As Rolled Dual Phase Steel," *J. of Metals*, **Vol.** 30, No. 4, pp. 6-19.

25. ***Coldren***, A. P., Eldis, G. T., Buck, R. M., Tither, G., Boussel, P. and Chihara, T., (1980), *Journal of Molybdneum Technology*, **Vol.** 14, No. 3, pp. 3-12.

26. ***Czichos***, H. and Habig, K. H., (1986), "Wear of Medium carbon Steel: A Systematic Study of the Influences of Materials and Operating Parameters," *Wear*, **Vol.** 110, pp. 389-400.

27. ***Dabkowski***, D. S. and Speich, G. R., (1977), "Transformation Products and the Stress-Strain Behaviour of Control-Rolled Mn-Mo-Cb Line-Pipe Steels," *Proc. of XV Conf. on Mechanical Working and Steel Processing, AIME*, New York, pp. 284-312.

28. ***Davies***, R. G., (1978), "Influence of Martensite Composition and Content on the Properties of Dual Phase Steels," *Metall. Mater. Trans. A*, **Vol.** 9A, pp. 671-79.

29. ***Eldis***, G. T. and Coldren, A.P., (1980), "Using CCT Diagrams to Optimize the Composition of an As Rolled Dual Phase Steel," *J. of Metals*, **Vol.** 32, No. 4, pp. 41-48.

30. ***Eyre***, T. S., (1976), "Wear Characteristics of Metals," *Trib. Int.*, **Vol.** 9, No. 3, pp. 203-12.

31. ***Eyre***, T. S., (1978), "The Mechanisms of Wear," *Trib. Int.*, **Vol.** 11, No. 2, pp. 91-96.

32. ***Furukawa***, T., Morikawa H., Takechi, H. and Koyama K., (1979), "Process Factors for Highly Ductile Dual Phase Sheet Steels," *Proc. Conf. on Structure and Properties of Dual-Phase Steels*, Kot, R.A. and Morris, J.W., eds., Kot, R. A. and Morris, J.W., ed.; AIME, New York, pp. 281-303.

33. ***Glaeser***, W. A., (1992), "Materials for Tribology," Tribology Series, 20, Elsevier, Amsterdam.

34. ***Greenwood***, J. A. and Williamson, J. B. P., (1966), "Contact of Nominally Flat Rough Surfaces," *Proc. Roy. Soc. London, Ser. A* 295, pp. 300-19.

35. ***Hayami***, S. and Furukawa, T., (1977), "A Family of High Strength Cold Rolled Steels," *In Micro-Alloying 75, Proceedings*, Union Carbide Corporation, New York, pp. 311-20.

36. ***Iwabuchi***, A., Hori, K. and Kubosawa, H., (1988), "The Effect of Oxide Particles Supplied at the Interface Before Sliding on the Severe-Mild Wear Transition," *Wear*, **Vol.** 128, pp. 123-37.

37. ***Jahanmir***, S., (1980), "On The Wear Mechanisms and Wear Equations," In N. P. Suh and N. Saka (eds.), *Proc. Int. Conf. on the Fundamentals of Tribology*, MIT Press, Cambridge, MA, pp. 455-67.

38. ***Kalousek***, J., Fegredo, D. M. and Laufer, E. E., (1985), "The Wear Resistance and Worn Metallography of Pearlite, Bainite and Tempered Martensite Rail Steel Microstructures of High Hardness," in K. C. Ludema (ed.), *Proc. Int. Conf. on Wear of Materials*, Vancouver, April 14-18, *ASME*, New York, pp. 212-32.

39. ***Kerlins***, V., (1992), "Modes of Fracture," ASM Handbook, **Vol.** 9, p. 13.

40. ***Koo***, J. Y., Young, M. J. and Thomas, G., (1980), "On the Law Of Mixtures in Dual Phase Steels," *Metall. Mater. Trans. A.*, **Vol.** 11A, pp. 852-54.

41. ***Kubaschewaski***, O. and Hopkins, B.E., (1962), *Oxidation of Metals and Alloys*, Butterworth & Co. Ltd., London, p. 115.

42. ***Kragelskii***, I. V., (1965), *Friction and Wear*, Butterworths, London.

43. ***Leslie***, W. C. and Sober, R. J., (1967), "The Strength of Ferrite and of Martensite as Functions of Composition, Temperature, and Strain Rate," *Trans. ASM*, **Vol.** 60, pp. 459-84.

44. ***Li***, X., Wang, Y. and Liu, J., (1991), "A Study on Dry Friction of Eutectoid Steel," *Wear*, **Vol.** 150, pp. 59-65.

45. ***Lim***, S. C. and Brunton, J. H., (1986), "The Unlubricated Wear of Iron," *Wear*, **Vol.** 113, pp. 383-93.

46. ***Lim***, S. C., Ashby, M. F. and Brunton, J. H., (1987), "Wear–Rate Transitions and Their Relationship to Wear Mechanisms," *Acta metall.*, **Vol.** 35, No. 6, pp. 1343-48

47. ***Lim***, S. C. and Ashby, M. F., (1987), Wear–Mechanism Maps," *Acta Metall.*, **Vol.** 35, No. 1, pp. 1-24.

48. ***Liu***, Y., Lim, S. C., Ray, S. and. Rohatgi, P.K, (1992), "Friction and Wear of Aluminum–Graphite Composite: The Smearing Process of Graphite During Sliding," *Wear*, **Vol.** 159, pp. 201-5.

49. ***Liu***, Y., Rohatgi, P. K. and Ray, S., (1993), "Tribological Characteristics of Aluminum – 50 vol. Pct Graphite Composite," *Metall. Mater. Trans.*, **Vol.** 24 A, pp. 151-59.

50. ***Madakson***, P. B., (1983), "The Frictional Behaviour of Metals," *Wear*, **Vol.** 87, pp. 191-206.

51. ***Matsuoka***, T. and Yamoori, K., (1975), "Metallurgical Aspects of Cold-Rolled High Strength Steel Sheets," *Metall. Mater. Trans.*, **Vol.** 6A, pp. 1613-22.

52. ***Mileiko***, S. T., (1969), "The Tensile Strength and Ductility of Continuous Fibre Composites," *J. Material Science*, **Vol.** 4, pp. 974-77.

53. ***Mokhtar***, M. O. A., Zaki, M. and Shawki, G. S. A., (1979), "Effect of Mechanical Properties on Frictional Behaviour of Metals", *Trib. Int.*, **Vol.** 12, No. 6, pp. 265-68.

54. ***Mould***, P. R. and Skena, C.C., (1979), "Structure and Properties of Cold-Rolled Ferrite-Martensite (Dual Phase) Steel Sheets," *Proc. on Formable HSLA and Dual-Phase Steels*, Kot, R.A. and Morris, J.W., ed., AIME, New York, pp. 183-205.

55. ***Nath***, S. K., (1989) "Influence of Intercritical Annealing on the Mechanical Properties of Plain-Carbon Dual Phase Steels," *Ph.D. Thesis*, University of Roorkee, Roorkee, p. 91.

56. ***Nath***, S. K., Ray, S., Mathur, V. N. S. and Kapoor, M. L., (1993), "A Single-Particle Model for Theoretical Estimation of Tensile Strength of Dual-Phase Steel," *Int. Conf. on Advanced Composite Materials* held in Australia, Eds., T. Chandra and A. K. Dhingra, The Mineral, Metals and Materials Soc., USA.

57. ***Nath***, S. K., Ray, S., Mathur, V. N. S. and Kapoor, M. L., (1994), "Non-Isothermal Austenitisation Kinetics and Theoretical Determination of Intercritical Annealing Time for Dual-Phase Steels," *Iron Steel Inst. Jpn. Int.*, **Vol.** 34(2), pp. 191-97.

58. ***Quinn***, T. F. J., (1978), "The Classifications, Laws, Mechanisms and Theories of Wear," In N. P. Suh and N. Saka (eds.), *Proc. Int. Conf. on the Fundamentals of Tribology*, MIT Press, Cambridge, MA, pp. 477-90.

59. ***Quinn***, T. F. J., (1983), "Review of Oxidational Wear Part I: The Origins of Oxidational Wear," *Trib. Int.*, **Vol.**16, pp. 257-71.

60. ***Quinn***, T. F. J., (1967), "The Effect of 'Hot Spot' Temperatures on the Unlubricated Wear of Steels," *Am. Soc. of Lub. Engrs. Trans.*, **Vol.** 10, pp. 158-68.

61. ***Rabinowicz***, E., (1965), *Friction and Wear of Metals*, John Wiley and Sons, Inc; New York, USA.

62. ***Rabinowicz***, E., (1981), *J. of Lub. Tech., ASME*, **Vol.** 103, pp. 188-94.

63. ***Ramesh***, C. S., Seshadri, S. K. and Iyer, K. J. L., (1991), "A Survey of Aspects of Wear of Metals," *Ind. J. of Tech.*, **Vol.** 29, pp. 179-85.

64. ***Ramos***, L. F., Matlock, D. K., and Krauss, G., (1979), "On the Deformation Behaviour of Dual Phase Steels," *Metall. Mater. Trans.*, **Vol.** 10A, pp. 259-61.

65. ***Rashid***, M. S., (1976), "A Unique High-Strength Sheet Steel with Superior Formability," *SAE preprint*, No.760206, **Vol.** 85, Section 2, pp. 938-49.

66. ***Rashid***, M. S., (1979), "Relationship Between Steel Microstructure and Formability," *Conf. Proc. on Formable HSLA and Dual-Phase Steels*, Kot, R.A. and Morris, J.W., ed., AIME, New York, pp. 1-24.

67. ***Repas***, P. E., (1979), "Physical Metallurgy of Dual Phase Steels," *Proc. of XVII Conf. on Mech. Working and Steel Processing*, AIME, New York, pp. 277-305.

68. ***Rohatgi***, P. K., Ray, S. and Liu, Y., (1992), "Tribological Properties of Metal Matrix-Graphite particle Composites," *Int. Mater. Review*, **Vol.** 37, No. 3, pp. 129-49.

69. ***Saka***, N., (1980), "Effect of Microstructure on Friction and Wear Behaviour of Metals," In N. P. Suh and N. Saka (eds.), *Proc. Int. Conf. on the Fundamentals of Tribology*, MIT Press, Cambridge, MA, pp. 135-169.

70. ***Saka***, N., Eleiche, A.M. and Suh, N.P., (1977), "Wear of Metals at High Sliding Speeds," *Wear*, **Vol.** 44, pp. 109-25.

71. ***Saka***, N., Pamies-Teixeira, J. J. and Suh, N. P., (1977), "Wear of Two-Phase Metals," *Wear*, **Vol.** 44, pp. 77-86.

72. ***Sarkar***, A. D., (1976), *Wear of Metals*, Pergamon Press Ltd., Headington Hill Hall, Oxford OX3 0BW, England.

73. ***Sawa***, M. and Rigney, D. A., (1987), "Sliding Behaviour of Dual Phase steels in Vacuum and in Air," *Wear*, **Vol.**119, pp. 369-90.

74. ***Shafia***, M. S. and Eyre, T. S., (1980), "The Effect of Surface Topography on the Wear of Steel," *Wear*, **Vol.** 61, pp. 87-100.

75. ***Sherman***, A. M. and Davies, R. G., (1979), "Fatigue of a Dual Phase Steel," *Metall. Mater. Trans. A*, **Vol.** 10 A, pp. 929-33.

76. ***Shaw***, M. C., (1977), "Dimensional Analysis of Wear Systems," *Wear*, **Vol.** 43, pp. 263-66.

77. ***Sin***, H. -C, Saka, N. and Suh, N. P., (1979), "Abrasive Wear Mechanisms and Grit Size Effect," *Wear*, **Vol.** 55, pp. 163-90.

78. ***Smith***, A. F., (1986), "The Friction and Sliding Wear of Unlubricated 316 Stainless Steel in Air at Room Temperature in the Load Range 0.5 – 0.90 N," *Wear*, **Vol.** 110, pp. 151-68.

79. ***Smith***, A. F., (1988), "The Unlubricated Reciprocating Sliding Wear of A Martensitic Stainless Steel in Air and CO_2 Between 20 and 300 ^{0}C," *Wear*, **Vol.** 123, pp. 313-31.

80. ***Speich***, G.R. and Miller, R.L., (1979), "Mechanical Properties of Ferrite-Martensite Steels," *Conf. Proc. on Structure and Properties of Dual-Phase Steels*, Kot, R.A. and Morris, J.W., eds., AIME, New York, pp. 145-82.

81. ***Stott***, F.H. and Wood, G.C., (1978), "The Influence of Oxides on the Friction and Wear of Alloys," *Trib. Int.*, **Vol.** 11, No. 4, pp. 211-18.

82. ***Stott***, F. H., (1998), "The Role of Oxidation in the Wear of Alloys," *Trib. Int.*, **Vol.** 31, No. 1-3, pp. 61-71.

83. ***Suh***, N. P., (1986), *Tribophysics*, Prentice – Hall Inc., Eaglewood Cliffs, New Jersey, USA.

84. ***Suh***, N. P. and Sin, H. -C., (1981), "The Genesis of Friction," *Wear*, **Vol.** 69, pp. 91-114.

85. ***Suh***, N. P., (1973), "The Delamination Theory of Wear," *Wear*, **Vol.** 25, pp. 111-24.

86. ***Suh***, N. P., (1977), "An Overview of the Delamination Theory of Wear," *Wear*, **Vol.** 44, pp. 1-16.

87. ***Sui***, X., Zhao, X., Li, X., Yao, W., Wang, Q., Ying, H., and Bi, W., (1992), *Proc.Conf. on Low carbon Silicon-Niobium dual phase steel wires for wear resistant screens, H.S.L.A Steels: Processing, Properties and Applications*, Beizing, China, 28 Oct-2 Nov 1990, *The Minerals, Metals and Materials Society*, 420, Commonwealth Dr., Warrendale, Pennsylvania 15086, USA, pp. 483-88.

88. ***Sullivan***, J. L. and Hodgson, S. G., (1988), "A Study of Mild Oxidational wear for Conditions of Low Load and Speed," *Wear*, **Vol.** 121, pp. 95-106.

89. ***Sullivan***, J. L., Quinn, T. F J. and Rowson, D. M., (1980), "Developments in the Oxidational Theory of Mild Wear," *Trib. Int.*, **Vol.** 13, No. 4, pp. 153-158.

90. ***Tanaka***, T., Nishida, M., Hashiguhi, K. and Kato, T., (1979), "Formation and Properties of Ferrite Plus Martensite Dual Phase Structures," *Conf. Proc. on Structure and Properties of Dual-Phase Steels*, Kot, R.A. and Morris, J.W., ed.; AIME, New York, pp. 221-41.

91. ***Venkatesan***, S and Rigney, D. A., (1992), "Sliding Friction and Wear of Plain Carbon Steels in Air and Vacuum," *Wear*, **Vol.** 153, pp. 163-78.

92. ***Wang***, Y., Pan, L. and Lei, T. C., (1991), "Sliding Wear Behavior of Pearlitic Structures in Eutectoid Steel," *Wear*, **Vol.** 143, pp. 57-69.

93. ***Wang***, Y., and Lei, T., (1996), "Wear Behavior of Steel 1080 with Different Microstructures During Dry Sliding," *Wear*, **Vol.** 194, pp. 44-53.

94. ***Wang***, Y., Lei, T and Liu, J., (1999), "Tribo-metallographic Behavior of High Carbon Steels in Dry Sliding II. Microstructure and Wear," *Wear*, **Vol.** 231, pp. 12-19.

95. ***Waterhouse***, R, B., (1977), "The Role of Adhesion and Delamination in the Fretting Wear of Metallic Materials," *Wear*, **Vol.** 45, pp. 355-64.

96. ***Wayne***, S. F. and Rice, S. L., (1983), "The Role of Microstructure in the Wear of Selected Steels," *Wear*, **Vol.** 85, pp. 93-106.

97. ***Welsh***, N. C., (1965), "The Dry Wear of Steels: I. The General Pattern of Behaviour," *Phil. Trans. R. Soc. A*, pp. 31-49.

98. ***Welsh***, N. C., (1965), "The Dry Wear of Steels: II. Interpretation and Special Features," *Phil. Trans. R. Soc. A*, pp. 51-70.

99. ***Whitehouse***, D. J., (1980), "The Effects of Surface Topography on Wear," in *Fundamentals of Tribology*, N. P. Suh and N. Saka, eds., MIT Press, Cambridge, MA.

100. ***Wilson***, J. E., Stott, F. M. and Wood, G. C., (1980), "The development of Wear Protective Oxides and Their Influence on Sliding Friction," *Proc. R. Soc. London, Ser. A*, pp. 557-74.

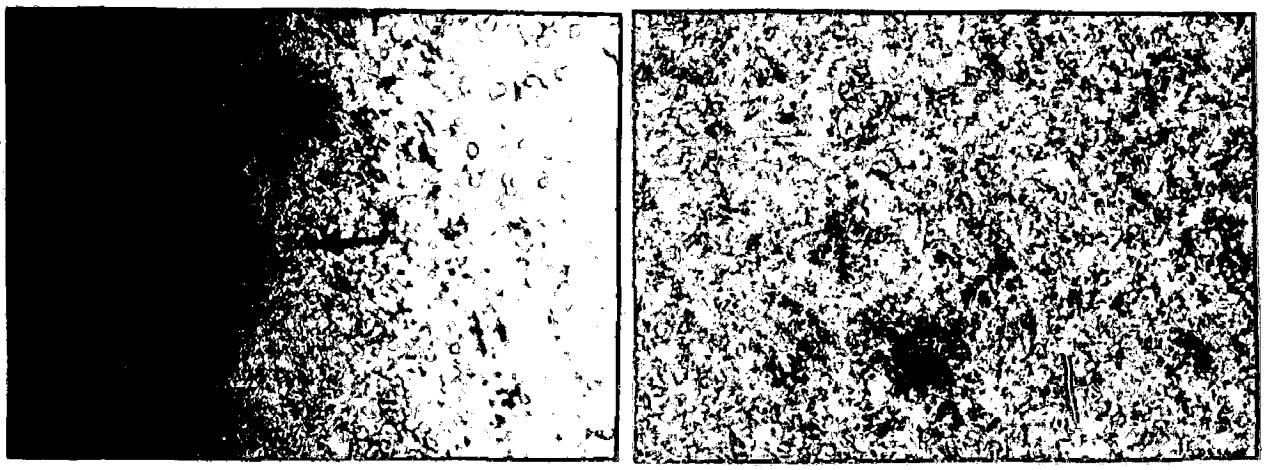

(a) (b)

Fig. 6.56 Optical micrographs showing subsurface microstructure of fully martensitic steel after sliding through a distance of 39.74 km at the normal loads of (a) 24.5 N, X 200 and (b) 34.3 N, X 200.

Fig. 6.57 SEM micrograph of the subsurface of the specimen of fully martensitic steel after sliding through a distance of 39.74 km under a load of 34.3 N, X 551, showing cracking below the subsurface (marked by arrow).

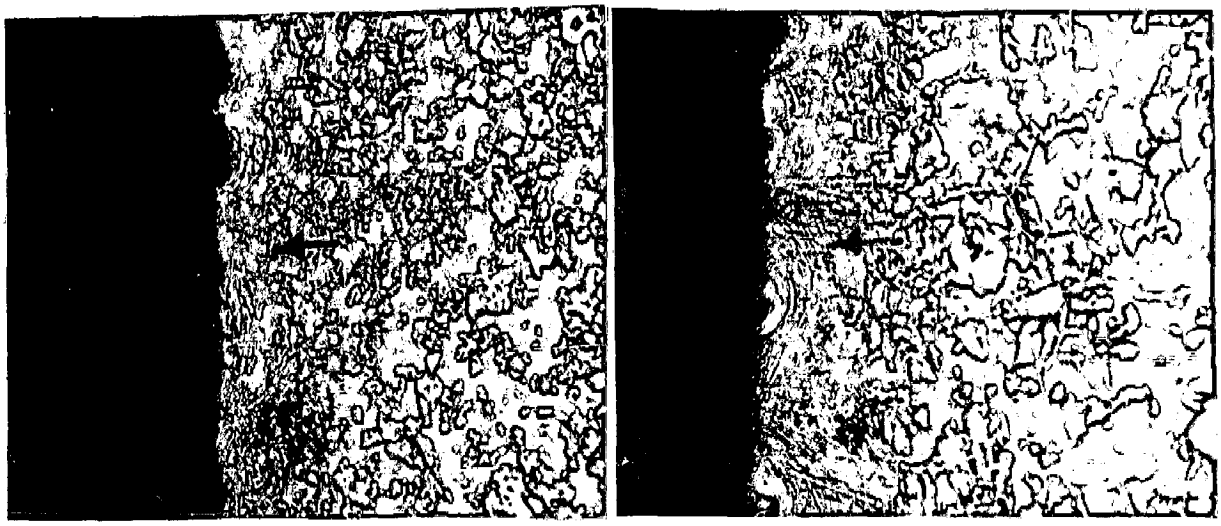

(a) (b)

Fig. 6.58 Optical micrographs showing subsurface microstructure of normalised steel after sliding through a distance of 39.74 km at the normal loads of (a) 14.7 N, X 200 and (b) 24.5 N, X 200. Arrow indicates the deformed layer of material.

Fig. 6.59 SEM micrograph of the subsurface of the specimen of normalised steel after sliding through a distance of 39.74 km under a load of 34.3 N, X 1010, showing cracking below the subsurface (marked by arrow).

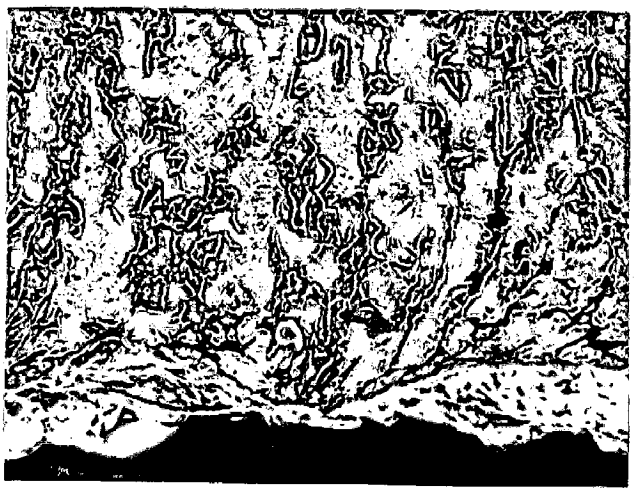

Fig. 6.60 SEM micrograph of the subsurface of the specimen of dual phase steel, DP1, after sliding through a distance of 39.74 km under a normal load of 34.3 N, X 801, showing cracking below the subsurface (marked by arrow).

(iv) Dual Phase Steels

Figure 6.60 shows the SEM micrograph of the subsurface of the specimen of DP1 steel after sliding through a distance of 39.74 km under a normal load of 34.3 N and at a fixed sliding velocity of 1.15 m/s. The deformed layer of the material in the subsurface region is visible in this micrograph. The subsurface cracks are also observed to be present and have been marked by the arrows in the micrograph.

The SEM micrographs of the subsurface of the specimens of DP2 steel after sliding through a distance of 39.74 km under the normal loads of 14.7, 24.5 and 34.3 N respectively, are shown in Figs. 6.61 (a) to (c). The deformed layer of material in the subsurface region is clearly visible and it is seen that the extent of deformation increases as the normal load increases. The subsurface cracks could also be observed in the Fig. 6.61 (c) as marked by arrow.

Figures 6.62 and 6.63 show the SEM micrographs of the subsurface of the specimens of DP3 and DP4 steels respectively, after sliding through a distance of 39.74 km under a normal load of 34.3 N. The deformed layer of the material in the subsurface region is visible in these micrographs. The subsurface cracks are also observed to be present and have been marked by the arrow in respective micrographs.

It is further observed that for a constant load of 34.3 N the extent of deformation in the subsurface region decreases as the volume fraction of the martensite increases in the dual phase steels from DP1 to DP4 as seen from the Figs. 6.60, 6.61, 6.62.and 6.63 respectively.

The subsurface microstructure of the DP4 steel after sliding through a distance of 39.74 km under the normal loads of 14.7, 24.5 and 34.3 N has also been examined under the optical microscope and the micrographs are shown in the Figs. 6.64 (a) to (c) respectively.

The microstructure near the subsurface region is different as compared to the region that is away from the subsurface as shown by the arrows in these micrographs. It can also be seen from these micrographs that the extent of the deformed layer increases with increasing load.

6.1.4 Examination of Wear Debris

The wear debris of Armco iron, fully martensitic steel, normalised steel and dual phase steels generated during sliding under different normal loads has been examined under the optical and the Scanning Electron (SEM) Microscope. Wear debris corresponding to both the linear segments i.e., run-in and steady state has been analysed separately. For the purpose of examination under the optical microscope, the wear debris collected during sliding was spread on a white paper and then photographed. Whereas for the purpose of examination under SEM the debris was sprinkled on an adhesive, coated and then photographed. The examination under Scanning Electron (SEM) Microscope is carried out to know the shape, size and nature of the wear particles.

(i) Armco Iron

The optical micrographs of the wear debris of Armco iron corresponding to the first linear segment (run-in), generated after sliding under the normal loads of 14.7, 24.5 and 34.3 N and at a fixed sliding velocity of 1.15 m/s are shown in Figs. 6.65 (a) to (c), respectively. The optical micrographs of the wear debris of Armco iron corresponding to the second linear segment (steady state), generated after sliding under the normal loads of 14.7, 24.5 and 34.3 N and at a fixed sliding velocity of 1.15 m/s are shown in Figs. 6.66 (a) to (c), respectively.

Some finer oxide particles apart from a few relatively larger agglomerates of oxides flaked off from the transfer layer are observed in both run-in and steady state of wear. No

(a)

(b)

(c)

Fig. 6.61 SEM micrographs of the subsurface of the specimen of dual phase steel, DP2, after sliding through a distance of 39.74 km under the normal loads of (a) 14.7 N, X 801, (b) 24.5 N, X 801 and (c) 34.3 N, X 801, showing deformed layer of material (marked by arrows).

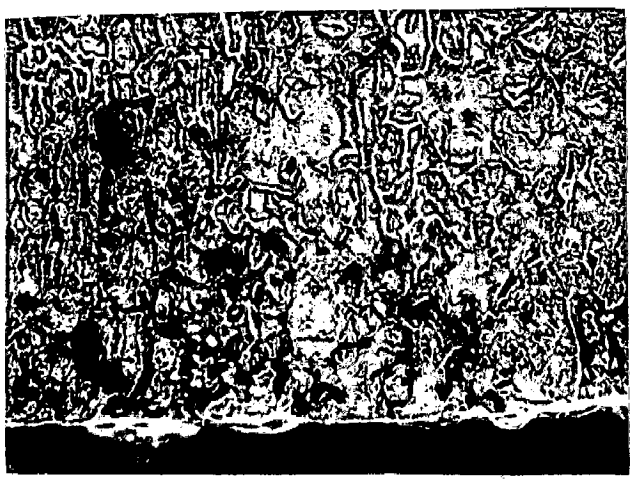

Fig. 6.62 SEM micrograph of the subsurface of the specimen of dual phase steel, DP3, after sliding through a distance of 39.74 km under a normal load of 34.3 N, X 801, showing cracking below the subsurface (marked by arrow).

Fig. 6.63 SEM micrograph of the subsurface of the specimen of dual phase steel, DP4, after sliding through a distance of 39.74 km under a normal load of 34.3 N, X 801, showing cracking below the subsurface (marked by arrow).

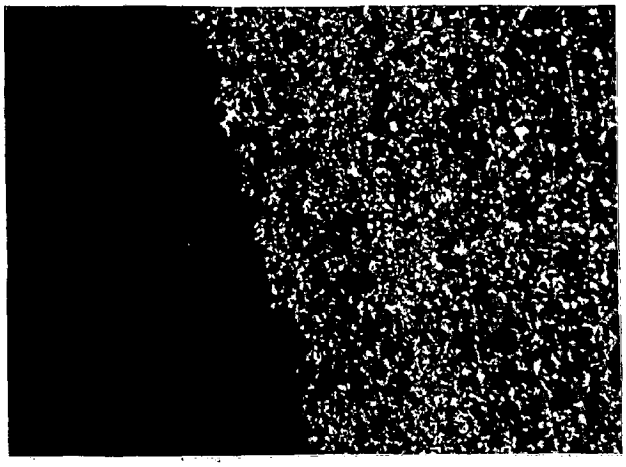

(a)

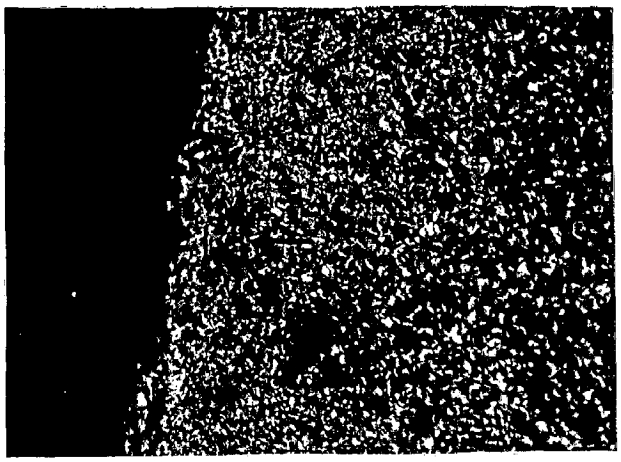

(b)

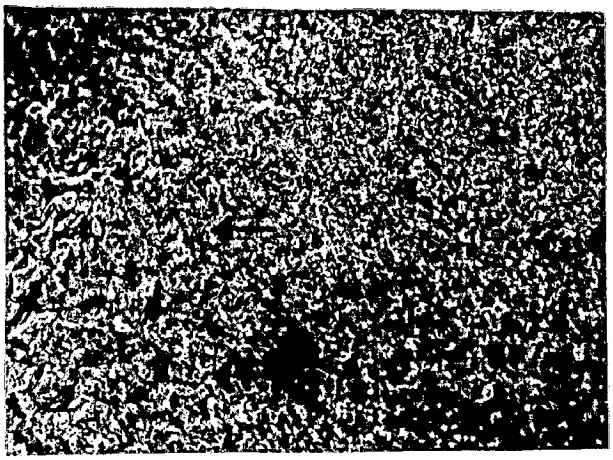

(c)

Fig. 6.64 Optical micrographs showing subsurface microstructure of dual phase steel, DP4, after sliding through a distance of 39.74 km at the normal loads of (a) 14.7 N, X 200 and (b) 24.5 N, X 200 and (c) 34.3 N, X 200.

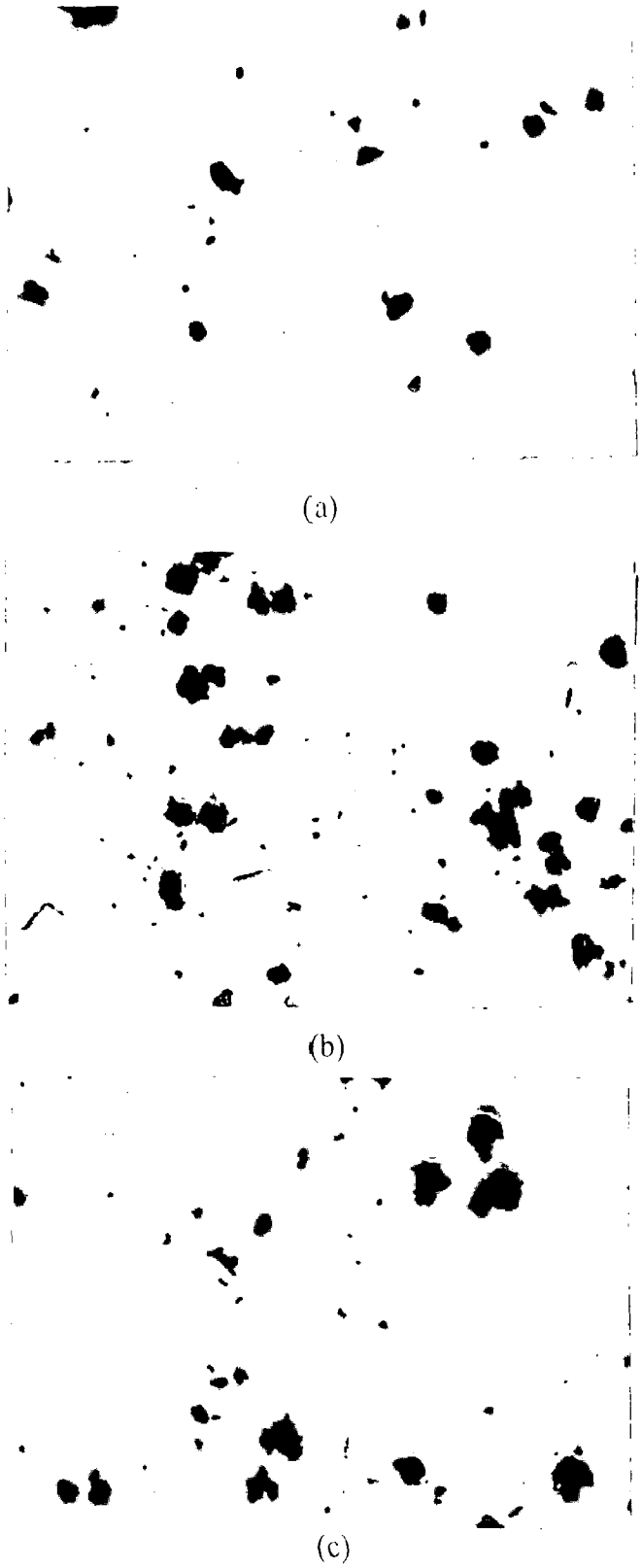

Fig. 6.65 Optical stereo micrographs showing wear debris of Armco iron spread on white paper, for short sliding distance corresponding to run-in stage at the normal loads of (a) 14.7 N, X 25, (b) 24.5 N, X 25 and (c) 34.3 N, X 25.

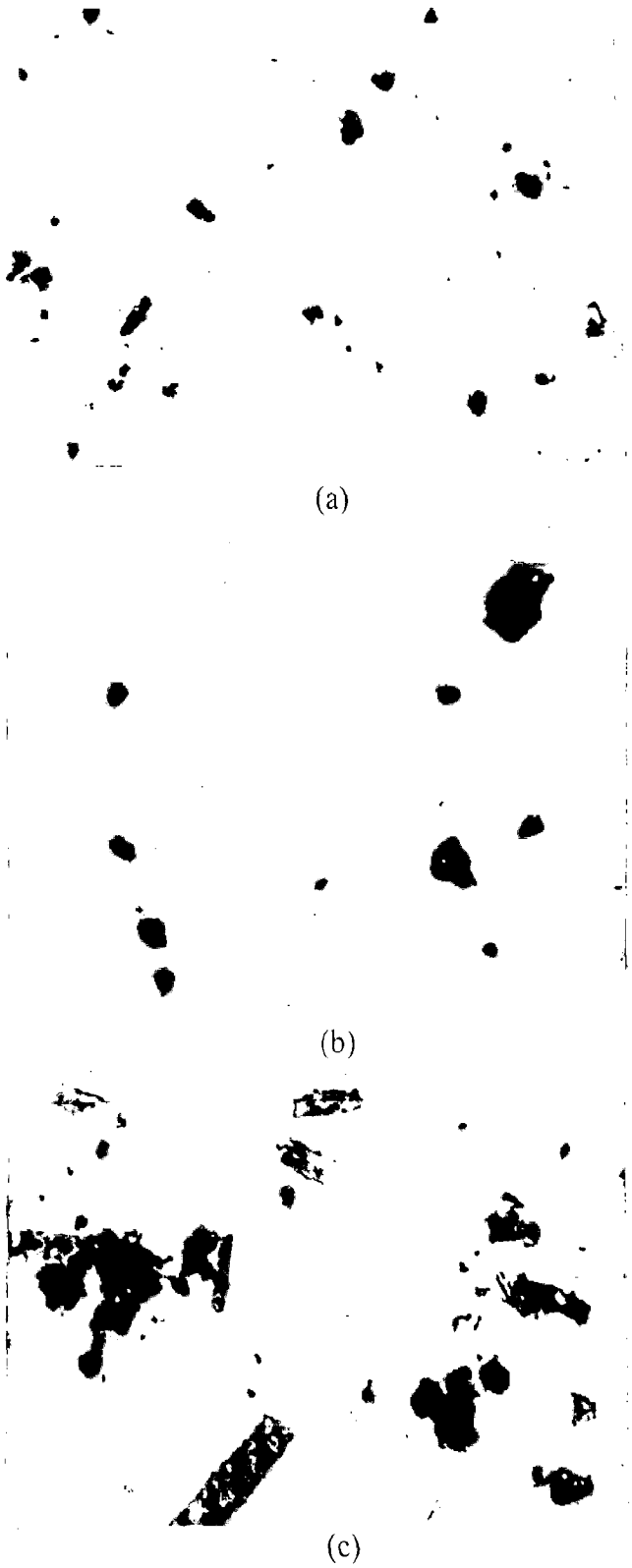

Fig. 6.66 Optical stereo micrographs showing wear debris of Armco iron spread on white paper, for longer sliding distances corresponding to steady state at the normal loads of (a) 14.7 N, X 25, (b) 24.5 N, X 25 and (c) 34.3 N, X 25.

metallic particle is observed in the wear debris of both the run-in and the steady state. The wear debris particles are found to be ferromagnetic in nature.

The SEM micrographs of the wear debris of Armco iron generated during run-in stage are shown in Figs. 6.67 (a) and (b) whereas the Figs. 6.68 (a) and (b) show the SEM micrographs of the wear debris generated during steady state of wear. It can be seen from these micrographs that most of the agglomerates are just clusters of flaked off transfer layer. However, some spherical particles are also present which could be inclusions, as seen in Figs. 6.67 (a) and (b). The debris particles are observed to be finer in the steady state as compared to those in run-in stage which can be judged from the Figs. 6.67 (a) and 6.68 (a).

(ii) Fully Martensitic Steel

The optical micrographs of the wear debris of FMS corresponding to the first linear segment (run-in), generated after sliding under the normal loads of 14.7, 24.5 and 34.3 N are shown in Figs. 6.69 (a) to (c), respectively. The optical micrographs of the wear debris of FMS generated during steady state wear after sliding under the normal loads of 14.7, 24.5 and 34.3 N are shown in Figs. 6.70 (a) to (c), respectively.

The presence of some finer oxide particles apart from the flaked off transfer layer of oxide can be clearly seen from these micrographs of debris generated in both the run-in and the steady state of wear. It is further observed that the size of the agglomerates of wear debris decreases with increasing load in both the run-in and the steady state as seen from Figs. 6.69 (a) to (c) and 6.70 (a) to (c). No metallic particle is observed to be present in the wear debris generated either in run-in or in steady state.

The SEM micrographs of the wear debris of the FMS corresponding to the steady state are shown in Figs. 6.71 (a) and (b). Some finer oxide particles apart from the agglomerates of the flaked off transfer layer are present as seen from the micrographs. It is further observed from the micrographs that the size of the agglomerates is relatively smaller compared to those of Armco iron shown in Figs. 6.68 (a) and (b).

(iii) Normalised Steel

Figures 6.72 (a) and (b) show the optical micrographs of the wear debris of normalised steel generated in the run-in and the steady state, respectively. Some finer oxide particles apart from a few larger agglomerates of oxide are observed in both these micrographs but the size of the wear debris agglomerates is smaller in the steady state as compared to that in the run-in stage as seen from Figs. 6.72 (a) and (b).

Figures 6.73 (a) and (b) show the SEM micrographs of the wear debris of normalised steel generated during run-in stage whereas Figs. 6.74 (a) and (b) show the SEM micrographs of the wear debris of this steel generated during steady state wear. The flaked off particles from transfer layer of oxide can be seen in the micrographs. The particles or agglomerates of compacted transfer layer are observed to be finer for the steady state as compared to that for run-in stage of wear as seen from the Figs. 6.73 (a) and 6.74 (b).

(iv) Dual Phase Steels

Figures 6.75 (a) and (b) show the optical micrographs of the wear debris of DP1 steel generated during the run-in and the steady state wear, respectively. There are some larger agglomerate of flaked off transfer layer apart from finer oxide particles in the wear debris corresponding to both run-in and steady state but the difference in the size of the larger

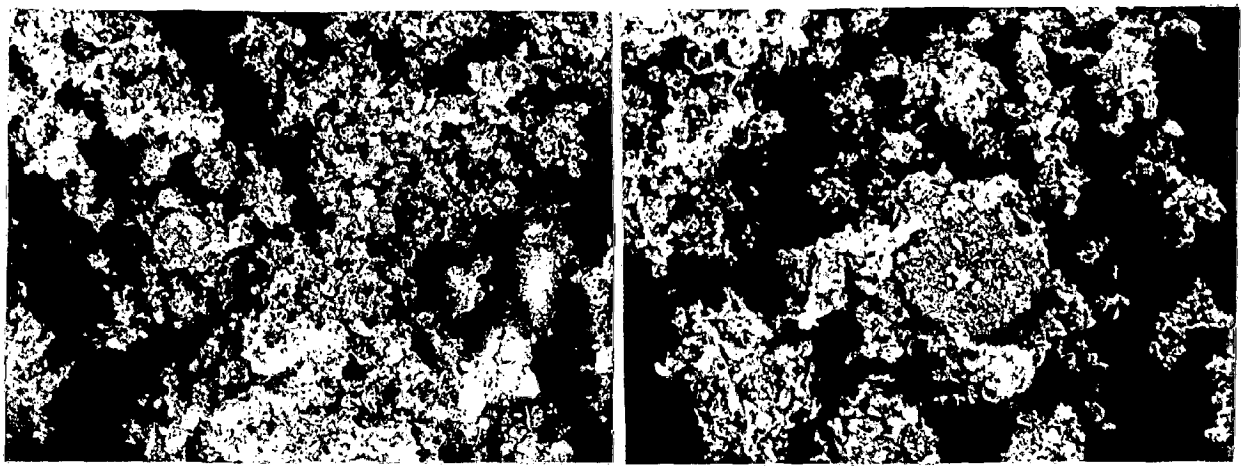

(a) (b)

Fig. 6.67 SEM micrographs showing wear debris of Armco iron corresponding to the run-in stage (a) X 150 and (b) X 400.

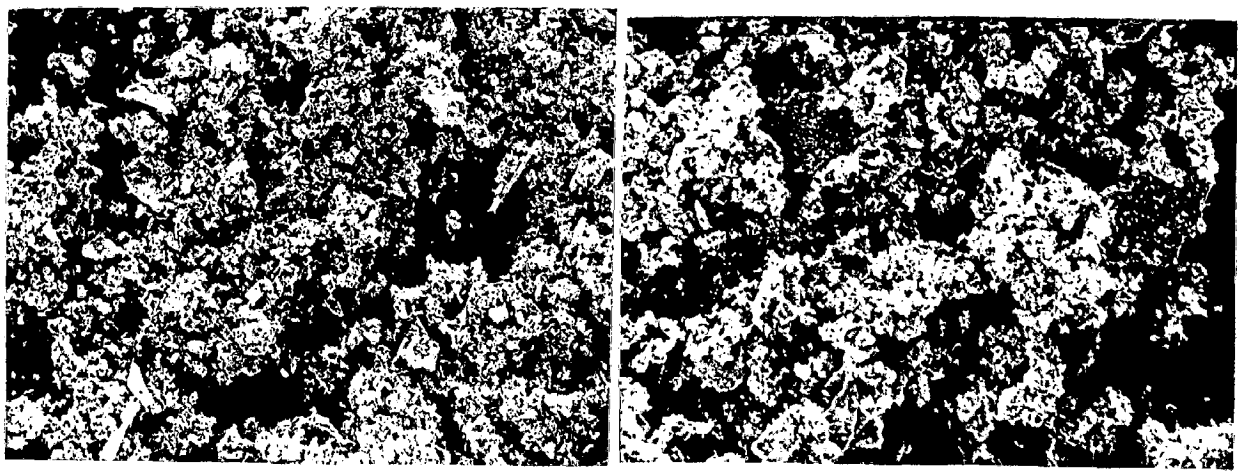

(a) (b)

Fig. 6.68 SEM micrographs showing wear debris of Armco iron corresponding to the steady state (a) X 150 and (b) X 400.

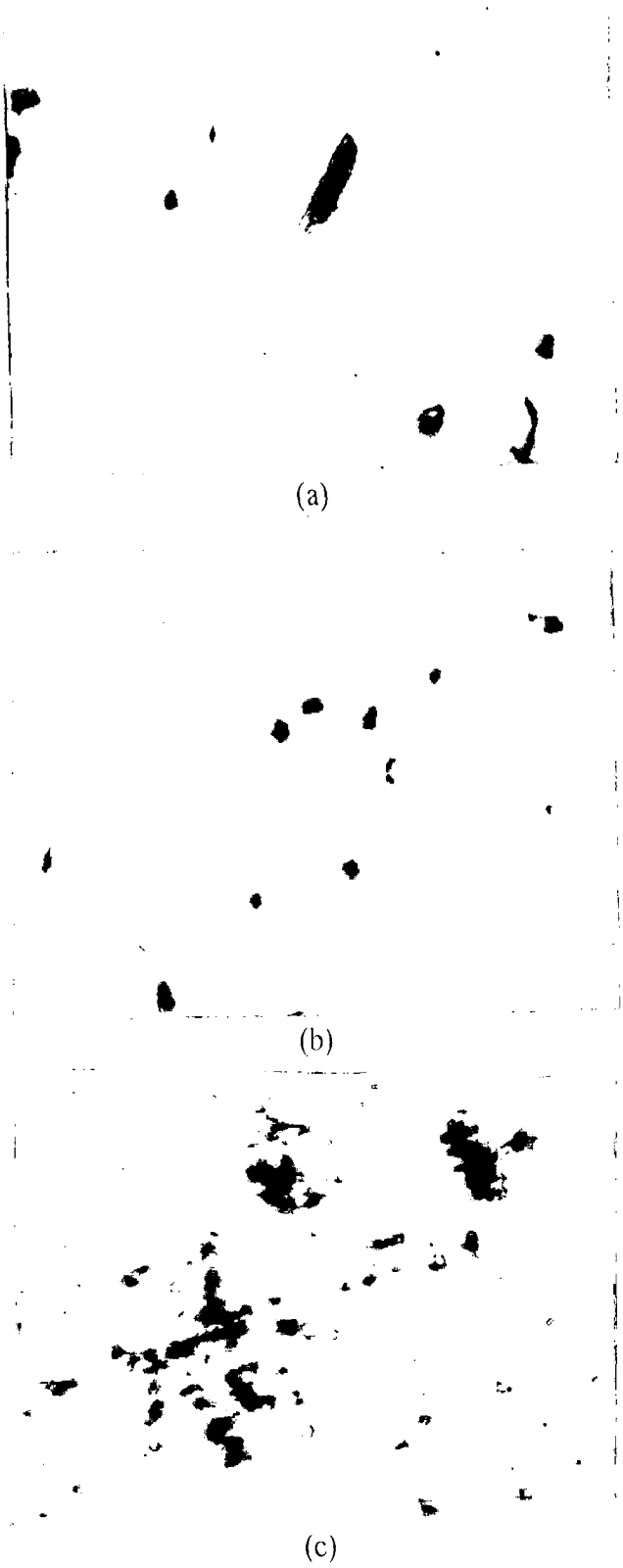

Fig. 6.69 Optical stereo micrographs showing wear debris of FMS spread on white paper, for short sliding distances corresponding to run-in stage at the normal loads of (a) 14.7 N, X 25, (b) 24.5 N, X 25 and (c) 34.3 N, X 25.

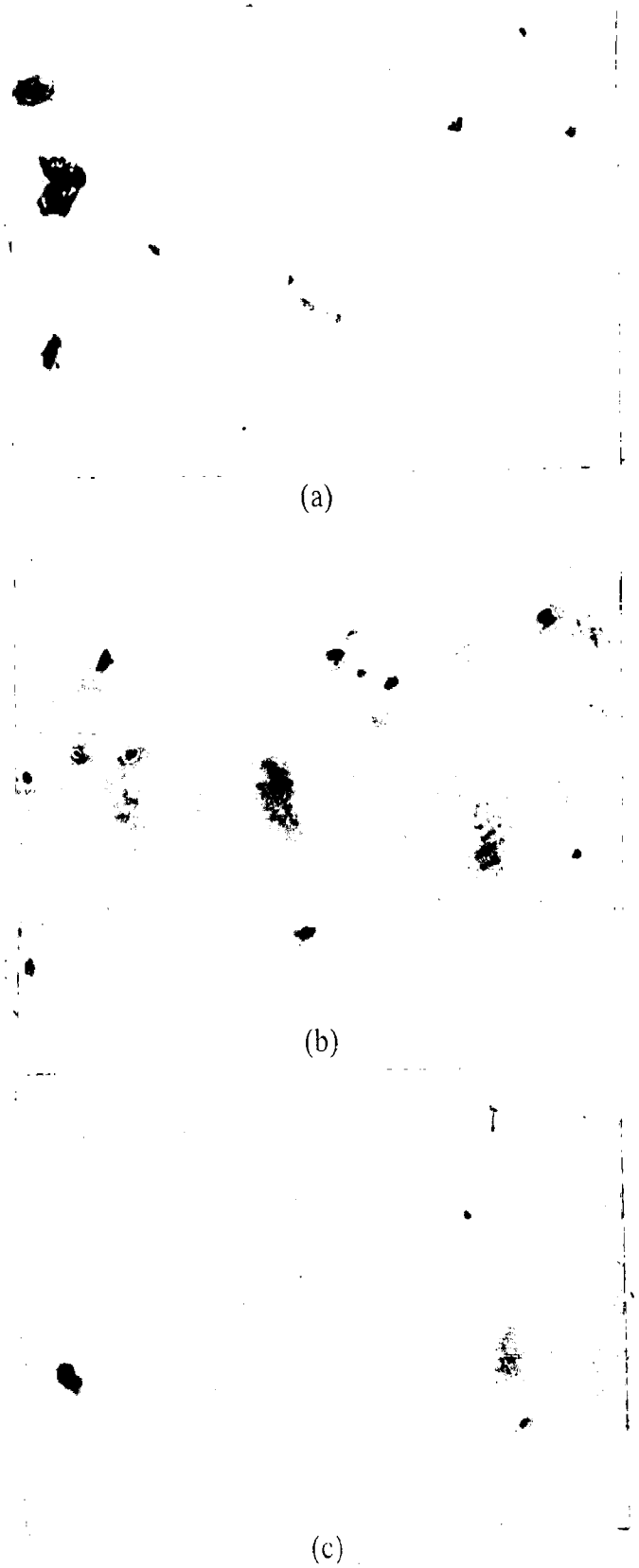

Fig. 6.70 Optical stereo micrographs showing wear debris of FMS spread on white paper, for longer Sliding distances corresponding to steady state at the normal loads of (a) 14.7 N, X 25, (b) 24.5 N, X 25 and (c) 34.3 N, X 25.

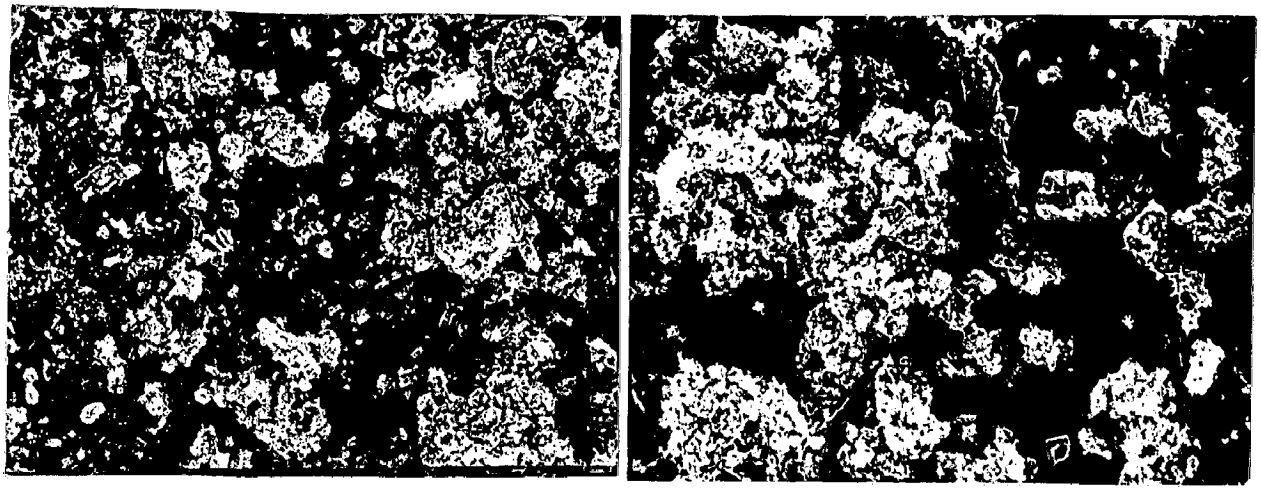

(a) (b)

Fig. 6.71 SEM micrographs showing wear debris of FMS corresponding to the steady state (a) X 150 and (b) X 400.

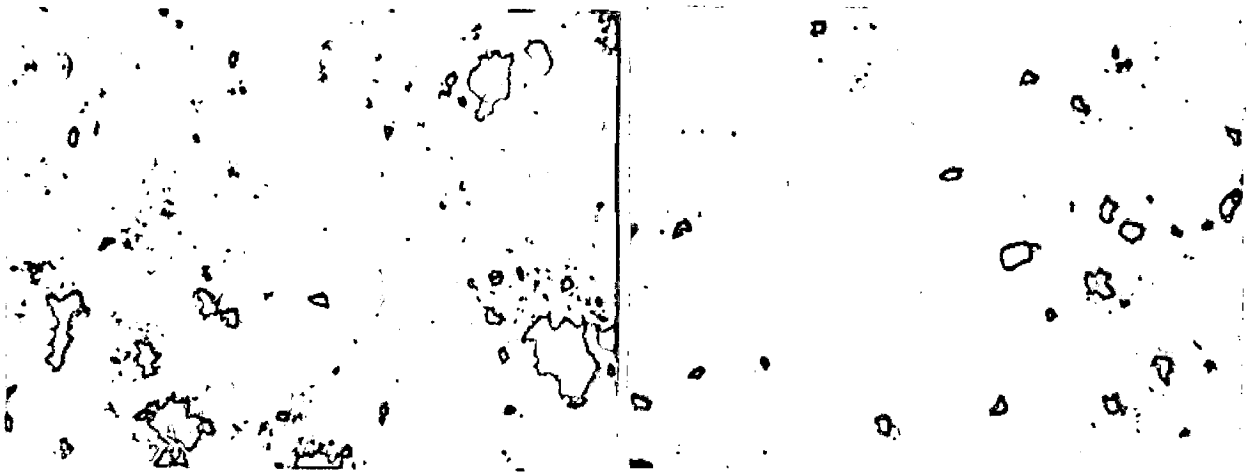

(a) (b)

Fig. 6.72 Optical stereo micrographs showing wear debris of N steel spread on white paper, for (a) short sliding distances corresponding to run-in, X 25 and (b) longer sliding distances corresponding to steady state, X 25.

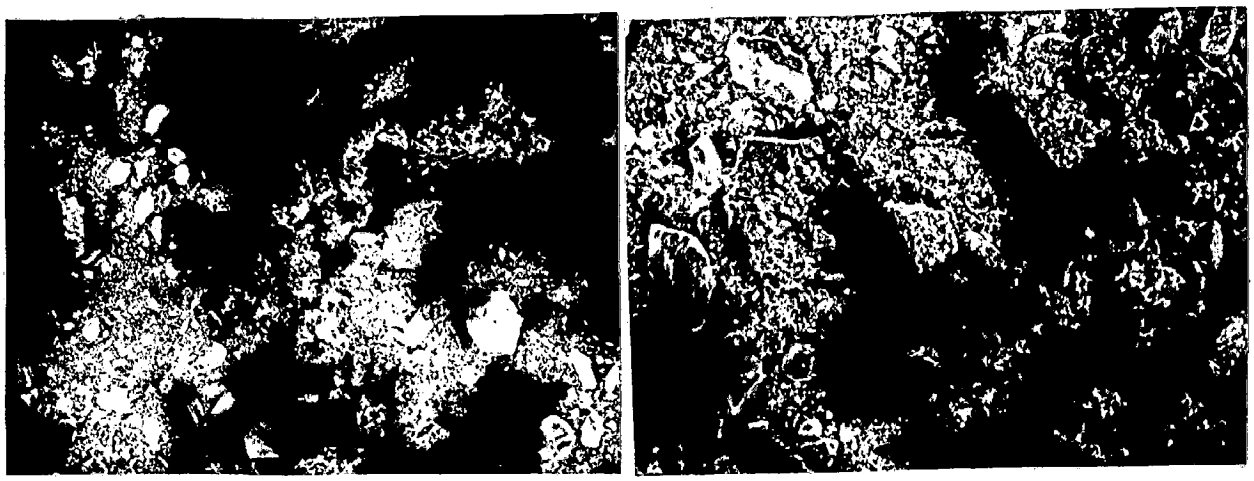

(a) (b)

Fig. 6.73 SEM micrographs showing wear debris of N steel corresponding the run-in stage (a) X 150 and (b) X 400

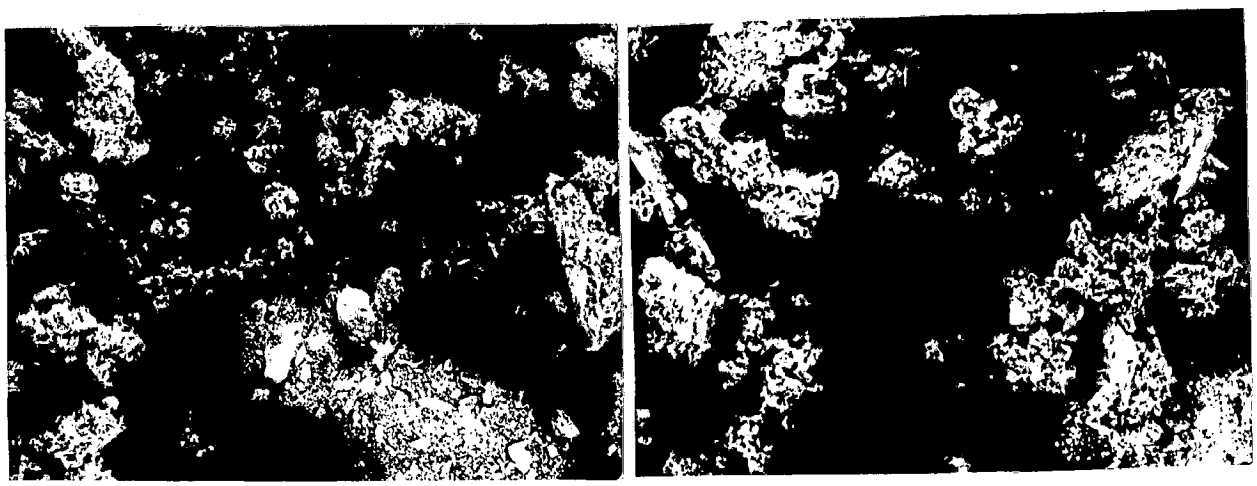

(a) (b)

Fig. 6.74 SEM micrographs showing wear debris of N steel corresponding to the steady state (a) X 150 and (b) X 400.

agglomerates and other fine particles is less in the steady state as compared to that in the run-in stage. It can also be seen that the size of the agglomerates of wear debris is smaller in the steady state as compared to that in the run-in stage of wear as seen from Figs. 6.75 (a) and (b). The agglomerates of the flaked off particles from transfer layer appear to be more compacted in nature in the steady state as compared to those generated during the run-in stage of wear. No metallic particle is observed in the wear debris corresponding to both the run-in and the steady state wear.

Figures 6.76 (a) and (b) show the optical micrographs of the wear debris of DP2 steel generated during the run-in and the steady state wear. It can be seen that the size of the wear debris is smaller in the steady state as compared to that in the run-in stage It is further observed that the agglomerates are more compacted in nature in the steady state as compared to those for the run-in stage of wear. No metallic particle is observed to be present in the wear debris corresponding to both the run-in and the steady state wear.

Figures 6.77 (a) and (b) show the optical micrographs of the wear debris of DP3 steel generated during the run-in and the steady state wear. The size of the wear debris is observed to be smaller in the steady state as compared to that in the run-in stage. It is further observed that the agglomerates are more compacted in nature in the steady state as compared to those in the run-in stage of wear. No metallic particle is observed to be present in the wear debris generated during both the run-in and the steady state wear.

Figures 6.78 (a) and (b) show the optical micrographs of the wear debris of DP4 steel generated during the run-in and the steady state wear. It can be seen that the size of the wear debris is smaller in the steady state as compared to that in the run-in stage. It is further observed that the agglomerates generated during steady state wear are more compacted in nature as compared to those generated during the run-in stage of wear. No metallic particle is

observed to be present in the wear debris generated during both the run-in and the steady state wear.

It is further observed that in dual phase steels the size of the wear debris decreases and becomes finer as the martensite volume fraction increases from DP1 to DP4 and this is true for both the run-in and the steady state wear as seen from Figs. 6.75 to 6.78.

The SEM micrographs of the wear debris of the DP2 steel generated during the run-in and the steady state wear are shown in Figs. 6.79 (a) and (b), respectively. Some irregularly shaped flaked off compacted transfer layer of oxides form the debris that corresponds to run-in stage as seen in Fig. 6.79 (a), but a few finer oxide particles could be observed apart from these larger flakes in the debris generated during the steady state wear as seen from the Fig. 6.79 (b). It can further be observed from these micrographs that the flaked off compacted debris are smaller in size in the steady state as compared to that in the run-in stage of wear.

6.1.5 X-Ray Diffraction Studies

The X-ray diffraction studies have been carried out on the wear debris of Armco iron, N steel and DP steels by using an iron target. The debris generated during the run-in stage of wear has been analysed separately from that generated during the steady state wear. The X-ray diffraction studies could not be carried out on the wear debris of the fully martensitic steel because of the very little amount of the debris generated.

Figure 6.80 shows the X-ray diffraction pattern of the wear debris of Armco iron generated during the steady state wear. The pattern shows only three broad peaks and all of these peaks correspond to α-Fe_2O_3 as observed by comparing with ASTM chart.

Fig. 6.75 Optical stereo micrographs showing wear debris of DP1 steel spread on white paper, for (a) short sliding distances corresponding to run-in, X 25 and (b) longer sliding distances corresponding to steady state, X 25.

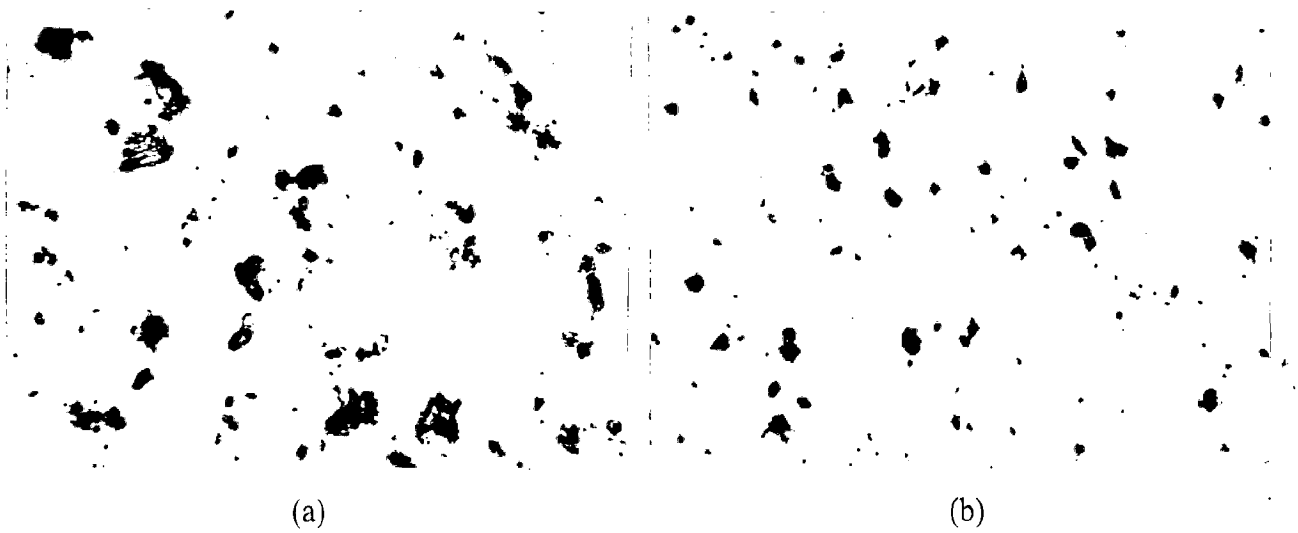

Fig. 6.76 Optical stereo micrographs showing wear debris of DP2 steel spread on white paper, for (a) short sliding distances corresponding to run-in, X 25 and (b) longer sliding distances corresponding to steady state, X 25.

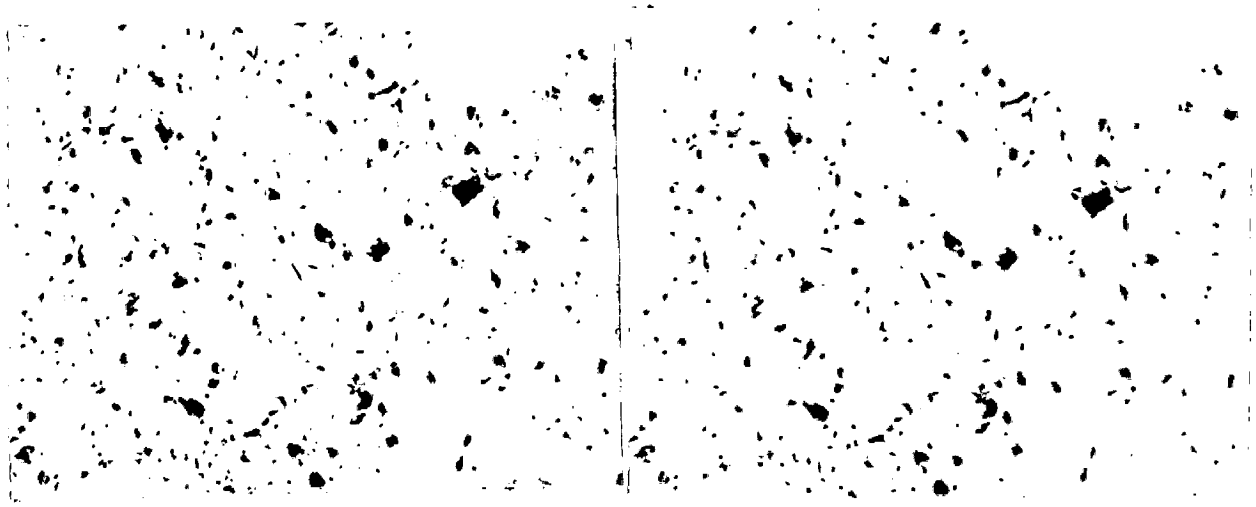

(a) (b)

Fig. 6.77 Optical stereo micrographs showing wear debris of DP3 steel spread on white paper, for (a) short sliding distances corresponding to run-in, X 25 and (b) longer sliding distances corresponding to steady state, X 25.

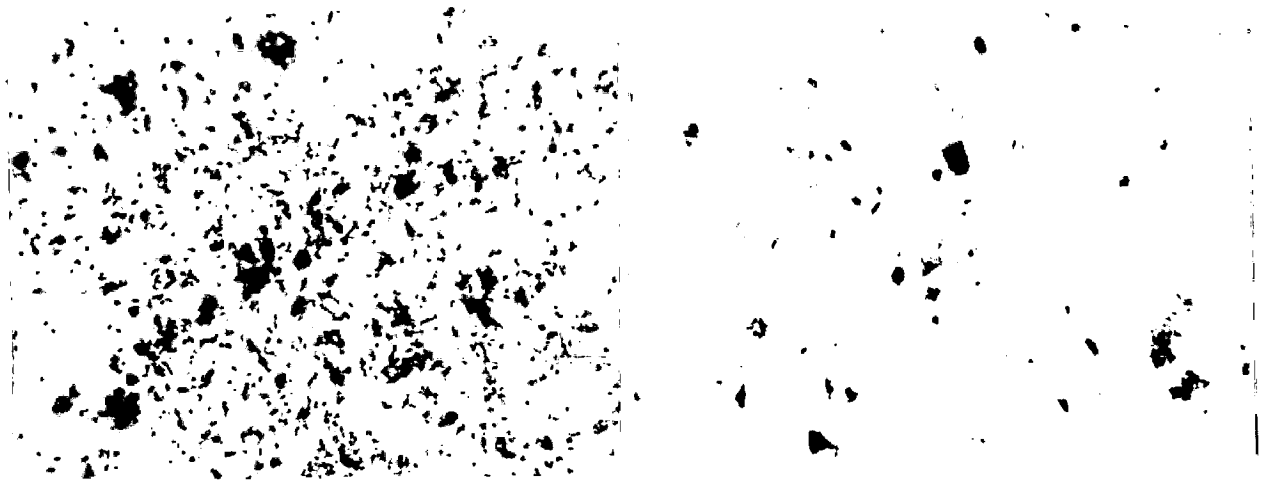

(a) (b)

Fig. 6.78 Optical stereo micrographs showing wear debris of DP4 steel spread on white paper, for (a) short sliding distances corresponding to run-in, X 25 and (b) longer sliding distances corresponding to steady state, X 25.